

# Frustration Phenomena due to Elastic Anisotropy in Thin Liquid Crystal Films

Submitted by

Timothy James Atherton

to the University of Exeter as a thesis for the degree of  
Doctor of Philosophy in Physics, December 2006

This thesis is available for Library use on the understanding that it is copyright material and that no quotation from the thesis may be published without proper acknowledgement.

I certify that all material in this thesis which is not my own work has been identified and that no material has previously been submitted and approved for the award of a degree by this or any other University.

*to Dad, in memoriam*

*“For now we see as through a glass, darkly”*

—I Corinthians 13:11

*“Iamque opus exegi, quod nec Iovis ira nec ignis  
nec poterit ferrum nec edax abolere vetustas.  
cum volet, illa dies, quae nil nisi corporis huius  
ius habet, incerti spatium mihi finiat aevi:  
parte tamen meliore mei super alta perennis  
astra ferar, nomenque erit indelebile nostrum,  
quaque patet domitis Romana potentia terris,  
ore legar populi, perque omnia saecula fama,  
si quid habent veri vatum prefagia, vivam.”*

—Ovid, *Metamorphoses* Book XV

# Abstract

Spontaneous pattern formation is a well-known phenomenon in the liquid crystal field; the competing influence of different physical effects—surface alignment, chirality, applied electromagnetic fields, smectic ordering—that favour incompatible ground states typically cause the system to self-organize into some compromise configuration. The aim of the work presented in this thesis is then to analyse and elucidate the physical origin of some recently observed examples of pattern formation.

The first system is a nonchiral smectic liquid crystal in a cell with opposing easy axes (a “hybrid-aligned” cell), which was recently shown to adopt the configuration of an array of fan-shaped domains arranged on a hexagonal lattice. This system is studied for the first time by confocal microscopy, and the very regular arrangement shown to be due to nucleation of the domains through an intermediate striped structure. Comparison is made with earlier work, and the unusual shape of the domains is shown to be very likely due to surface pretilt at the planar substrate.

The second system is a nematic in contact with a surface patterned with alternate micron-width stripes that favour homeotropic and planar alignment respectively. It was recently experimentally shown in such a cell that, even if the easy axis of the planar stripes were set to lie orthogonal to their length, that the nematic would nonetheless “escape to the third dimension”, rotating to lie along the length of the stripes. It is shown that this is due to elastic anisotropy and a quantitative model is developed. For the first time, a complete phase diagram for the system is presented including the possibility of adopting uniform configurations. The use of such surfaces to construct devices is also discussed and the model extended so as to explain some anomalous results from efforts to build Twisted Nematic cells from striped substrates. Finally, static numerical simulations of the switching of such a device are carried out.

# Contents

Acknowledgements	13
Introduction	15
I Background	18
1 Liquid Crystal Physics	19
1.1 Liquid Crystalline Order . . . . .	19
1.1.1 The Nematic Phase . . . . .	20
1.1.2 Smectic Phases . . . . .	20
1.1.3 Order Parameters . . . . .	22
1.1.4 Theoretical Descriptions of Liquid Crystals . . . . .	25
1.2 Nematic Continuum Theory . . . . .	26
1.2.1 Fundamental Equations . . . . .	27
1.2.2 Formulations of Continuum Theory for Numerical Solution . . . . .	29
1.2.2.1 Polar Coordinates . . . . .	29
1.2.2.2 Cartesian Director Components . . . . .	29
1.2.2.3 Q-Tensor . . . . .	30
1.3 Surface Effects . . . . .	30
1.3.1 Physical Origin of Surface Anchoring . . . . .	30
1.3.2 Phenomenological Descriptions . . . . .	31
1.4 Example: HAN Cell Statics . . . . .	35

2	Microscopy of Liquid Crystal Structures	38
2.1	Polarizing Microscopy . . . . .	38
2.2	Confocal Microscopy . . . . .	42
II	Results	53
3	What Configuration does a Smectic-A Adopt in a Hybrid Aligned Cell?	54
3.1	Cell Construction . . . . .	56
3.2	Polarizing Microscopy . . . . .	58
3.3	Effect of Cell Thickness . . . . .	63
3.4	Confocal Microscopy . . . . .	69
3.5	Discussion . . . . .	73
4	Models for Smectic-A in a Hybrid-Aligned Cell	79
4.1	Physics of the Nematic-Smectic-A Transition . . . . .	80
4.1.1	Experimental Measurements of the Critical Exponents . . . . .	81
4.1.2	Self-organized Periodic Structures in other Liquid Crystal Geometries . . . . .	82
4.2	The “Stripe” Structure . . . . .	84
4.3	Structure of the V-shaped Defects . . . . .	88
4.4	Behaviour in the Smectic Phase . . . . .	89
4.4.1	In Cells Prepared with Silicon Oxide as an Aligning Layer . . . . .	89
4.4.2	The structure of Ruan <i>et al.</i> . . . . .	100
4.5	Summary . . . . .	103
5	Nematics in Contact with Patterned Surfaces	106
5.1	Applications of Surface Patterning . . . . .	106
5.2	Techniques for Surface Micropatterning . . . . .	107
5.3	Nematic in Contact with a Striped Surface . . . . .	109
5.4	Anomalous Behaviour of Splay-Bend Structures at Short Wavelength . . . . .	113
5.4.1	Experiment . . . . .	113
5.4.2	Model . . . . .	114

5.4.2.1	Rigid Polar Anchoring . . . . .	116
5.4.2.2	Finite Anchoring . . . . .	118
5.5	Uniform–Distorted Transition due to Weak Polar Anchoring . . . . .	120
5.6	Switchable Diffraction Gratings . . . . .	122
5.7	Discussion . . . . .	126
6	Twisted Nematic Cells Constructed From Micropatterned Substrates	128
6.1	A Novel Uniform Configuration in a Micropatterned TN Cell . . . . .	129
6.2	Numerical Simulation of TN Cells Constructed From Micropatterned Surfaces . . . . .	136
6.3	Simulation of a Twisted Nematic Cell with Micropatterned Surfaces . . . . .	140
6.4	Smectic Liquid Crystals in Contact with Micropatterned Surfaces . . . . .	141
6.5	Discussion . . . . .	145
III	Conclusions	147
7	Conclusion	148
7.1	Summary of Results . . . . .	148
7.2	Open Problems and Future Work . . . . .	151
7.3	Publications . . . . .	152
7.4	Conference Presentations . . . . .	153
	Appendices	155
A	Natural Boundary Conditions for Liquid Crystal Problems	155
B	Reconstruction of the Director from Microscope Images	157
C	Critical Exponents for the Elastic Constants in 8CB	161
D	The Nematic Euler–Lagrange Equations	164
E	Stability of Explicit Solvers for Nematics	166

# List of Figures

1.1	Schematic of the molecular ordering in a nematic phase. . . . .	21
1.2	Schematic of the molecular ordering in a smectic-A phase. . . . .	21
1.3	The six families of surface that are compatible with the condition of constant layer spacing for an incompressible smectic. . . . .	23
1.4	Schematic of pure splay, twist and bend deformations which are associated with the $K_1$ , $K_2$ and $K_3$ elastic constants respectively. . . . .	28
1.5	Two possible configurations for the nematic director field adjacent to a sinusoidal grating; the uniform planar state has no elastic distortion and therefore lower energy. . . . .	32
1.6	Schematic of smectic layers adjacent to a flat surface. While homeotropic (a) and planar (b) orientations are compatible, a tilted (c) configuration ought to require the nucleation of defects. . . . .	34
1.7	Static HAN Profiles for $K_1 \ll K_3$ , $K_1 = K_3$ and $K_1 \gg K_3$ with rigid anchoring. . . . .	37
2.1	Polarizing microscope images taken with crossed polarizers of a hybrid aligned cell with planar degenerate surface in (a) the nematic phase and (b) the smectic phase. . . . .	40
2.2	Schematic of some possible configurations of the director field around a point disclination in the plane in which the core of disclination sits with (bottom) simulated images as might be seen under the polarizing microscope. Disclinations are characterised by their strength $s$ . Note that disclinations of the same magnitude with opposing signs are indistinguishable from a single image alone. . . . .	41
2.3	Reconstructed in-plane component of a possible configuration of the director field from a polarizing microscope image of a nematic in a hybrid aligned cell. . . . .	42
2.4	The Leica SP5 confocal microscope installed in the School of Physics at the University of Exeter. . . . .	44
2.5	Schematic of a confocal microscope illustrating how light from the in-focus plane is allowed to pass through the pinhole while light from an out of focus plane is excluded. . . . .	44



2.6	Schematic of how spatial orientation of a dye-doped liquid crystal produces a variation of fluorescence intensity within a region at the focus of a pump laser. The anisotropic dye molecules are aligned in the liquid crystal by the guest-host effect and the local average orientation of the dye molecules is parallel to that of the liquid crystal. . . . .	45
2.7	(Top) Cross sections reconstructed from FCM images of a planar Freedericks cell with several values of applied voltage. (Below) Intensity profiles obtained by averaging over the width of each cross section. . . . .	49
2.8	Intensity profile from cross sections of a $6\mu\text{m}$ planar cell with no applied voltage, taken with the alignment direction at $0^\circ$ , $45^\circ$ and $90^\circ$ to the optic axis of the polarizer. . . . .	49
3.1	Polarizing microscope image of Ruan <i>et al</i> 's fan-shaped structure. . . . .	55
3.2	Ruan <i>et al</i> 's model of spherocylinders for the smectic structure . . . . .	55
3.3	Transmission spectrum of an empty (air-filled) $2.7\mu\text{m}$ thick cell. . . . .	57
3.4	Polarizing microscope image of 8CB in a HAN cell in the nematic phase. . . . .	58
3.5	Polarizing microscope images of the phase sequence of 8CB in a HAN cell as the liquid crystal goes through the nematic-smectic transition with decreasing temperature. . . . .	60
3.6	Images of the stripe structure under the polarizing microscope where the cell is rotated with respect to the fixed polarizers. . . . .	60
3.7	Detailed view of a 'V' defect as the cell is cooled from the stripe structure into the focal conic structure. . . . .	61
3.8	Polarizing microscope images of the interaction of two opposing 'V' defects. (Left) Defects with a single stripe in common annihilate. (Right) Defects on adjacent pairs of stripes pass each other unaffected. . . . .	62
3.9	Polarizing microscope images extracted from a video recording of the phase sequence of 8CB in a HAN cell as the liquid crystal goes through the nematic-smectic transition. . . . .	64
3.10	Polarizing microscopy image of a hybrid aligned cell in the nematic phase following repeated cooling and heating through the nematic-smectic transition. The intensity of illumination is high revealing a "surface memory" of the low temperature "fan" structure even though the liquid crystal is here in the nematic phase as may be seen from the presence of disclination lines. . . . .	65
3.11	Focal conic structure with evaporated silicon oxide as the planar aligning layer. . . . .	65
3.12	Custom image processing program used to extract the period of the stripes. . . . .	66

3.13 (Top) Plot of a single line from a digital polarizing microscope image of the “stripe” structure. (Below) The period of the structure is found automatically from the Fourier modulus transform or the autocorrelation function of the signal; both are plotted with arbitrary scales on the vertical axis. . . . .	68
3.14 Variation of the period of (a) the “stripe” structure and (b) the “modulated stripe” structure with the cell thickness. Each point represents a single cell and the vertical extent of the bars indicate 95% confidence intervals. Data from Ruan <i>et als</i> ’ paper is shown in red; the vertical extent has no significance for these points. . . . .	70
3.15 FCM Cross section of a HAN cell with an intensity profile obtained by averaging the image horizontally. . . . .	71
3.16 Confocal microscope (FCM) image of the disclination between two HAN states. The horizontal sections are taken from (left) the planar surface at $0.9\mu\text{m}$ intervals to (right) approximately the centre of the cell. A reconstructed cross section through the cell (top) reveals the structure of the disclination and is marked with the location of the horizontal sections. . . . .	71
3.17 FCM of the “stripe” structure taken with the confocal microscope . . . . .	72
3.18 FCM axial section of a HAN cell near but above the planar substrate of the “modulated stripe” structure. . . . .	73
3.19 FCM axial sections and cross sections in two sequences of orthogonal planes of Ruan <i>et als</i> ’ structure. . . . .	74
3.20 FCPM image of a unit cell from the hexagonal structure in a HAN cell prepared with a silicon oxide planar surface: (left) reconstructed cross section from a line oriented parallel to the polarizer through the centre of the domain and (right) axial sections through the structure. . . . .	75
3.21 Simulated confocal microscope images of a line disclination that separates two opposite HAN configurations with different pretilt angles at the planar surface; a real FCM image is shown below. . . . .	77
3.22 Schematic of the toroidal focal conic domain structure formed by 8CB with a silicon oxide surface. . . . .	78
4.1 Schematic of the model of Cladis and Torza for the “stripe” structure as a wrinkled layer of nematic coexisting with smectic “wedges”. (Redrawn following [1]) . . . . .	87
4.2 Smectic layer structure around a V-shaped defect using the analogy with edge disclinations in a smectic. . . . .	90

4.3	Fitted linearized solution to zipper defect with $\lambda/b = 1.4$ . . . . .	90
4.4	Schematic of toroidal coordinates . . . . .	92
4.5	Overhead schematic of a Toroidal Focal Conic Domain (a) identifying distinct regions and variables for integration (b) shape of the domain with interdomain separation $R$ fixed and $r$ varying between $1/2$ (circular) and $1/\sqrt{3}$ (hexagonal). . . . .	93
4.6	Cross section of a Toroidal Focal Conic Domain . . . . .	94
4.7	Contributions to the energy of a Toroidal Focal Conic Domain with the interdomain separation $R = 1$ , $1/2 < a < 1/\sqrt{3}$ and $d/R = 0.9$ ; the contributions are in ‘bare’ form with their governing prefactor chosen to be 1. . . . .	99
4.8	Set of confocal ellipses of different eccentricity with corresponding confocal hyperbola. . . . .	101
4.9	Azimuthal anchoring energy density of a Dupin Cyclide FCD along the planar surface. . . . .	102
4.10	Schematic of a tilted Toroidal Focal Conic Domain . . . . .	103
4.11	(a) Sections through a Toroidal Focal Conic Domain, at different depths $z$ from the plane of the defect circle and inclined at an angle $\psi$ to it, showing the polar anchoring energy density as a function of position. (b) The section that minimizes the total polar anchoring energy within the red section illustrated. . . . .	104
5.1	Production of a patterned surface using the photoalignment technique and an appropriate mask. . . . .	108
5.2	Nanopatterns inscribed with the stylus of an AFM. The dark arrows indicate the orientations that the director may align with in the bulk in each of the stable states. . . . .	109
5.3	Schematic of the director field $\mathbf{n}(x, z)$ for a nematic with $K_1 = K_2 = K_3$ in contact with a surface patterned with period $\lambda$ and relative homeotropic stripe width $a$ . . . . .	111
5.4	Schematic of a liquid crystal cell constructed from patterned substrates with stripes of different width; the black regions on the substrates promote planar alignment and the white stripes promote homeotropic alignment. . . . .	113
5.5	Polarizing microscopy images of “splay-bend” and “twist” structures with aligned polarizers in different orientations. White arrows represent the wavevector of the patterning. ( <i>Images reproduced with the kind permission of Dr N. J. Smith</i> ) . . . . .	113
5.6	Numerical integration of the free energy density over the region excluding the two defects is achieved by dividing the domain into seven regions. . . . .	117

5.7	Critical azimuthal anchoring energy as a function of $a$ for $\lambda = 10\mu\text{m}$ , $K_1 = 1 \times 10^{-11}\text{N}$ and with rigid polar anchoring. Solid lines were computed with $r_c = 10^{-8}\text{m}$ and dashed lines with $r_c = 5 \times 10^{-8}\text{m}$ . Note that a transition from splay-bend to twist is feasible if $W_\phi < W_{\phi\text{critical}}$ . . . . .	118
5.8	Critical azimuthal anchoring energy as a function of $\lambda$ with rigid anchoring for $a = 0.5$ , $r_c = 10^{-8}\text{m}$ and $K_1 = 1 \times 10^{-11}\text{N}$ . . . . .	119
5.9	Critical azimuthal anchoring energy as a function of the polar anchoring energy $W_\theta$ for $a = 0.5$ , $\lambda = 10\mu\text{m}$ and $K_1 = 1 \times 10^{-11}\text{N}$ . . . . .	121
5.10	Phase diagram showing the regions of stability of the uniform homeotropic (UT), uniform planar (UP), splay bend and twist configurations for a semi-infinite nematic in contact with a splay-bend type surface. Critical lines for several values of the penetration depths associated with (a) polar and (b) azimuthal anchoring are shown. . . . .	123
5.11	Phase diagram showing the regions of stability of uniform states parallel to ( $U_{\parallel}$ ) and perpendicular to ( $U_{\perp}$ ) the length of the stripes as well as the distorted configuration for a semi-infinite nematic in contact with a striped surface with planar stripes of antagonistic azimuthal easy axis. Critical lines for several values of the penetration depths associated with azimuthal anchoring are shown. . . . .	124
6.1	Variation of the amplitude of tilt perturbation in a twisted nematic cell as a function of the ratio of the twist and splay elastic constants. . . . .	130
6.2	Polarizing microscope images of domains in a $20\mu\text{m}$ twisted nematic cell constructed from two micropatterned surfaces with $1\mu\text{m}$ wide alternate homeotropic and planar stripes. ( <i>Images reproduced with the kind permission of J. Bramble</i> ) . . . . .	131
6.3	Schematic of (a) the High Tilt Twisted Nematic (HTTN) and (b) the Uniform Nematic (UN) states. . . . .	132
6.4	Energy difference between the Uniform Nematic and High Tilt Twisted Nematic states as a function of the polar anchoring energy of the micropatterned surfaces. . . . .	134
6.5	Schematic of the director field between the HTTN and UN domains. . . . .	135
6.6	Equilibrium bulk tilt angle $\bar{\theta}$ where $n_z = \sin \theta$ as a function of relative homeotropic stripe width $a$ with rigid anchoring. . . . .	141
6.7	Director profiles for a simulated cell of $20\mu\text{m}$ thickness with identically patterned substrates of $2\mu\text{m}$ period for different values of $K_2/K_1$ . Director values are shown averaged over the $x$ coordinate. . . . .	142

6.8	Director profiles for a simulated cell of $20\mu m$ thickness with identically patterned substrates of $2\mu m$ period for different values of $K_3/K_1$ . Director values are shown averaged over the $x$ coordinate. . . . .	143
6.9	Director profile, averaged over the $x$ coordinate, for a simulated cell of $20\mu m$ thickness with identically patterned substrates of $2\mu m$ period at several values of applied voltage; the elastic constants used are typical of common nematic materials i.e. $K_3/K_1 = 1.6$ , $K_2/K_1 = 0.6$ . . . . .	144
6.10	FCM images of Dupin cyclide focal conic domains (above) an axial section near the micropatterned surface (below) reconstructed cross section with fitted hyperbolae. . . . .	146
B.1	Mapping of the azimuthal component of the director field to the observed intensity. . . . .	158
B.2	(a) Deconstruction of a polarizing microscope image of a HAN cell with defects and domain wall into a graph representation of its distinct areas showing one possible quadrant labelling for each node (b) redrawn version of the graph with quadrants labelled by number and (c) a simplified notation for the same graph. . . . .	159
C.1	Normalized probability distribution functions for the critical exponents associated with the elastic constants in 8CB (a) the twist exponent $\nu_2$ , (b) the bend exponent $\nu_3$ . . . . .	163

# Acknowledgements

I SHOULD LIKE to thank Prof J Roy Sambles, my supervisor at the University of Exeter, for his warmth, encouragement and motivation throughout the project and for reading draft copies of this thesis.

I am indebted to Dr Nathan Smith, my industrial supervisor at Sharp Laboratories of Europe, for his support and good humour throughout the project but moreover for first presenting me with the problem that is solved in Chapter 5 and, together with Catherine Raptis, also for sharing the microscope images reproduced in fig. 5.5.

It has, also, been a great pleasure to work with so enthusiastic a collaborator as Jonathan Bramble from the University of Leeds. I am grateful to Jonathan for presenting me with the problem solved in chapter 6 and for a very productive visit to look at a very interesting system with confocal microscopy (the results of which are presented in section 6.4).

I would also like to thank Prof Paul O'Shea and Mrs Kelly Vere of the University of Nottingham for allowing me the use of their Leica SP4 confocal microscope and for helping me obtain some of the microscope images that were used to produce figures 3.15, 3.16, 3.17 and 3.18 in Chapter 3.

I must also thank Prof Bill Barnes for allowing me the use of the Leica SP5 confocal microscope at the University of Exeter which was used to produce figures 2.7 and 2.8 in Chapter 2, figures 3.20 and 3.19 in Chapter 3 and figure 6.10 in Chapter 6.

I'd very much like to thank my mother, Jennifer Atherton and my brother Jonathan Atherton for their support and encouragement through life and in particular for the time I spent in Birmingham whilst I wrote this thesis.

I'd also like to thank friends and colleagues from the Thin Film Photonics group at the University of Exeter; Gemma, John, Steph and Tim, for reading draft sections of this thesis, Sharon, Jim, Steve, Lucy, Baptiste, Ian, Andy, George, Mike, Alistair, Matt, James, Joe, Pete, Rob, Zhuo and the most recent additions Ciaran, Tom and James. I'm also very grateful to the staff at Sutton Coldfield and Birmingham Public Libraries for assistance with photocopying etc.

Finally, let me thank a few of the many others who have made my time at Exeter so pleasurable: Rachel, Jemma, Lucy, Mette, Brutus, John, Adam, Luke, Zoe, Laura, Dave, Dona, Anna, Paul, Ash, Kristin, Steve,

Kate, Luke, Nathan, Alain, Lou, Simon, Jo, Sandrine, Matt, Skullfish, Av, Martin, Gail, Dave, Ned, Matt, Rich, Steph, Bonnie, Sam, Pete, Jo, Amy, Lou, Lucy, Dave, Tim, Ralph and Owen.

# Introduction

**L**IQUID CRYSTALS are perhaps best introduced from the point of view of their symmetry with respect to the familiar liquid and crystalline phases: An idealized infinite sample in the liquid phase has continuous spherical rotational symmetry and continuous translational symmetry while the crystalline phase has only discrete translational and rotational symmetry. It may be imagined that there might exist phases of intermediate symmetry; perhaps with continuous translational symmetry but cylindrical rotational symmetry or with cylindrical rotational symmetry but discrete translational symmetry in one direction and continuous translational symmetry in any orthogonal direction. These two phases exist—they are known as the *nematics* and *smectics* respectively—and all such phases with symmetry between that of a liquid and a crystal are collectively known as *liquid crystals*.

The mathematical expressions that describe the energy of a liquid crystal often appear very complicated; they contain many terms of indefinite sign and many free parameters. The many examples of pattern formation in liquid crystals, and the very rich variety of possible configurations that may be adopted by a liquid crystal even within a single device, may be explained by the notion of *frustration*: different terms in the free energy may favour incompatible ground states and the actual configuration adopted depends critically on the value of the governing parameters for each term. In particular, frustration may cause the liquid crystal to *self-organize* into an ordered structure on length scales much greater than the size of the molecules. Recent advances in surface patterning multiply greatly the possibilities to impose conflicting influences on a liquid crystal film.

The aim of the work within this thesis is to explain the physical origin of the configuration adopted by several examples of frustrated liquid crystal systems. To do so it shall be necessary to draw on diverse evidence: from polarizing microscopy and confocal microscopy, previous measurements of the governing parameters, theories of related or analogous systems from the literature, and many simplified analytical models as well as numerical studies.

The foundations of liquid crystal physics are set out in Chapter 1 from the established literature. The different phases are described and the respective mathematical description of their ordering—a quantity referred to as the *order parameter*—introduced. The continuum theory used in this thesis, which regards the liquid crystal as a continuous medium and the order parameter as a differentiable field quantity<sup>1</sup>, is

---

<sup>1</sup>The order parameter is continuously differentiable over the three dimensional region of liquid crystal except possibly in two or



described and contrasted with other theoretical descriptions of the liquid crystal phases. Application of variational calculus to the continuum theory is described and used to solve the simple problem of finding the configuration adopted by a liquid crystal in a cell with opposing boundary conditions.

To study complicated structures formed by liquid crystal films, it is necessary to have some experimental tool to examine their configuration. In chapter 2, therefore, the two microscope techniques are introduced: Polarizing microscopy has been used by chemists throughout the history of liquid crystals to identify liquid crystal phases and a great deal of useful information about their configuration can be gained in this way; the much more recent innovation of confocal microscopy permits the reconstruction of full three-dimensional images of a liquid crystal film and its use and limitations are discussed with reference to the literature.

The first problem addressed is the physical origin of a self-organized periodic array of domains, recently discovered by Ruan *et al.*[2], that is adopted by a nonchiral smectic liquid crystal in a cell with opposing boundary conditions upon cooling from the nematic phase. In particular, the physical parameters that influence the period of the array are explored. The structure is shown in chapter 3 to develop on cooling through two intermediate configurations that exist over a very narrow temperature range around the nematic–smectic transition. Each of these intermediate configurations is studied using polarizing microscopy and confocal microscopy, and many cells with different thickness and surface treatment are each tested.

In chapter 4 the stability of the intermediate structures is analysed using certain techniques from the literature. The intermediate structure is very similar to one discovered long ago in much thicker cells and in the smectic phase those cells adopted a configuration similar to that of Ruan *et al.*

but more symmetric. A model to explain this difference is proposed and the two other explanations that have been put forward in the literature are shown to be insufficient.

The second example of a frustrated liquid crystal system to be considered is, in chapter 5, the configuration adopted by a nematic in contact with a striped surface. A brief review of micropatterning techniques is presented followed by a thorough review of the literature on striped surfaces. Some experimental results from Sharp Laboratories of Europe are considered that suggest a nematic in contact with a striped surface may adopt a configuration apparently inconsistent with the boundary conditions. A model for the system is developed that shows that this is indeed the case and that the effect is due to anisotropic elasticity of the nematic. The energy of this novel configuration is then calculated and a complete phase diagram for the case of a semi-infinite nematic in contact with a striped surface presented for the first time. Furthermore, it is shown that the distortion of the nematic order near a striped surface even with planar degenerate stripes is usually sufficient to promote a preferred orientation in the bulk.

This effect is explored further in chapter 6 which considers cells constructed from micropatterned surfaces. The model developed in chapter 5 is extended to consider the stability of possible configurations for the one-dimensional subregions (*walls* and *disclination lines* respectively) across which it may change value by some finite amount.

nematic in an analogue of the well-known Twisted Nematic cell constructed from micropatterned surfaces; these results are used to interpret some experimental results from the University of Leeds. Finally, a numerical simulator of the nematic in a cell with micropatterned surfaces is developed that is free of the approximations made in the analytical models in chapter 5 and the first part of chapter 6; the program is then used to contrast the behaviour of the micropatterned TN cell with that of a conventional TN cell with respect to variations of the elastic constants and under the influence of an applied electric field.

This thesis concludes with a summary of original results, a discussion of remaining problems, some suggestions for further work and finally, some general conclusions. A few matters of interest tangential to the main text are included as appendices.

Part I

Background

# Chapter 1

## Liquid Crystal Physics

### 1.1 Liquid Crystalline Order

**L**IQUID CRYSTALS are a generic term for a number of states of matter with molecular ordering intermediate to that of the liquid and crystalline phases[3, 4, 5]; the term is also used to refer to compounds or mixtures that exhibit such phases. Like a liquid, the molecules in a liquid crystal phase (also referred to as a *mesophase*) are free to move around, but like a crystal the phase also exhibits long-range order. Unlike the discrete translational symmetry of a crystal, molecules in a liquid crystal phase are continuously distributed in space but tend to align in a preferred direction giving rise to orientational order. They consequently are more symmetric than crystalline phases as they have continuous, rather than discrete, rotational and translational symmetries. Additionally, some phases are characterized by self-organization of the molecules into layers and also short range order.

The orientational ordering arises because the constituent molecules are very anisotropic in shape and rather inflexible. Long thin molecules form *calamitic* liquid crystals while thin, flat molecules form *discotic* liquid crystals. Liquid crystal phases may occur in a pure compound as the temperature is changed—these are referred to as *thermotropic* liquid crystals—or they may occur in the presence of a solvent such as water in which case they are *lyotropic* liquid crystals. This thesis shall treat calamitic thermotropic phases exclusively.

Liquid crystals exhibit a number of interesting properties: they may be aligned by an applied electric field; they exhibit *birefringence*[6]; their preferred orientation may be controlled by an appropriately treated surface; they can sustain an elastic deformation; they may also exhibit very rich phase behaviour or *polymorphism*. The first four of these properties permit the construction of a variety of devices that are *switchable* and able to *guide light*. The tremendous commercial success of liquid crystal displays, now ubiquitous in society, explains the profusion of research published in the field and many further applications—beam-steering[7, 8], switchable diffraction gratings[9], cheap spectrometers[10], biosensors[11]—have been proposed.

The remainder of this chapter describes the principal liquid crystal phases and outlines the theoretical descriptions of liquid crystals pertinent to this thesis.

### 1.1.1 The Nematic Phase

The word “nematic” is from the Greek “nematos” or thread: a reference to the threadlike appearance of domain walls which occur in the phase under the polarizing microscope. Molecules in the nematic phase tend to point, on average, in a certain preferred direction; for calamitic materials this is along the long axis of the molecule (fig. 1.1). The ordering is long-range, although the average orientation may vary spatially as the nematic phase is capable of sustaining an elastic distortion.

The degree of alignment may be characterized by an *orientational distribution function*[3]. For most nematic materials the alignment is symmetric with respect to arbitrary rotations about the axis of preferred alignment and these materials are consequently referred to as *uniaxial*; some liquid crystals exhibit asymmetry with respect to rotations around the preferred axis of alignment or *biaxiality*. Although many nematic materials consist of polar molecules the nematic phase is nonpolar and so the orientational distribution function is additionally symmetric with respect to spatial inversion.

An important class of liquid crystal materials are composed of molecules that exhibit *chirality* or the absence of inversion symmetry. The property is often referred to as *handedness* as the human hand lacks this symmetry. Liquid crystals composed of unequal numbers of left- and right-handed molecules will exhibit a *cholesteric* or chiral nematic phase which is similar to the nematic save that the ground state for a cholesteric liquid crystal is a helix.

Commercial materials such as ZLI2293 and E7 which are used in displays are mixtures of pure liquid crystal compounds designed to have nematic phases with a wide temperature range around room temperature and desirable properties such as low viscosity and high birefringence.

### 1.1.2 Smectic Phases

In a smectic phase the constituent molecules are arranged in layers. The layering is not rigid; X-ray diffraction experiments reveal that the distribution of mass in a smectic is very nearly sinusoidal (fig. 1.2)[3]. Smectic phases, having only discrete translational symmetry, have lower symmetry than the nematic phase and so tend to occur at lower temperatures although in highly polar compounds low temperature or *re-entrant* nematic phases may be exhibited[12, 13]. It is ambiguous as to whether the smectic order may in fact be correctly termed long-range as a well-known theorem—the Landau–Peierls instability—predicts that fluctuations will always destroy any one dimensional ordering in an infinite three dimensional system (discussed more fully in [4, 14]) and its effects have been observed experimentally[15].

A large number of smectic phases exist: The most symmetric, denoted Smectic-A, has the average orientation of the molecules orthogonal to the layers and no ordering in the plane of the layers; in the smectic-C

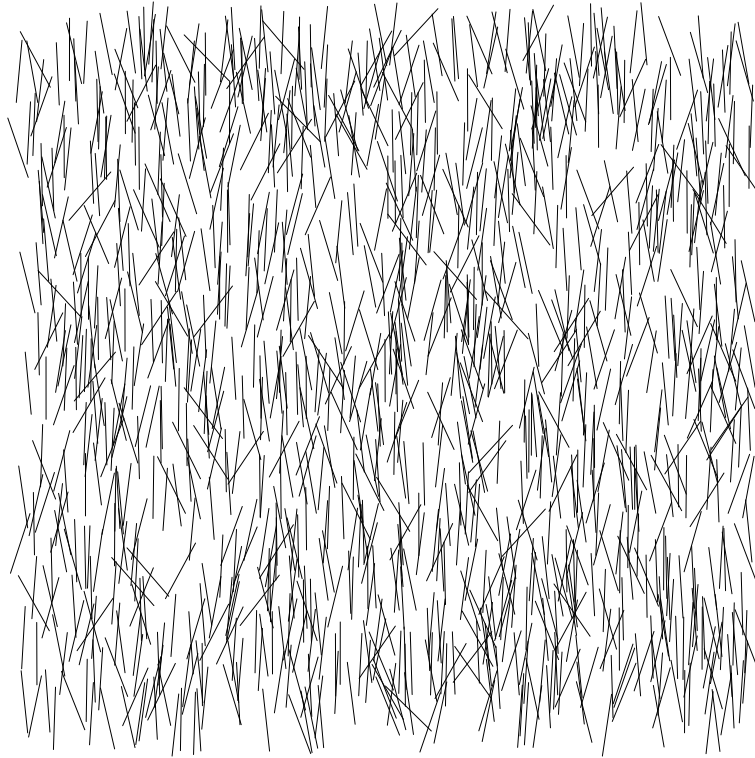


Figure 1.1: Schematic of the molecular ordering in a nematic phase.

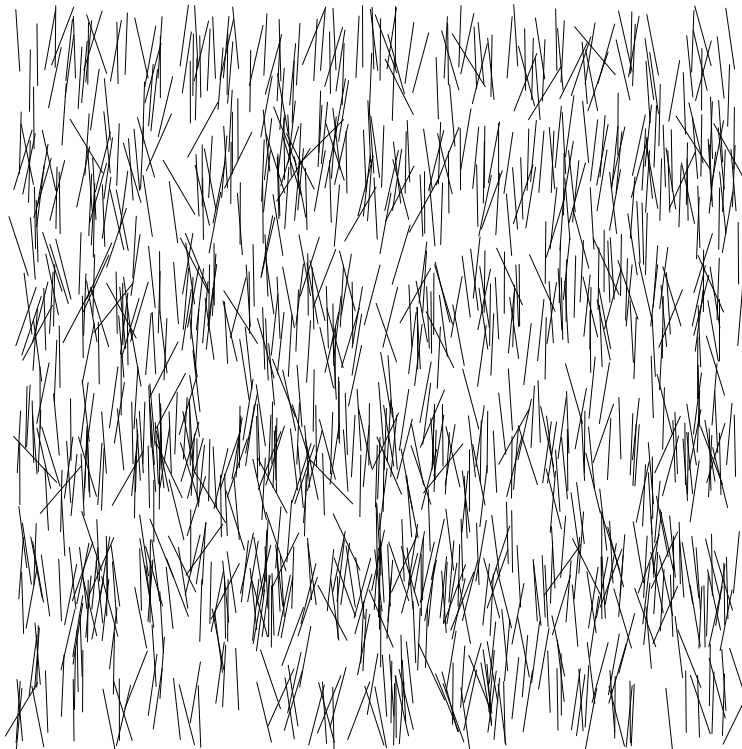


Figure 1.2: Schematic of the molecular ordering in a smectic-A phase.

Phase	Order
A	Preferred orientation orthogonal to layers
B	Preferred orientation orthogonal to layers; short range hexagonal order
C	Preferred orientation at an angle to layers
C*	Chiral Smectic C

Table 1.1: Classification of some smectic phases

phase the molecules are tilted on average at some angle to the layers. The smectic B phase is similar to smectic-A except that molecules within a particular layer have short range hexagonal order. There also exist phases with bicontinuous layers, i.e. the layers consist of polar molecules of alternately opposite orientation. The nomenclature of the smectic phases is purely historical and confers no information as to the type of ordering, although a convention exists that chiral phases are suffixed with an asterisk.

The layers are rather incompressible which places some important constraints on the macroscopic arrangement of smectics: an important result from differential geometry is that, in the limit of totally incompressible layers and therefore constant layer spacing, only six families of surface can fill space: planes, cylinders, spheres, tori[16], Dupin cyclides[17] and parabolic cyclides[18] (fig. 1.3). The latter three are constructed from confocal conic sections in orthogonal planes and are referred to as the *focal conics*; they are discussed in greater detail in chapter 4. All six of these configurations have been observed experimentally where the particular configuration adopted depends on material elasticity, surface treatments and the system geometry[19, 20, 21].

### 1.1.3 Order Parameters

In a transition between two phases, some physical component of the system in question—in the case of liquid crystals the mass density or the orientational distribution function—changes in symmetry. Typically, the high temperature phase is more symmetric and the low temperature phase less symmetric. The physical quantity that changes may be described by some suitable mathematical object of appropriate symmetry.

For example consider the nematic-smectic-A transition which breaks the continuous translational symmetry of the density of mass. The mass density may be represented by a scalar field  $\rho$ . The nematic phase has continuous translational symmetry and  $\rho$  must therefore be some constant  $\rho_0$ . The smectic phase has only discrete translational symmetry:  $\rho$  is periodic and may naturally be expanded in a Fourier series

$$\rho(\mathbf{r}) = \rho_0 + \rho_1 \cos \left[ \frac{2\pi}{a} (\mathbf{q} \cdot \mathbf{r} - \phi) \right] + \rho_2 \cos \left[ \frac{4\pi}{a} (\mathbf{q} \cdot \mathbf{r} - \phi) \right] + \dots \quad (1.1)$$

where  $a$  is the layer spacing,  $\phi$  is a phase factor and  $\mathbf{q}$  is a unit vector orthogonal to the layers. The second and third terms with associated coefficients (frequently referred to in the literature as *amplitudes*)  $\rho_1$  and  $\rho_2$  are examples of *order parameters*: objects derived from the physical component of a system that in the high temperature more symmetric phase are 0, and in the low temperature less symmetric phase have some finite value. The mass density distribution in a smectic is very nearly sinusoidal and so only the first term of

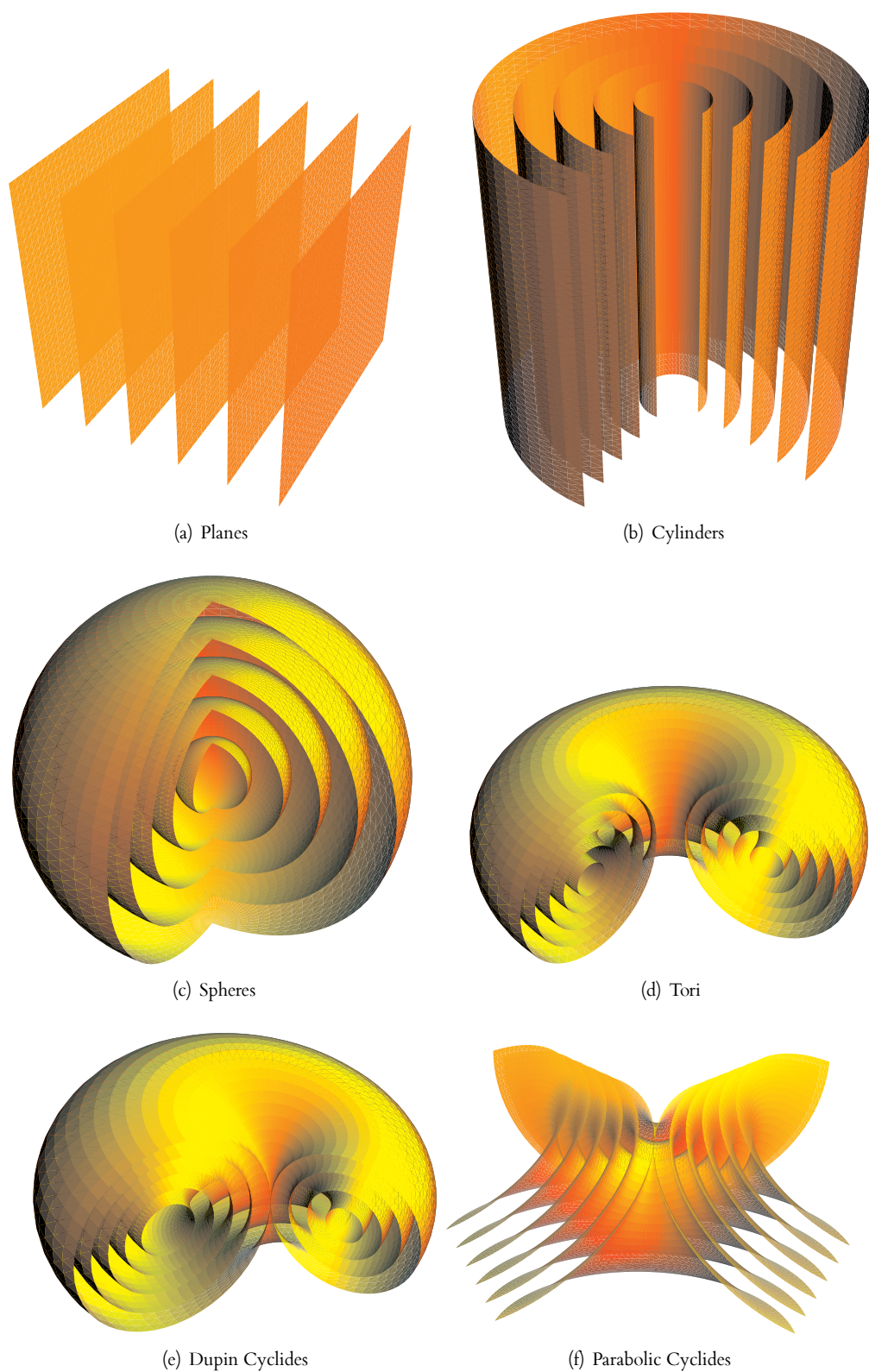


Figure 1.3: The six families of surface that are compatible with the condition of constant layer spacing for an incompressible smectic.



(1.1) is retained; the quantity  $\rho_1$  (often denoted  $\psi$  in the literature e.g. [22]) is used as the order parameter for nematic–smectic transitions.

Order parameters are fundamental to the description of phase transitions. Phase transitions are categorized by the behaviour of the order parameter at the transition point: if the order parameter is discontinuous—suddenly taking a finite value—at the transition point, the transition is *first order*; if the order parameter varies continuously from zero, the transition is *second order*.

It is evident that the symmetry group of the order parameter must be consistent with the symmetry group of the less symmetric phase (indeed it must form a representation of it). A scalar is often insufficient as an order parameter: the isotropic–nematic transition, for example, is characterized by the orientational distribution function of the nematic changing from being spherically to cylindrically symmetric. It is natural to expand the orientational distribution function in the Legendre polynomials[3]

$$f(\cos \theta) = P_0 + \frac{P_2}{2} (3 \cos^2 \theta - 1) + \frac{P_4}{8} (35 \cos^4 \theta - 30 \cos^2 \theta + 3) + \dots \quad (1.2)$$

where the angle  $\theta$  is measured from the axis of average orientation. Odd terms were removed because of the symmetry requirement that  $f(\cos \theta) = f(-\cos \theta)$ . The successive moments of the distribution function  $P_2, P_4$  etc. each provide a measure of the degree of alignment of the liquid crystal. If all coefficients are zero the alignment is uniform or isotropic. They are nonetheless inadequate as order parameters as they are tied to the frame of reference of the average orientation.

In the laboratory frame, it is possible to define a unit vector that points in the direction of average orientation  $n_i$ . This vector cannot be an order parameter as it is clearly inconsistent with the requirement that the order parameter be invariant under the transformation  $n_i \rightarrow -n_i$ . A second rank tensor is however suitable as an order parameter if constructed so as to be traceless[3]

$$Q_{ij} = \frac{P_2}{2} (3n_i n_j - \delta_{ij}) \quad (1.3)$$

where  $\delta_{ij}$  is the Kronecker delta. The magnitude  $P_2$ —ubiquitously denoted  $S$  in the literature and often (incorrectly) referred to as the *scalar order parameter*—ensures that  $Q_{ij}$  is zero in the isotropic phase and finite in the nematic phase. Experimental values of  $S$  lie in the interval  $0.3 < S < 0.6$ ;  $S$  is larger at lower temperatures. An analogous fourth rank tensor can be constructed which is associated with the  $P_4$  moment of the orientational distribution function. Experimental measurements of the magnitude  $P_4$  from Raman scattering find it is generally negative for some temperatures within the nematic phase and small ( $|P_4| \sim 0.1$ )[4]. Hence,  $Q_{ij}$  although in some sense an approximation, albeit one that is nonetheless group theoretically exact[14], is widely used as “the” order parameter for the nematic–isotropic transition.

### 1.1.4 Theoretical Descriptions of Liquid Crystals

The various theoretical approaches constructed to describe liquid crystal phenomena may be broadly divided into the following categories: *molecular-statistical* theories which seek to understand the physical origin of liquid crystalline order by considering molecular interactions; *Landau-de Gennes* theories that attempt to describe critical phenomena; *continuum* theories that describe macroscopic effects by regarding the liquid crystal as a continuous medium and the order parameter as a field quantity and, finally, *computational* approaches (excluding numerical versions of continuum theory) which aim to simulate the behaviour of liquid crystals composed of more-or-less realistic molecules.

The majority of this thesis will attempt to explain a number of phenomena associated with liquid crystal films by application of the various forms of continuum theory (which is described in section 1.2). It is nonetheless pertinent to outline the other main theories—if only to the extent of their areas of applicability—so that where continuum theory is only able to make phenomenological predictions, it is clear from what quarter assistance might be found.

Molecular-statistical descriptions of liquid crystals rely on some approximation to the intermolecular potential (which is complicated). Historically the first such theory for the nematic phase, due to Onsager (described in [3]), considers the ordering of long, hard, cylindrical rods as a function of density with no molecular forces other than the exclusion of molecular interpenetration. He showed that at a critical value of density, the system underwent a transition from an isotropic to a uniaxial nematic-like phase.

Maier and Saupe developed a mean field statistical theory (again described in [3])—one in which the detailed intermolecular electromagnetic forces experienced by each individual molecule are replaced by a time-averaged field—of the nematic phase at constant volume and varying temperature, a more physically applicable situation than the Onsager theory. The theory predicts a temperature dependence in  $S(T)$  and a universal critical value of  $S$ ,  $S_c \approx 0.44$  at the nematic–isotropic transition, which is in rough agreement with experimental values of  $0.3 - 0.45$ . McMillan extended the Maier–Saupe theory to the nematic–smectic–A transition[23].

The Landau approach (see [4]) eschews consideration of the detailed molecular interactions instead assuming that their symmetry—as manifested by the order parameter—is of paramount importance. The free energy difference between two phases must be expressible as some function of the order parameter. The insight of Landau was that, for second order transitions, the order parameter is small around the transition and the free energy consequently may be expanded in a series of successive powers of the order parameter. For example for the nematic–smectic–A transition

$$\Delta f = \frac{\partial^2 f}{\partial \psi^2} \psi^2 + \frac{\partial^4 f}{\partial \psi^4} \psi^4 + \dots = A\psi^2 + B\psi^4 + \dots \quad (1.4)$$

where the derivatives, which are of course unknown, are each replaced by *phenomenological* coefficients

(often referred to as the Landau coefficients)  $A$ ,  $B$ , etc. As the free energy must be invariant under the symmetry group of the low temperature phase (it is by definition that the order parameter is zero in the high temperature phase), terms which are not invariant are excluded from the expansion. In the series above for the nematic–smectic–A transition, odd terms were excluded for this reason.

The Landau–de Gennes approach has also been used with care to describe weakly first–order transitions (including pretransitional effects above the isotropic–nematic transition for which  $S$  is suitably small), i.e. those for which the order parameter is discontinuous over the transition point but nonetheless small. By assuming some temperature dependence of the Landau coefficients, typically only of the first coefficient, useful predictions about the dependence of such quantities as birefringence and elastic constants with temperature may be drawn (see chapter 4).

An important reason why the mean–field and Landau–de Gennes approaches as described above yield results only qualitatively consistent with experiment is that they ignore time dependent *fluctuations* of the molecular ordering. Theories which include the effect of fluctuations have been derived and explain, for example, optical scattering by nematics (see [3] and references therein).

Rather than try to approximate the detailed microscopic Hamiltonian, a recent popular approach has been *computational simulation* of liquid crystal molecules. In a typical simulation, a number of objects—atoms, molecules or parts thereof—are assigned some position and momentum in a computational domain and allowed to move under simulated forces. Standard algorithms such as Metropolis[24] and Molecular Dynamics[25] are well–used in the field. Order parameters and other macroscopic variables may then be computed naturally from the system as the simulation progresses although results must be interpreted with some care due to the constrained simulation size.

Computer simulations vary according to their *resolution* or level of detail, ranging from atomistic simulations of real molecules, which can capture conformational effects, to simulations of solid ellipsoids or cylinders. An approach known as *coarse-graining* (e.g. [26]) can be used to incorporate physical effects such as molecular polarity into low resolution simulations: a high resolution simulation is conducted with a few molecules to determine the detailed intermolecular potential and this is then used in the low resolution simulation. Limitations in computing power presently prohibit true device–scale simulations even for hard cylindrical models, simulations of dimension  $\sim 1\mu\text{m} \times 50\text{nm} \times 50\text{nm}$  represent the state of the art. Current topics of research include the prediction of material parameters such as elastic constants from molecular structure[27] and analysis of liquid crystal–surface interactions[28].

## 1.2 Nematic Continuum Theory

The active component of most liquid crystal devices is a thin ( $\sim 5\mu\text{m}$ ) layer of nematic liquid crystal film which is nonetheless orders of magnitude thicker than a liquid crystal molecule (1nm). It is therefore

unnecessary to know the precise location and alignment of every molecule in a device; it is sufficient to know the local order parameter averaged over a correlated volume. The order parameter may therefore be promoted to a field quantity which is continuous except at defects and may be differentiated. An elastic theory may then be formulated [3, 5, 14] by constructing all possible derivatives up to a desired order of the order parameter, retaining only those consistent with the symmetry of the phase. The elastic energy is then the summation of all those remaining terms that are linearly independent of all others each with an associated elastic constant.

The continuum free energy for the nematic phase comprises an elastic energy derived above and other contributions describing the interaction of the liquid crystal with the electric and magnetic fields. If the scale length of distortions are of the order of the size of the device and much longer than the correlation length, the magnitude  $S$  of the continuous order parameter does not change significantly throughout the device and the terms which involve derivatives of the orientational part of the nematic continuous order parameter dominate the free energy. Hence, most formulations of the nematic free energy for device applications use only the orientational part of the continuous order parameter: this vector quantity is known as the *director* and is conventionally written  $\mathbf{n}$ . The director is, as discussed above, insufficient as an order parameter (it is not consistent with the symmetry of the nematic phase).

The continuum theory may be cast in time-independent (*static*) or time-dependent (*dynamic*) form [29]: the former is due to Oseen, Zöcher and Frank; the most commonly employed formulation of the latter is due to Ericksen and Leslie and reduces to the Oseen-Zöcher-Frank theory in the static limit. The phenomena discussed in this thesis are purely static and this section therefore outlines the Oseen-Zöcher-Frank theory only.

### 1.2.1 Fundamental Equations

The actual configuration adopted by a liquid crystal is given by the director field which minimizes the free energy. The elastic part of the free energy is the well-known Frank energy [3, 29, 5]

$$f_{elastic} = \frac{K_1}{2}(\nabla \cdot \mathbf{n})^2 + \frac{K_2}{2}(\mathbf{n} \cdot \nabla \times \mathbf{n})^2 + \frac{K_3}{2}|\mathbf{n} \times \nabla \times \mathbf{n}|^2 + (K_2 + K_{24})\nabla \cdot [\mathbf{n}(\nabla \cdot \mathbf{n}) + \mathbf{n} \times \nabla \times \mathbf{n}] \quad (1.5)$$

where  $K_1$ ,  $K_2$  and  $K_3$  are referred to as the splay, twist and bend elastic constants (fig. 1.4) and are of typical magnitude  $1 \times 10^{-11}$  N. The final term, with the associated *saddle-splay* elastic constant  $K_{24}$  is a total derivative and may therefore be converted to a surface term by the divergence theorem; it is identically zero when the director field is confined to a single plane and is often omitted in the literature. For cholesteric liquid crystals, there is no requirement that the free energy is invariant under spatial inversion and so a term linear  $k_2(\mathbf{n} \cdot \nabla \times \mathbf{n})$  must also be included and, furthermore, that the saddle-splay term must be excluded i.e.  $K_2 + K_{24} = 0$ . The ratio  $k_2/K_2$  turns out to be the natural pitch length of the cholesteric and it is

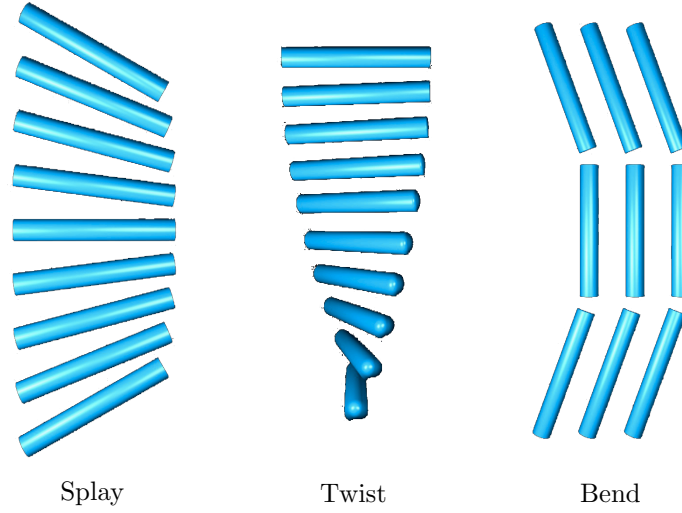


Figure 1.4: Schematic of pure splay, twist and bend deformations which are associated with the  $K_1$ ,  $K_2$  and  $K_3$  elastic constants respectively.

convenient to include this term within the twist term

$$\frac{K_2}{2}(\mathbf{n} \cdot \nabla \times \mathbf{n} + q_0)^2 \quad (1.6)$$

where  $q_0$  is the wavevector of the cholesteric helix in a very large sample.

The interaction of the nematic with an applied field is described by a term

$$f_{electric} = -\frac{1}{2}\epsilon_0\epsilon_{\perp}(\mathbf{E} \cdot \mathbf{E}) - \frac{1}{2}\epsilon_0\Delta\epsilon(\mathbf{n} \cdot \mathbf{E})^2 \quad (1.7)$$

where  $\Delta\epsilon = \epsilon_{\parallel} - \epsilon_{\perp}$  and  $\epsilon_{\parallel}$  is the dielectric permittivity associated with the long axis of the molecule and  $\epsilon_{\perp}$  is the dielectric permittivity associated with directions orthogonal to the long axis. The electric energy is minimised either, if  $\Delta\epsilon > 0$ , when the nematic director is parallel to the electric field or, if  $\Delta\epsilon < 0$ , when the director is orthogonal to the electric field.

A final term

$$f_{flexo} = -[e_1\mathbf{n}(\nabla \cdot \mathbf{n}) + e_3\mathbf{n} \cdot \nabla\mathbf{n}] \cdot \mathbf{E}, \quad (1.8)$$

known as the flexoelectric term and with the flexoelectric constants  $e_1$  and  $e_3$ , is normally also included into the free energy. Flexoelectricity is a spontaneous polarization that is produced when a liquid crystal consisting molecules of anisotropic shape is elastically distorted[30]. A typical magnitude for the flexoelectric coefficients is  $1 \times 10^{-11}\text{Cm}^{-1}$ ; their sign may be negative or positive[31].

The governing equations for continuum theory are obtained by variational calculus; the free energy integral may be identified with the action integral of classical mechanics textbooks[32] and the free energy density with the Lagrangian. The configuration of the liquid crystal is the solution of the Euler-Lagrange

equations

$$\frac{\partial F}{\partial q_i} - \nabla \cdot \frac{\partial F}{\partial \nabla q_i} = 0 \quad (1.9)$$

where there is an equation for each independent component  $q_i$  of the director or order parameter. The Euler-Lagrange equations must, if necessary, be supplemented by some appropriate normalisation constraint so that  $\mathbf{n} \cdot \mathbf{n} = 1$ .

## 1.2.2 Formulations of Continuum Theory for Numerical Solution

Practical problems in liquid crystal physics usually amount to formulating and solving the Euler-Lagrange equations incorporating all desired effects and with boundary conditions appropriate to the device geometry. The nematic order parameter and director may each be represented in a number of ways each of which has particular advantages appropriate to certain device geometries[29].

### 1.2.2.1 Polar Coordinates

The director is a unit vector and is therefore conveniently represented

$$\mathbf{n} = (\cos \theta \cos \phi, \cos \theta \sin \phi, \sin \theta) \quad (1.10)$$

where  $\theta$  is the polar angle and  $\phi$  is the azimuthal component. This parametrization is particularly convenient if the director is confined to a single plane as only one angle is necessary to characterize the director field; analytical solutions are occasionally possible, although they frequently involve elliptic functions. Some care is required to use the polar representation if the director is at any point oriented in the  $z$ -direction with  $\theta = \pi/2$  as the solution of the azimuthal equation is ill-posed in the sense that an arbitrarily large variation in  $\phi$  at that point does not change the energy. By redefining  $\theta$  and  $\phi$  appropriately, alternative polar representations of the director may be constructed; such representations will nonetheless always have one variable ill-defined when the director lies along some particular axis. It is possible, if awkward, to combine more than one representation in different coordinate regions joined appropriately so that the director remains continuous. A final consideration is that the saving in computational expense and storage by only having two field quantities to solve for is somewhat offset by the necessity of evaluating many expensive trigonometric functions.

### 1.2.2.2 Cartesian Director Components

It is, of course, also possible to write the director in terms of its Cartesian components:

$$\mathbf{n} = (n_x, n_y, n_z) \quad (1.11)$$

where it is understood that  $\mathbf{n}$  must locally satisfy a constraint  $\mathbf{n} \cdot \mathbf{n} = 1$ . The constraint may be enforced locally by adding an auxiliary functional to the free energy density

$$L' = L - \lambda(\mathbf{n} \cdot \mathbf{n} - 1) \quad (1.12)$$

where  $\lambda$  is a Lagrange multiplier field. The Euler-Lagrange equations consequently gain an additional term

$$\frac{\partial F}{\partial n_i} - \nabla \cdot \frac{\partial F}{\partial \nabla n_i} - 2\lambda n_i = 0, \quad i \in \{x, y, z\} \quad (1.13)$$

and must be locally solved simultaneously with the constraint equation

$$n_x^2 + n_y^2 + n_z^2 = 1. \quad (1.14)$$

### 1.2.2.3 Q-Tensor

In problems where variation of the magnitude  $S$  of the order parameter is important, for example if there are *disclinations* or defects in the system or near rough surfaces, the full tensor nematic order parameter  $Q_{ij}$  (referred to as the Q-Tensor) may be used[33]. The first few terms in the Landau expansion, typically up to sixth order, are included in the free energy in addition to the elastic, electric and flexoelectric terms; the Landau terms promote an equilibrium value of  $S$ . Since  $Q_{ij}$  must be represented by five independent numerical quantities, computational solution of the Euler-Lagrange equations is much more demanding than with the director-based approaches.

## 1.3 Surface Effects

The interaction of liquid crystals with surfaces is important for the construction of devices: with an appropriate surface treatment, the adjacent liquid crystal may be constrained to adopt a particular orientation. Surfaces which tend to promote an alignment orthogonal to the substrate are referred to as *homeotropic*, and those which promote alignment parallel to the substrate are known as *planar* or *homogeneous*. The preferred orientation typically is neither exactly orthogonal nor parallel to the surface, rather it is characterized by some *pretilt angle* which is measured from the substrate. Planar surfaces may additionally promote a particular azimuthal orientation, or may be *planar degenerate*.

### 1.3.1 Physical Origin of Surface Anchoring

Homeotropic orientation is normally achieved by the deposition of *amphiphilic* surfactant molecules onto the substrate: a typical surfactant consists of a hydrophilic head group and one or more hydrophobic hydrocarbon tail[34]. The molecule attaches to the glass by the head group leaving the liquid crystal

molecules to pack around the tail groups resulting in homeotropic alignment. A layer of surfactant may be deposited by the Langmuir-Blodgett technique[35] or more crudely by covering the substrate with a solution of surfactant in some volatile solvent and allowing the solvent to evaporate (see section 3.1). Surfactants may also be printed and allowed to *self-assemble*[36, 37, 38] (see section 5.2).

Homeotropic alignment occurs in other circumstances: clean glass is hydrophobic and so promotes homeotropic alignment[34]; the air-liquid crystal interface promotes homeotropic alignment due to surface tension. In the latter case, the shape of the air-liquid crystal boundary is unconstrained.

Alignment of nematics on rubbed surfaces may be explained by a purely geometric argument due to Berreman[39], although others have suggested that bonding between the surface and liquid crystal molecules play an important role. Suppose the rubbing creates approximately sinusoidal channels of size greater than the nematic correlation length. Consider two possible states: the first in which the director is homeotropic (fig. 1.5(a)), and which consequently must be elastically distorted near the surface relaxing out to a uniform bulk state; the second in which the director is planar and lies along the length of the stripes (fig. 1.5(b)). It is manifest that, if the interaction between the surface and liquid crystal is independent of the director orientation, the latter state has lower energy as there is no elastic distortion; it is furthermore clear that any rotation of the director field in the bulk, either polar or azimuthal, must involve create some distortion of the director field which implies an energy increase. The planar state lying along the length of the grooves is therefore the ground state.

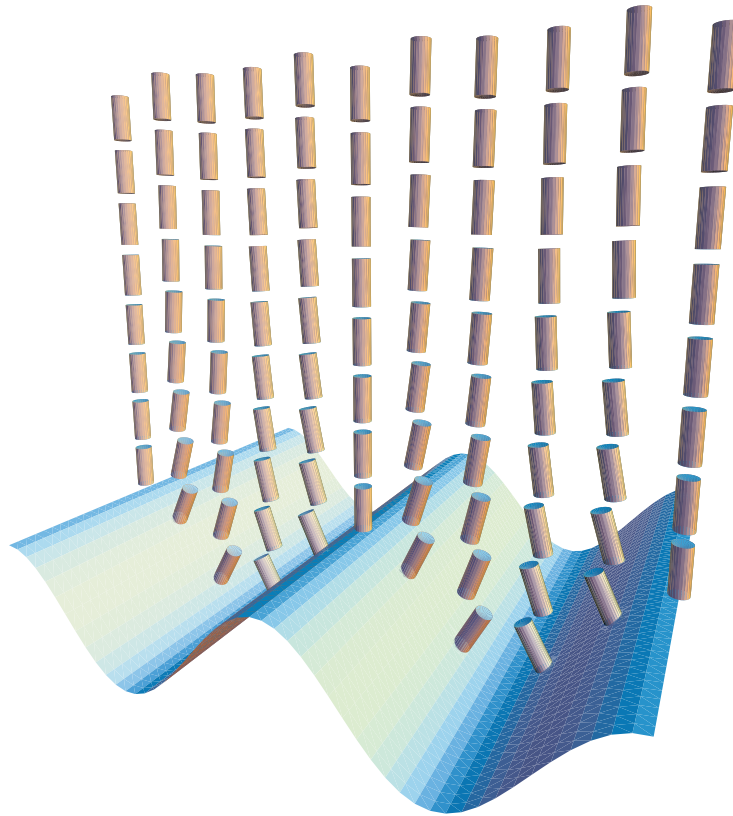
Predictions of the nature of the anchoring potential from such a simple model are limited by a number of important effects. Firstly, the continuum theory described above assumed that elastic distortions were much greater than the correlation length, and consequently considered only first derivatives of the director field; this is not so in the case of the grooved surface and strictly one ought to include nonlinear elastic terms into the free energy. Secondly, the elastic distortion of orientational order may be compensated for by a reduction in  $S$ .

Alignments such as evaporated silicon oxide have additional structure or “roughness” along the direction orthogonal to the channels of scale length in between the correlation length of a nematic and the scale size of the channels. Such structure is responsible for “surface melting”—strong reduction in  $S$  around such rough features—predicted by Barbero[40] and observed by Kerslake[41]. Sufficiently flat surfaces, on the other hand, may promote an enhancement of  $S$  to a surface value  $S_0$ . Additionally, flat homeotropic surfaces have been shown promote local smectic-like order immediately above the surface that may be disrupted by surface inhomogeneity[42].

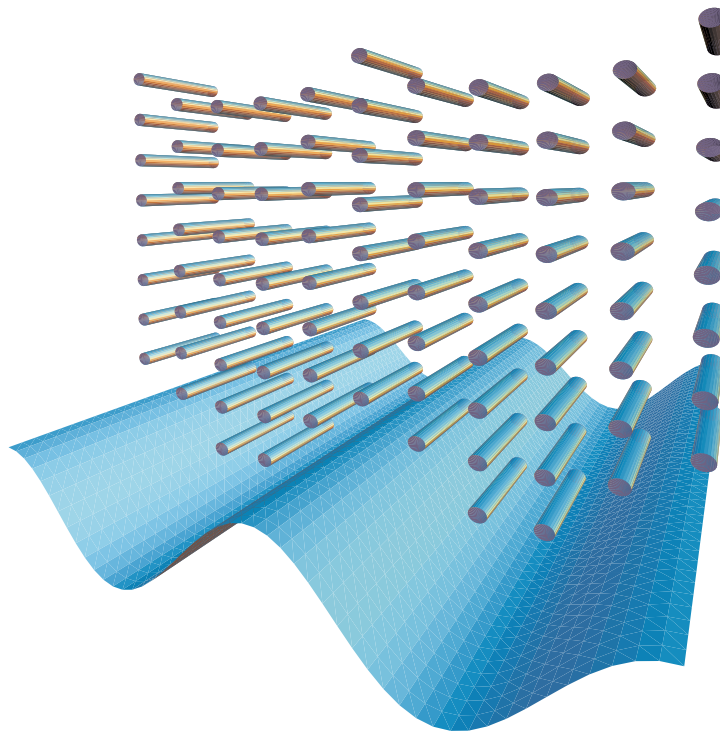
### 1.3.2 Phenomenological Descriptions

A common simplification, known as the *rigid anchoring* approximation, in the solution of practical problems is to assume that the director is fixed at a surface[29]: the numerical solution of the Euler-Lagrange





(a) Distorted homeotropic state



(b) Uniform planar state

Figure 1.5: Two possible configurations for the nematic director field adjacent to a sinusoidal grating; the uniform planar state has no elastic distortion and therefore lower energy.

equations with commercial packages is greatly simplified by the use of Dirichlet boundary conditions. Many interesting phenomena, however, occur as a result of *frustration*: the competition between opposing influences on a system that favour incompatible ground states. Surfaces are an important constraint on a liquid crystal film, and so the interaction of the nematic with the surface must be somehow included in the continuum theory free energy.

The most popular approach is to define some phenomenological *anchoring potential* that quantifies an energy cost as the director moves away from a preferred orientation or *easy axis*. The potential is then integrated over the surfaces which confine the liquid crystal to give a surface energy. The Rapini-Papoular potential is a particularly common choice for nematics[43]

$$f_s = \frac{W}{2} |\mathbf{n} - \mathbf{n}_e|^2 \quad (1.15)$$

where  $W$  is the *anchoring energy* and  $\mathbf{n}_e$  is the easy axis. A natural length scale for the nematic-surface interaction is

$$L = K/W \quad (1.16)$$

where  $K$  is of the order of the nematic elastic constants and  $L$  is known as the *extrapolation length*; if  $L$  is of the order of the molecular length then the anchoring is *strong* and the rigid anchoring approximation is valid as deviations from the easy axis are too expensive; if  $L$  is much larger than the molecular length the anchoring is *weak*. Normally at a planar surface it is less energetically costly to rotate the director in the plane of the surface or azimuthally rather than to pull the director away from the surface. A commonly used potential to reflect this is

$$f_s = \frac{W_\theta}{2} \sin^2(\theta - \theta_e) + \frac{W_\phi}{2} \cos^2 \theta \sin^2(\phi - \phi_e) \quad (1.17)$$

where  $W_\theta$  is the polar anchoring energy and  $W_\phi$  is the azimuthal anchoring energy. Shiyankovskii *et al.* have proposed an elegant generalization by defining an anchoring tensor  $W_{ij}$  and writing the anchoring potential[44]

$$f_s = W_{ij} n_i n_j; \quad (1.18)$$

the polar and azimuthal anchoring energies are related to the eigenvalues of this tensor which is diagonal in the frame of the easy axis.

Experimental measurements of the dependence of  $f_s$  on  $\mathbf{n}$  have caused others to suggest other potentials that are more applicable in certain circumstances (for example with strong applied external fields)[34]. One such proposal is the expansion of  $f_s$  in Legendre polynomials,

$$f_s = \sum_i W_i P_{2i}(\sin(\theta - \theta_e)) \quad (1.19)$$

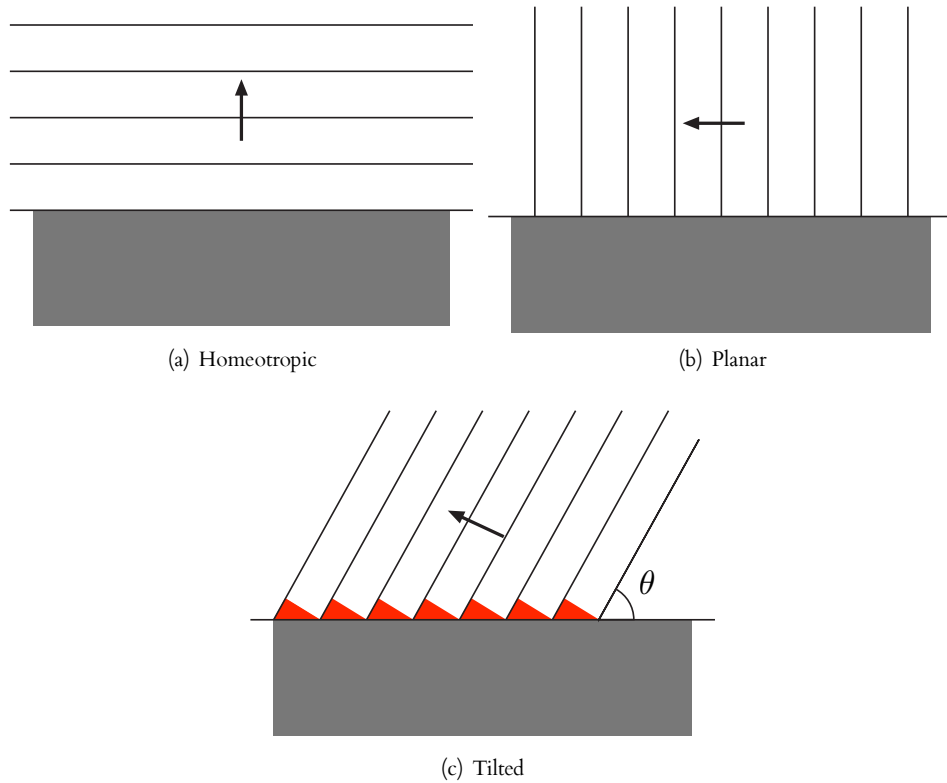


Figure 1.6: Schematic of smectic layers adjacent to a flat surface. While homeotropic (a) and planar (b) orientations are compatible, a tilted (c) configuration ought to require the nucleation of defects.

which may be seen to provide a convenient generalization of the Rapini-Papoular potential which is equivalent to the first term. It is also, perhaps less naturally, possible to expand  $f_s$  in a Fourier series

$$f_s = \sum_i W_i \sin(2i(\theta - \theta_e)). \quad (1.20)$$

A further possibility is to use an elliptic function as a potential

$$f_s = \frac{W}{2} \operatorname{sn}^2(\theta - \theta_e | m) \quad (1.21)$$

where  $m$ , the parameter of the elliptic function, may be varied.

The literature is comparatively scant on the applicability of the Rapini-Papoular potential to smectics. As Li and Lavrentovich note, only true homeotropic or planar alignment may exist without defects at the end of the layers and so one might intuitively expect a sharp minimum in the anchoring potential around these two orientations (fig. 1.6)[45]. This has not been observed experimentally, and experimental measurements of the anchoring energy for smectics yield a range of values which are either comparable to those for nematics or much higher. In the absence of a microscopic theory of anchoring for smectics, one might envisage any number of physical explanations: It is possible, for example, that the smectic order vanishes near rough surfaces and the boundary region is essentially nematic; this nematic region then aligns the adjacent smectic.

To solve device problems with continuum theory the surface energy must be included in the boundary conditions. For a potential  $g(\theta)$ —no surface potential has been suggested which depends on  $\nabla\theta$ —the boundary condition is of the form

$$\nu \cdot \frac{\partial f(\theta, \phi)}{\partial \nabla \theta} = \frac{\partial g(\theta)}{\partial \theta} \quad (1.22)$$

where  $f$  is the bulk energy density and  $\nu$  is the surface normal. Textbooks on variational calculus (e.g. [32]), which normally approach the subject from the point of view of classical mechanics, generally omit the derivation of boundary conditions when surface terms are present and so a derivation is provided in Appendix A. For the purposes of numerical solution of the Euler-Lagrange equations, the prototypical boundary condition (equation 1.22) yields a so-called Neumann-Dirichlet (mixed) boundary condition, which relates the derivative of a field quantity to its value.

## 1.4 Example: HAN Cell Statics

A Hybrid Aligned Nematic (HAN) cell consists of a nematic layer of thickness  $d$  confined between two substrates, one of which promotes planar alignment and the other homeotropic alignment. Typically, the planar surface is treated (by rubbing as described in section 1.3 or photoalignment as described in section 5.2) to fix the azimuthal angle. The director is therefore constrained to single plane: adopting Cartesian coordinates with  $x$  perpendicular to the rubbing direction and parallel to the surface and  $z$  normal to the surface, the director is constrained to the  $y - z$  plane and may be parametrized by a single coordinate  $\theta$

$$\mathbf{n} = (0, \cos \theta, \sin \theta). \quad (1.23)$$

Furthermore, the director is a function of the distance through the cell only  $\theta = \theta(z)$ . The Frank free energy density (equation 1.5) is therefore

$$f_{HAN} = \frac{1}{2}(K_1 \cos^2 \theta + K_3 \sin^2 \theta)\theta'^2 \quad (1.24)$$

where the prime indicates a derivative taken with respect to the  $z$  coordinate. Letting  $\tau = 1 - K_3/K_1$ , the Euler-Lagrange equation obtained from 1.24 is

$$\theta'' = \theta'^2 \frac{\tau \sin \theta \cos \theta}{1 - \tau \sin^2 \theta}. \quad (1.25)$$

which may be integrated directly following some manipulation

$$\begin{aligned} \int \frac{\theta''}{\theta'} dz &= - \int \theta' \frac{\tau \sin \theta \cos \theta}{1 - \tau \sin^2 \theta} dz. \\ \ln \theta' &= -\frac{1}{2} \ln (1 - \tau \sin^2 \theta) + c \\ \theta' &= \frac{c_1}{\sqrt{1 - \tau \sin^2 \theta}} \end{aligned} \quad (1.26)$$

and integrated again with respect to  $z$  over definite limits from  $z = 0$  to some arbitrary dimensionless coordinate  $l = z'/d$  at which the director adopts an unknown angle  $\Theta$

$$\begin{aligned} \int_0^{z'/d} \theta' \sqrt{1 - \tau \sin^2 \theta} dl &= \int_0^{z'/d} c_1 dl \\ \int_0^\Theta \sqrt{1 - \tau \sin^2 \theta} d\theta &= c_1 \frac{z'}{d} + c_2 \\ E(\Theta|\tau) &= c_1 \frac{z'}{d} + c_2 \end{aligned} \quad (1.27)$$

where  $E(\Theta|\tau)$  is an incomplete Elliptic integral of the second kind and  $c_1$  and  $c_2$  are arbitrary constants to be determined from the boundary conditions. Imposing rigid anchoring conditions  $\Theta = 0$  at  $z' = 0$  and  $\Theta = \pi/2$  at  $z' = d$  yields an implicit equation for  $\Theta$  as a function of  $z$

$$E(\Theta(z)|\tau) = \frac{z}{d} E\left(\frac{\pi}{2}|\tau\right) \quad (1.28)$$

where primes are omitted. Solutions  $\Theta(z)$  are plotted for a number of values of  $K_3/K_1$  in fig. 1.7; note that there exist two limiting profiles as  $K_1 \ll K_3$  and  $K_1 \gg K_3$ .

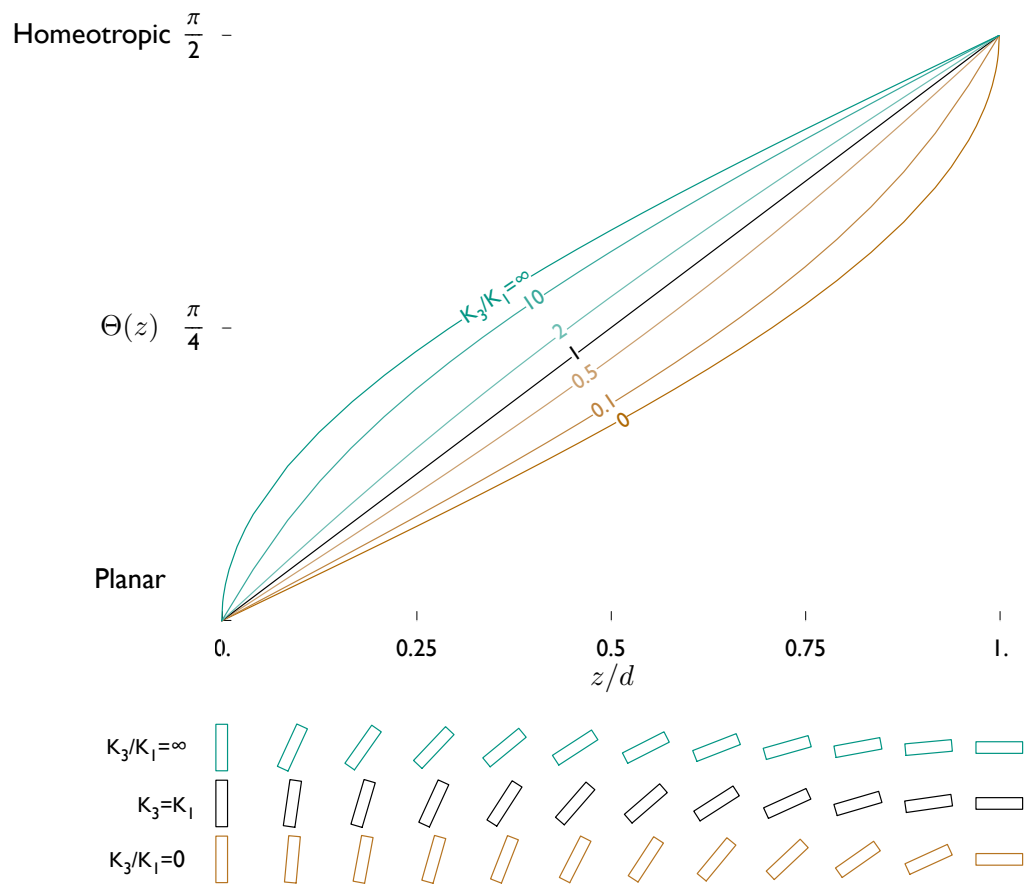


Figure 1.7: Static HAN Profiles for  $K_1 \ll K_3$ ,  $K_1 = K_3$  and  $K_1 \gg K_3$  with rigid anchoring.

## Chapter 2

# Microscopy of Liquid Crystal Structures

### 2.1 Polarizing Microscopy

**P**OLARIZING MICROSCOPY has been an important tool for the study of liquid crystals since their discovery [3]. Liquid crystals are *birefringent* and it is this property that causes them to affect the propagation of polarized light: if the director field changes slowly with respect to the wavelength of incident polarized light, then the polarization axis of the light will tend to follow the director field. Certain configurations of the liquid crystal are therefore able to *convert* the polarization state of incident light so that the light transmitted from the other side of the cell has a different and even possibly orthogonal polarization state. When viewed under the microscope between crossed polarizers these regions will appear bright. The effect is wavelength dependent due both to the structure of the liquid crystal and also due to dielectric dispersion. Polarizing microscope images are for these reasons often brightly coloured.

Each of the various liquid crystal mesophases often has a certain characteristic appearance or texture due to the presence of *disclinations* or discontinuities in the director field and these textures are well documented[20]. For the chemist, a polarizing microscope with a temperature stage together with other techniques such as differential scanning calorimetry offer the possibility of identifying the particular phase sequence of some newly synthesized compound. For the physicist the objects of interest are generally the structures themselves and the questions to be addressed correspondingly rather different: *What is this structure? How does the director field vary in space? What physical effects cause the liquid crystal to adopt this structure?*

The axial resolution or *depth of field* of the conventional polarizing microscope is generally comparable to a typical display cell thickness  $\sim 5\mu\text{m}$ [46, 3] and so the image formed by the microscope represents the integrated response of light passing through the entire cell. For thicker cells the focal plane can be moved through the sample to give some rough indication of the vertical liquid crystal structure; it is normally possible to focus on irregularities on either surface for example.

Nonetheless, a polarizing microscope image contains very little information about the axial dependence of the director field but a great deal about the dependence across the cell. With crossed polarizers, if the director is homeotropic over some region through the whole thickness of the cell, by symmetry no polarization conversion can take place and so that homeotropic region appears dark even when the cell is rotated azimuthally. Regions of planar liquid crystal where the director is parallel to the axis of either of the polarizers through the distance of the cell also appear dark, but become bright and dark again as the cell is rotated azimuthally. The transmitted intensity is proportional to  $\sin^2 2\alpha$  where  $\alpha$  is the angle between the optic axis of one of the polarizers and the director. A  $90^\circ$  twisted configuration, like that in the conventional Twisted Nematic or TN cell, will always appear bright as the cell is rotated azimuthally between the polarizers. By comparing the light and dark regions in several images taken at different angles the in-plane component of the director field may be reconstructed (it is of course necessary to ensure, prior to taking such images, that the centre of the rotating stage is properly adjusted to lie at the optic axis of the objective). There exists a certain ambiguity in the reconstruction, however, as the liquid crystal appears dark when it is aligned with either of the polarizers and so it is not possible to discriminate between a director at some angle  $\theta$  and a director at an angle  $\theta + \pi/2$  from some common reference direction.

By way of a (well known [3]) example, figure 2.1(a) shows a  $10\mu\text{m}$  hybrid aligned cell constructed with a planar degenerate substrate where the liquid crystal (8CB) is in the nematic phase. As the cell is cooled to just above the nematic–smectic transition, the liquid crystal adopts a novel striped configuration [fig. 2.1(b)] which shall be the subject of the next chapter.

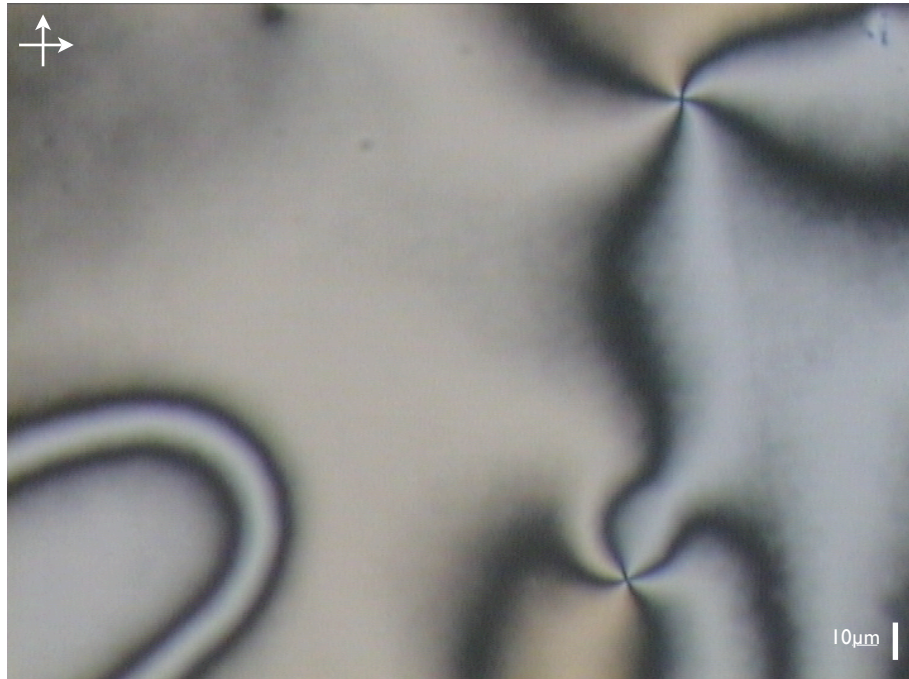
In the upper (nematic) image, the two crosses or *brushes* on the right are characteristic of the nematic phase and are known as *Schlieren* textures. One possible configuration for the in-plane component of the director field near each cross is everywhere radial from a point defect located on the planar surface, and many other inverted solutions are possible (fig. 2.2, bottom left). Other sorts of point disclination, of different strength, may also be observed in nematic samples (fig. 2.2 right). On the bottom left of fig. 2.1(a) is a “wall”<sup>1</sup> that separates two HAN domains of opposite orientation. The azimuthal component of the director reorients by  $\pi$  radians going across the wall and hence appears under the polarizing microscope as a bright band surrounded by two black bands. The wall in the figure is somewhat atypical because the planar anchoring in this particular HAN cell happened to be prepared so as to be azimuthally degenerate and so the director is able to rotate azimuthally with no surface energy cost. If the planar substrate were prepared, as is more common, so as to have a preferred azimuthal orientation, the reorientation wall would be much narrower to reduce the surface anchoring energy cost or, if the azimuthal anchoring energy was sufficiently strong, the reorientation would occur through a line disclination (an example of which is to be found in chapter 3).

Towards the top left of the figure, away from the disclinations, the nematic adopts a spatially uniform

<sup>1</sup>The term “wall” is used in two senses in liquid crystal physics: more properly, a wall may be a sheet defect at which some part of the order parameter is discontinuous (such as in a biaxial nematic); the second, and the one implied here, is a narrow region in which the order parameter field is distorted (but still continuous) that separates two domains where the director is uniform in the plane of the cell.



Crossed Polarizers



(a)

Crossed Polarizers



(b)

Figure 2.1: Polarizing microscope images taken with crossed polarizers of a hybrid aligned cell with planar degenerate surface in (a) the nematic phase and (b) the smectic phase.

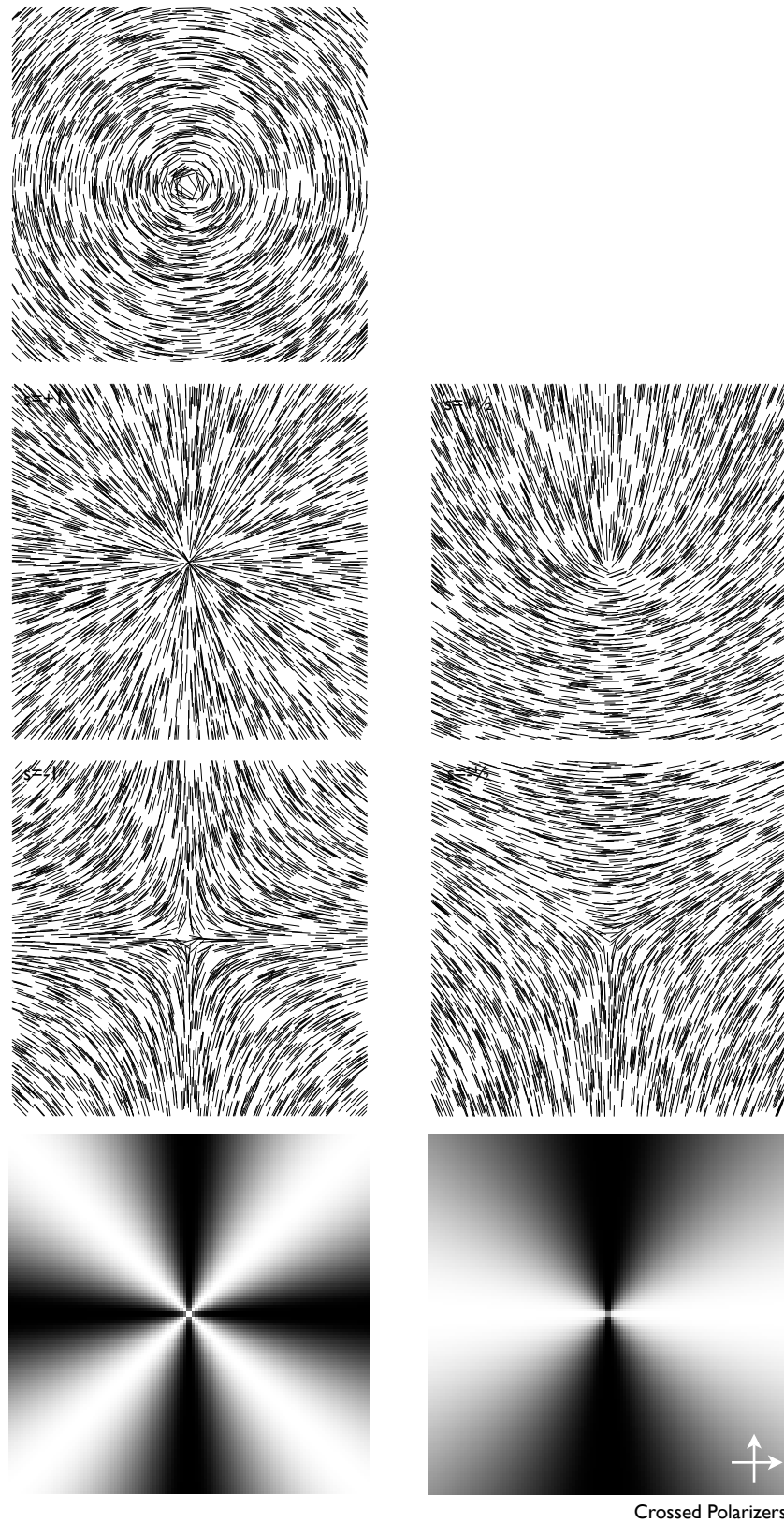


Figure 2.2: Schematic of some possible configurations of the director field around a point disclination in the plane in which the core of disclination sits with (bottom) simulated images as might be seen under the polarizing microscope. Disclinations are characterised by their strength  $s$ . Note that disclinations of the same magnitude with opposing signs are indistinguishable from a single image alone.

Crossed Polarizers

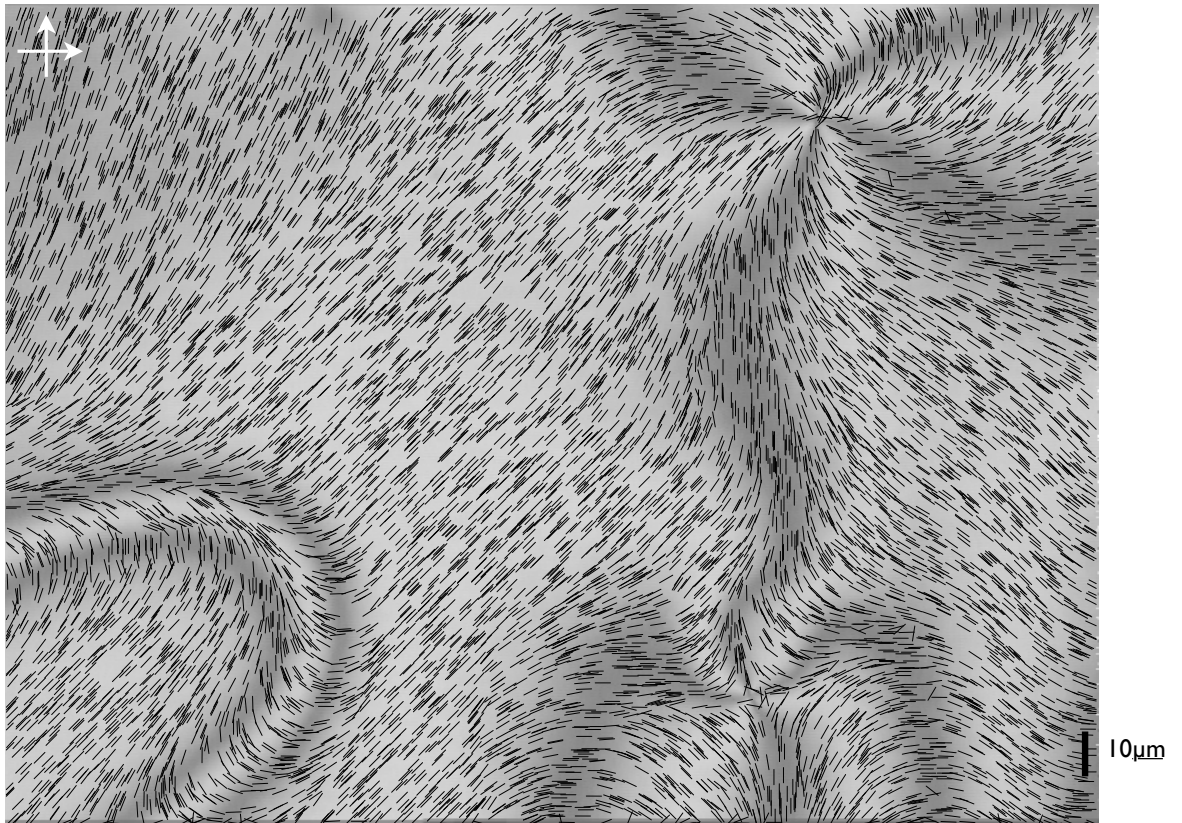


Figure 2.3: Reconstructed in-plane component of a possible configuration of the director field from a polarizing microscope image of a nematic in a hybrid aligned cell.

appearance and since it appears bright one may deduce that the in-plane component of the director field is approximately  $45^\circ$  to the polarizers; one can in this case use the known  $\sin^2 2\alpha$  law to reconstruct a possible configuration of the in-plane component of the director across the entire image (fig. 2.3). In fact there are sixteen distinct director configurations that might have produced the observed image, even taking into account the physical requirements that the director field must be continuous except at disclinations and the two disclinations shown must have the same absolute strength. Further information on the how the director field was automatically reconstructed from the image may be found in Appendix B.

## 2.2 Confocal Microscopy

A significant restriction of the polarizing microscope is that it provides only a two dimensional view of a liquid crystal film which, although thin, may have three-dimensional structure: there is nothing in fig. 2.1 to give information on the variation of the director through the thickness of the cell might be. As the image represents the integrated response of the polarized light as it has propagated through the film, it is not possible to deduce the vertical part of the director field either around the disclinations or through the domain wall, both of which are problems of interest.

It is pertinent to briefly mention some other techniques that have been used to deduce liquid crystal structure: The very powerful guided mode techniques are capable of resolving axial behaviour [47, 48, 49, 50, 41, 51, 52] but are only suitable for systems that are laterally uniform as they work by reconstructing the axial dependence of the director field from shifts in the guided modes observed in the transmitted and reflected light. Guided mode studies have, for example, elucidated the static and dynamic behaviour of a nematic in a HAN cell to applied electric fields[50]. Some information on the three dimensional behaviour may also be obtained by electron microscopy[3] or X-ray diffraction studies (e.g. [53, 15, 54]); these techniques are however either invasive or destructive respectively. Both guided mode studies and X-ray diffraction studies suffer from the problem that the measured quantity is related to the object of interest—the three-dimensional director field—by some complicated transform and therefore must be reconstructed by a fitting process.

Confocal microscopy is a technique in common use in Biology[46, 55] that is capable of forming depth-resolved images in a noninvasive and nondestructive manner. In a conventional microscope, light illuminating the sample is magnified by an objective and secondary optical elements such as an eyepiece and brought to a focus either on the retina of an observers eye or on the CCD of a camera. The whole focal plane (with a relatively wide depth of field) may be seen simultaneously. In a confocal microscope (fig. 2.4), light from the sample is passed through a pinhole which acts as a spatial filter (fig. 2.5): light from a narrow depth of field—a single ‘plane’—of the sample will be brought to a focus at the centre of the pinhole and allowed to pass through; light from all other depths in the cell will be out of focus at the pinhole and their intensity consequently greatly attenuated. The transmitted light from the pinhole is then typically detected with a photomultiplier tube or equivalent device. An image of the entire in-focus plane may be formed by scanning either the stage, the pinhole or more rapidly by altering the beam path under the electrically controlled influence of galvanic mirrors. The focal plane may also be adjusted with a stepper motor to collect optical *sections* of the sample and from these it is then possible to reconstruct a three dimensional image of the sample by computer.

Biological samples such as cells are typically stained with some fluorescent *tag* compound that is selectively absorbed by a structure of interest[46, 55]. The microscope’s optics focus a pump laser over a small volume or *voxel* and collect any light emitted by the marker dye. It is necessary to remove the pump laser light and so appropriate filters are placed in front of the photodetector. The sample is then scanned over a desired region to produce the image and hence the technique is referred to in the (expansive) biological literature as Confocal Laser Scanning Microscopy (CLSM). It is important to emphasise that the image contrast is caused by variations in dye concentration due to selective absorption of the dye molecules. If such a dye is introduced into a liquid crystal film, and it does not phase separate, then the dye concentration will be uniform in space except in regions of high spatial gradients in the order parameter such as disclinations. A CLSM image of such a system will consist of an uninteresting uniform band of light. If, on the other hand, rather than tagging the liquid crystal fluorescent microparticles are dispersed in the liquid crystal

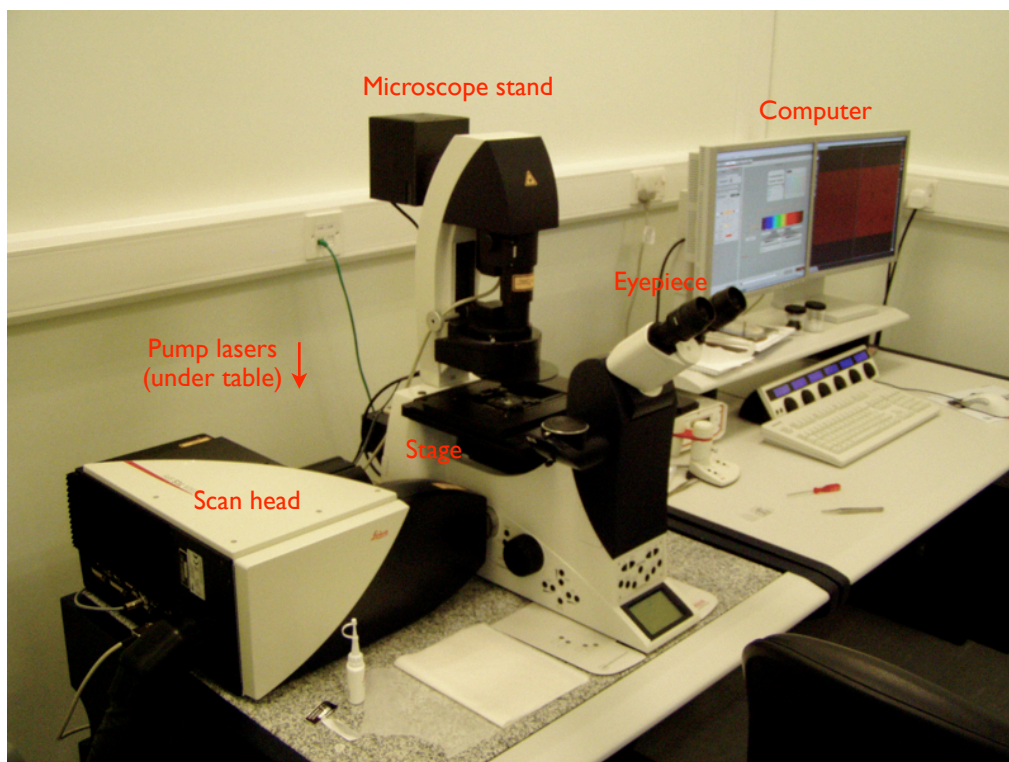


Figure 2.4: The Leica SP5 confocal microscope installed in the School of Physics at the University of Exeter.

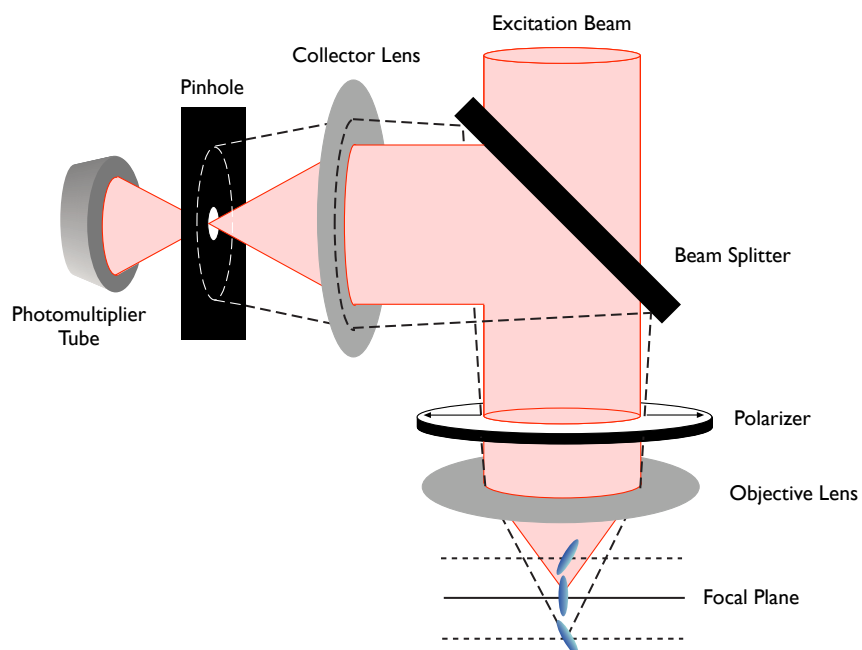


Figure 2.5: Schematic of a confocal microscope illustrating how light from the in-focus plane is allowed to pass through the pinhole while light from an out of focus plane is excluded.

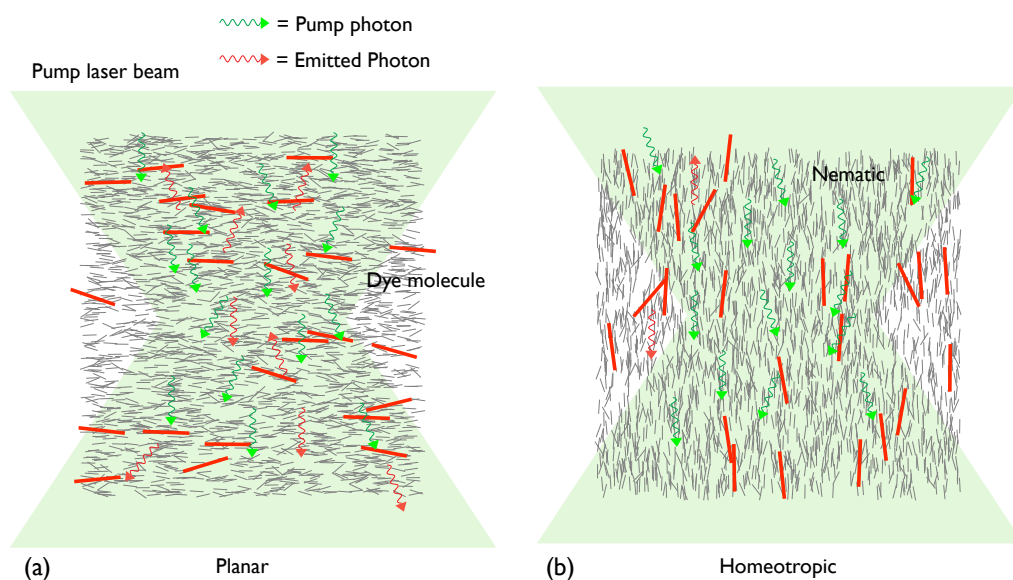


Figure 2.6: Schematic of how spatial orientation of a dye-doped liquid crystal produces a variation of fluorescence intensity within a region at the focus of a pump laser. The anisotropic dye molecules are aligned in the liquid crystal by the guest-host effect and the local average orientation of the dye molecules is parallel to that of the liquid crystal.

film, or a polymer-dispersed liquid crystal film is prepared with a small percentage of fluorescent monomer, then CLSM may nonetheless produce a useful image [56, 57].

The innovation of the Lavrentovich group[58] was to dope the liquid crystal with a dye of very anisotropic molecular shape which is then aligned by the liquid crystal by the well-known *guest-host* effect (fig. 2.6). Just like the nematic molecules, the dye molecules themselves may be characterized by an orientational distribution function which must be related to the distribution function of the fluorescence excitation and emission dipoles of the dye. Suppose the excitation and emission dipoles lie along the length of an idealized dye molecule: if the electric field vector of an incident photon is parallel to the excitation dipole the molecule may be excited and will later emit a photon with some shifted wavelength [fig. 2.6(a)]; if the photon's electric field vector is orthogonal to the excitation dipole, there is no possibility of excitation [fig. 2.6(b)]. One can envisage three characteristic time scales: one  $\tau_{em}$  the fluorescence lifetime of the dye, one  $\tau_{rot}$  associated with rotation of the dye molecules and a final timescale  $\tau_d$  the average length of time taken for a dye molecule to diffuse across a length of the order of the optical resolution of the microscope. If  $\tau_{em} \ll \tau_{rot} < \tau_d$  then, even allowing for the imperfectly ordered dye molecules and the mix of polarization states of incident photons within the illuminated cone, homeotropic regions will appear darker than planar regions and so it ought to be possible to resolve regions of differing polar orientation with the confocal microscope. This approach is referred to in the liquid crystal literature as Fluorescence Confocal Microscopy (FCM)[58].

A further refinement (used by the same group) is possible: if the polarization state of incident pump photons is set with a polarizer—or at least characterized by an anisotropic azimuthal distribution function—then in a planar region with some variation of the azimuthal orientation of the director, those molecules with

their excitation dipole perpendicular to the electric field of the incident photon will not be excited. Those molecules, on the other hand, with their excitation dipole parallel to the polarization of an incident photon may be excited and consequently emit. The polarization state of the emitted photon is parallel to the emission dipole of the emitting molecule and so the emitted light is typically passed through a second polarizer in front of the detector to enhance the contrast. It is therefore possible to resolve with so-called Fluorescence Confocal Polarizing Microscopy (FCPM) the azimuthal *and* polar orientation[59]. The fluorescence intensity is proportional to

$$I \propto \langle \cos^4 \phi \cos^2 \theta \rangle \quad (2.1)$$

where  $\theta$  and  $\phi$  refer to the polar and azimuthal components of the director as defined in the previous chapter (the  $z$ -axis is taken to be parallel to the optic axis of the microscope objective) and the average is to be taken over all molecules in a single voxel. Unlike conventional polarizing microscopy, there is no ambiguity between regions of perpendicular azimuthal orientation if the liquid crystal is known to be planar; it is however the case that (infinitely) many director configurations map to any given intensity value and so the problem of reconstructing the director profile from an intensity profile is ill-posed: Prior knowledge of the system, such as the surface easy axes, and physical constraints such as continuity of the director field, must be used to resolve the ambiguity.

Having outlined the technique, it is helpful to review the sorts of system that confocal microscopy has helped to elucidate. Confocal microscopy was first used to study liquid crystal systems in 1997 when Held *et al.* [56] studied the switching process of a polymer-stabilized cholesteric liquid crystal. Instead of using anisotropic dye molecules to produce the image as described earlier, a small percentage of the monomer was replaced by a functionalized fluorescent monomer. Following photopolymerization, the polymer network could be imaged by confocal fluorescence microscopy, and was shown to follow the helix of the cholesteric. A much later paper by Petkovsek *et al.*[57] used the same technique to observe the switching of a polymer-stabilized ferroelectric liquid crystal.

An intriguing possibility, heretofore unexplored, would be to incorporate an anisotropic dye with a fluorescence emission peak that does not overlap that of the tag used to mark the polymer network—this could be achieved for example by using two dyes of different excitation wavelength. The sophisticated wavelength filtering abilities of the modern confocal microscope could then be used to study the behaviour of the polymer network and the liquid crystal simultaneously.

CLSM is not the only microscopy technique that is capable of producing a depth-resolved image; an alternative is to probe the sample with a tightly focused pump beam with the intention of generating light by nonlinear optical effects which naturally provide a wavelength shift. These effects are sufficiently weak that the overwhelming majority of light collected must have come from the focus of the probe beam. Second-harmonics cannot be excited in uniaxial liquid crystals because of the inversion symmetry and so third-harmonic microscopy was used to image the phase transition of a liquid crystal in a twisted nematic

cell[60]. Although useful in that no dopant need be introduced into the system, the technique is limited by the laser powers required to generate sufficient intensities of third-harmonic light.

Anisotropic dyes were used for the first time by Smalyukh and Lavrentovich[59, 58] in 2001 with FCPM to obtain images of focal conic domains in a smectic liquid crystal confined between two homeotropic substrates. In the same paper, they presented cross sections of a planar Fredericks cell at several values of applied voltage. This latter situation shall be discussed later; the Fredericks transition is so well understood that it is a useful system to analyse the performance of confocal microscopy.

The same authors later applied the technique to a very famous system[58, 61] namely the Grandjean-Cano wedge that consists of two planar substrates held at a small wedge angle (such that the thickness ranges from less than  $1\mu\text{m}$  to around  $100\mu\text{m}$  over a lateral distance of millimetres) and filled with a cholesteric liquid crystal of micron-scale pitch. Only a half-integral number of turns of the cholesteric helix are consistent with the boundary conditions, and with the polarizing microscope such regions are observed separated by disclination lines that run perpendicular to the inclined direction of the wedge. In cross sections produced with FCPM, the helix appears as a series of horizontal stripes as the director rotates around and the structure of the edge disclinations was made visible for the first time. These disclinations shall later prove of some interest as they are of the same class as certain defects observed in a quite different system in chapter 3 and shall be discussed in chapter 4.

A second very famous system, that of a liquid crystal confined in a cylinder with radial anchoring at the surface, was recently looked at using FCPM by Matthias *et al.* [62]. The cylinders used were novel in that their radius was modulated along length of the cylinders and this modulation was shown to stabilize the periodic escaped configuration that is only metastable in a regular cylinder.

A third paper by Smalyukh *et al.*[63] contrasted the behaviour of a nematic and that of a biaxial smectic liquid crystal in a hybrid aligned cell with regard to the disclinations observed in a *Schlieren* texture: these two liquid crystal phases are very difficult to distinguish with conventional polarizing microscopy. In cross sections obtained with FCPM, however, it is apparent that in the nematic case the disclinations are points confined to the surface and the director relaxes—“escapes to the third dimension”—into the bulk; in the biaxial smectic case the disclinations are lines that extend perpendicular to the substrate into the bulk.

An interesting development was the incorporation of tagged fluorescent particles, cylinders or spheres, into a liquid crystal which could then be manipulated either by electrophoresis[64] or with laser tweezers[65]. Images of the included particle and the liquid crystal were obtained simultaneously and used to measure certain of the liquid crystal viscosities[65].

Having reviewed the available literature on FCM and FCPM it is helpful to scrutinize the sort of images that may be obtained using the technique and it is particularly useful to apply the technique to a cell geometry whose behaviour is well studied. A suitable liquid crystal system is the classic planar Fredericks cell with an applied electric field, and FCPM images of this system have in fact already been



published[59]. A  $6\mu\text{m}$  cell with planar substrates, prepared so that their azimuthal easy axes were parallel, was constructed and filled with E7 doped with approximately 0.01% by weight of the dye *N,N*-bis(2,5-di-*tert*-butylphenyl)-3,3,9,10-perylenedicarboximide (BTBP). Due to the very short working range of the objectives in commercial confocal microscopes, it was necessary to prepare one surface of the cell on a thin coverslip. The cell was imaged in FCM mode (i.e. intensity contrast due to the polar component of the director only) in a Leica SP5 confocal microscope using the  $20\times$  objective and 488nm pump laser and collecting emitted light over the 510 – 560nm range. Image stacks of axial sections were taken at several different applied voltages and the cross sections reconstructed (fig. 2.7) from the image stacks obtained. The cross sections were then averaged across the width of the image to give average intensity profiles (fig. 2.7). It may be seen that in the 0V state the intensity profiles appear high—the cell is, as expected, planar—and do not change below 2V. The cell switches rapidly: the centre of the cell has apparently become homeotropic by 5V and has almost completely switched by 6V as the profile changes after that very little up to 20V. The observed *contrast ratio*,

$$C = \frac{(\text{intensity in planar region} - \text{intensity in homeotropic region})}{(\text{intensity in planar region} - \text{background})}, \quad (2.2)$$

an important ‘figure of merit’ that indicates how well homeotropic and planar regions are resolved, is  $\sim 0.4$ . A second similarly prepared cell with no applied voltage was then imaged in FCPM mode in three azimuthal orientations (fig. 2.8) to illustrate polarization contrast; the contrast ratio achieved was somewhat better,  $\sim 0.6$ . The intensity profiles in both figures 2.7 and 2.8 appear quite different to what one might naively expect: they are asymmetric with respect to the cell centre, the edges of the cell do not appear sharp and lobes in the intensity profile from the regions of the cell near the edges that might be expected to remain planar (and hence bright) are not present. To understand why this is the case, it is necessary to review the factors that affect the quality of the images produced:

*Laser intensity and dye concentration* It is clear from the cross sections that FCM images are rather noisy.

The signal-to-noise ratio depends on the number of photons emitted by the sample which in turn is affected by the laser power and the dye concentration. There is a compromise to be reached: as FCM is intended to be a non-invasive technique the dye concentration must be kept low otherwise the material parameters of the liquid crystal will be affected; on the other hand if the laser power is rather high then laser-induced molecular reorientation[66, 67] will reduce the contrast ratio. It is, of course, always possible to increase the signal-to-noise ratio by extending the integration time and therefore reducing the scanning rate of the microscope. Laser heating of the sample, which inevitably destroys the structure of interest, occurs if the laser power is sufficiently high. A practical value for laser intensity, that used in figure 2.7, is around 200nW; others have suggested 120nW[59].

*Molecular properties and ordering of dye* Dye molecules are oriented about the director of the liquid crystal

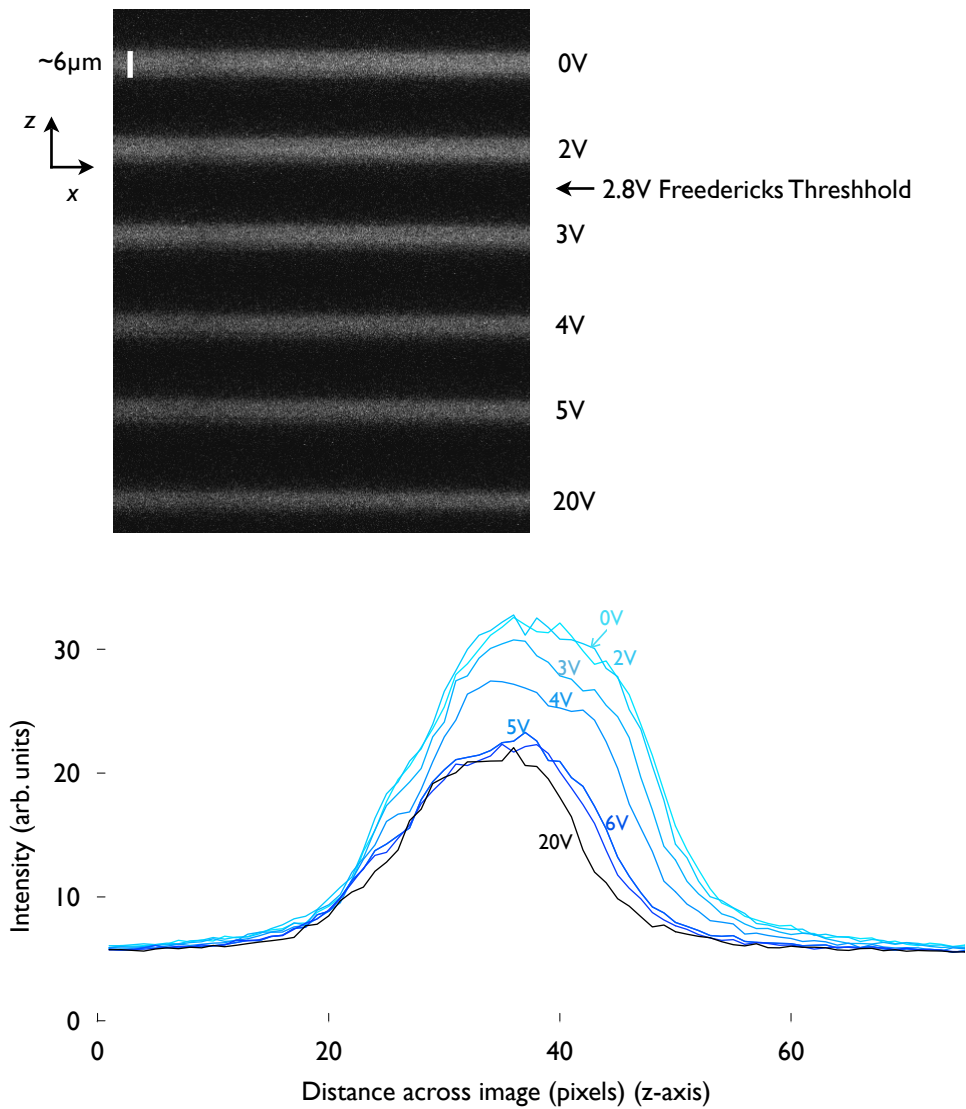


Figure 2.7: (Top) Cross sections reconstructed from FCM images of a planar Fredericks cell with several values of applied voltage. (Below) Intensity profiles obtained by averaging over the width of each cross section.

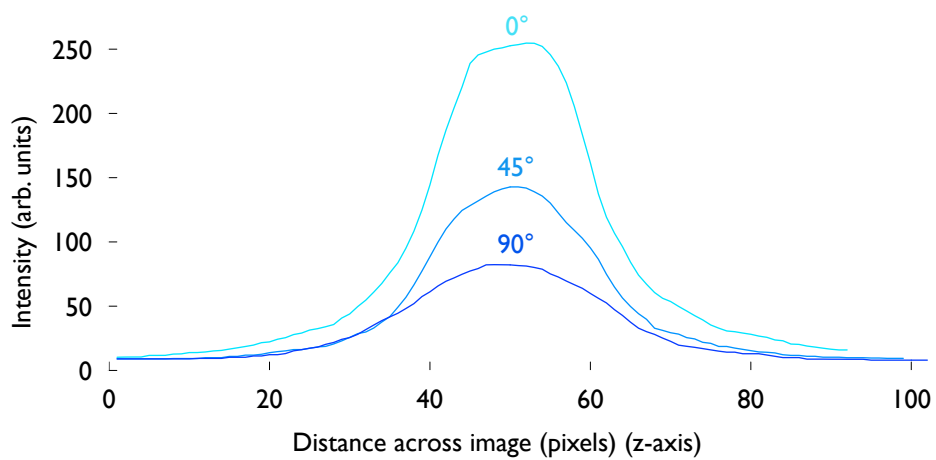


Figure 2.8: Intensity profile from cross sections of a  $6\mu\text{m}$  planar cell with no applied voltage, taken with the alignment direction at  $0^\circ$ ,  $45^\circ$  and  $90^\circ$  to the optic axis of the polarizer.

according to some distribution function which has the same symmetry and hence the same mathematical form as a nematic (eq. 1.2 on page 24). As the dye ordering decreases, the contrast ratio is reduced. If the excitation dipole is not parallel to the long axis of the molecule but instead makes some angle  $\alpha$ , then even if the order parameter of the dye is 1 the excitation dipoles will nonetheless be distributed about the director in a cone and the contrast ratio will be less than 1. As the angle  $\alpha$  increases the contrast ratio is reduced.

It is, finally, necessary to select a dye with sufficiently large *Stokes shift*[46]—the difference  $\Delta\lambda$  in wavelength between the absorbed and emitted photons—in order that the pump laser can be effectively removed from the detected signal.

*Point spread function of microscope* The idealized picture presented earlier is that the pump laser is brought to focus over a tiny region of liquid crystal and that only light emitted from this small volume is detected. In a real microscope, factors such as the finite size of the pinhole and properties of optical elements (e.g. numerical aperture of the objective) mean that light is collected over a finite (albeit small) volume with a relative weighting described by a *point spread function*[46, 55, 68, 69]. The measured intensity distribution is therefore the convolution of the “true” intensity distribution with the point spread function. In fig. 2.7 the intensity at the left and right hand sides of the cell falls away smoothly rather than sharply because when the focal plane is scanned through the cell thickness, first the edges and then the centre of the point spread function enter the liquid crystal layer. The point spread function widens considerably and gains secondary maxima as the scanning depth is increased[46, 68, 69].

If the point spread function were known, it would be possible to remove the blurring from the image by *deconvolution*. The point spread function of a real microscope is, however, generally unknown and complicated: while Fourier deconvolution methods are inappropriate due to the poor signal-to-noise ratio of FCM images of liquid crystal samples, a wealth of literature exists on *blind deconvolution* techniques (see [70] for a useful review), mostly Bayesian, that aim to reconstruct simultaneously the point spread function and the true image given some prior knowledge (a set of ‘priors’) about both [70, 71]. These techniques applied naively to FCM and FCPM images of liquid crystals may not perform well because the point spread function depends on the distance through the cell and, perhaps less strongly, the director profile above the point of interest. Figure 2.7 suggests an intriguing possibility, thus far unexplored: one knows that the left and right hand edges of the cell in the “true” intensity distribution ought to be sharp and so the shape of the intensity distribution at the edges of the cell in fact depend very strongly on the point spread function and weakly on the gradient of the “true” intensity distribution immediately adjacent to the edge of cell. This seemingly very powerful prior is unique to confocal microscope images of liquid crystal cells.

*Birefringence* The point spread function becomes greatly complicated by the birefringence of the liquid

crystal; rather than being brought to focus over a small volume as in the case of a uniaxial medium, the probing beam is split into an ordinary and extraordinary component which are brought to focus at different points. The width of the point spread function is increased (the image is blurred) by a distance of order  $\sim g(\Delta n/\langle n \rangle)d$ [58] where  $\Delta n$  and  $\langle n \rangle$  are the birefringence and average refractive index respectively of the liquid crystal,  $d$  is the depth of scanning and  $g$  is a factor of order unity that depends on the optical components used in the beam path of the microscope. Lavrentovich proposes that a typical value is around a micron[58].

A second effect is that as the cell is switched, the effective refractive index of the cell changes and hence the cone angle of the pump light is modified as it passes into the liquid crystal layer: this alters the distance at which the confocal pump rays are brought to focus. Equally the axial distance from which fluorescence appears to emanate is altered by the same amount and so as the cell is switched the image is rescaled in the axial direction. This effect is very noticeable in fig. 2.7 as the low and high voltage states have quite different apparent thicknesses.

Both these effects may be reduced by choosing to study, as the Lavrentovich group have done, liquid crystals with low birefringence although useful results such as those illustrated may be obtained from conventional materials. The problem is not unique to the study of liquid crystals as many biological samples exhibit some degree of birefringence.

*Light scattering and absorption* Due to molecular fluctuations, nematics scatter light effectively and consequently, as the focal plane is moved further into the liquid crystal layer, the intensity of pump light reaching the focal point and the intensity of emitted light is attenuated. This effect is exacerbated by dielectric absorption of light by the liquid crystal. In fig. 2.7, the objective and pump laser are on the left hand side of the intensity distribution and so, although the director configuration in the cell is known to be symmetric, the intensity profile decreases going to the right.

*Concentration Gradients* It is assumed that the dye is equally concentrated throughout the nematic. Near disclinations, high gradients in the director field may reduce the ordering of the dye as they do to that of the host nematic. Alternatively, phase separation may occur where the dye molecules either aggregate at the defect core or are excluded from it. Such effects may be beneficial in allowing disclinations to be resolved but defy any attempt to recover the director field.

A separate cause of inhomogeneous dye concentrations is the surface treatment used in the construction of the cell: it is possible that a surface treatment might selectively absorb the dye leading to anomalous lobes at the edge of the cell. Quenching of fluorescence by certain surfaces may also reduce the intensity.

*Adiabatic following of polarization* Birefringence causes the polarization state of incident light to follow a rotating director field if the director varies in a plane orthogonal to the wavevector of the

light. FCPM studies of certain structures, for example cholesterics of pitch comparable to the cell thickness, require careful interpretation as the polarization state of the emitted photons will have been altered by the structure through which they have passed.

With the above reservations in mind, the two techniques of polarizing microscopy and confocal microscopy were applied to study a smectic liquid crystal in a hybrid aligned cell; that work is the subject of the next chapter.

## Part II

# Results

## Chapter 3

# What Configuration does a Smectic-A Adopt in a Hybrid Aligned Cell?

**A** SMECTIC in a hybrid aligned cell is a frustrated system: the surfaces favour a distorted state that includes bend distortion while the nearly incompressible smectic layers exclude twist and bend distortions from the liquid crystal and therefore favour one of the six configurations that preserve the interlayer spacing (fig. 1.3 on page 23). The system resolves the frustration by imposing a periodic array of fan-shaped domains (fig. 3.1) which were first observed by Ruan *et al.*[2] and shown to strongly diffract.

The pitch of the array was shown to depend linearly on the cell thickness and the authors of that paper proposed a model (fig. 3.2) for the domains as sections of spherocylinders. The relative size of the cylindrical and spherical parts of the domain, and consequently the pitch, could be adjusted so as to minimize the free energy, and such a model successfully predicts the linear relationship between pitch and cell thickness. The gradient of the line was related to the difference between the anchoring energies at the top and bottom surface. This model was, however, later refuted by Pishnyak *et al.*[72] who proposed, based on observations with a confocal microscope, that the structures were in fact incomplete toroidal or Dupin cyclide focal conic domains.

As an interesting example of self-organization, a number of practical applications can be envisioned. The structure might be useful as a template; one can envisage photopolymerizing the structure in place and then when the liquid crystal is heated up to the nematic phase it might retain in some form the hexagonal structure. If, however, the structure is to have any use, then it is necessary to understand the physical origin of the structure, how to ensure that it is as regular as possible and if there are further parameters that might allow the pitch of the structure to be controlled: these questions shall be considered first in this chapter by experiment and, in the next chapter, theoretically.

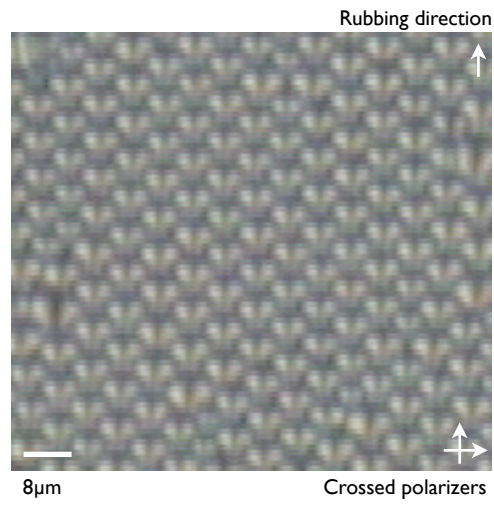


Figure 3.1: Polarizing microscope image of Ruan *et al*'s fan-shaped structure.

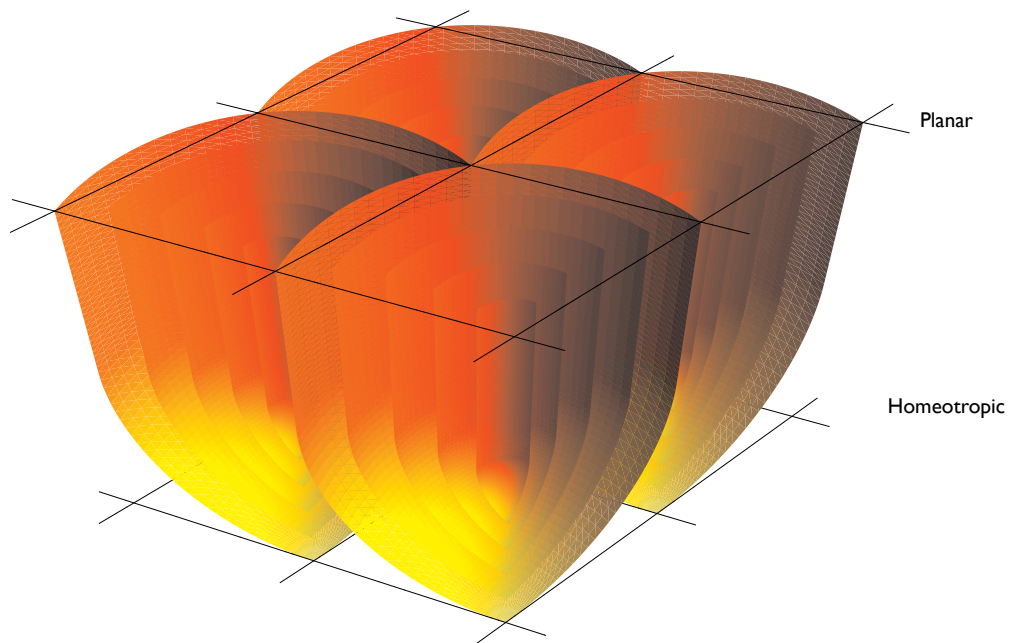


Figure 3.2: Ruan *et al*'s model of spherocylinders for the smectic structure



### 3.1 Cell Construction

A liquid crystal cell consists of two glass substrates that have been treated to promote a desired easy axis and are held apart by a suitable spacer. If electrical contact is required, glass substrates coated with 10 nm of Indium Tin Oxide (ITO) are used. To allow uniform coating with alignment material, the glass substrates must be thoroughly cleaned: They are first rinsed with deionized water and roughly 10% by volume detergent (Decon 90) in an ultrasonic bath for 30 minutes and then rinsed again with pure deionized water and left overnight in acetone. Each substrate is then ‘drag’ cleaned with strips of fine tissue paper dipped in a little solvent; acetone is used for rough cleaning followed by isopropanol for finer cleaning.

The cleaned substrates are then treated to promote a desired orientation in the adjacent liquid crystal. A variety of treatments exist and are efficacious to varying degrees for different liquid crystal materials; different treatments may be used to provide quite different anchoring energies.

**Polyimides** Many different polyimides have been synthesized specifically for liquid crystal alignment applications, and polyimides remain the most common choice for commercial fabrication of displays[34]. A proprietary polyimide, X201, was used to promote planar alignment. A second proprietary polyimide, RN1663 diluted with 50% n-methylpyrrolidone (NMP) by volume, was used to promote homeotropic alignment. The substrates are spin coated with polyimide in clean room conditions at 6000rpm for X201 and 2400rpm for RN1663, pre-baked on a hotplate at 80°C for 1 minute and then baked in an oven at 200°C for 1 hour. The planar polyimide is then rubbed with a nylon cloth to promote a particular azimuthal easy axis.

**Lecithin** A surfactant, lecithin promotes homeotropic alignment[34]. Pure lecithin is dissolved in ether (about 10% by volume) and then applied to the substrate with a slip of fine tissue paper in a similar manner to drag cleaning. The ether rapidly evaporates leaving lecithin molecules attached to the surface. Lecithin may alternatively be deposited using the Langmuir-Blodgett technique[35]. The quality of alignment depends on the density of lecithin molecules which should be rather low: lecithin films are known to undergo phase transitions from a quasi-solid to quasi-liquid to quasi-gas state with decreasing number density and experimental observations have shown that the anchoring energy is temperature dependent.

**Silicon Oxide** may be evaporated onto the substrate. If the substrate is held at oblique incidence—60°—to the source beam, the silicon oxide forms oblique steps that tend to promote planar alignment along the length of the channels. Homeotropic alignment may also be achieved by evaporating the silicon oxide at 30° to the source.

The cells are then assembled from the treated substrates in clean room conditions. A variety of spacers were used: to construct cells of 2 – 8 $\mu$ m, glass beads of known size and dispersion were mixed into UV-curable glue and painted sparingly on the side of the substrate before assembly. A variant of this method

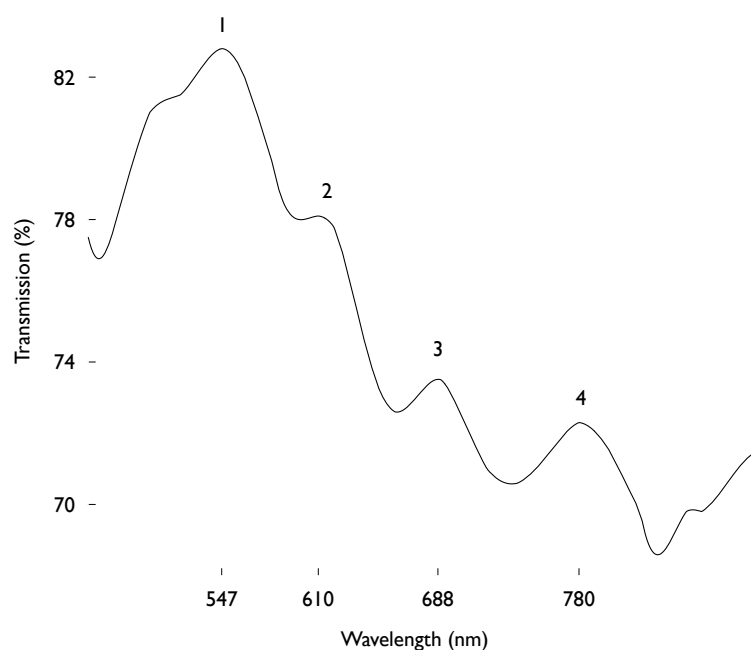


Figure 3.3: Transmission spectrum of an empty (air-filled)  $2.7\mu\text{m}$  thick cell.

was used for the majority of cells: beads were dispersed across the substrate from a dispenser with a burst of compressed nitrogen. The latter method reduces the problem of volume changes during filling and the periodic structures described below are unaffected by the presence of beads throughout the cell. For thicker cells, i.e.  $10 - 30\mu\text{m}$ , strips of mylar of appropriate thickness were cut and glued at the edges as a spacer.

Having assembled the cell and cured the glue, each cell was placed in a spectrograph and a transmission spectrum taken over the optical regime. The two air-glass interfaces act as a Fabry-Perot resonator and weak maxima are observed in the spectrum. If there are maxima at wavelengths  $\lambda_1$  and  $\lambda_2$ ,

$$2d = n_1\lambda_1 = n_2\lambda_2$$

where  $n_1$  and  $n_2$  are unknown integers and  $d$  is the unknown cell thickness. Solving for  $d$ ,

$$d = \frac{(n_2 - n_1)\lambda_1\lambda_2}{2(\lambda_2 - \lambda_1)}$$

it is clear that the cell thickness may be determined from two observed maxima and by counting the number of maxima that separate them. Some cursory judgement on the flatness of the cell was also made after the cell was assembled by viewing the empty cell by eye. If a cell is of nonuniform thickness, coloured interference fringes may be observed; a common flaw is that the cell is slightly wedge-shaped in cross section in which case the fringes take the form of a series of parallel bands which lie orthogonal to the direction in which the cell thickness changes. Following this scrutiny, poor cells were discarded.

Experiments were performed with the liquid crystal octocyanobiphenyl (8CB) which exhibits the following

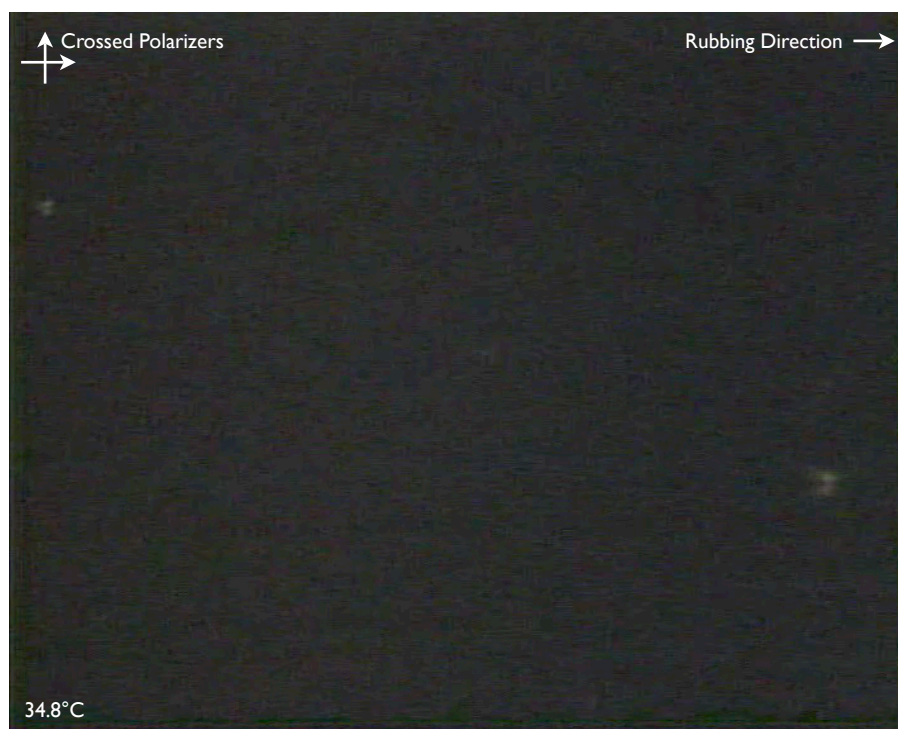


Figure 3.4: Polarizing microscope image of 8CB in a HAN cell in the nematic phase.

phases at atmospheric pressure[73, 3]

$$Cr \xrightarrow{21.5^{\circ}C} S_A \xrightarrow{33.5^{\circ}C} N \xrightarrow{40.5^{\circ}C} I.$$

The liquid crystal sample and cell are heated up to the isotropic phase on a heat stage and the cell is filled by capillary action. The cell is cooled slowly and then sealed with epoxy resin.

## 3.2 Polarizing Microscopy

Fresh cells were constructed and their thickness characterized as described above and filled in the isotropic phase with 8CB in a Mettler heat stage. The stage was mounted on the rotating stage of a polarizing microscope with crossed polarizers in such a way that observations of the behaviour of the liquid crystal could be made as the cell was slowly cooled first into the nematic phase and then the smectic phase. Videos and still images as appropriate were recorded using a video camera attached to the microscope and were digitized on a computer.

In the nematic phase, the behaviour characteristic of a HAN cell was observed: when the rubbing direction is aligned with the axis of one of the polarizers, the cell appears very dark (fig. 3.4); as the cell is rotated, some light is transmitted and the cell appears bright when the rubbing direction is at  $45^{\circ}$  to the axes of the polarizers. Imperfections in the alignment were observed as slight variations in the brightness; otherwise the intensity moving laterally across the cell was uniform.

As the cell was cooled towards the nematic–smectic transition, a periodic modulation of light and dark

bands appeared, apparently continuously, perpendicular to the rubbing direction. As the cell was cooled further, the bands became more distinct [fig. 3.5(a)]. The temperature stage was then held at constant temperature for several minutes and this “stripe” structure remained stable. The “stripe” structure was found to be stable over a very narrow temperature range ( $\sim 0.1 - 0.2\text{K}$ ) which was only slightly larger than the temperature stability of the temperature stage.

The cell was then rotated under the microscope (fig. 3.6): as the cell was rotated with respect to the polarizers the contrast between alternate stripes increased; by  $23^\circ$  one set of stripes is bright and the other is just visible and by  $45^\circ$  only one set of stripes is visible. The cell was then rotated in the opposite direction and it was found that the set of stripes which previously had grown fainter with rotation this time grew brighter and similarly those stripes which had previously grown brighter this time became fainter. Each pair of stripes therefore corresponds to a unit period of the structure, which is mirror symmetric about the centre of the two stripes.

The “stripe” structure was typically interspersed with V-shaped defects. During the course of observing the cell through repeated heating and cooling, it was observed that the defects moved in a consistent manner as the temperature was changed: as the cell was cooled the defect moved along the stripes in the direction of the wide end of the ‘V’ (see fig. 3.7) and as the cell was heated the defect moved in the direction of the narrow end of the ‘V’ (some indication of defect movement may be seen in fig. 3.5 as the position of the centre of the defect in previous images are indicated by blue markers). If the cell was cooled rapidly (e.g. by changing the temperature on the Mettler from  $35^\circ\text{C}$  to  $25^\circ\text{C}$  and allowing the cell to cool as quickly as the stage allowed) into the “stripe” structure, the number of defects observed was much higher. Defects in both possible orientations—the ‘V’ may either point along or against the rubbing direction—were observed. Defect collision and annihilation was also observed where two defects of opposite orientation either straddled the same pair of stripes or had at least one stripe in common (fig. 3.8).

As the cell was cooled further, modulations in intensity appeared, again continuously, along the centre of each pair of stripes parallel to the rubbing direction [fig. 3.5(b)]. Unlike the “stripe” structure, it was not possible to stabilise this intermediate state although this is possibly due to the limited temperature stability ( $\sim 0.1\text{K}$ ) of the Mettler stage used. The modulations became more distinct as the cell was cooled further and the stripes broke up into domains [fig. 3.5(c)] which rapidly rearranged themselves into Ruan *et al*s’ structure [fig. 3.5(d)].

The cell was then heated back through the nematic–smectic transition. The fan-shaped domains recombined into the “stripe” structure which this time was observed to have a much higher density of V-defects (fig. 3.9). The temperature was then held constant and many of these defects annihilated within a few minutes. The cell was then heated further into the nematic phase where the liquid crystal resumed the conventional HAN configuration described above. The cell was then repeatedly cooled and then heated again through the nematic–smectic transition and it was found that each time the stripe structure and Ruan *et al*s’ fan structure both reassembled as before and melted away again.

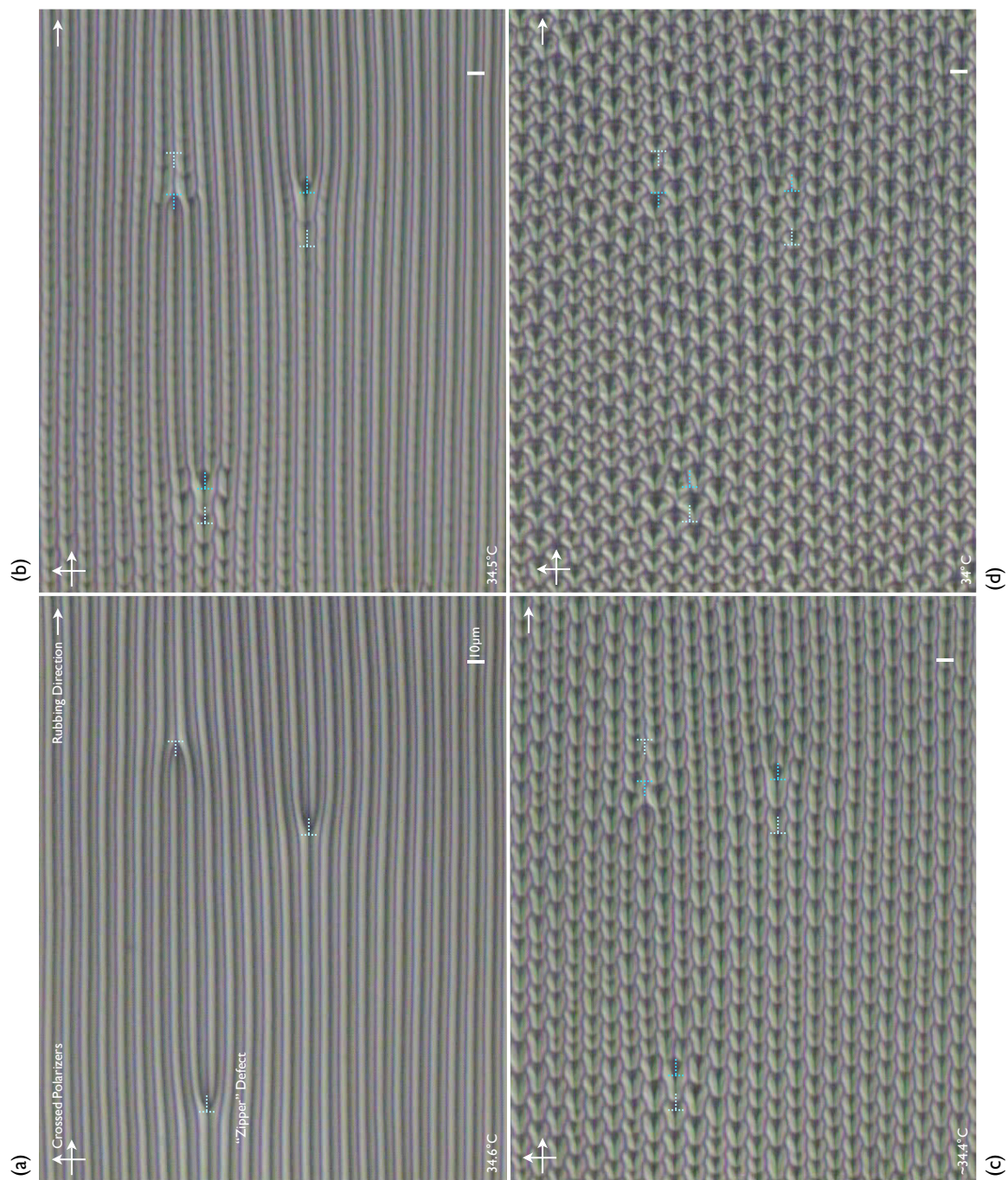


Figure 3.5: Polarizing microscope images of the phase sequence of 8CB in a HAN cell as the liquid crystal goes through the nematic–smectic transition with decreasing temperature.

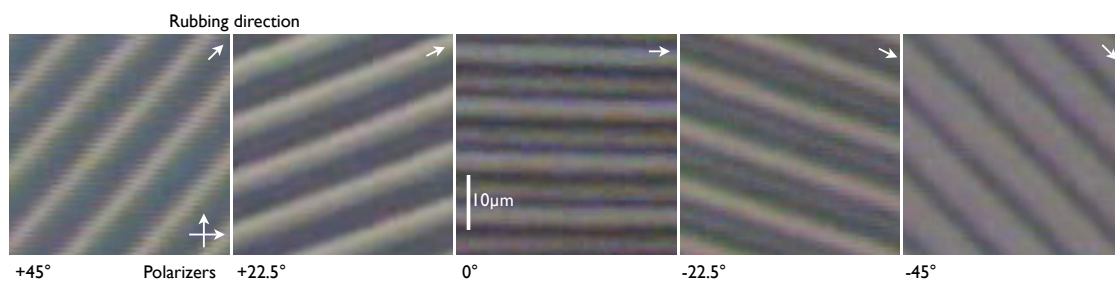


Figure 3.6: Images of the stripe structure under the polarizing microscope where the cell is rotated with respect to the fixed polarizers.

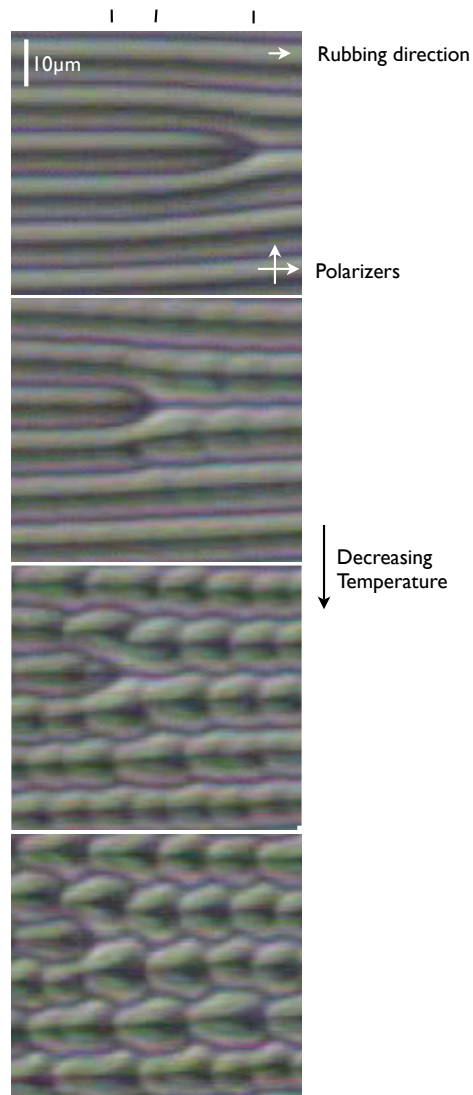


Figure 3.7: Detailed view of a 'V' defect as the cell is cooled from the stripe structure into the focal conic structure.

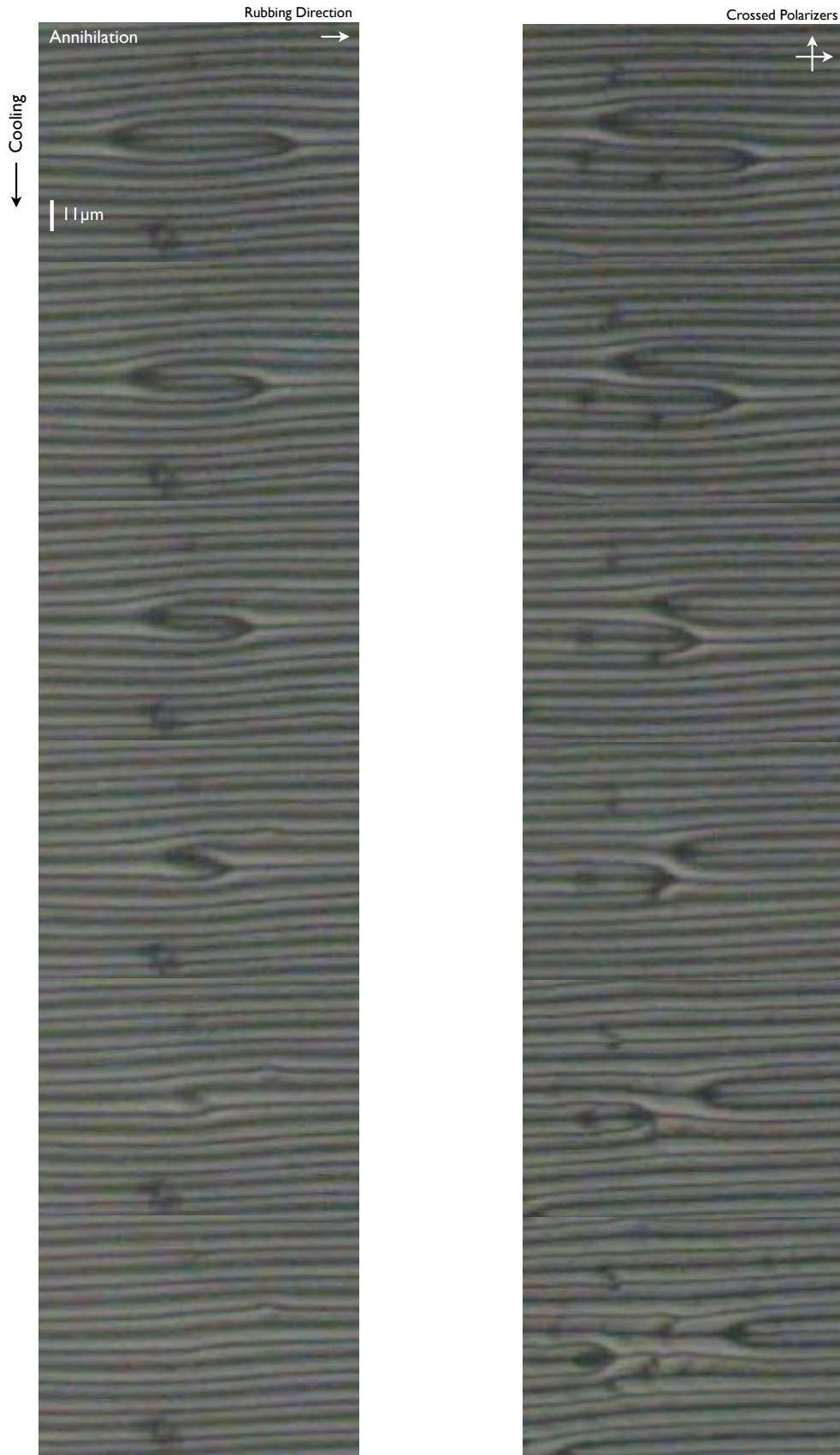
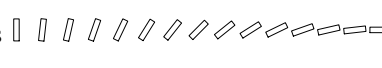
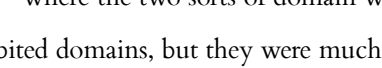


Figure 3.8: Polarizing microscope images of the interaction of two opposing 'V' defects. (Left) Defects with a single stripe in common annihilate. (Right) Defects on adjacent pairs of stripes pass each other unaffected.

Observations were repeated with other identically prepared cells: it was often observed that, after the cells had been heated from the fan-shaped structure back into the nematic phase, some faint modulation in intensity was still visible in the HAN state with similar structure—including recognisable defects—to the fan structure observed at low temperature. These modulations in the HAN state are not observed in fresh cells cooled straight after filling from the isotropic phase, but become increasingly apparent if the cell is repeatedly heated and cooled: it would appear that the smectic structure is sufficient to modify the surface alignment (fig. 3.10).

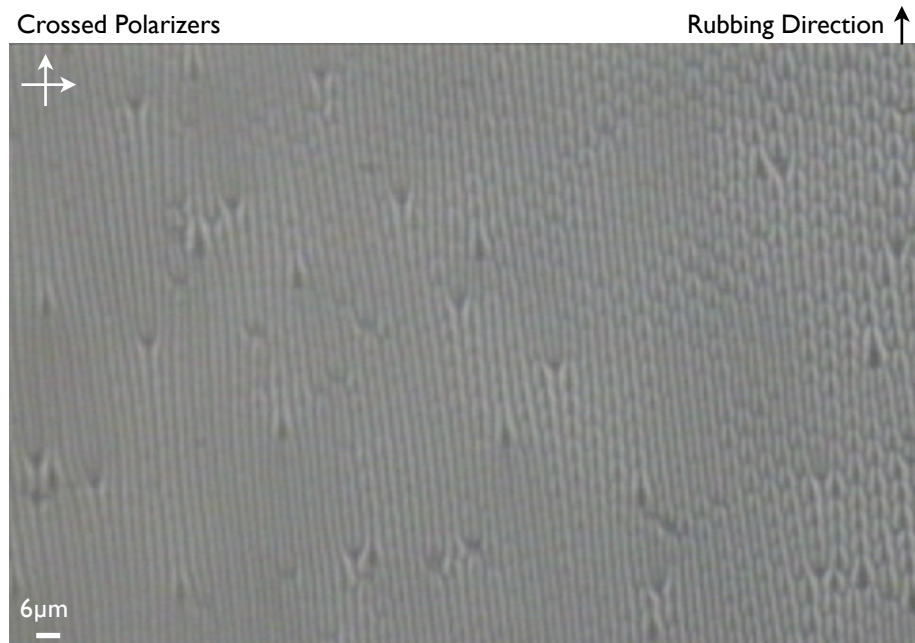
It was expected from Ruan *et als'* model that it might be possible to control the pitch of the structure by varying the anchoring energy through the use of different surface treatments. Cells were therefore constructed with different polyimides—PI2555 and SE7792—and also with evaporated silicon oxide ( $\text{SiO}_x$ ) to promote planar alignment and a two other homotropic alignment layers: lecithin and a homeotropic polyimide, RN1773. No consistent change in pitch however was observed with different combinations of polyimide and lecithin.

For cells prepared with silicon oxide, however, the shape of the domains in the smectic phase was different; the domains are circular rather than fan-shaped (fig. 3.11). The “stripe” structure appeared identical to that of the rubbed polyimide cells and exhibited the same optical behaviour; as the cells were cooled and the stripes broke up into domains, those domains initially appeared fan-shaped but as the cell was cooled fully into the smectic phase they adjusted their shape to become circular. In the nematic phase of such cells, HAN domains of opposing orientation were observed—if the pretilt at the planar surface is zero the two configurations  and  are energetically degenerate—where the two sorts of domain were separated by walls (cells prepared with rubbed polyimide also exhibited domains, but they were much more usually observed after cooling from the isotropic phase in silicon oxide cells). When the cells were cooled through the nematic–smectic transition, stripes appeared in both sorts of domain and, upon further cooling, the stripes broke into metastable fans: the fans within HAN domains of opposite orientation pointed in the opposing directions.

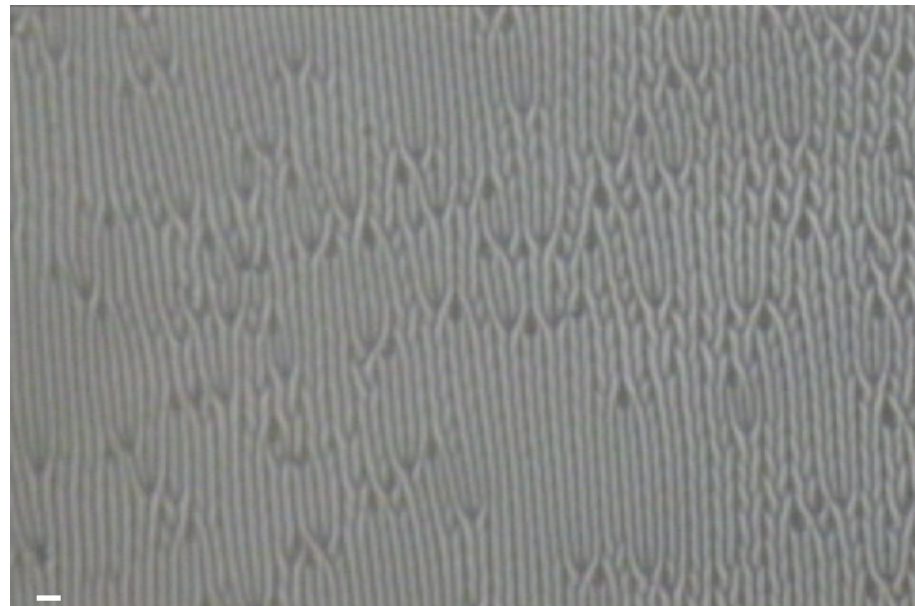
### 3.3 Effect of Cell Thickness

Ruan has previously shown that the pitch of the fan structure depended linearly on the cell thickness, albeit over the narrow thickness range  $3 - 6\mu\text{m}$  tested[2]. It is natural to ask: does this behaviour persist for thicker and thinner cells? A large number of cells were therefore constructed with thickness in the interval  $2 < d < 30\mu\text{m}$  with appropriate spacers and their thicknesses characterized by the interference method described above. The alignment for each cell was rubbed X201 for planar alignment and RN1663 for homeotropic alignment. Each cell was filled with 8CB in the isotropic phase and cooled slowly (at  $0.2^\circ\text{C}$  per minute) in a Mettler stage set up on the rotating stage of a polarizing microscope; videos were recorded of the cell as it cooled from the nematic phase through the intermediate structures and into the





(a) Cooling from the nematic phase



(b) Heating from the smectic phase

Figure 3.9: Polarizing microscope images extracted from a video recording of the phase sequence of 8CB in a HAN cell as the liquid crystal goes through the nematic–smectic transition.



Figure 3.10: Polarizing microscopy image of a hybrid aligned cell in the nematic phase following repeated cooling and heating through the nematic–smectic transition. The intensity of illumination is high revealing a “surface memory” of the low temperature “fan” structure even though the liquid crystal is here in the nematic phase as may be seen from the presence of disclination lines.

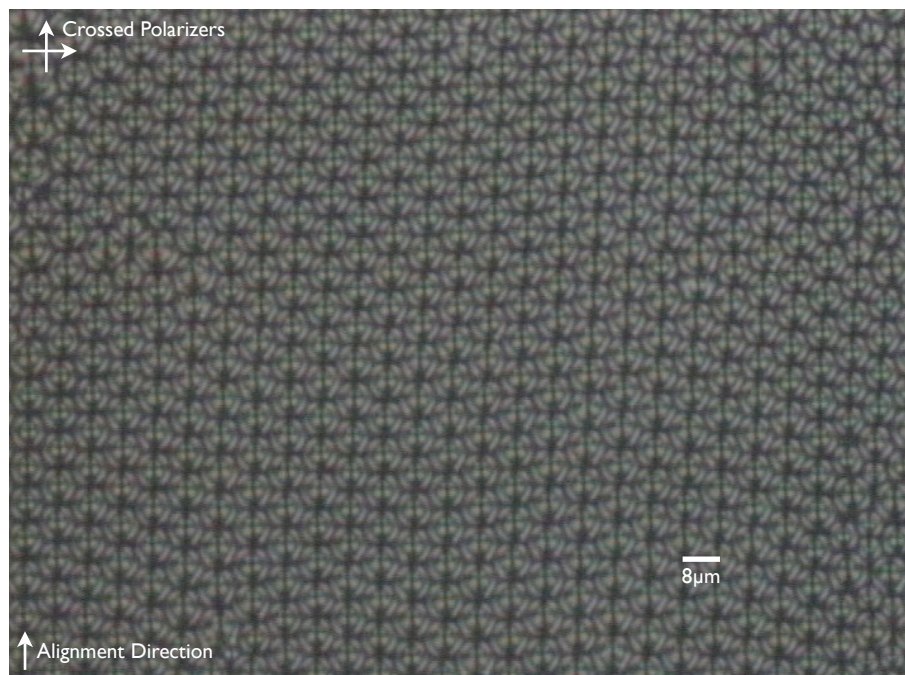


Figure 3.11: Focal conic structure with evaporated silicon oxide as the planar aligning layer.

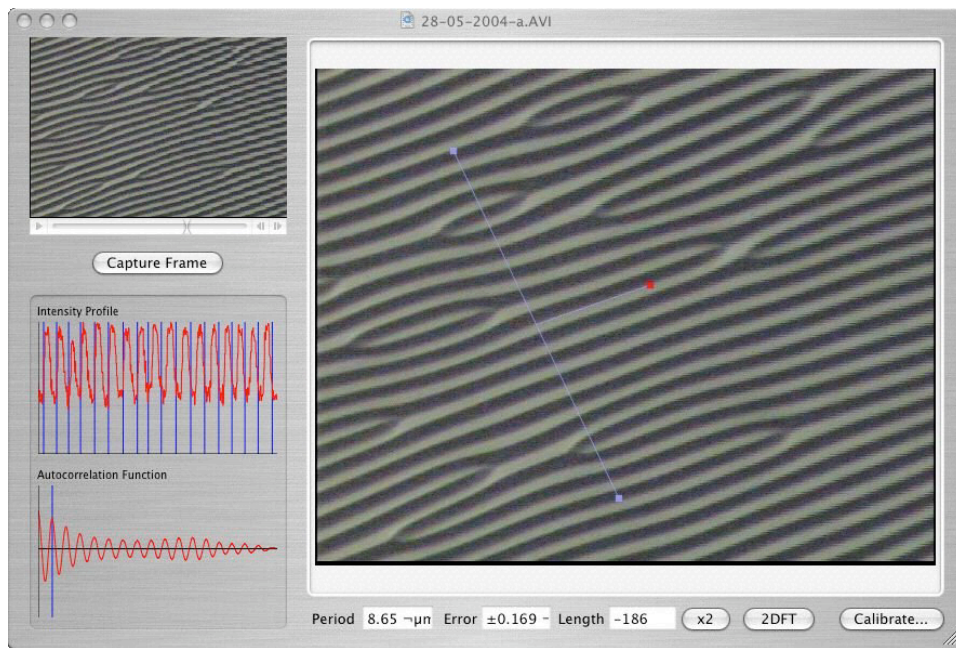


Figure 3.12: Custom image processing program used to extract the period of the stripes.

smectic phase.

The period of the “stripe” and “modulated stripe” structures was then calculated from still images extracted from the recorded videos by a custom-written image processing application (fig. 3.12). The utility of this approach is that firstly it permits investigation of any changes in period with temperature and secondly that it is possible to estimate the variance of stripe widths in a single cell. A single line, or part of a line, of the image is selected from the image (fig. 3.13) and the period calculated from the intensity profile.

The problem of finding the period from a sequence of measurements—a *signal*—is an old one and worth remarking on: a classic example from astronomy is to determine the period of sunspot activity from published observations—data for which exists from 1700—and in fact the problem is ubiquitous in contemporary astronomy[74]. The famous Nyquist sampling theorem also arises from the problem[75]. Surprisingly then, rigorous statistical methods for estimating the period were only developed as late as 1987[74]; it is therefore relevant to discuss the method used.

A common strategy is to find maxima of the Schuster periodogram

$$C(\omega) = \frac{1}{N} \left| \sum_{j=1}^N d_j e^{i\omega x_j} \right|^2 \quad (3.1)$$

where the sum is over  $N$  pixel intensity values  $d_j$  at locations  $x_j$  and the angular frequency  $\omega$  is a real number. This is essentially the square of the Fourier modulus transform and so has a maximum value when  $\omega = 2\pi/\lambda$  where  $\lambda$  is the period of the signal (fig. 3.13). It is necessary to remove the large peak at  $\omega = 0$  by subtracting from the signal its average value and it is convenient to rescale the measured values  $p_j$  (which are naturally expressed as integers 0 – 255) to be of order unity. The very careful analysis of

Bretthorst[74] shows that use of the Schuster periodogram is formally justified only if the signal is harmonic and contains a single stationary frequency (i.e. with constant amplitude and phase), if the noise is gaussian with known variance and small compared to the data, and if the wavelength of the signal is much longer than the sampling interval (i.e. far away from the Nyquist limit) but the signal nonetheless captures a number of periods. Most of these assumptions are justifiable with regards to the problem of finding the period of the stripes from a microscope image, except that of the course the intensity profile is not a single harmonic. A further limitation is that the Schuster periodogram contains nothing to give a formal estimate of the variance associated with the estimated period. A more general scheme from Bayesian analysis was derived by Bretthorst[74]: the relevant quantity to be maximised is the probabilistic likelihood function for a single harmonic frequency present in a signal<sup>1</sup> (here displayed in unnormalized form)

$$P(\omega|D, I) \propto \left(1 - \frac{R(\omega)^2/c_+ + I(\omega)^2/c_-}{N\bar{d}^2}\right)^{\frac{2-N}{2}} \quad (3.2)$$

where  $R(\omega)$  and  $I(\omega)$  are the real and imaginary parts of the discrete Fourier transform respectively,  $\bar{d}^2$  is the mean-square value of the signal and

$$c_{\pm} = \frac{N}{2} \pm \frac{\sin(N\omega)}{2\sin(\omega)}. \quad (3.3)$$

Since 3.2 is a probability distribution, estimates of the variation or error in  $\omega$  may quite naturally be made—following normalization—by seeking an upper and lower bound such that the integral of the probability distribution between these limits corresponds to a desired confidence level; this procedure was performed automatically by the image processing application described above.

The Schuster periodogram and likelihood function both suffer from the problem that the maximum is atop a very narrow peak and is not easy to find with gradient-based search routines. A good starting point for the peak finding algorithm, if the number of samples is reasonably large and the samples equally spaced, may be found from the *autocorrelation function*

$$A(t) = \sum_{i=1}^{N-t} d_i d_{i+t}$$

where  $t$ , an integer, is the *lag coefficient*. The autocorrelation function has a maximum value at  $t$  equal to the nearest integer to  $\lambda$  in pixels and that maximum is much wider (fig. 3.13) than that of the Schuster periodogram or student-t distribution. Furthermore, unlike the spurious extra peaks observed in the Schuster periodogram, the estimated period is guaranteed to correspond to the first maximum (if the signal is sinusoidal) or to the second maximum if the signal (as depicted in fig. 3.13) has a more complex

---

<sup>1</sup>The  $P(\omega|D, I)$  is to be read “the probability of a harmonic signal with angular frequency  $\omega$  present given the data  $D$  and prior information  $I$ ”. The prior information, in this case, is not very informative: the signal is assumed to have no structure (harmonic) and the noise is assumed to be gaussian. A great advantage of the Bayesian approach is that if further information is known about structure of the signal or the parameters to be estimated, that information can be incorporated into the likelihood function and the estimates of the desired parameters consequently improved. Furthermore, note that 3.2 is independent of the amplitude of the model signal and the variance of the noise—these “nuisance” parameters were integrated out!

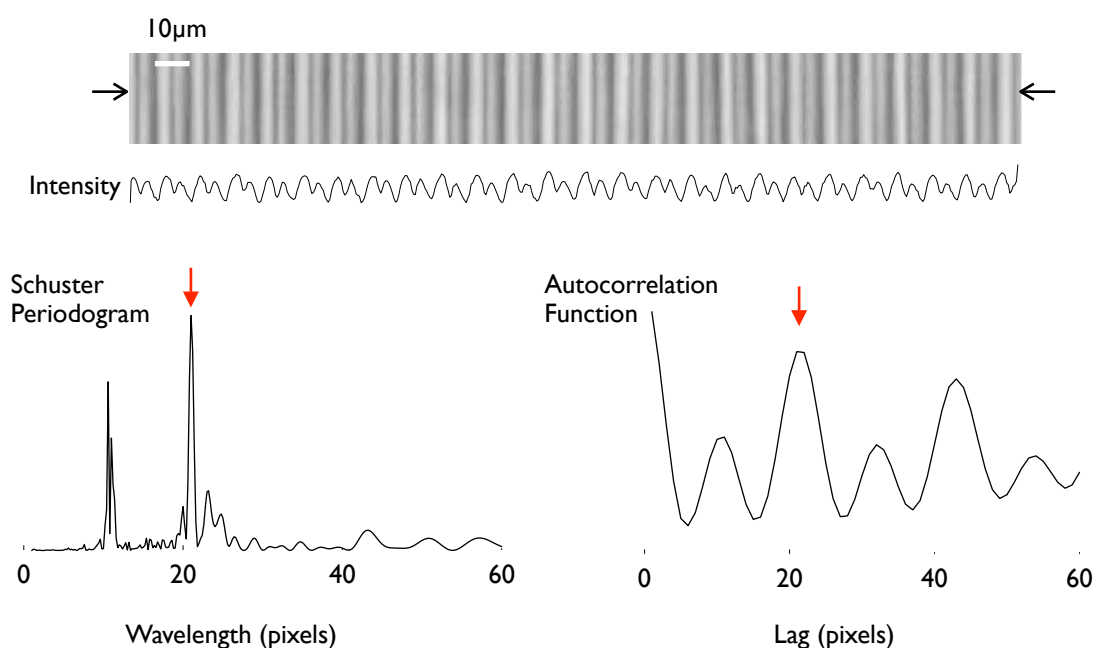


Figure 3.13: (Top) Plot of a single line from a digital polarizing microscope image of the “stripe” structure. (Below) The period of the structure is found automatically from the Fourier modulus transform or the autocorrelation function of the signal; both are plotted with arbitrary scales on the vertical axis.

structure; the correct one may be chosen based on whichever peak is higher.

Two further refinements to the program proved necessary: the cell was not always perfectly aligned with the rectangle of the video camera's view, and so the program allowed the direction of the stripes to be specified explicitly and the estimate of the period and confidence interval adjusted appropriately. Secondly, the estimate of the period from the above is in the natural units of the image—pixels—and it is necessary to convert the measurement must be converted to physical units. A suitable approach is to take an image of one or more diffraction gratings of known pitch and use that image to find the physical width of a pixel for a particular microscope objective.

The program was then used to analyse the period of the “stripe” structure from the recorded videos [fig. 3.14(a)] which was found to obey well the linear scaling with cell thickness proposed by Ruan *et al.* over the larger thickness range explored in the present study. Within individual cells, the confidence interval of the stripe widths was found to be very narrow, less than  $1\mu\text{m}$ , but varied over a much wider range  $1 - 2\mu\text{m}$  between cells of comparable thickness; this very likely represents the limit to which surface effects can alter the period. The data is clumped around certain thicknesses due to the limited availability of spacers. The program was used to estimate the period of several images at different temperatures and no variation of period with temperature was found.

The program was then used to analyse the period of the “modulated stripe” structure (i.e. the period along the stripes) [fig. 3.14(b)]. While the stripes appeared visually of very similar thickness within each sample (and consequently the confidence interval on the period was rather narrow), there were unit cells within the modulated stripe structure that were visibly of different width and so the confidence intervals on the

period are proportionately wider. The variation between cells is also appreciably larger ( $\sim 4\mu\text{m}$ ) and such that it is not possible to fit a meaningful model function to the scaling behaviour with thickness other than to say it does not appear linear. Interestingly, the aspect ratio of the unit cell changes dramatically with cell thickness: the units are much longer than they are wide at low cell thickness and shorter than they are wide at higher thickness; this will be discussed in the next chapter.

### 3.4 Confocal Microscopy

*The author is extremely grateful to Prof. Paul O'Shea for the use of the Leica SP4 Confocal Microscope at the University of Nottingham and to Mrs. Kelly Vere for assistance in obtaining many of the image stacks used to produce figures in this section.*

Fresh HAN cells were prepared with the planar substrate being a glass coverslip as described in the previous chapter; rubbed X201 was used to promote planar alignment and RN1663 to promote homeotropic alignment. The planar surface was prepared on a coverslip to overcome the limited working distance of the microscope objectives. After checking the thickness of the cells by spectroscopy, the cells were filled with 8CB doped with approximately 0.01% by weight of the dye *N,N*-bis(2,5-di-tert-butylphenyl)-3,3,9,10-perylenedicarboximide (BTBP). The cells were then imaged in FCM mode in a Leica SP4 Confocal Microscope equipped with a heat stage using the 40 $\times$  objective with 488nm pump laser and emitted light collected over the 510 – 560nm range.

In the nematic phase with the microscope in PM mode, the cell appeared uniform with observable domains separated by very thin dark lines. A cross section in FCM mode (fig. 3.15) through a uniform area reveals, after averaging out the noise (in this initial image the laser power was reduced to less than 100nW), that the liquid crystal has apparently adopted the typical HAN configuration: contrasting figure 3.15 with cross sections of the planar Fredericks cell in the last chapter (fig. 2.7), in the HAN cell the intensity falls away much more rapidly and there is little evidence of a second shoulder on the right hand side of the profile. The domains, it may be surmised, are HAN domains of opposing orientation.

Intriguingly, by adjusting the axial focus, it is apparent that the fluorescence intensity of HAN domains is quite different near the planar surface, although scanning through the cell each is clearly a HAN configuration. In a cross section (fig. 3.16) taken across the intervening region between two domains, it is clear that reorientation of the director field takes place through a line disclination pinned to the planar surface and the director (and therefore the fluorescence intensity) relaxes into the bulk of the cell.

The cell was then cooled into the “stripe” phase and axial stacks were taken with FCM over a small region. Cross sections perpendicular to the length of the stripe were reconstructed (fig. 3.17); the temperature stability of the stage attached to the confocal microscope was rather poor (the temperature fluctuated by  $\sim 0.5\text{K}$  on the timescale of minutes) and so it is not meaningful to attach temperatures to these cross

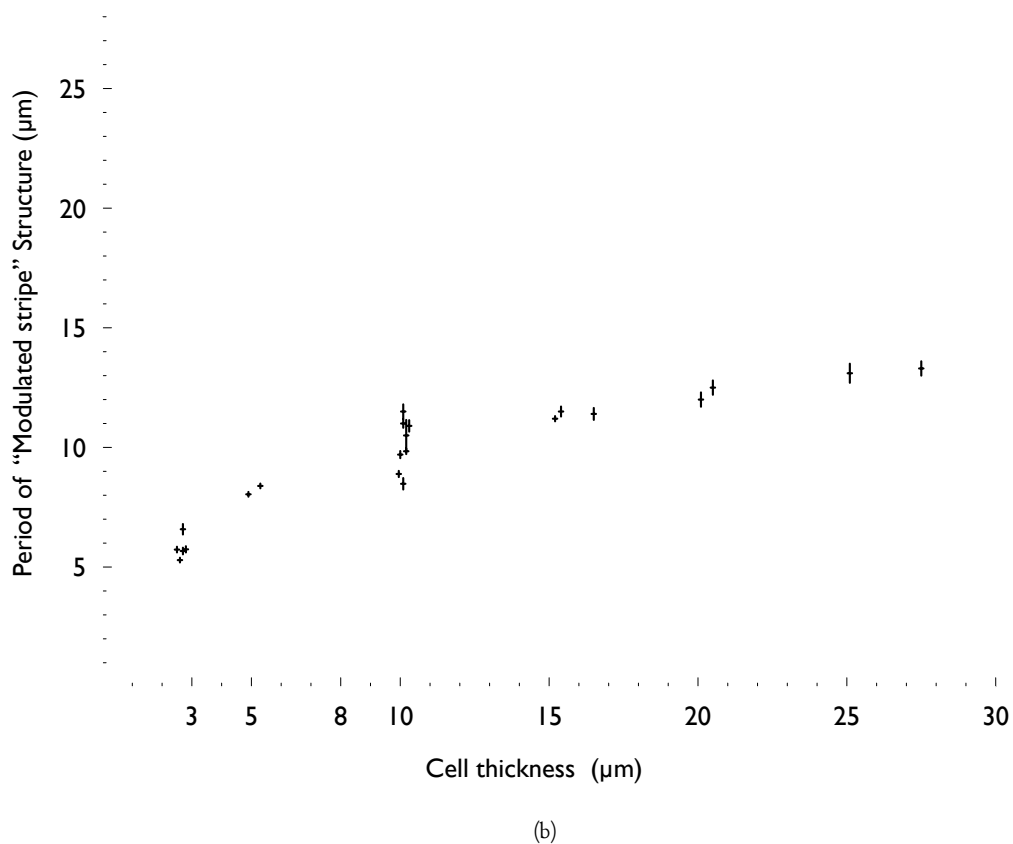
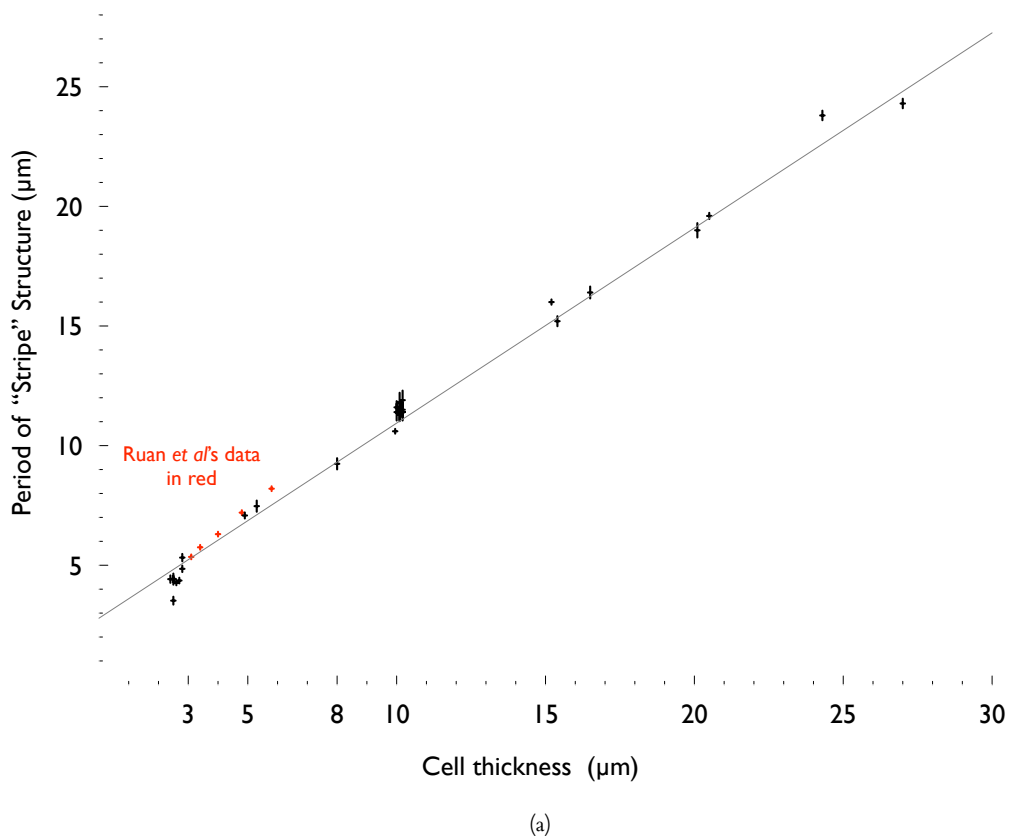


Figure 3.14: Variation of the period of (a) the "stripe" structure and (b) the "modulated stripe" structure with the cell thickness. Each point represents a single cell and the vertical extent of the bars indicate 95% confidence intervals. Data from Ruan *et als*' paper is shown in red; the vertical extent has no significance for these points.

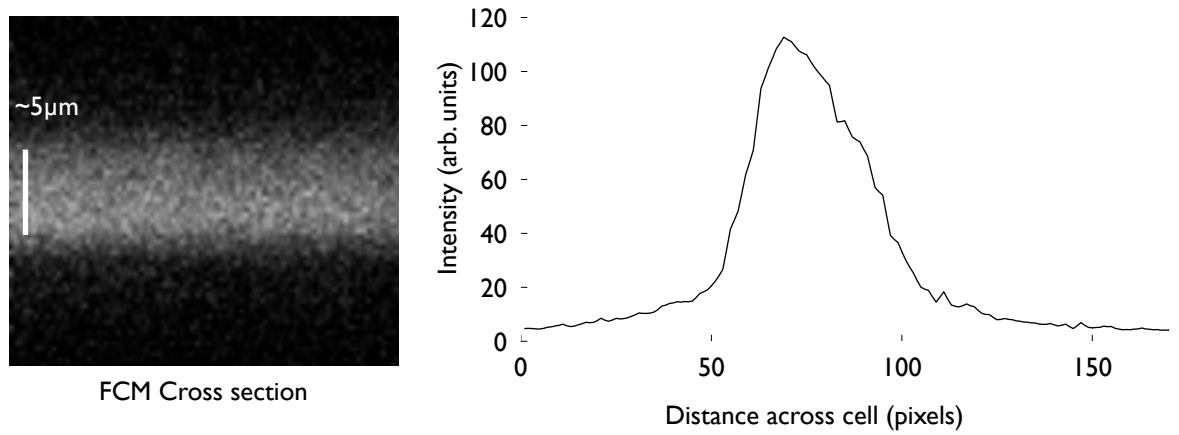


Figure 3.15: FCM Cross section of a HAN cell with an intensity profile obtained by averaging the image horizontally.

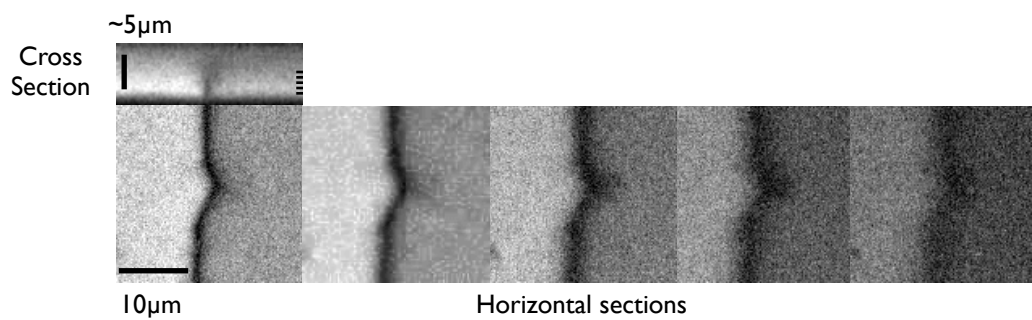


Figure 3.16: Confocal microscope (FCM) image of the disclination between two HAN states. The horizontal sections are taken from (left) the planar surface at  $0.9\mu\text{m}$  intervals to (right) approximately the centre of the cell. A reconstructed cross section through the cell (top) reveals the structure of the disclination and is marked with the location of the horizontal sections.



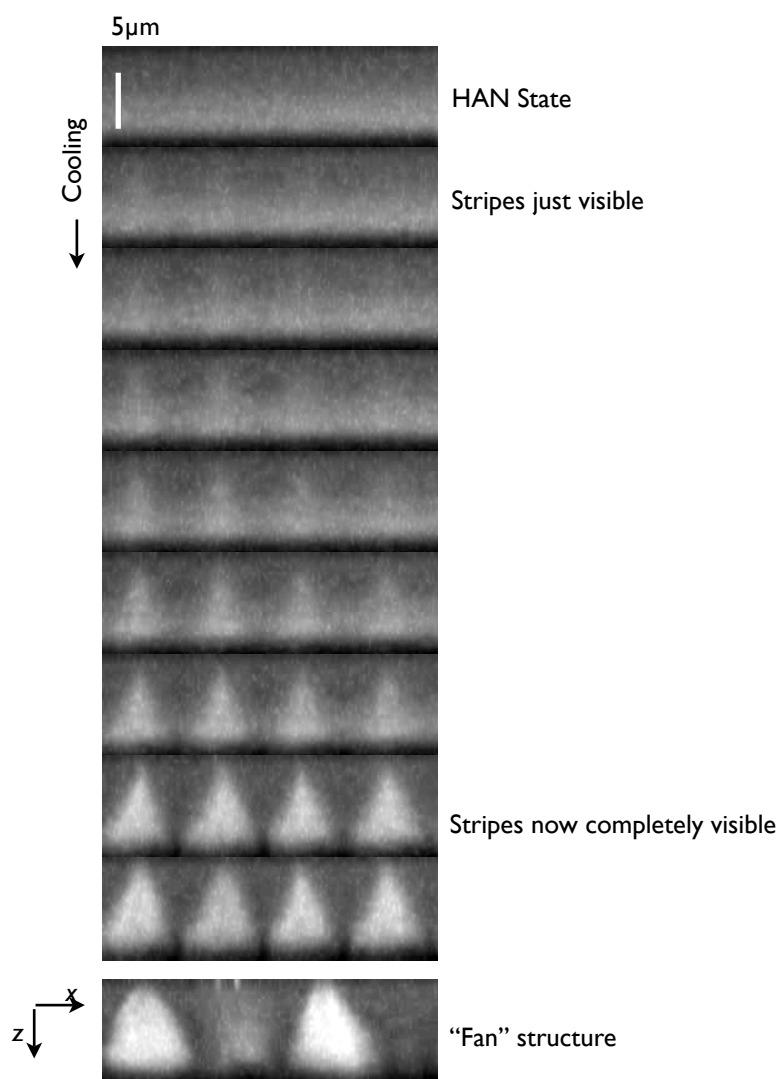


Figure 3.17: FCM of the “stripe” structure taken with the confocal microscope

sections. Nonetheless, it may be seen that the stripes seem to appear throughout the whole cell and gradually grow brighter, eventually becoming bright wedges attached to the planar surface. There is no evidence that corresponding wedges form on the homeotropic surface. The wedges appear much brighter even than the region adjacent to the planar surface in the nematic phase and this must be caused by an enhancement of the magnitude of the dye order parameter as the surrounding liquid crystal becomes more smectic: so great an increase in fluorescence intensity cannot be explained solely by supposing that the nematic becomes planar over a larger volume. The fluorescence intensity from the wedges is in fact very nearly as great as that from region of the “fan” structure at much lower temperature and so in those wedges the magnitude of the smectic order parameter must have nearly attained its maximal value.

It proved impossible, due to the limited temperature stability of the heat stage, to take a complete set of axial sections of the “modulated stripe” structure. Nonetheless, a single axial FCM section from just above the planar surface (fig. 3.18) shows clearly domains the shape of which appears quite different from that of the Ruan *et al.*'s structure with apparently a disclination at the bottom. As the cell is cooled fully into

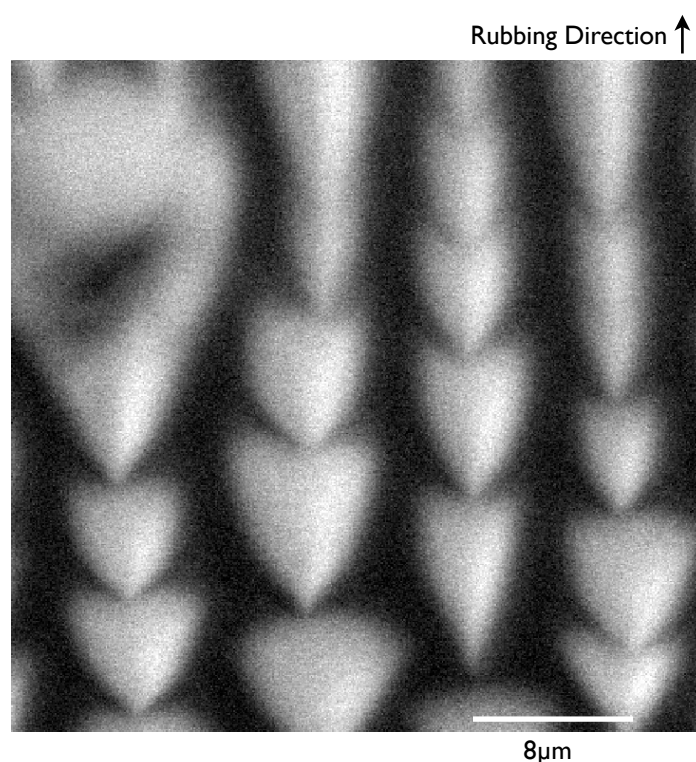


Figure 3.18: FCM axial section of a HAN cell near but above the planar substrate of the “modulated stripe” structure.

the smectic phase, these domains reorganize to give the familiar “fan-like” configuration (fig. 3.19).

A different cell, this time prepared with an evaporated silicon oxide planar alignment surface, was imaged in the smectic phase with the Exeter SP5 microscope in FCPM mode (fig. 3.20). Axial sections near the planar surface have a characteristic “bow-tie” appearance familiar from the work of Smalyukh *et al.* [59] on imaging ordinary focal conic domains in smectics. It is reasonable to conclude, therefore, that the hexagonal structure in silicon oxide cells is some form of focal conic domain. The defect core perpendicular to the substrate is clearly visible in cross section through the centre of the domain; it appears to be either a straight line or a hyperbola of very low eccentricity.

### 3.5 Discussion

In this chapter the physical origins of the self-organized periodic array of domains observed by Ruan *et al.* have been explored by conventional polarizing microscopy and fluorescence confocal microscopy. In particular, it was shown that Ruan *et al.*'s structure formed from the well-known HAN state by means of two intermediate configurations that are stable only over a very narrow temperature range around the nematic–smectic transition: the liquid crystal first adopts a “stripe” configuration periodic in the direction perpendicular to the azimuthal easy axis; this structure becomes modulated along the length of the stripes and finally unit cells in the modulated stripe structure change their shape to become units in Ruan *et al.*'s structure. In contrast to the prediction of Ruan's model, the period or pitch of the structures observed

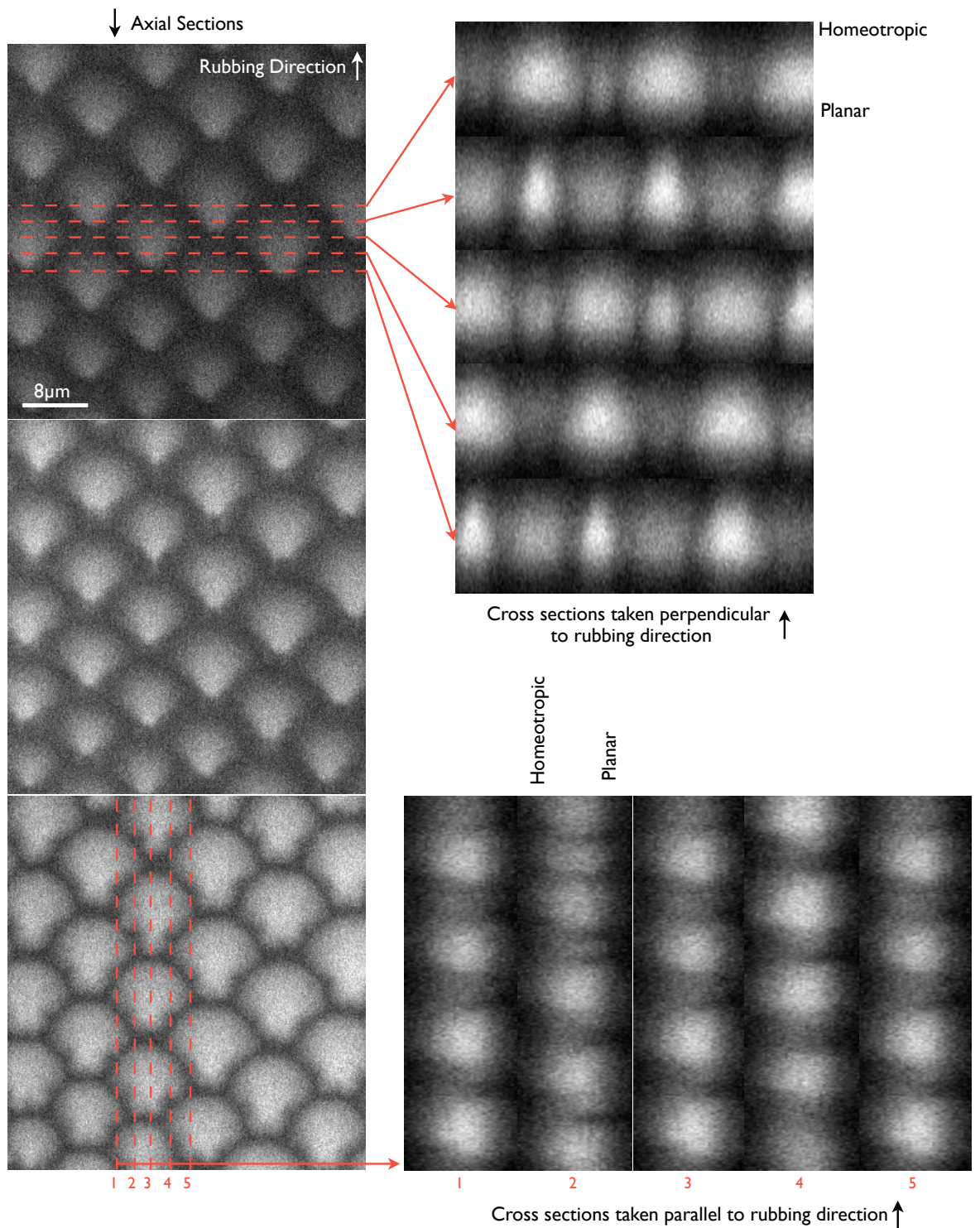


Figure 3.19: FCM axial sections and cross sections in two sequences of orthogonal planes of Ruan *et al*'s structure.

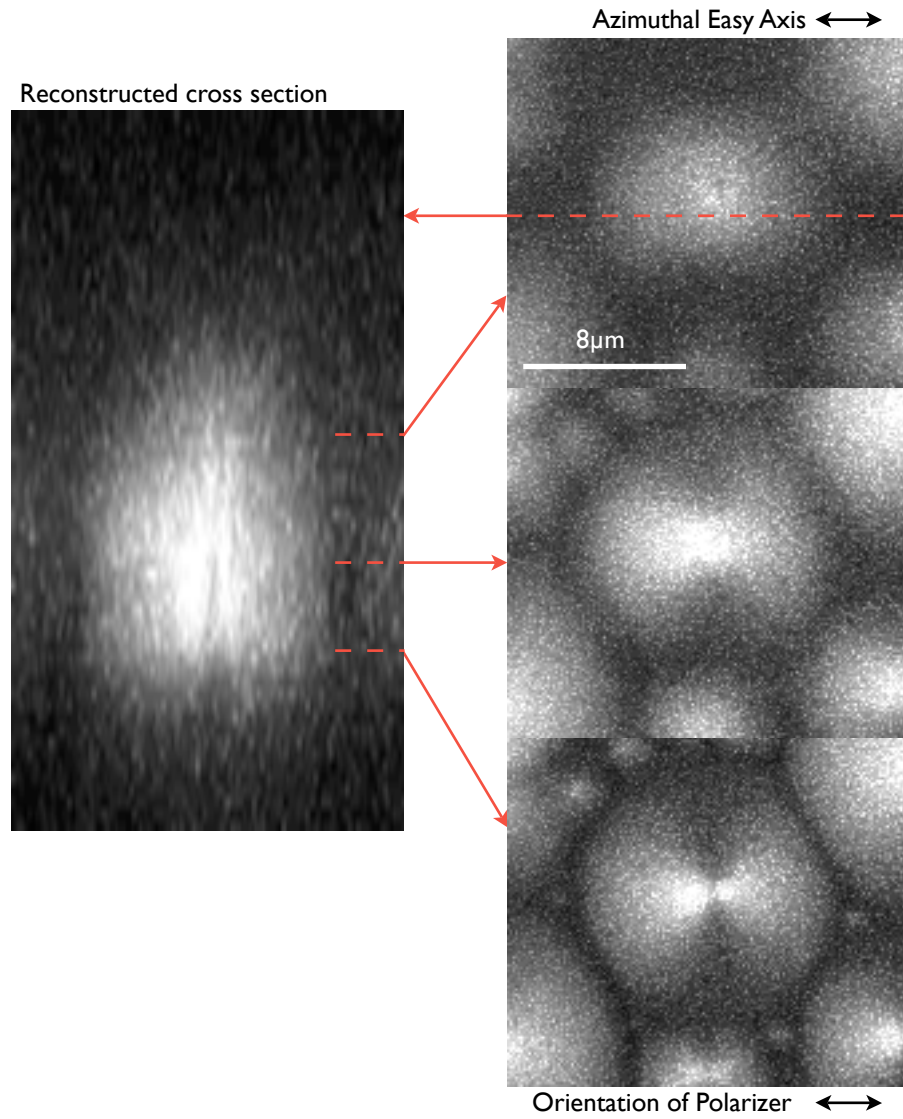


Figure 3.20: FCPM image of a unit cell from the hexagonal structure in a HAN cell prepared with a silicon oxide planar surface: (left) reconstructed cross section from a line oriented parallel to the polarizer through the centre of the domain and (right) axial sections through the structure.

was shown to be rather insensitive to the choice of surface material and was shown only to depend on the thickness of the film; nor was it sensitive to the rate of cooling. The pitch must therefore be related to bulk properties of the liquid crystal, i.e. elasticity (as there is no magnetic or electric field applied) and their behaviour around the transition (it is possible that flexoelectricity might also influence the system). The pitch of Ruan *et al.*'s structure is a consequence of the period of the "stripe" phase and the well-ordered nature of the array is due to this intermediate structure.

The "stripe" configuration has in fact been observed before in much thicker HAN cells[1] and a configuration analogous to Ruan *et al.*'s was observed in the smectic phase of such cells; the domains in that structure, however, were not fan-shaped but were cylindrically symmetric like those observed in this chapter in cells prepared with silicon oxide. The FCM images of Ruan *et al.*'s structure presented in this chapter are consistent with Pishnyak's suggestion that the units cells are in fact focal conic domains of the Dupin cyclide type that are novel in that the disclination ellipses are incomplete. This latter property cannot be due to the liquid crystal material as the same material has been shown to adopt both the fan-shaped domain and cylindrically symmetric domains with different materials used for planar alignment. It is the contention of this thesis that the incomplete nature of Ruan *et al.*'s structure is due to the large surface pretilt promoted by rubbed polyimides not present with silicon oxide surfaces.

The asymmetry of fluorescence in the nematic phase between opposing HAN domains observed with FCM is strongly suggestive of surface pretilt. If the director at the planar surface is constrained to lie not parallel to the surface but with some pretilt  $\alpha$ , then the two possible director configurations are modified: in one configuration the director angle  $\theta$  (defined as in equation 1.10 on page 29) must rotate from  $\alpha$  to  $\pi/2$  (rather than from 0 to  $\pi/2$  in the zero pretilt case) and in the other the director must *overrotate* back from  $\pi + \alpha$  to  $\pi/2$ . The director field around the disclination line that separates two such domains was simulated in the one constant approximation (fig. 3.21) and corresponding simulated FCM images were obtained by applying the rule  $I = \cos^2 \theta$ . The overrotated domain appears much brighter as the director is near to planar over a much thicker axial region.

The stability of the overrotated domain is of interest as in the one constant approximation it has a much higher energy; it is possible that elastic anisotropy reduces the energy difference—the overrotated domain is more strongly splayed at the planar surface and the underrotated domain is more bent—since for most liquid crystals,  $K_1 < K_3$ . It is also possible that the overrotated domain is essentially metastable, having appeared due to rapid cooling, and that the disclination line has been 'pinned' into place by some surface irregularity.

Compared to the simulations, the pretilt angle in the observed FCM image seems to be quite high (certainly  $> 10^\circ$ ) which is at least consistent with the value measured by Jewell *et al.* [50] in a HAN cell prepared with a rubbed polyimide planar surface. It is difficult to extract a precise value for the pretilt as this would require estimation of the ratio of the peak intensities in both domains and those peaks have been inevitably damaged by axial convolution; furthermore, the elastic anisotropy ought also to be included in the model

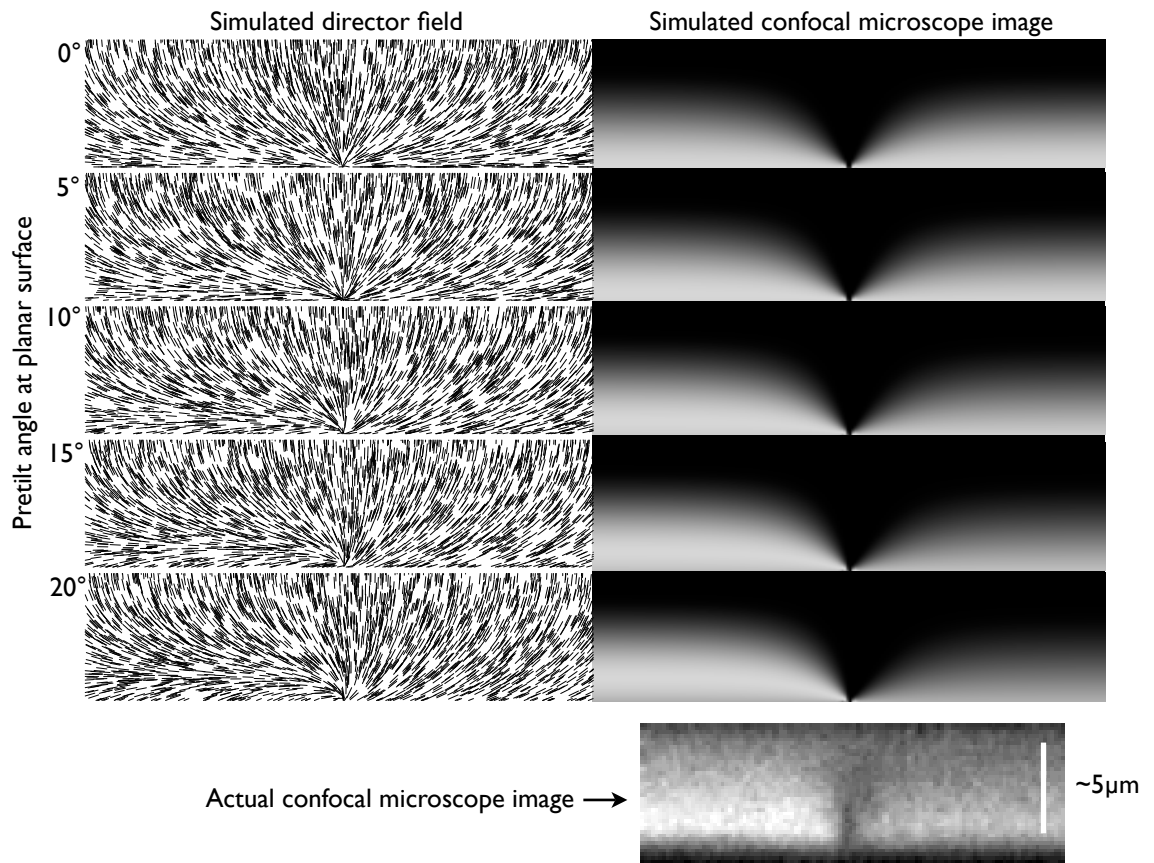


Figure 3.21: Simulated confocal microscope images of a line disclination that separates two opposite HAN configurations with different pretilt angles at the planar surface; a real FCM image is shown below.

for the director field.

The “stripe” structure was observed interspersed with novel defects which were observed to move as the cell was heated or cooled. The mobility of the V-defects suggests that at least some part of the liquid crystal remains in the nematic phase: comparing the micrographs in figure 3.7, it is clear that the defects move relatively little once the modulations along the stripes appear (which one supposes is indicative of an increasingly smectic character). From cross sections obtained by confocal microscopy, the stripe structure appears to consist of smectic wedges that form on the planar surface; the appearance of the rest of the cell is consistent with the liquid crystal in that region being nematic.

Finally, on the cylindrically symmetric domains observed with HAN cells prepared with silicon oxide to promote planar alignment: The silicon oxide deposition process produces a surface which has not only mirror symmetry about an axis parallel to the direction of preferred alignment but also another mirror symmetry axis perpendicular to the direction of preferred alignment. For rubbed surfaces that latter symmetry is necessarily broken. A structure consistent with the observed rotational symmetry is that of the toroidal focal-conic domains (TFCD) illustrated in figure 3.22. This structure is also consistent with the FCPM axial sections. The observed structure requires that, although the layers are arranged as concentric parts of tori, the domains are nonetheless hexagonal and hence that the domain is surrounded by a wall where

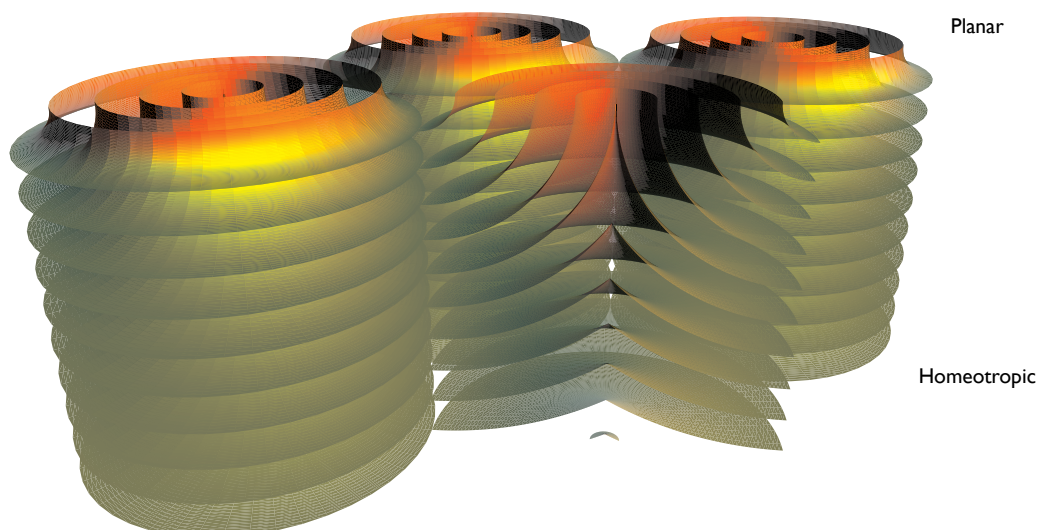


Figure 3.22: Schematic of the toroidal focal conic domain structure formed by 8CB with a silicon oxide surface.

the director field is discontinuous. A second possible arrangement is to have circular domains arranged in a hexagonal array with the intermediate triangular regions filled with homeotropic liquid crystal; this arrangement however implies an energetic cost at the planar surface. The conditions under which each might be favourable shall be discussed in chapter 4.

In the next chapter various configurations—the “stripe” structure, Ruan *et als*’ structure, and the Toroidal Focal Conic structure in cells prepared with silicon oxide—are each considered theoretically with reference to the evidence from polarizing and confocal microscopy presented in this chapter, and each placed in the context of the existing literature on spontaneous pattern formation in liquid crystals.

## Chapter 4

# On the Physical Origin of the Configuration Adopted by a Smectic in a Hybrid-Aligned Cell

**I**N THE LAST CHAPTER, the self-organized structure discovered by Ruan *et al.* was studied, in order to understand its physical origin, experimentally using polarizing and confocal microscopy, and also by constructing cells with different thickness and alignment materials. In contrast to the model proposed by Ruan *et al.*, the period of the array of domains was shown to be set by the period of an intermediate structure and was shown to be quite insensitive to the surface treatments used. It may therefore be inferred that the period of the stripe structure is controlled by the bulk properties of the liquid crystal, and in the absence of applied electric fields or chirality, the two remaining possible causes are elasticity and flexoelectricity.

The behaviour of a smectic—CBOOA—in a hybrid aligned cell has been studied some time ago by [1] in cells much thicker than those in the previous chapter ( $\sim 140\mu\text{m}$ ). A similar phase sequence was observed: a typical HAN state in the nematic; an intermediate striped structure appearing just above the nematic–smectic transition; domains arranged onto a hexagonal lattice in the smectic. This latter state was apparently first discovered by Kahn[76], who proposed its use in an early form of storage display but did not study its origin extensively.

The principal difference between the observations presented in the previous chapter and by Ruan *et al* and those of Cladis and Torza is the shape of the domains observed in the smectic phase. Those of Ruan *et al.* appear fan-shaped; those of Cladis *et al.* are circular and in order to accommodate the hexagonal packing are separated from one another by small homeotropic regions.

In the last chapter, it was shown that the domains had an appearance much closer to those of Cladis



and Torza if the planar surface was prepared with silicon oxide rather than a rubbed polyimide film, the difference being that with the silicon oxide treatment in thinner cells, the edges of the domains were hexagonal and there were no intermediate homeotropic regions. Observations with FCM suggest that the silicon oxide structure is a Toroidal Focal Conic Domain (TFCD) bounded by hexagonal walls for thinner cells. This is consistent with Cladis and Torzas' own model of their domains[1] and more recent observations of TFCDs formed at a nematic–isotropic interface [77]. It has recently been suggested by Pishnyak *et al.*[72] that the smectic layers in the structure of Ruan *et al.* are arranged as Dupin cyclides with the feature that the disclination ellipse is incomplete.

This chapter attempts to explain the physical reasons for the above behaviour. Following a review of some supplementary background material on other striped structures that spontaneously appear in liquid crystal films, and their physical reasons for doing so, the model proposed by Cladis and Torza for the stripe structure is re-examined in light of the observations of the previous chapter. The structure of the V-shaped defects that were observed for the first time in the previous chapter is shown to be well described by an existing linearized theory of two-dimensional smectics. Finally, the open problem of the shape of Ruan *et al.*'s structure is examined in light of the above conclusion that the domains are incomplete parts of Dupin cyclides; the closely related problem of why the domains in a silicon oxide cell are bounded by hexagonal walls is also considered.

## 4.1 Physics of the Nematic–Smectic–A Transition

Firstly, to briefly review the continuum theory of smectics and the critical phenomena associated with the nematic–smectic–A transition. From chapter 1, an order parameter for the nematic–smectic–A transition is the part of the mass density that breaks translational symmetry

$$\psi(\mathbf{r}) \cos \left[ \frac{2\pi}{a} \Phi(\mathbf{r}) \right] \quad (4.1)$$

which depends on two functions: the magnitude  $\psi(\mathbf{r})$  and the phase  $\Phi(\mathbf{r}) = \mathbf{n} \cdot \mathbf{r} - u$  where  $\mathbf{n}$  is locally normal to the layers and  $u$  is some arbitrary phase. The layers in this *Eulerian* description of the smectic are assumed to lie at contours separated by the layer spacing  $a$  of the phase  $\Phi(\mathbf{r})$ ; the alternative *Lagrangian* description of the smectic is to label each discrete layer by an integer  $m$ .

The elastic free energy density of the smectic A is

$$F = \frac{1}{2} K_1 (\nabla \cdot \mathbf{n})^2 - K_{24} \nabla \cdot [\mathbf{n} (\nabla \cdot \mathbf{n}) + \mathbf{n} \times \nabla \times \mathbf{n}] \quad (4.2)$$

where  $K_1$  and  $K_{24}$  are the splay and saddle-splay elastic constants defined in Chapter 1. The lack of twist

and bend terms in 4.2 may be explained by considering a line integral over an arbitrary path  $C$

$$I = \int_C \mathbf{n} \cdot d\mathbf{l}$$

where  $\mathbf{n}$  is a unit vector locally normal to the layers. The value of the integral is simply equal to the number of layers traversed. In particular if the path is closed, then a trivial application of Stokes' theorem yields an equivalent integral over any  $S$  that is bounded only by  $C$ :

$$\oint_C \mathbf{n} \cdot d\mathbf{l} = \int_S \nabla \times \mathbf{n} \, dS.$$

If the smectic is incompressible, then the integrals must be zero as no layers are traversed around a closed path. Since this is true for any  $C$  and any appropriate  $S$ , the integrand  $\nabla \times \mathbf{n}$  must be everywhere zero. The implication of this is that twist and bend elastic deformations are forbidden within a bulk smectic if it is incompressible.

Above the nematic–smectic-A transition temperature  $T_C$ , the magnitude of the smectic order parameter  $\psi$  is on average zero. There are nonetheless fluctuations in  $\psi$ ; temporary, correlated volumes or *cybotactic clusters* form and reform of size proportional to a *correlation length*  $\xi(T)$ . These smectic-like correlated volumes tend to exclude twist and bend distortion and so, as a nematic sample is cooled toward the nematic–smectic-A transition temperature, the twist and bend elastic constants  $K_2$  and  $K_3$  must diverge, in the limiting case where the layers are incompressible the elastic constants become infinite. The problem of finding the temperature dependence of the twist and bend elastic constants,

$$K'_i = K_i^N + \delta K_i (T - T_C)^{-\nu_i}, \quad i \in \{2, 3\} \quad (4.3)$$

where  $K_i^N$  is the value of the elastic constant far above  $T_C$ , is reduced in the context of existing theory to finding some value for the critical exponents  $\nu_2$  and  $\nu_3$ . Application of the Landau approach within the mean-field approximation predicts that  $\nu_2 = \nu_3 = 1/2$  [4]. De Gennes, invoking an analogy with superconductivity, proposes that if fluctuations of the smectic order parameter are important then  $\nu_2 = \nu_3 = 2/3$  [22] (see [14] for a critique of the de Gennes theory). Each of these predictions only hold while the transition is strictly second order (see section 1.1.4 on page 25). Experimental measurements of the critical exponents  $\nu_2$  and  $\nu_3$  from many different compounds suggest values that lie anywhere from 0.4 to 1[3]; as Chandrasekhar observes “*The exponents are neither universal nor do they agree with any of the theoretical models.*”

#### 4.1.1 Experimental Measurements of the Critical Exponents

In view of the above, it is necessary to review experimental studies of the specific compounds of interest that exist in the literature. Elastic constants cannot, of course, be measured directly but must be inferred

from some other quantity such as the electric or magnetic threshold field in a Fredericks transition or the intensity of Rayleigh scattering.

The material used in the study of Cladis and Torza [1], p-cyanobenzylidene-p-n-octyloxyaniline (CBOOA), has in fact been studied by each of these methods specifically with the intention of measuring  $\nu_2$  and  $\nu_3$ [78, 79, 80, 81]: The first published measurements by Cheung *et al.* of the magnetic Fredericks threshold field of a homeotropic cell yielded the bend critical exponent  $\nu_3 = 0.653 \pm 0.05$  [78]. A paper published days later by Delaye *et al.* using the Rayleigh scattering technique concluded that the twist exponent was  $0.66 \pm 0.05$  [79]. Both of these measurements are therefore in agreement with the de Gennes model. However, a later paper by Cladis that measured again the magnetic Fredericks threshold field concluded  $\nu_3 = 0.52 \pm 0.03$  in agreement with the mean-field prediction for a specially purified sample and that for a less pure sample  $\nu_3 = 0.60 \pm 0.01$ [80]. Finally, Chu *et al.* measured  $\nu_2$  from the intensity of Rayleigh scattering and concluded that  $\nu_2 = 0.48 \pm 0.08$ [81].

There have similarly been a number of studies of the temperature dependence of the elastic constants in 8CB[82, 83, 84, 85, 86]. Very few of these, however, report values of the critical exponents and it is necessary to extract them from the published data (described in appendix C). Some general remarks may be made: Away from the nematic-smectic transition, the elastic constants obey the usual trend, i.e. that  $K_2 < K_1 \leq K_3$  and the ratios  $K_{22}/K_{11} \approx 0.5$  and  $K_{33}/K_{11} \approx 1.1$ . All three constants increase as the temperature is lowered away from the nematic-isotropic transition due to the increasing magnitude of the nematic order parameter, but only the twist and bend elastic constants diverge at the nematic-smectic-A transition. The nematic-smectic-A transition itself appears in 8CB to be very nearly second order[83]. There is little justification to claim that either the de Gennes or McMillan model is correct from the experimentally measured probability distribution function for the critical exponents, but it is most likely that they lie in the intervals  $0.45 < \nu_2 < 0.7$  and  $0.6 < \nu_3 < 1.0$ . It is therefore very likely that  $\nu_3 > \nu_2$  and consequently for all temperatures that  $K_3 > K_2$ .

#### 4.1.2 Self-organized Periodic Structures in other Liquid Crystal Geometries

The “stripe” structure that spontaneously forms in the hybrid-aligned cell above the nematic-smectic transition is not a unique phenomenon in the field of liquid crystal films. It is therefore useful to select from the literature a few examples of spontaneous stripe formation that occur in other systems, and to outline the models proposed in each case to describe their physical origin.

Perhaps the most influential paper on the subject is the work of Lonberg and Meyer[87] who observed a striped state in a planar cell with magnetic field applied perpendicular to the cell and above a certain threshold field, which was measured to be lower than the expected Fredericks threshold. The period of the stripes was of the order of the thickness of the cell ( $\lambda \sim 32\mu\text{m}$ ), and the stability of the striped configuration was attributed to the elastic properties of the rather exotic material used: a polymer liquid

crystal for which  $K_2 \ll K_1$  by an order of magnitude. The model proposed used a linearization of the full Euler-Lagrange equations for very small perturbations of the director field away from the zero applied field uniform configuration—and was therefore only valid in the immediate vicinity of the threshold field. The model made two important predictions: a wavelength for the stripes comparable to that observed and that the minimum anisotropy required for such a transition was not large  $K_2/K_1 \lesssim 0.3$ .

Such a linearized model gives, by its nature, no indication of the final configuration adopted by the liquid crystal above the threshold field. In order to find the actual director configuration adopted in such a circumstance, it is necessary to minimize the nematic Frank energy numerically. Two later studies have performed this feat and hence predicted the dependence of the threshold field on the ratio of the elastic constants[88] as well as complete phase diagrams[89].

A similar striped configuration has been shown to occur in homeotropic Freedericks cells with magnetic field in the plane of the cell at temperatures just above the nematic–smectic–A transition by Allender *et al.*[90]. A linear stability analysis very close to that of Lonberg and Meyer showed that, in contrast to the planar geometry, the conventional Freedericks transition always occurs at some threshold field. If, however, the bend elastic constant is sufficiently greater than the splay constant, then the uniformly distorted Freedericks state, at some higher threshold field, becomes unstable with respect to periodic modulations of the director field. Near the nematic–smectic–A transition, expulsion of bend distortions by the fluctuating pre-smectic order provides the requisite elastic anisotropy. Later work suggests that, in fact, the stripe configuration may occur *below* the conventional Freedericks threshold if the bend elastic constant is sufficiently larger than both the splay and twist elastic constants[91].

A rather different cause of periodic instability, without the need for an applied field, was later suggested by Barbero and Pergamenschchik[92]. They predicted that in a planar nematic cell, the surface-like saddle-splay term might favour, if the twist elastic constant were sufficiently large, a spontaneous modulation of wavelength much longer than the cell thickness. Pergamenschchik proposed later[93] that the  $K_{13}$  term  $\propto \nabla \cdot [\mathbf{n}(\nabla \cdot \mathbf{n})]$  might further favour a periodic state in the planar cell. It is beyond the scope of this thesis to discuss the contentious  $K_{13}$  term: a useful review of its possible effects in the context of pattern formation is to be found in [94]; a group theoretical argument against its existence is to be found in [14].

The final geometry to be considered is the familiar hybrid aligned film. It is well known that sufficiently thin hybrid aligned films will always adopt a uniform tilted or planar configuration with no elastic distortion[95]; however it has been shown experimentally[96] that submicron films thicker than this limit with an applied magnetic field will spontaneously adopt a striped configuration (visually very similar to those in the previous chapter, and with similar defects) of wavelength much thicker than the film thickness  $\sim 20\mu\text{m}$ . It is particularly noteworthy that this phenomenon does *not* require anisotropy of the elastic constants. By means of a linearized perturbation theory, Pergamenschchik has shown that the saddle-splay elasticity may produce a similar long-wavelength distortion in an a thin hybrid-aligned film even in the absence of an applied field[97]. Lavrentovich and Pergamenschchik attempted to use this effect

experimentally[98] in a Langmuir-Blodgett deposited film of 5CB to measure the  $K_{24}$  elastic constant from the dependence of the stripe period with film thickness, but found that it was necessary to include the  $K_{13}$  term in order to fit their data.

A common theme in much of the above work is that spontaneous stripe formation is very often associated with elastic anisotropy (and hence usually occurs above the nematic-smectic transition). Linearized theories around the transition have been widely used with some success to predict the qualitative features of the phase diagram of many situations, and provide some estimate of the dependence of the wavelength on relevant parameters; numerical solution of the Euler-Lagrange equations may be used in nematic systems to obtain the actual configuration of the director field within the stripes.

## 4.2 The “Stripe” Structure

The usual static configuration of the liquid crystal in a HAN cell, as derived in chapter 1, involves both splay and bend distortions. As the HAN cell is cooled towards the nematic-smectic transition, the bend elastic constant diverges and the one dimensional solution derived in section 1.4 (on page 35) converges on a limiting functional form. Importantly, however, the director field in that limiting form retains considerable bend distortion. The situation is therefore in some sense analogous to the original work of Lonberg and Meyer in that an elastic distortion is imposed on the system—in their case by a magnetic field, in the present case by the strong anchoring at the boundary—and the elastic constants are very different. Extending that analogy, it may be envisioned that a bulk periodic modulation of the director field along a direction perpendicular to the plane of the distortion, might in principle reduce the energy.

The conventional approach to assessing the stability of the ground state to a periodic modulation, namely to consider the energy change due to an infinitesimal periodic perturbation of the uniform state, is very difficult to apply in the present case. For one thing the elastic constants are clearly very far from being equal, and so the one constant approach of [96] may not be applied; secondly, the director in the ground state is not constant but dependent on spatial coordinates. It is nonetheless straightforward enough to construct a linearized theory, and has for the case  $K_{11} = K_{33}$  been done before [97]. Generalizing the earlier work, consider a periodic perturbation of the components of the director field from the ground state  $\theta(z)$  where the director is confined to the  $x - z$  plane,

$$\begin{aligned}\tilde{\theta}(x, z) &= \theta(z) + \alpha f(z) \cos\left(\frac{2\pi y}{\lambda}\right) \\ \tilde{\phi}(x, z) &= \pi/2 + \alpha g(z) \sin\left(\frac{2\pi y}{\lambda}\right)\end{aligned}\tag{4.4}$$

where  $\alpha$  is infinitesimal. The  $y$ -dependence of the perturbation may be thought of as the lowest harmonic of a Fourier expansion of the director (the higher harmonics are inevitably elastically more expensive and so must have lower amplitude), and it has shown to be sufficient[87, 97], because of the inversion symmetry

and translational symmetry in the  $x$ -direction of the free energy, to arbitrarily choose the perturbation of one of the director components to be even and the other to be odd. The perturbed director may then be substituted into the Frank energy, terms collected in powers of  $\alpha$ , and then integrated over a single period  $\lambda$ . The linear variation of the energy  $\delta F$  is identically zero and so the leading variation in the energy per unit area from such a perturbation is quadratic:

$$\alpha^2 \frac{\delta^2 F}{K_3} = \int_0^d dz \left[ \frac{2\pi^2}{\lambda^2} (k_2 f^2 + k_1 \cos^2 \theta g^2) - \frac{2\pi}{\lambda} \cos^2(\theta) (k_2 g' f + k_1 f' g) + 2 \cos^2(\theta) (k_2 + (1 - k_2) \sin^2 \theta) g'^2 + (\cos(2\theta) (k_1 - 1) + k_1 + 1) f'^2 \right] \quad (4.5)$$

where  $k_1 = K_1/K_3$  and  $k_2 = K_2/K_3$ . If this quantity is negative, then a spontaneous elastic distortion ought to appear in the bulk. The first, third and fourth terms are positive definite but the second is not and so may be able to cause spontaneous distortions. The conventional procedure, to minimize (4.5) by variational calculus yields a set of Euler-Lagrange equations that are difficult to solve numerically (this is a general problem with the HAN configuration; see [97]).

The linearized model just described assumed that the transition to the “stripe” state took place due to the diverging elastic anisotropy above the nematic–smectic-A transition temperature; and that the smectic order parameter was on average zero throughout the cell. The model originally proposed by Cladis and Torza, on the other hand, explains the phenomenon due to the smectic order growing in from the substrates and compressing the nematic into a progressively smaller central region. The nematic region is stabilized because the presence of twist and bend distortions with  $|\nabla \times \mathbf{n}| \neq 0$  effectively lower the transition temperature to the smectic phase as predicted by de Gennes[22]

$$T'_c = T_c - l T_c^S |\nabla \times \mathbf{n}| \quad (4.6)$$

where  $l$  is the molecular length and  $T_c^S$  is the nematic–smectic-A transition temperature; furthermore, the nematic–smectic transition must be very nearly second order as only in this case can the nematic and smectic phases coexist without an energetically expensive boundary. A consequence of 4.6 is that temperature dependence of the twist and bend constants is modified by the presence of  $|\nabla \times \mathbf{n}|$  deformations

$$K'_i = K_i^N + \delta K_i (T - T_c + l T_c^S |\nabla \times \mathbf{n}|)^{-\nu_i}, \quad i \in \{2, 3\}. \quad (4.7)$$

The insight of Cladis and Torza was that at some thickness it might be energetically favourable for the nematic layer to buckle (fig. 4.1) so that the nematic layer is surrounded by interdigitated smectic wedges in such a way as to maintain a constant thickness of the nematic layer. The wrinkled nematic has a lower bend energy by a factor of  $1/\cos \theta$  at the expense of increasing the twist energy; since  $K_2 < K_3$  for CBOOA (and 8CB) even near the nematic–smectic-A transition, the wrinkling may nonetheless reduce

the overall energy of the nematic layer. The energy of the wrinkled layer per unit area was shown to be

$$2F_{NL} = K_3 \left[ \frac{E(k')}{d_0} + \frac{K_2}{K_3} \tan^2 \theta \left( \frac{E(k')}{d_0} + \frac{\pi}{t - d_0} \right) \right] \quad (4.8)$$

with  $d_0$  the thickness of the nematic layer,  $\theta$  the angle of the wedge, and  $t$  is defined in fig. 4.1;  $E(k')$  is the complete elliptic integral of the second kind and

$$k' = \sqrt{\frac{(K_3 - K_1)\xi^2}{K_3\xi^2 + K_2(t - d_0)^2}} \quad (4.9)$$

where  $2\xi$  is the period of the stripes. The parameters  $\xi$ ,  $d_0$ ,  $\theta$  and  $t$  are not independent but related by

$$t - d_0 = \xi \tan \theta \quad (4.10)$$

and there is a natural constraint that  $t$  must be less than the cell thickness. The procedure to determine the period of the stripes is to find  $\xi$  and  $\theta$  that minimize  $F_{NL}/d_0$  for various values of  $\Delta T = T - T_C$ , taking into account the temperature dependence of the elastic constants (4.6) with

$$\langle |\nabla \times \mathbf{n}| \rangle = \frac{E(\cos \theta)}{d_0 \cos \theta}; \quad (4.11)$$

for  $\Delta T = 0$  the minimum is always at  $\theta = 0$ , corresponding to the unwrinkled state, while for  $\Delta T < 0$  the minimum may occur at some finite  $\theta$  and  $\xi$ . Since the period cannot change except by the nucleation of defects, Cladis and Torza supposed that the period would not change with temperature and so that the actual period would be the one which minimized  $F_0/d$  at the temperature where the wrinkled state just had lower energy than the non wrinkled state.

For CBOOA, Cladis and Torza used  $lT_c^S = 1.2\mu\text{m}$  [99] and critical exponents  $\nu_2 = \nu_3 = 1/2$  and the minimization of  $F_{NL}/d_0$  at  $T - T_c = -0.01K$  yielded a configuration  $\theta = 26^\circ$  and  $0.68 < 2\xi/d < 0.72$  which agreed well with their experimental value of  $2\xi/d = 0.66$ . A reanalysis of their model retaining the same values was attempted looking for the critical temperature at which the wrinkled state becomes lower than the unwrinkled state; this yielded  $T - T_C = -0.0091K$  with  $\theta = 16^\circ$  and  $2\xi/d = 0.8$  which agrees less well with the experimental value. The predicted period is affected by the choice of critical exponents used, for example with  $\nu_2 = 1/2$ ,  $\nu_3 = 2/3$ , the minimal value of  $F_{ND}/d_0$  occurs at  $\Delta T = -0.0062K$  and  $\theta = 29^\circ$ ,  $2\xi/d = 0.51$ ; with  $\nu_2 = 2/3$ ,  $\nu_3 = 2/3$ , the minimal value of  $F_{ND}/d_0$  occurs at  $\Delta T = -0.0073K$  and  $\theta = 35^\circ$ ,  $2\xi/d = 0.75$ .

Reducing the cell thickness increases the magnitude of the curl term in (4.11) and therefore increases proportionately the critical temperature at which the the wrinkled nematic layer has lower energy than the unwrinkled form. The parameter  $lT_c^S$  plays a similar role; for 8CB the transition temperature is lower than that of CBOOA (see section 3.1 on page 56) as is the molecular length and so  $lT_c^S \sim 0.67$ . The

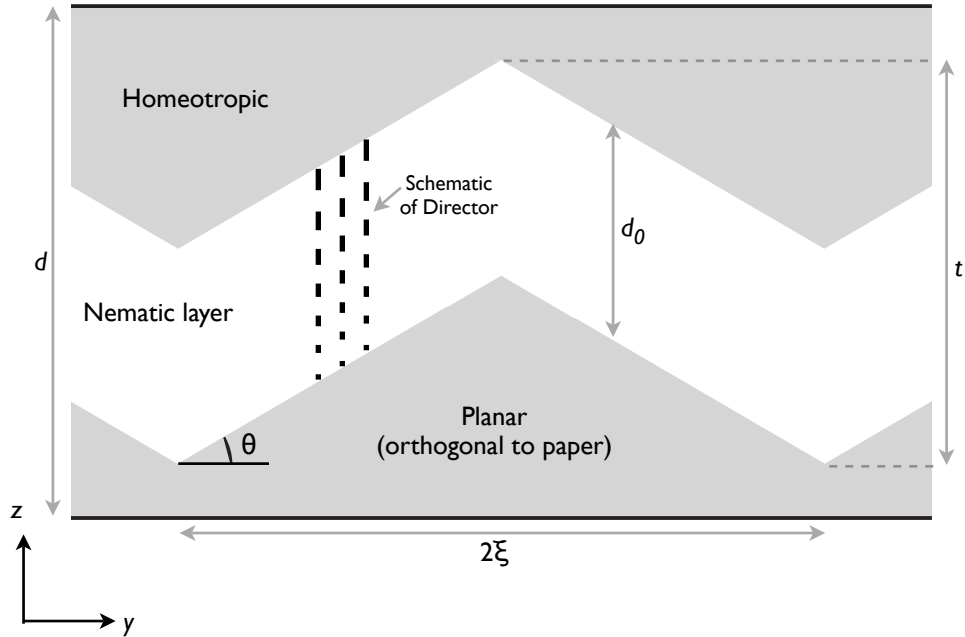


Figure 4.1: Schematic of the model of Cladis and Torza for the “stripe” structure as a wrinkled layer of nematic coexisting with smectic “wedges”. (Redrawn following [1])

minimization procedure described above was performed with these values using a range of values for the critical exponents in the intervals  $0.4 < \nu_2 < 0.7$  and  $0.5 < \nu_3 < 1$  and also with ratios of the elastic constants far above the nematic–smectic-A transition as measured by others (see Appendix C). It was found that the predicted period varied only weakly with the values of the critical exponents, in the range  $0.5 < 2\xi/d < 0.8$ , in marked disagreement with the experimental value of  $2\xi/d \sim 1.2$  from the previous chapter. Altering  $lT_c^I$  over an order of magnitude changed the transition temperature as expected, but did nothing to move the predicted period outside this interval; the minimization procedure was then performed with values of  $K_2^N/K_3^N$ ,  $\nu_2$  and  $\nu_3$  outside the range of experimentally measured values and the predicted period did not change significantly. It must be concluded then, that the model of Cladis and Torza *does not* describe the situation with 8CB completely.

There are a number of possible explanations for the discrepancy between the theoretical and experimental values for  $2\xi/d$ . Firstly, the model assumed that the nematic–smectic-A transition was second order: as discussed in the previous section this is not quite the case for 8CB. If the latent heat of transition is very small, a term proportional to the volume of the nematic region ought to be included in the free energy.

Nonetheless, the evidence of confocal microscopy (fig. 3.17 on page 72) suggests that the final configuration of the “stripe” phase is very close to the model of Cladis and Torza. In particular there are ‘wedges’ at the planar surface that are clearly smectic due to the enhanced fluorescence. One might expect to see a region of correspondingly decreased fluorescence near the homeotropic substrate, but this was not seen with the confocal microscopy. Because the original model of Cladis and Torza was inferred from the formation of planar smectic wedges around an included wire treated to promote planar alignment (and the homeotropic wedges were not observed in that case), there is in fact no experimental evidence to suggest



that these homeotropic wedges exist. It is possible that the smectic order grows in from each substrate with wrinkling only at the planar surface; the director configuration in such a configuration, however, must depend on two coordinates and cannot be found analytically with the anisotropic elastic constants necessary.

There is further evidence from the confocal microscope cross-sections that a more sophisticated model might be necessary: when the wedges first become visible, their emission intensity is not significantly greater than the maximum emission intensity observed in the nematic phase. As they form, the magnitude of the smectic order parameter within the wedges must be rather small, and hence they cannot be ignored entirely as in the model above. Properly, one ought to incorporate the smectic order parameter into the free energy—both elastic and Landau terms—as a spatially dependent quantity, and seek the configuration that minimizes the free energy as the temperature is lowered through the nematic–smectic-A transition; effects such as surface smectic ordering[34] are then included quite naturally. It is noteworthy that recent computer simulation of nematics using the Q-tensor representation of the director that, for example, capture the movement of disclinations, (e.g. [100, 101, 33]) have no counterpart with smectics. The field of spontaneous pattern formation might well benefit from a similar approach.

### 4.3 Structure of the V-shaped Defects

The intermediate stripe phase is interspersed with what were termed in the previous chapter V-shaped defects. On one side of the defect an additional pair of stripes is included and the stripes on the other side are forced to bend round (in a manner that resembles a ‘V’) to accommodate the inclusion. This section considers the configuration of the stripes around the defect and relates the observations in section 3.2 to previous theoretical work.

A useful approach is to ignore the vertical structure of the stripes (i.e. the  $z$  dependence in the coordinate system defined in the previous section) and to regard the stripe structure as a two dimensional smectic by representing each stripe as a single “smectic” layer. In this picture, the HAN–Stripe transition would be regarded as a two-dimensional nematic–smectic transition and may be characterized by an order parameter of the form (4.1). The full free energy of the stripe phase is replaced by the two-dimensional smectic free energy

$$F = \frac{1}{2} \int_S \tilde{K}_1 (\nabla \cdot \mathbf{n})^2 + \tilde{B} (|\nabla \Phi| - 1)^2 d^2x \quad (4.12)$$

where the compressibility  $\tilde{B}$  and the splay elastic constant  $\tilde{K}_1$  (there can be no saddle–splay deformation in two dimensions) are now notionally related in some complicated manner to the ‘bare’ material constants  $K_1, K_2, K_3$  as well as the vertical configuration of the liquid crystal. Within this description, the V-shaped defects should have the same structure as edge disclinations in smectic liquid crystals—a problem that has already been extensively studied theoretically[102, 103, 3] and experimentally [61].

A suitable choice of coordinate system is, following [102],  $x$  measured along the length of the stripes and  $y$  perpendicular to the stripes with the line  $y = 0$  along the centre of a single isolated defect. Adopting the Eulerian description of the smectic (discussed earlier in section 4.1), the phase  $\Phi(x, y)$  along the line  $y = 0$  must, at the core of the defect, jump discontinuously by some value  $b/2$  where  $b$  is called the *Burger's number* of the disclination (analogous to the Burger's vector for defects in a crystal). The energy of the defect may be found by promoting the phase factor  $u(x, y)$  to a field quantity and substituting  $\Phi(x, y) = y + u(x, y)$  into (4.12), making use of the relation  $\mathbf{n} = \nabla\Phi/|\nabla\Phi|$ ; Euler-Lagrange equations may then be derived from this energy and solved subject to the boundary condition

$$u(x, 0) = \begin{cases} 0 & x < 0 \\ a/2 & x \geq 0 \end{cases};$$

this need only be performed for the region  $y > 0$  since the defect must be symmetric about its centre. The full Euler-Lagrange equations for  $u(x, y)$  are nonlinear, but may be linearized if  $b < \sqrt{K_1/B}$  and solved to yield

$$u(x, y) = \frac{1}{4}b \operatorname{sgn}(y) \left[ \operatorname{Erf} \left( \frac{x}{2\sqrt{\lambda}\sqrt{|y|}} \right) + 1 \right] \quad (4.13)$$

where  $\lambda = \sqrt{\tilde{K}_1/\tilde{B}}$ . A recent interesting development[102] has been the analytical minimization of (4.12) which yields

$$u(x, y) = 2\lambda \operatorname{sgn}(y) \log \left\{ \frac{1}{2} \left( e^{\frac{b}{4\lambda}} - 1 \right) \left[ \operatorname{Erf} \left( \frac{x}{2\sqrt{\lambda}\sqrt{|y|}} \right) + 1 \right] + 1 \right\} \quad (4.14)$$

The structure of the layers around the defect is plotted in fig. 4.2 for different values of  $\lambda/b$ . The nonlinear theory agrees closely with the linearized theory for  $\lambda/b > 1$  as expected. The two theories were fitted to a typical V-shaped defect observed in the stripe phase (fig. 4.3) where values of the ratio  $\lambda/b$  for the disclination in the interval  $1.1 < \lambda/b < 1.5$  gave good and visually indistinguishable fits. The V-shaped defects are therefore well described by the linearized theory. As the cell is cooled so that modulations appear along the length of the stripes, however, the shape of the V-defects changes in a manner consistent with  $\lambda$  decreasing (compare fig. 3.7 on page 61 with 4.2). The presence of other nearby defects generally limits the applicability of (4.2) and (4.14) to the first few layers around the defect (as may be seen from fig. 4.3).

## 4.4 Behaviour in the Smectic Phase

### 4.4.1 In Cells Prepared with Silicon Oxide as an Aligning Layer

The structure adopted in the smectic phase in cells prepared with silicon oxide to promote planar alignment differed considerably from the structure of Ruan *et al.* Observations from confocal microscopy and polar-

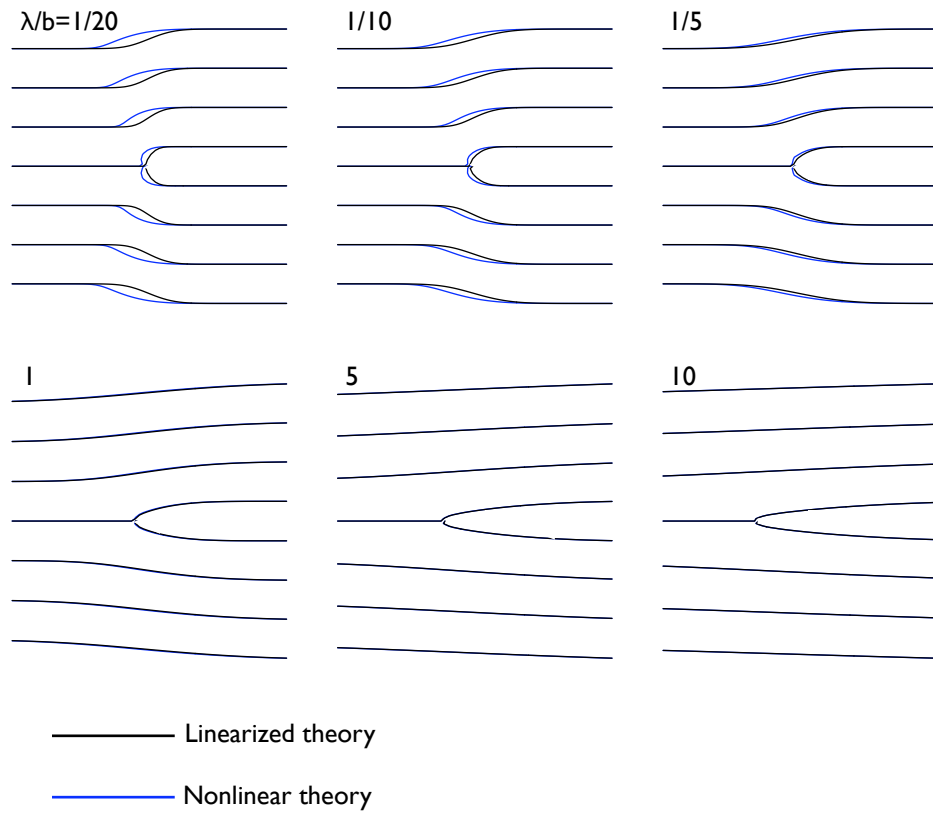


Figure 4.2: Smectic layer structure around a V-shaped defect using the analogy with edge disclinations in a smectic.

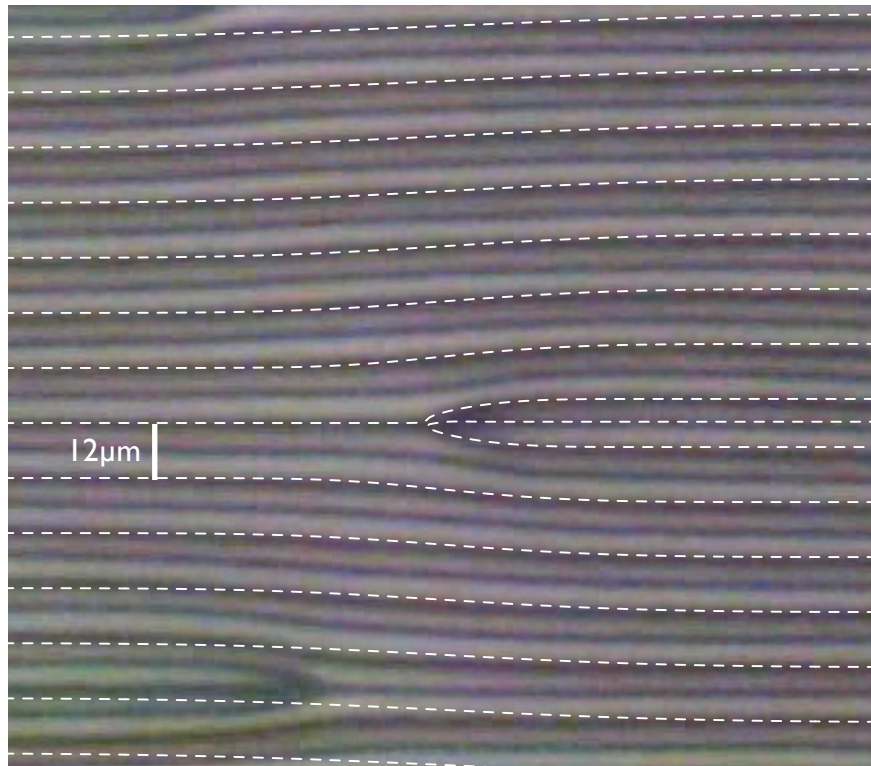


Figure 4.3: Fitted linearized solution to zipper defect with  $\lambda/b = 1.4$

izing microscopy in the previous chapter confirm that it is composed of Toroidal Focal Conic Domains. The structure is much closer to that observed in the work of Cladis and Torza[1] with one difference: in that work, the domains were circular and separated by small dark triangular regions, a configuration referred to hereafter as C-TFCD; in the present work (see fig. 3.11 on page 65) the domains are hexagonal in shape, more closely packed, and there are no intermediate dark regions (henceforth denoted H-TFCD). The principal difference between the two cases is—neglecting the choice of surface treatment that Cladis does not describe—that Cladis’s cells are around  $140\mu\text{m}$  thick while those in the previous chapter were an order of magnitude thinner.

In order to explain this difference, it is necessary to evaluate the free energy of each situation. The free energy of each state is a sum of many terms: a bulk elastic contribution; a contribution from the azimuthal anchoring energy at the planar surface; a contribution from the polar anchoring energy in the intervening regions between the C-TFCDs; a contribution from the polar anchoring energy at the homeotropic surface and, finally, a contribution from the walls between the H-TFCDs where the director is discontinuous. It is necessary to determine the strength and scaling behaviour of each of these contributions. Fortunately, a good deal of work has already been done on TFCDs[16, 104, 105, 77, 106, 107].

Before each contribution is evaluated individually, it is necessary to define a few common parameters:  $R$  is the distance between the line disclination cores in adjacent domains (it is exactly Ruan *et al.*’s definition of the pitch of their structure);  $a$  is the radius of the circular disclination confocal with the line disclination in the centre of the domain (the “natural” radius of the domain); the cell thickness is  $d$ . Note particularly that  $R$  and  $d$  are not independent quantities as was supposed by Ruan *et al.*; their ratio is set by the intermediate “stripe” phase that exists above the smectic phase in temperature.

The natural coordinate system of the Toroidal Focal Conic Domain  $\{r, u, v\}$  are toroidal coordinates defined by considering a line from some point on the defect circle to a point on the line (fig. 4.4): that line is specified by an azimuthal angle  $v$  around the circle and a polar angle  $u$  between the line and the plane of the central defect line while length along that line is specified by a third coordinate  $r$ . The value of  $u$  where  $\hat{r}$  points toward the bottom of the central defect line defines the *cone angle* for the domain  $\gamma = \arctan(a/d)$ . In this coordinate system, the director everywhere has a very simple form  $\{n_r, n_u, n_v\} = \{1, 0, 0\}$ . For convenience, suppose a Cartesian coordinate system is simultaneously defined with origin at the centre of the domain in the plane of the circle disclination, and where the  $z$ -axis points parallel to the line defect; the  $x$ -axis may be take to lie parallel to the plane defined by  $v = 0$  and the  $y$ -axis is then oriented so that the system is right-handed (fig. 4.4). The azimuthal easy axis at the planar surface is defined to lie parallel to the  $y$ -axis.

Within these definitions, if  $a = R/2$  then the domains are circular and are separated by interdomain homeotropic regions while if  $a = R/\sqrt{3}$ , the domains are exactly hexagonal in shape and the size of the interdomain homeotropic regions vanishes as  $a \rightarrow R/\sqrt{3}$  [fig. 4.5(a)]. Between  $R/2 < a < R/\sqrt{3}$  parts of the domain are separated from adjacent domains by walls across which the director is discontinuous.

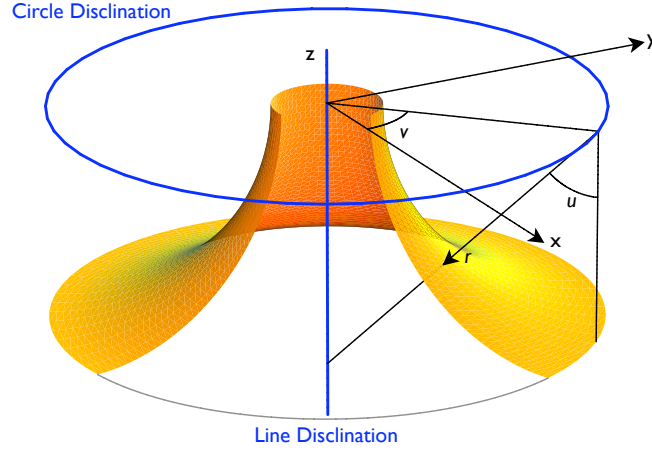


Figure 4.4: Schematic of toroidal coordinates

Within this regime, it is useful to define the angle  $\psi = \arccos(\frac{R}{2a})$  subtended between a line normal to the domain wall and a line from the centre of the domain to the edge of that domain wall; it is also helpful to define the half angular size  $\alpha = \pi/6 - \psi$  of the parts of the domain which appear as sectors of a circle when viewed from above [fig. 4.5(b)]. In order to specify the limits of integration later, it is convenient to define a length  $t(v) = a - \frac{1}{2}R \cos v$  which is the radial distance between the wall and the circle disclination as a function of the azimuthal coordinate  $v$  (fig. 4.6).

The bulk elastic energy of a Toroidal Focal Conic Domain has already been calculated for the circular case[104]: it is, correcting a minor error in the saddle splay term as presented in the paper, and substituting the earlier definitions

$$F_{cTFCD} = \pi K_1 a \left[ \frac{\pi}{2} \ln 2 + L(\pi/2 - \gamma) + (\pi - 2\gamma) \left( \ln \frac{a}{\xi} - 2 \right) + \gamma \ln \frac{ad}{\xi \sqrt{a^2 + d^2}} - 2 \frac{d}{a} \ln \left( 1 + \frac{a^2}{d^2} \right) \right] - \pi K_{24} d \left[ \frac{\pi a}{d} - 2 \frac{a}{d} \gamma + \ln \left( 1 + \frac{a^2}{d^2} \right) \right] \quad (4.15)$$

where  $L(x) = -\int_0^x \ln \cos t \, dt$  (the representation supplied in [104] appears to be incorrect and so we calculate this very simple integral numerically),  $\xi$  is the core radius of the disclination i.e. the characteristic length around a disclination over which elastic distortion is sufficient to reduce the magnitude of the smectic order parameter to zero. Since the TFCD has cylindrical symmetry,  $F_{cTFCD}/2\pi$  represents the energy per radian of an incomplete domain nonetheless bounded by a circle of radius  $a$  and so the energy of the type I regions [fig. 4.5(b)] is

$$F_{bI} = 12\alpha F_{cTFCD}/(2\pi) \quad (4.16)$$

To compute the total elastic energy of the domain it is necessary to supplement with the integral of the elastic energy density over the type II regions. It is well known[16] that in the toroidal coordinate system that the elastic energy density at a point may be expressed as a function of the principal radii of curvature  $R_1 = r$  and  $R_2 = r - a/\sin u$  of the torus that that point lies on. The splay energy density is exactly the

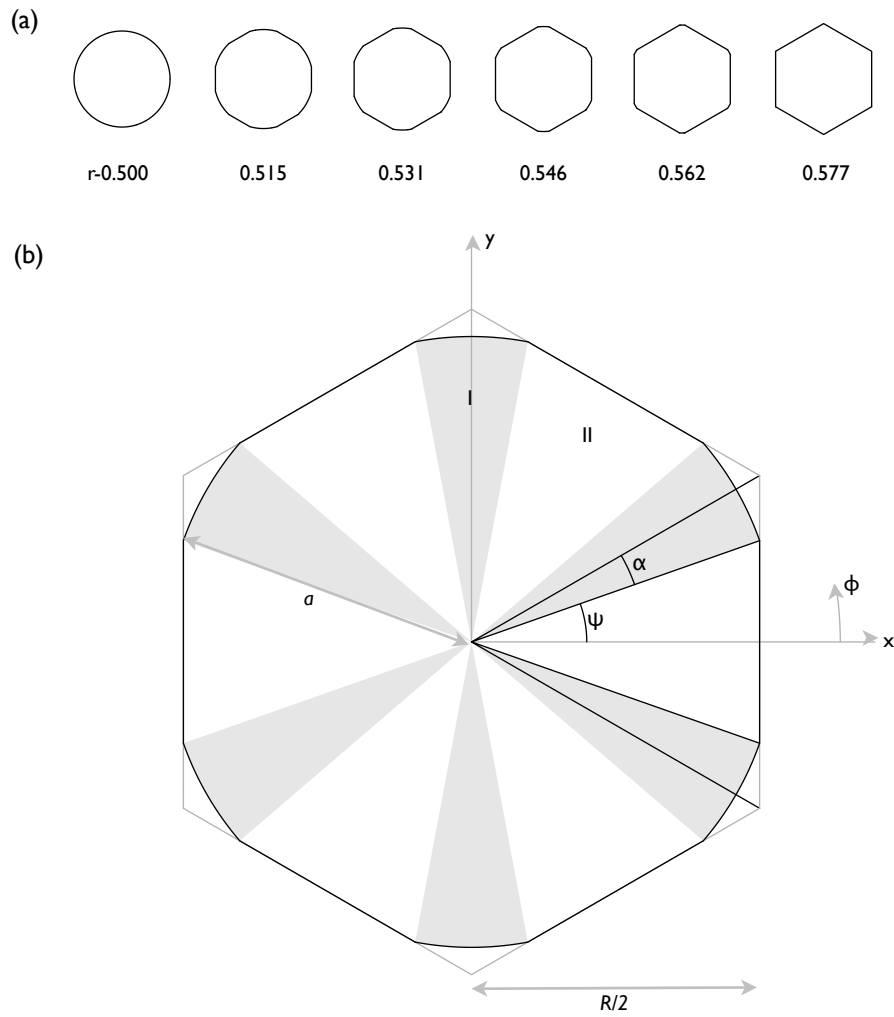


Figure 4.5: Overhead schematic of a Toroidal Focal Conic Domain (a) identifying distinct regions and variables for integration (b) shape of the domain with interdomain separation  $R$  fixed and  $r$  varying between  $1/2$  (circular) and  $1/\sqrt{3}$  (hexagonal).

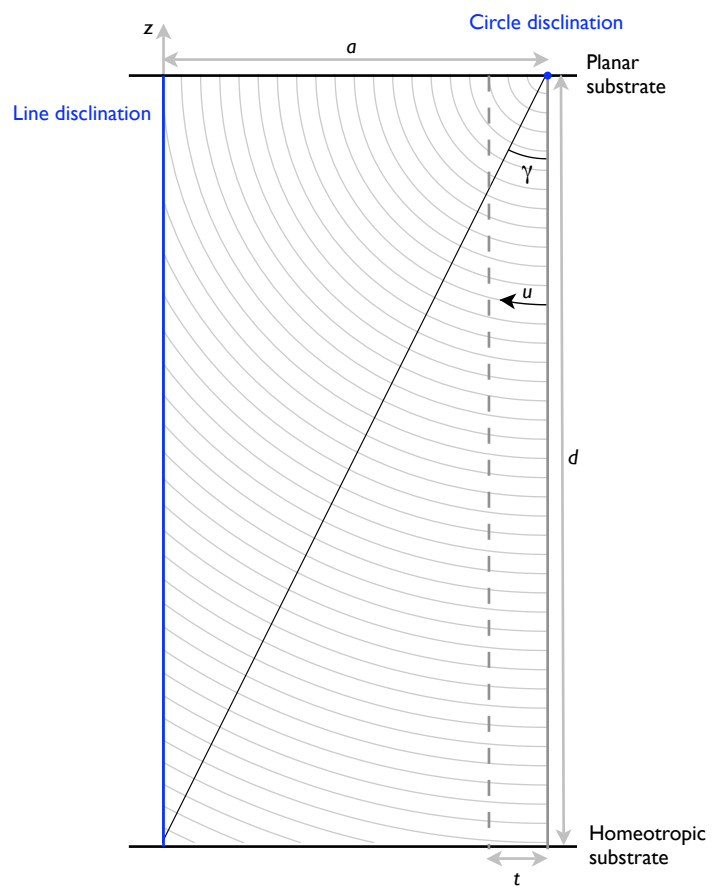


Figure 4.6: Cross section of a Toroidal Focal Conic Domain

square of the mean curvature of that torus

$$f_1 = \frac{K_1}{2} \left( \frac{1}{R_1} + \frac{1}{R_2} \right)^2 \quad (4.17)$$

and the saddle-splay energy density is exactly the Gaussian curvature

$$f_{24} = K_{24} \frac{1}{R_1 R_2} \quad (4.18)$$

which is negative in sign within the TFCd since  $R_2$  is negative. Following Lavrentovich *et al.*, the integral over a single section of type II region may be further divided into an inner part IIa defined by  $\gamma < u < \pi/2$  and an outer part IIb  $0 < u < \gamma$  where  $\gamma = \arctan([a - t(v)]/d)$  (fig. 4.6). Due to the awkward shape of the domains, it is easiest to evaluate the integrals numerically. The volume element is

$$dV = r(a - r \sin u) dr du dv \quad (4.19)$$

and in region IIa the limits of integration are then

$$\begin{aligned} 0 < v < \psi \\ \gamma < u < \pi/2 \\ \frac{t(v)}{\sin u} < r < \frac{a}{\sin u} - \xi \end{aligned} \quad (4.20)$$

while in region IIb they are

$$\begin{aligned} 0 < v < \psi \\ \arctan \frac{t(v)}{d} < u < \gamma \\ \frac{t(v)}{\sin u} < r < \frac{d}{\cos u}. \end{aligned} \quad (4.21)$$

The total energy of the hexagonal TFCd is therefore 12 times the integral of (4.17) and (4.18) over a single region IIa with limits (4.20) and region IIb with limits (4.21), as well as the additional contribution (4.16) from the type I regions.

At the planar surface and within the focal conic domain, the director lies everywhere parallel to the substrate and so there is no contribution to the polar anchoring energy. Furthermore, it is convenient to change to polar coordinates  $\phi$  (which is equivalent to  $v$  in toroidal coordinates) and  $\rho$  the distance from the line disclination at the centre of the domain. The azimuthal anchoring energy of the TFCd with



complete circular base is

$$\begin{aligned}
 F_{cP\phi} &= \frac{W_{P\phi}}{2} \int n_x^2 dS \\
 &= \frac{W_{P\phi}}{2} \int_0^{2\pi} \int_0^a \cos^2 \phi \rho d\rho d\phi \\
 &= \frac{W_{P\phi} a^2 \pi}{4}
 \end{aligned} \tag{4.22}$$

where again it is assumed that the Rapini-Papoular anchoring energy is valid when the angle between the in-plane component of the director and the azimuthal easy axis is not small. For the situation where  $a > R/2$ , it is necessary to divide the region in the same way as for the bulk energy into regions of type I and II [fig. 4.5(b)]. Since the integrand of the azimuthal anchoring energy lacks the cylindrical symmetry of the bulk energy, having only inversion with respect to the  $x$ - and  $y$ -axes as symmetry operations, it is necessary to integrate over the quarter of the domain defined by  $0 < \phi < \pi/2$  and multiply the result by four. The type I regions are straightforward; using the earlier definition of  $\alpha$

$$\begin{aligned}
 F_{P\phi I} &= W_{P\phi} a^2 \left( \int_{\pi/6-\alpha}^{\pi/6+\alpha} \cos^2 \phi d\phi + \int_{\pi/2-\alpha}^{\pi/2} \cos^2 \phi d\phi \right) \\
 &= W_{P\phi} a^2 3i \left[ \log(2) - \log \left( i \frac{R}{a} + \sqrt{4 - \frac{R^2}{a^2}} \right) \right] - \pi a^2.
 \end{aligned} \tag{4.23}$$

The type II regions are then

$$\begin{aligned}
 F_{P\phi II} &= 2W_{P\phi} \left( \int_0^\psi \int_0^{\frac{R}{2 \cos \phi}} \cos^2 \phi \rho d\rho d\phi + \int_{\pi/6+\alpha}^{\pi/2-\alpha} \int_0^{\frac{R}{2 \cos(\phi-\pi/6)}} \cos^2 \phi \rho d\rho d\phi \right) \\
 &= W_{P\phi} \frac{R^2}{2} \left( \frac{\psi}{2} + \int_{\pi/6+\alpha}^{\pi/2-\alpha} \frac{\cos^2 \phi}{\cos^2(\phi-\pi/3)} d\phi \right)
 \end{aligned} \tag{4.24}$$

where the remaining integral is to be integrated numerically. The total azimuthal energy at the planar surface is the sum of (4.23) and (4.24).

Between the C-TFCDs is an intervening nearly triangular region that must be homeotropic in order to maintain continuity of the layers and there are two such regions per unit cell of the structure. At the planar surface, the director in these regions is exactly perpendicular to the easy axis and so incur an anchoring energy proportional to their area

$$F_{P\theta} = \frac{W_{P\theta}}{4} \left( \sqrt{3}R^2 - a \left[ -12 \arccos \left( \frac{R}{2a} \right) a + 2\pi a + 3R \sqrt{4 - \frac{R^2}{a^2}} \right] \right).$$

The next contribution to the total free energy comes from the polar anchoring energy at the homeotropic interface. Since the director is around the edge of the domain nearly homeotropic, this contribution is

expected to vary only weakly with  $a$  for fixed  $R$ . Since the energy density

$$f_{T\theta}(\rho) = \frac{(a - \rho)^2}{a^2 - 2\rho a + d^2 + \rho^2}$$

is cylindrically symmetric, it is necessary only to evaluate the energy in one type I region and one type II region producing the total by 12. Again adopting polar coordinates this time in the plane of the homeotropic substrate, the polar anchoring energy is

$$\begin{aligned} F_{T\theta} &= 6W_{T\theta} \left( \alpha \int_0^a f_{T\theta}(\rho) \rho \, d\rho + \int_0^\psi \int_0^{\frac{R}{2 \cos \phi}} f_{T\theta}(\rho) \rho \, d\rho \, d\phi \right) \\ &= \frac{W_{T\theta}}{4} \left\{ 36a^2 \arccos \frac{R}{2a} + 12\alpha a^2 - 24\alpha d a \arctan \frac{a}{d} + 3R \sqrt{4 - \frac{R^2}{a^2}} a + \right. \\ &\quad \left. + 2\pi d^2 \log \left( 1 + \frac{a^2}{d^2} \right) + 12aR \log \left[ \left( \frac{\cos(\psi/2) - \sin(\psi/2)}{\cos(\psi/2) + \sin(\psi/2)} \right) \left( \frac{2}{1 + \tan(\psi/2)} - 1 \right)^2 \right] \right\}. \end{aligned}$$

Each H-FCD is separated from its six neighbours by domain walls across which the director appears at the macroscopic scale to change discontinuously. At the microscopic scale, however, the layers bend round in such a way to maintain their continuity; although curvature on such a length scale will tend to reduce the magnitude of the smectic order parameter, the energy of such a reduction is tantamount to a renormalization of the wall width and so it is unnecessary to include this effect explicitly in the calculation. In the present case, since each of the walls has an identical configuration, it is necessary to compute only the energy of one wall and so it is sufficient to evaluate the energy of the wall perpendicular to the  $x$ -axis and defined by the limits  $-\psi < v < \psi$ . The energy density of the wall is postulated to be some function of the cross product of the two directors at either side of the wall  $\omega = |\mathbf{n}_1 \times \mathbf{n}_2|$ , a quantity that properly vanishes if  $\mathbf{n}_1$  and  $\mathbf{n}_2$  are parallel and so there is no discontinuity. This cross product is particularly simple to evaluate using the Cartesian representation of the director since the wall is a plane of mirror symmetry

$$\begin{aligned} \omega &= \begin{vmatrix} \hat{x} & \hat{y} & \hat{z} \\ n_x & n_y & n_z \\ -n_x & n_y & n_z \end{vmatrix} \\ &= 2\sqrt{n_x^2(1 - n_x^2)}. \end{aligned} \tag{4.25}$$

and depends only on  $n_x$ . In Cartesian coordinates,  $n_z = 1/\sqrt{1 + (t/z)^2}$  where the length  $t$  defined earlier (fig. 4.6) has the form  $t = a - \sqrt{y^2 + R^2/4}$ . The component of the director perpendicular to the wall  $n_x$

is

$$\begin{aligned}
 n_x &= (1 - n_z^2) \cos \left( \arcsin \frac{2y}{R} \right). \\
 &= 1 / \sqrt{\left( \frac{4y^2}{R^2} + 1 \right) \left[ 1 + \frac{4z^2}{(\sqrt{R^2 + 4y^2} - 2a)^2} \right]}. \quad (4.26)
 \end{aligned}$$

It has been shown that the energy density of a curvature wall is [105]

$$f_w = \frac{2K_1}{\lambda} (\tan \omega - \omega) \cos \omega \approx \frac{2K_1 \omega^3}{3\lambda} \quad (4.27)$$

where  $\lambda = \sqrt{K_1/B}$  is the smectic penetration depth and the approximate result is valid if  $\omega$  is small. The energy of half a single wall may be obtained by substituting (4.26) into (4.25) and then (4.25) into (4.27) and integrating the result over the interval  $0 < y < \sqrt{a^2 + R^2/4}$  and  $-d < z < 0$ . The total energy of all the walls is this value multiplied by 12.

Each of these terms is plotted in fig. 4.7 in ‘bare’ form, i.e. scaled so that the governing prefactor (which has units of energy per unit area) is 1. In front of the elastic terms is a factor  $K_i/R$ ; the magnitude of the splay elastic constant  $K_1$  is well known to be about  $1 \times 10^{-11} \text{N}$  [73, 86] and for the  $10 \mu\text{m}$  cell, the prefactor is hence  $10^{-5} \text{Jm}^{-2}$  and the splay term favours the hexagonal configuration by  $\Delta F_1 \approx 8 \times 10^{-5} \text{Jm}^{-2}$  [fig. 4.7(a)]. The saddle-splay constant  $K_{24}$  is known from theory to be smaller than but of the same order as the splay constant [e.g. [108] proposes  $K_{24} = (K_1 + K_2)/4$ ] and hence the saddle-splay term favours a near hexagonal configuration by a quantity two order of magnitude smaller than the splay term  $\Delta F_{24} \approx 5 \times 10^{-7} \text{Jm}^{-2}$  [fig. 4.7(b)].

The anchoring energies have not, however, been determined for the smectic phase with much precision; for the polar anchoring energy Lavrentovich reports that  $10^{-4} < W_\theta \lesssim 10^{-2} \text{Jm}^{-2}$  (compared with  $W_\theta \sim 1 \times 10^{-4} \text{Jm}^{-2}$  for nematics). The homeotropic anchoring energy of the interdomain region therefore favours the hexagonal configuration by between  $4 \times 10^{-6} < \Delta F_{\theta P} < 4 \times 10^{-4} \text{Jm}^{-2}$  [fig. 4.7(c)]; while the polar anchoring at the homeotropic substrate favours the circular configuration by  $4 \times 10^{-7} < \Delta F_{\theta T} < 4 \times 10^{-5} \text{Jm}^{-2}$  [fig. 4.7(d)]. The azimuthal energy does not appear to have been measured for smectics, but in nematics  $10^{-3} < W_\phi/W_\theta < 10^{-1}$  and for silicon oxide surfaces  $W_\phi \sim 1 \times 10^{-5} \text{Jm}^{-2}$ . If this trend is also true in the smectic phase, then  $10^{-6} < W_\phi < 10^{-3} \text{Jm}^{-2}$  and hence the azimuthal energy change at the planar surface favours the circular configuration by  $4 \times 10^{-7} < \Delta F_{\phi P} < 4 \times 10^{-5} \text{Jm}^{-2}$  [fig. 4.7(e)].

The remaining contribution is the energy of the curvature walls which have a prefactor of  $2K_1/(3\lambda)$  [105] where  $\lambda$  is of the order of the smectic coherence length i.e.  $\sim 10 \text{nm}$ . The prefactor is therefore  $7 \times 10^{-4} \text{Jm}^{-2}$  and so the wall energy in the hexagonal state is  $\sim 7 \times 10^{-5} \text{Jm}^{-2}$ .

The observed behaviour is that for thin cells, the hexagonal configuration is preferred, while for thicknesses

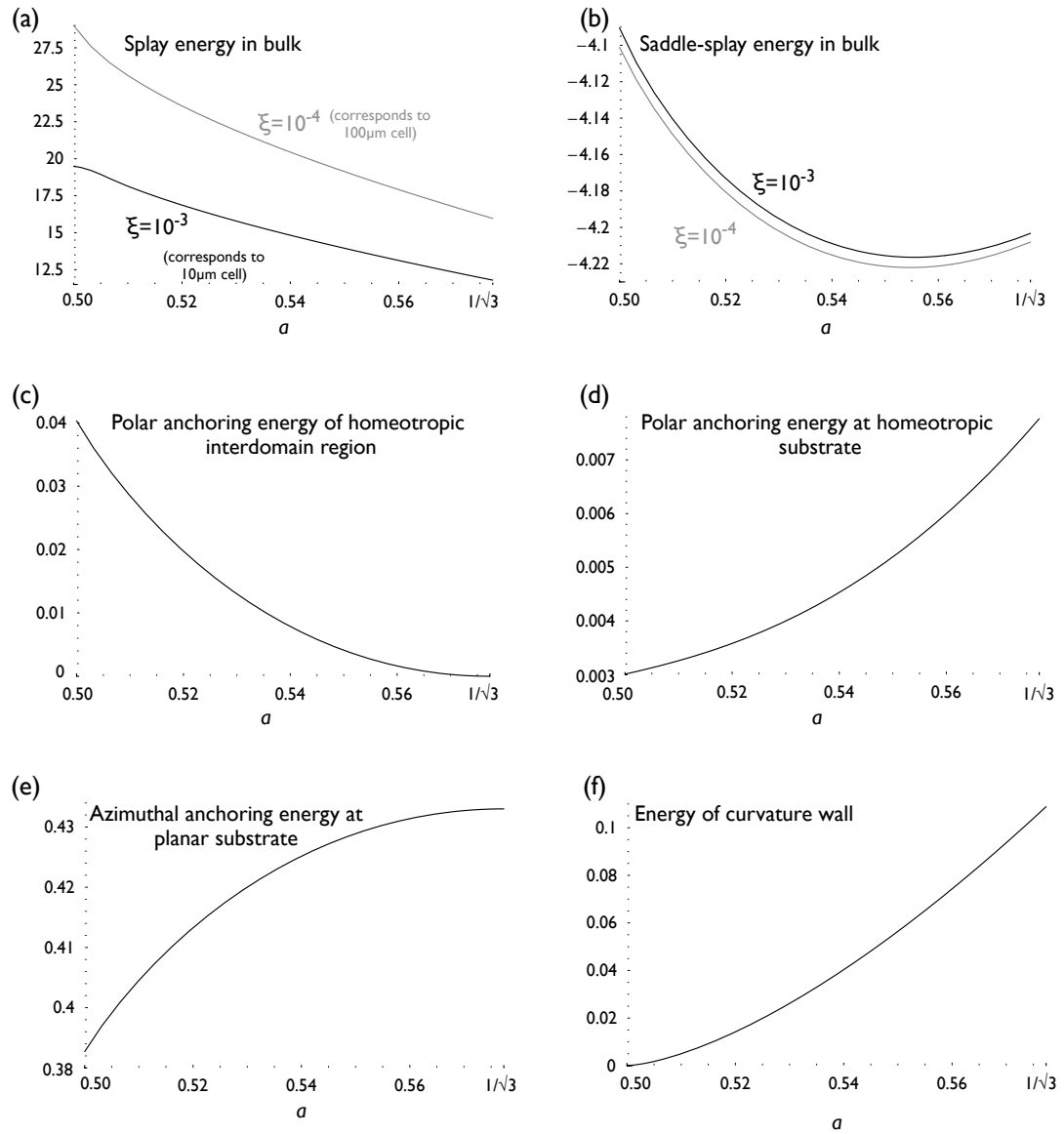


Figure 4.7: Contributions to the energy of a Toroidal Focal Conic Domain with the interdomain separation  $R = 1$ ,  $1/2 < a < 1/\sqrt{3}$  and  $d/R = 0.9$ ; the contributions are in ‘bare’ form with their governing prefactor chosen to be 1.

an order of magnitude larger, the circular configuration has lower energy. The above analysis suggests that the only terms relevant to the effect are the bulk splay energy, the wall energy and in principle the energy of the homeotropic inter-domain regions. With increasing cell thickness, the ratio  $R/d$  remains constant and so the bulk splay energy per unit area scales like  $\ln(d/\xi)$ ; the surface energy per unit area does not change; the wall energy per unit area scales linearly with  $d$  (due to the  $1/\lambda$  term in the prefactor). The energy of the walls increases much faster with cell thickness than the splay energy and so at some critical thickness the energy cost of forming the curvature walls exactly equals the saving in splay energy by adopting the hexagonal shape. Above this thickness, the circular shape has lower energy. If the polar anchoring energy is at least an order of magnitude larger than the value in the nematic phase, then the polar anchoring energy of the interdomain homeotropic regions will be of comparable magnitude to the leading terms for micron cell thicknesses and will raise the critical thickness.

Since radii of the TFCD in between  $1/2$  and  $1/\sqrt{3}$  have not been observed, it is very likely that the surface energy *is* significant: Competition between the two influences favouring the hexagonal shape (only one of which changes with thickness) and the influence favoring the circular shape (which grows rapidly with thickness) would suggest a sudden change from hexagonal to circular, competition that involves only the curvature walls and splay energy or only the curvature walls and the interdomain regions would suggest a more gradual transition with intermediate radii of the TFCD.

#### 4.4.2 The structure of Ruan et al.

It was described earlier that the most interesting aspect of the structure of Ruan *et al.* is that individual domains are not circular. Recent work by Pishnyak *et al.*[72] based on observations with a confocal microscope suggests that within those domains, the smectic layers are arranged as parts of incomplete Dupin cyclides. Furthermore, they suggest that the physical origin of the phenomenon is the azimuthal surface anchoring energy:

*“The missing parts of ellipses correspond to  $\mathbf{n}$  orthogonal to the rubbing direction. We relate the fragmentation to azimuthal anchoring caused by rubbing; it is absent at azimuthally degenerate interfaces such as SmA-isotropic fluid. It is well known that the hybrid-aligned SmA at the isotropic substrates shows hexagonal structures formed by FCDs with complete circular bases e.g. [72]”*

Before this claim is examined in detail, it is necessary to review the structure of the Dupin cyclides in greater detail than presented in chapter 1. The smectic layers are arranged around two disclinations: an ellipse and hyperbola that are confocal but lie in orthogonal planes. In the present case, the hyperbola lies in a plane orthogonal to the substrate and the ellipse lies in a plane usually parallel or possibly making some angle with the substrate. The layer normal at a particular point always lies parallel to a line connecting some point on the ellipse to another point on the hyperbola and passing through the point of interest.

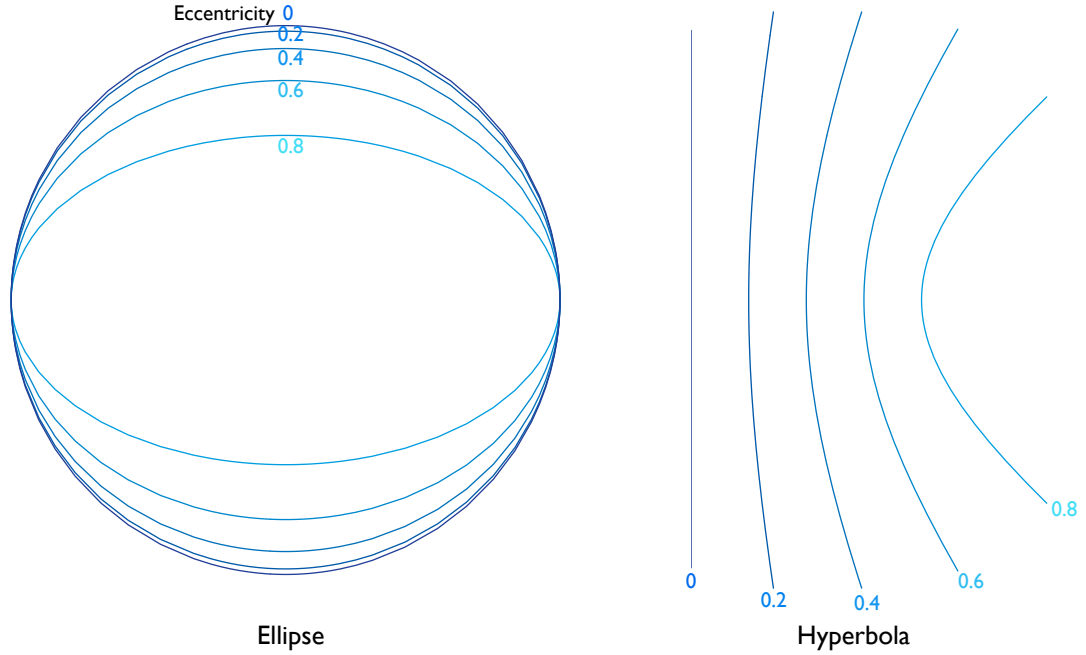


Figure 4.8: Set of confocal ellipses of different eccentricity with corresponding confocal hyperbola.

The disclination ellipse and hyperbola are characterized by a parameter called the eccentricity which is defined for the ellipse

$$e = \left| \sqrt{1 - \left( \frac{r_{\text{major}}}{r_{\text{minor}}} \right)^2} \right| \quad (4.28)$$

where  $r_{\text{major}}$  and  $r_{\text{minor}}$  are the major and minor radii; if the eccentricity is 0, the ellipse becomes a circle and the hyperbola becomes a straight line; hence the focal conic domain of zero eccentricity is a toroidal focal conic domain [16]. A series of ellipses and hyperbole with increasing eccentricity are plotted in fig. 4.8. The observations of the previous chapter, as well as those of Pishnyak *et al.*[72], are consistent with a value for the eccentricity of the focal conic domain of around 0.1 – 0.3.

The azimuthal anchoring energy density is plotted over the surface of the domain in fig. 4.9 on the next page. Indeed, as Pishnyak *et al.* suggest, the greatest contribution to the azimuthal energy is localised in the two areas immediately to the left and right of the defect; these are the very areas excluded in the structure of Ruan *et al.* It is also evident that, as the eccentricity of the domain increases, the regions with highest azimuthal anchoring energy density are moved further into the excluded regions and so the residual azimuthal anchoring energy should decrease with  $e$ .

The question nonetheless remains why, in cells prepared with silicon oxide (whose domains geometrically must have the same spatial dependence of the azimuthal anchoring energy density) the exclusion does *not* occur while in the rubbed polyimide cells it does. There are unfortunately no measurements for either of these alignment materials in the smectic phase. In the nematic phase, guided mode studies suggest  $W_\phi \sim 3 \times 10^{-6}$  for silicon oxide[49] and  $W_\phi \sim 10^{-5}$  for rubbed polymer surfaces[52]; the value for the silicon oxide surface is certainly lower, but by less than an order of magnitude. In the absence of a

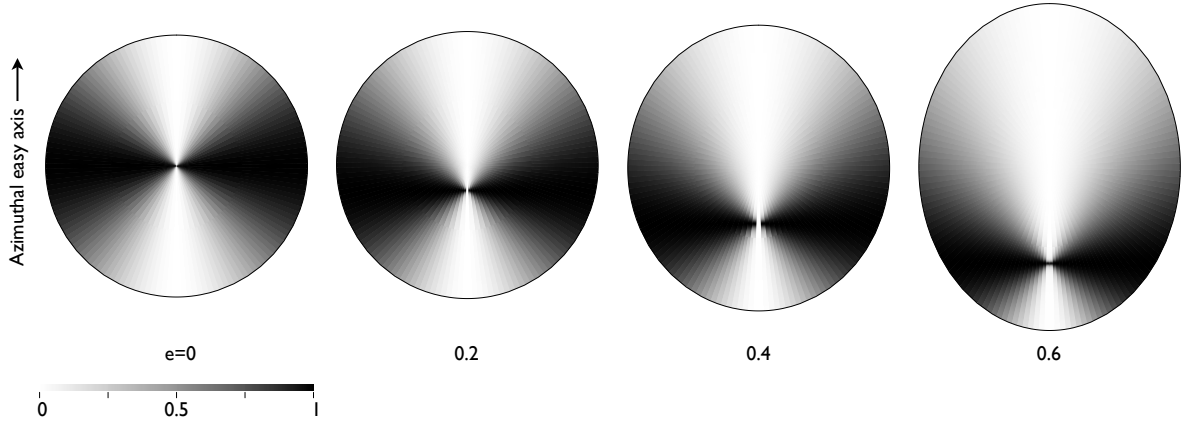


Figure 4.9: Azimuthal anchoring energy density of a Dupin Cyclide FCD along the planar surface.

persuasive discrepancy, it is natural to ask whether the azimuthal anchoring energy is the only influence on the system that favours exclusion of parts of the domain with the consequent introduction of curvature walls. Since in very thick cells the domains are circular it may be inferred that the phenomenon is caused by some part of the surface anchoring.

Confocal microscopy of the structure of domain walls in the nematic phase (see section 3.4 on page 69) indicates that the easy axis is definitely not parallel to the plane of the substrate, but rather makes a polar angle of around  $\theta_e \sim 15^\circ$  to it. If this phenomenon persists into the smectic phase, then for the case where the disclination ellipse lies in the plane of the substrate, the surface energy of the complete domain is

$$F_\theta \approx \frac{W_{\theta P}}{2} \pi a^2 \theta_e^2$$

which is, supposing that  $W_{\theta P}$  in the smectic phase remains an order of magnitude or more greater than  $W_{\phi P}$  as is the case in the nematic phase [49, 47], comparable to or greater than the azimuthal anchoring energy which must be of the same size as that calculated earlier for the zero eccentricity case (4.22).

One might suppose that the polar anchoring energy may be reduced by moving the plane of the ellipse to some distance  $z$  into the substrate, ignoring any other constraint that render the manoeuvre infeasible, so that the disclination ellipse is in effect ‘virtual’. The polar anchoring energy in this situation may be evaluated in polar coordinates where the radial component is scaled by the radius of the domain  $a$

$$\begin{aligned} F_{\theta P}(z, \theta_e) &= 2\pi a^2 \int_0^1 \sin\left(\theta_e - \arctan \frac{z}{1-r}\right)^2 dr \\ &= \frac{\pi}{2} a^2 [1 + (4 \log(z) z^2 - 2 \log(z^2 + 1) z^2 - 4 \tan^{-1}(z) z + 2\pi z - 1) \cos 2\theta_e + \\ &\quad + 2z (-2z \arctan(z) + \pi z - 2 \log(z) + \log(z^2 + 1) - 2) \sin 2\theta_e] \end{aligned}$$

which, since it contains only positive definite terms in  $z$  has a minimum value at  $z = 0$ . If however the substrates no longer are constrained to be parallel to the plane of the disclination ellipse but rather they

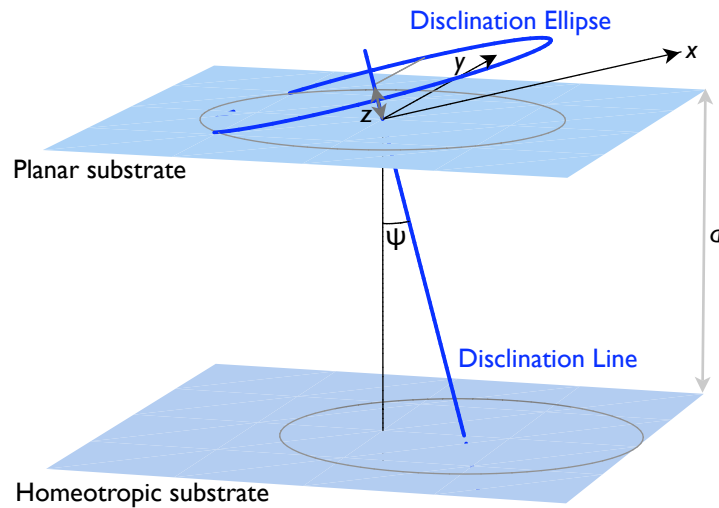


Figure 4.10: Schematic of a tilted Toroidal Focal Conic Domain

lie at some small angle  $\psi$  to it (fig. 4.10) with their surface normal in the  $x - z$  plane, then the polar anchoring energy density is greatest along the negative  $x$  end of the domain [see fig. 4.11(a)] and it is therefore energetically favourable to exclude those sections [fig 4.11(b)]. The polar anchoring energy per unit area of the tilted offset configuration was found numerically to have a minimum value of about 0.4 times that of the configuration where the disclination ellipse lies in the plane of the substrate.

The observations in the previous chapter and those of Pishnyak *et al.* are in fact consistent with a number of configurations: either a domain of finite eccentricity with disclination ellipses that lie in the plane of the substrate, or equally with a domain of zero eccentricity—a Toroidal Focal Conic Domain—rotated about an axis perpendicular to the rubbing direction by an angle of less than  $10^\circ$  or indeed with many suitable intermediate combination of rotation and eccentricity.

It has been shown that the polar anchoring energy, if the easy axis is not parallel to the substrate, also favours incomplete focal conic domains. A more complete phenomenological model, such as that developed earlier for cells prepared with silicon oxide, is of very limited utility while the anchoring energies remain unknown. The actual configuration adopted is very likely due to *both* the azimuthal and polar anchoring, as the offset and tilt of the domain reduces the azimuthal anchoring energy by some small amount and does not affect greatly its spatial dependence along the plane of the substrate.

## 4.5 Summary

This chapter has explored some of the physical effects that control the shape and size of the regular array of domains that form in the smectic phase of a hybrid aligned cell. This self-assembly is most unusual: in most other cell geometries, the smectic forms unordered Focal Conic Domains with a characteristic size determined by a compromise between the elastic and surface energies. In the hybrid-aligned cell, however, the domains nucleate along the length of wedges of planar smectic; notably, the size of the



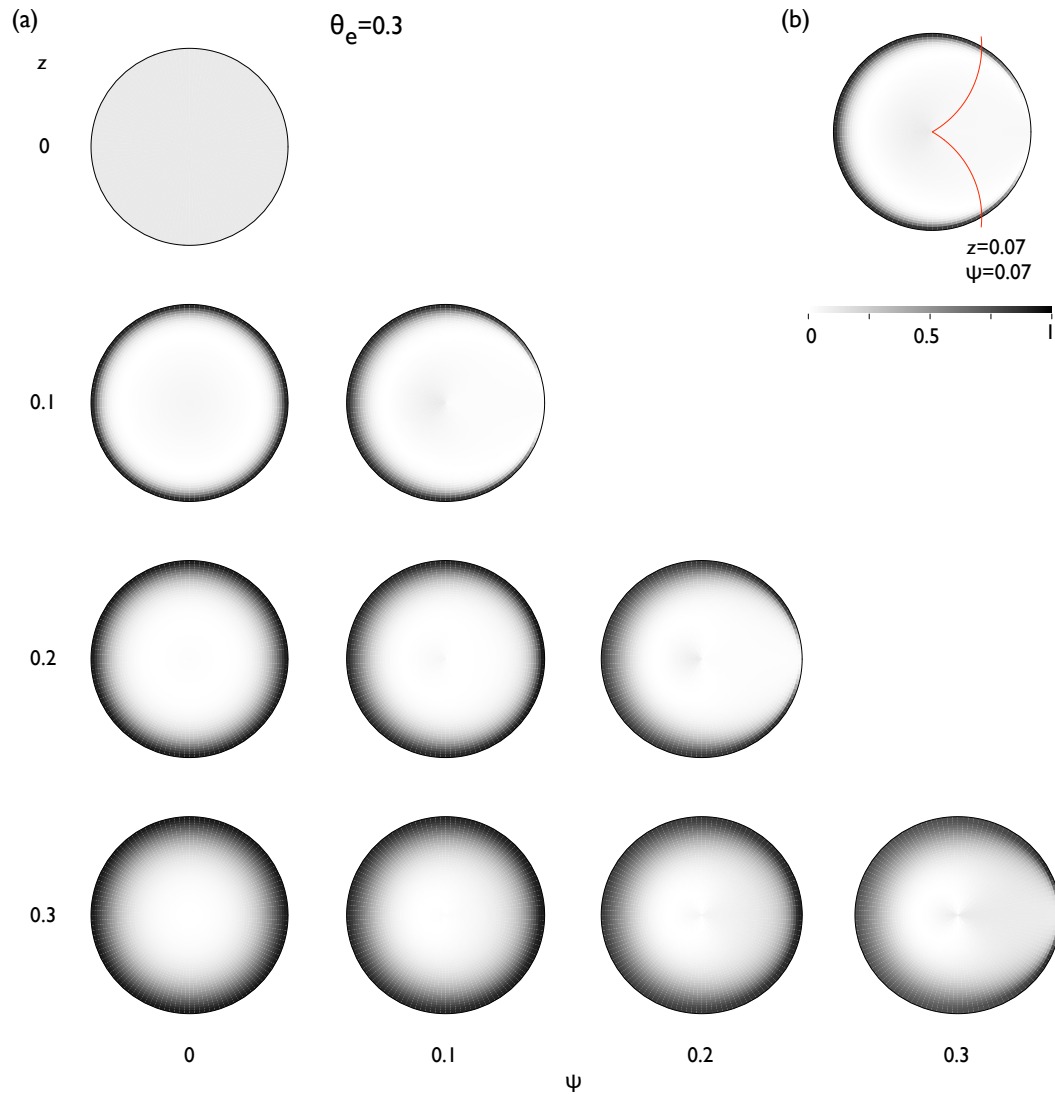


Figure 4.11: (a) Sections through a Toroidal Focal Conic Domain, at different depths  $z$  from the plane of the defect circle and inclined at an angle  $\psi$  to it, showing the polar anchoring energy density as a function of position. (b) The section that minimizes the total polar anchoring energy within the red section illustrated.

FCDs is not a free parameter but is imposed by the period of the intermediate striped phase. This imposed domain size does not necessarily correspond to an optimal configuration energetically speaking, and so the configuration that minimizes the free energy includes curvature walls and incomplete disclinations that normally are energetically unfavourable.

The stripe phase occurs due to the expulsion of the bend distortion present in the HAN configuration by the presmectic order, although the exact mechanism by which this occurs remains an open problem. It was shown to be possible *in principle* for a periodic modulation to reduce the energy of a nematic with a divergent bend elastic constant at the expense of a simultaneous modulation of the director angles  $\theta$  and  $\phi$ , although the linearized theory cannot give a quantitative prediction. The model of Cladis and Torza was applied to the thinner cells and different compound used, and partially justified by the observations from the previous chapter of smectic wedges at the planar surface; nonetheless, the predicted period is only in rough agreement with that observed, and so the precise sequence by which the stripes form must be regarded as an open problem. Nonetheless, the configuration of the stripes around the V-shaped defects observed in the stripe structure were shown to be well described by a known linear theory by considering the striped phase as a two dimensional smectic and the defects as edge dislocations.

The unusual shape of the Focal Conic Domains in the smectic was considered next: It was shown for the structure of Ruan *et al.* that this could be explained by nonzero surface pretilt at the planar substrate; the polar anchoring energy could be minimized in this situation if the domains tilted over and excluded some highly energetic regions. This new mechanism is entirely consistent with that proposed by Pishnyak *et al.* and will dominate if the polar anchoring energy is greater than the azimuthal anchoring energy as is the case in the nematic phase.

Finally, a complete phenomenological theory was constructed to explain the hexagonal, rather than circular, shape of domains in a cell prepared with a silicon oxide planar alignment layer. It was shown that the effect could be explained even if the surface energy was not significant as being due to a competition between the removal of highly distorted regions adjacent to the (now virtual) defect ellipse and the inclusion of curvature walls between the domains. It was shown that if the polar anchoring energy of the planar anchoring energy was in fact towards the upper end of the range of the (few) experimentally measured values, then the surface energy of the interdomain homeotropic regions would tend to favour the hexagonal shape.

## Chapter 5

# Nematics in Contact with Patterned Surfaces

### 5.1 Applications of Surface Patterning

**R**ATHER THAN the uniform homeotropic or planar surface treatments used in most commercial liquid crystal devices, there has in recent years been much interest in the use of periodically patterned surfaces[109, 110, 111, 112, 113, 114, 115, 38, 116, 117, 118, 119, 120, 121, 122, 123]. A patterned surface may incorporate regions of either homeotropic or planar alignment and may also have regions of planar alignment with antagonistic azimuthal easy orientation. If the pattern is on the micron scale, the director field adjacent to the surface is highly distorted as it is constrained to locally follow the easy orientation promoted by specific regions of the pattern; away from the surface however, the director adopts a uniform bulk orientation—an *effective easy axis*—that depends on the relative area of each region. A surface patterned on the nanoscale may also induce local “melting” of the liquid crystalline order if the elastic distortion is sufficiently great[124].

An important application of patterned surfaces is that it is possible to design a surface to promote any arbitrary orientation and with an arbitrary effective anchoring energy. Uniform surface treatments generally have a fixed preferred pretilt angle and the use of a different treatment is usually required if the surface orientation must be changed. The evaporation of silicon oxide is unusual in that it creates nanoscale surface structure, responsible for the alignment, but it may be applied over a wide area and the pretilt angle may be adjusted by changing the angle of evaporation [125]; the process is unfortunately incompatible with the mass-production techniques used for the commercial manufacture of displays while surface patterning techniques may be integrated relatively easily.

A second motivation for the study of surface patterning is as a route to construct *bistable* displays: in a conventional liquid crystal pixel an electric field must constantly be applied to maintain the director field

in the ‘on’ state. The director field in a *bistable* cell may however persist in either of two different stable configurations which may be switched between by the application of a suitable electric field for a short length of time. For reflection-mode displays such as those in watches, smart credit cards, electronic books the power consumption is greatly reduced. The benefit is negligible in a backlit display where the majority of power is consumed by the backlight; it is however no longer a necessity (because of the bistability) to construct the display with an array of transistors necessary for high resolution displays[126].

The geometry of a bistable cell must therefore permit two local minima of the free energy with respect to the director configuration and furthermore it is also necessary that there exists some way of switching predictably between the two states. The use of substrates with a periodic anchoring condition (either the surface shape or a pattern or even both simultaneously [117]) has proven to be an effective approach in the design of bistable devices[127, 128]; viable displays based on other strategies, including the use of cholesteric and ferroelectric materials, have been demonstrated. A variety of effects are responsible for switching including flow, elasticity, flexoelectricity and ferroelectricity.

The Zenithal Bistable Device[129] is composed of a uniform homeotropic substrate and a second substrate with an asymmetric grating—of wavelength and pitch  $\sim 1\mu\text{m}$ —which also has been treated to promote homeotropic alignment. The director field near the grating may either adopt a planar or homeotropic configuration and so the two stable states are a homeotropic one and a state that resembles the HAN. The ZBD switching process, which involves the movement of defects, is complicated and has been the subject of much theoretical attention[100, 101, 130].

A Post-Aligned Bistable Display[127] has, instead of the grating, a surface with a square array of roughly square submicron-sized posts; the sides of the post promote planar alignment and the director field is distorted around the post to satisfy this condition. The director can lie diagonal to the sides of the posts in either of two configurations.

## 5.2 Techniques for Surface Micropatterning

One technique for micropatterning surfaces is the so-called *photoalignment* technique in which a substrate is coated with a suitable prepolymer film and then exposed to polarized UV-light which polymerizes the film and induces an anisotropic, uniaxial orientation of polymer molecules on the surface[131]. A nematic in contact with the surface after photopolymerization is planar-aligned due to chemical interaction of the nematic molecules and the polymer molecules. The surface may be patterned by covering with an appropriate mask prior to exposure [fig. 5.1(a)]. Removal of the mask reveals a surface with regions that promote homeotropic and planar alignment [fig. 5.1(b)]. Repeated exposures may be used to further alter the easy axis and a convenient calculus, based on the tensor formulation of the anchoring energy, has been proposed to predict the easy axis and anchoring energy following repeated exposure. A second approach

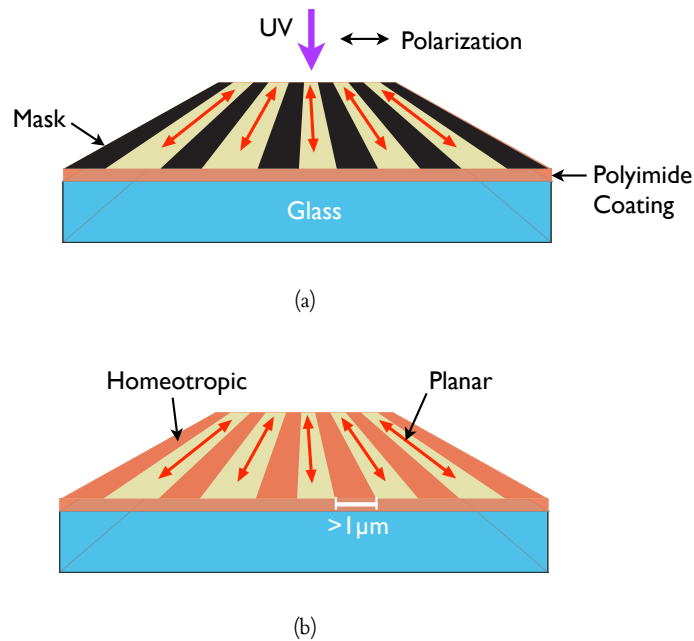


Figure 5.1: Production of a patterned surface using the photoalignment technique and an appropriate mask.

is to use polarization holography to develop a polarization grating on the photopolymerizable layer; the easy axis follows locally the polarization ellipse[111, 132].

Self Assembled Monolayers (SAMs) of a suitable compound such as an alkanethiol [ $\text{CH}_3(\text{CH}_2)_{n-1}\text{SH}$   $5 \leq n \leq 16$ ] may also be used to control the alignment of liquid crystals[36, 38]. An alkanethiol molecule consists of a hydrophobic head group ( $-\text{SH}$ ) and a long hydrocarbon tail; when the alkanethiol is deposited onto a clean uniform substrate coated with a thin ( $\sim 30\text{nm}$ ) layer of gold, the molecules self assemble to form a regular array where the head groups are attached to the gold. A SAM may promote either homeotropic, planar degenerate alignment or no particular alignment at all in an adjacent liquid crystal layer; the precise alignment depends on the length of the alkanethiol chain and also—a significant disadvantage—the particular nematic material. The methyl group on the end of the chain part of the alkanethiol molecule may be substituted with a functional group which may further alter the easy axis.

A patterned surface may be fabricated by *microcontact printing* of SAMs[37]: the production of a suitable stamp is analogous to the production of metal type: a negative is made by etching some clean, flat surface such as a silicon wafer; the stamp is then made by filling the negative with some polymer which is then thermally hardened. The stamp is then “inked” with the alkanethiol and then brought into contact with the substrate. Although good quality printing occurs only when the stamp is in conformal contact with the substrate, that surface need not be planar offering the possibility of patterning non-planar surfaces.

A further interesting development is the use of nanopatterning to create surfaces with multiple degenerate easy axes. Using the tip of an Atomic Force Microscope (AFM) in contact mode, trenches may be cut into a polyimide surface Wen et al. [115], Yoneya et al. [116]. One pattern is a checkerboard of squares[109, 133] [fig. 5.2(a)] with trenches that lie in orthogonal directions. The director above the surface, in a manner

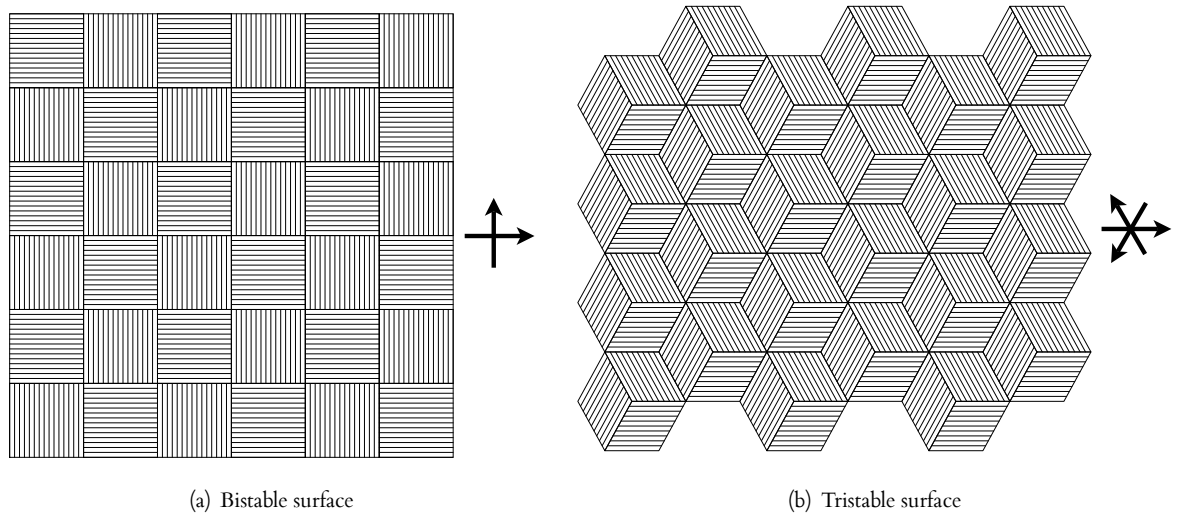


Figure 5.2: Nanopatterns inscribed with the stylus of an AFM. The dark arrows indicate the orientations that the director may align with in the bulk in each of the stable states.

analogous to the PABN, may lie parallel to the diagonal of the squares. A tristable surface fabricated in the same manner has also been demonstrated[110] where the surface is patterned with hexagons where the trenches lie in one of three different directions [fig. 5.2(b)]. Patterning at the nanometre scale causes significant variation of the magnitude of the nematic order parameter and indeed has been shown to suppress the isotropic–nematic phase transition[124].

### 5.3 Nematic in Contact with a Striped Surface

To find the director configuration in a particular device, a very common approximation is to assume that all three elastic constants are equal[3, 29], i.e. let  $K = K_1 = K_2 = K_3$ . If the director field is also constrained so that everywhere it is parallel to a single plane, the director may be parametrized by a single angle  $\theta$  and the Frank energy has a particularly simple form

$$F = \frac{K}{2} \int (\nabla\theta)^2 dV. \quad (5.1)$$

The Euler-Lagrange equation for  $\theta$  is then simply the Laplace equation

$$\nabla^2\theta = 0 \quad (5.2)$$

and any of the standard methods for its solution—conformal mapping, Fourier analysis, Green’s functions—may be used to derive an analytical solution for the director field subject to appropriate boundary conditions.

If the cell thickness is much greater than the period of the patterning, the penetration depth of the distorted region will be much smaller than the cell thickness and the director in the middle of the cell will be spatially

uniform. The director field in one half of the cell is then very nearly the same as that for a semi-infinite nematic in contact with a single surface and it is appropriate to solve that simpler problem instead. The free energy of the whole cell is then approximately twice the value of the semi-infinite case.

An appropriate choice of coordinate system for the semi-infinite nematic in contact with a single pair of stripes with periodic boundary conditions is to have the  $x$  coordinate along the surface and perpendicular to the length of the stripes and the  $z$  coordinate normal to the surface; it is convenient to scale both coordinates by the period of the pattern  $\lambda$ . The stripes alternately promote homeotropic and planar alignment and so the easy axis as a function of  $x$  may be written

$$\theta_e(x) = \begin{cases} \frac{\pi}{2} & 0 \leq x < a \\ 0 & a \leq x < 1 \end{cases}, \quad (5.3)$$

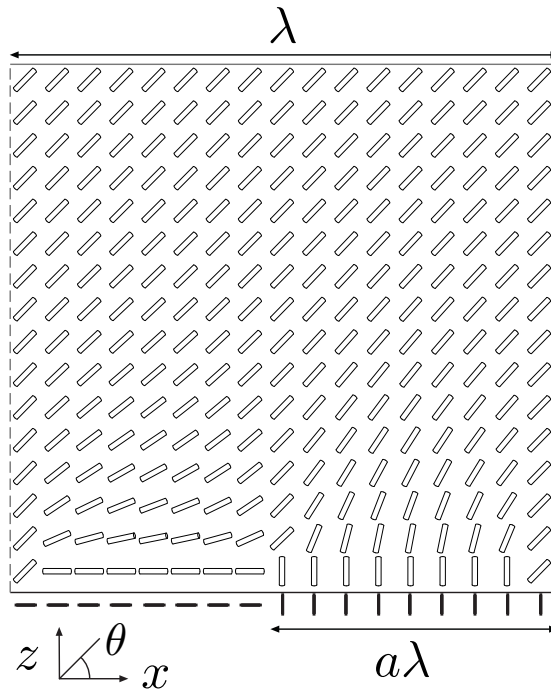
where  $a$  is the width, as a fraction of the period, of one homeotropic stripe. The azimuthal component of the director may be controlled by imposing an azimuthal easy axis at the planar stripe either by rubbing or photoalignment. Two particular choices are firstly that obtained by setting the azimuthal easy axis to be orthogonal to the length of the stripes, which will be referred to as a “splay-bend” surface [fig. 5.3(a)] and secondly where the azimuthal easy axis is parallel to the length of the stripes, referred to hereafter as a “twist” surface [fig. 5.3(b)].

Letting the angle  $\theta$  be the angle between the substrate and the local director, a general solution of Laplace’s equation for these configurations is a Fourier series where each harmonic component is multiplied by a decaying exponential

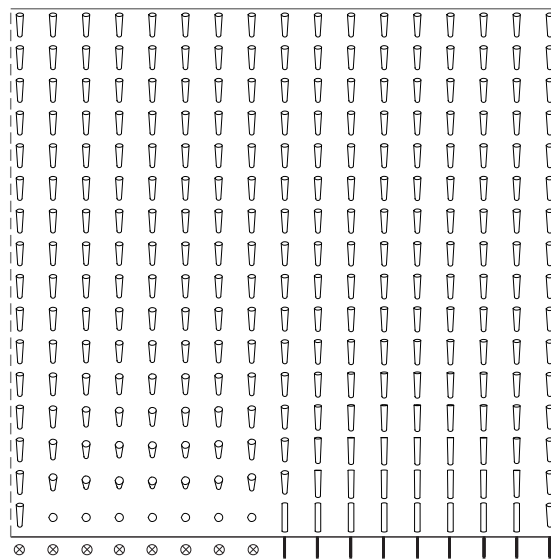
$$\theta(x, z) = \theta_0 + 2 \sum_{n=1}^{\infty} \exp(-2n\pi z) [p_n \sin(2n\pi x) + q_n \cos(2n\pi x)] \quad (5.4)$$

where  $\theta_0$  and the set of coefficients  $\{p_n\}$  and  $\{q_n\}$  are to be determined from the boundary conditions. The solution is regular as  $z \rightarrow \infty$  as required. Far away from the surface, the nematic adopts the  $\theta_0$ —the *effective easy axis*—which is simply the average value of  $\theta_e$  over the period  $\langle \theta_e \rangle = \pi a/2$ . In the next chapter, it will be shown by solving for the director field numerically that elastic anisotropy changes significantly the value of  $\theta_0$ . One may define a characteristic penetration depth  $L = \lambda/(2\pi)$  which is the depth at which the lowest harmonic—that vanishes slowest of all—has decayed to  $1/e$  of its amplitude at the surface  $z = 0$ . This quantity is useful to compare to the penetration depths  $L_\theta = W_\theta \lambda/K$  and  $L_\phi = W_\phi \lambda/K$  of polar and azimuthal anchoring respectively.

The splay-bend and other closely related configurations have attracted theoretical discussion previously and it is pertinent to review the principal conclusions. Barbero *et al.* [123] used a Fourier approach near to that outlined above to consider the uniform bulk orientation of a semi-infinite nematic promoted by a striped surface with alternate stripes of arbitrary easy axis and where the polar anchoring energies of the



(a) "Splay-Bend"



(b) "Twist"

Figure 5.3: Schematic of the director field  $\mathbf{n}(x, z)$  for a nematic with  $K_1 = K_2 = K_3$  in contact with a surface patterned with period  $\lambda$  and relative homeotropic stripe width  $a$ .



two stripes were also different. They also solved for the director field where the nematic was terminated at some distance above the first with a second substrate patterned so as to mirror the first.

Shortly afterwards, Evangelista and Barbero[120] estimated the effect of surface inhomogeneity on optical measurements of the polar anchoring energy by considering a similar surface with periodically varying easy axis and solving for the director field using the Green's functions. Extending their analysis to random fluctuations of the easy axis, they concluded that a strongly anchored surface with fluctuating easy axis was indistinguishable optically from a weakly anchored surface.

In a second paper[121], the same authors used a similar approach to elucidate the structure of the reorientation walls induced between a semi-infinite homeotropic surface and a semi-infinite planar surface both along the  $x$  axis, meeting at  $x = 0$  and with an identical surface some distance above the first. The director field for this structure may also in fact be obtained very easily using a conformal mapping as shown by Okano *et al.*[119], who also applied the technique to the situation of a surface with a finite region of planar anchoring surrounded by two semi-infinite regions of homeotropic anchoring; again with a second identical substrate above the first.

Returning to the splay-bend structure, Kondrat *et al.* [118] identified that, if the polar anchoring energy on either stripe were sufficiently weak, it would be feasible for the nematic to adopt a spatially uniform configuration rather than the distorted one; the nematic in this case effectively ignores the stripes with weaker anchoring energy. Using the Green's functions to reduce the two-dimensional problem of the director field to a one-dimensional boundary value problem which they solved numerically, they calculated phase diagrams for the transition; this feat was necessary because, unlike Barbero and Evangelista, they chose to use the full Rapini-Papoular anchoring potential. Their results are discussed further, and more complete phase diagrams presented, in section 5.5. Finally, a recent paper on the splay-bend structure by Yednak *et al.*[122] extended the analytical solution of Evangelista and Barbero to include the effect of an applied electric field.

All previous theoretical work on striped patterned surfaces has taken place within the one-constant approximation. If the elastic constants are different, certain configurations of the nematic that were previously degenerate in the one-constant approximation may no longer be degenerate. This is a possible source of frustration if the surface treatment prefers one configuration while some other configuration is preferred by the elastic forces due to anisotropy of the elastic constants; the precise configuration adopted by the nematic then depends critically on the system parameters. The rest of this chapter shall explore the possibility of frustration in nematics in contact with striped surfaces.

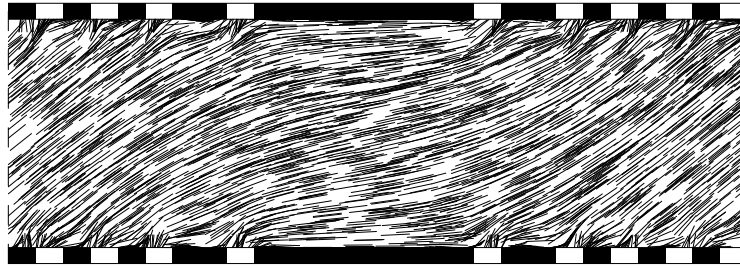


Figure 5.4: Schematic of a liquid crystal cell constructed from patterned substrates with stripes of different width; the black regions on the substrates promote planar alignment and the white stripes promote homeotropic alignment.

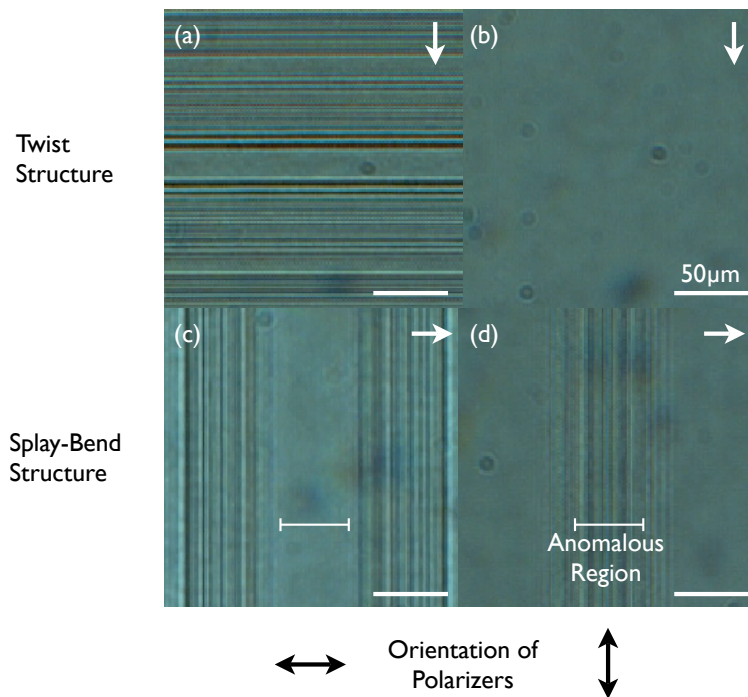


Figure 5.5: Polarizing microscopy images of “splay-bend” and “twist” structures with aligned polarizers in different orientations. White arrows represent the wavevector of the patterning. (Images reproduced with the kind permission of Dr N. J. Smith)

## 5.4 Anomalous Behaviour of Splay-Bend Structures at Short Wavelength

### 5.4.1 Experiment

*The devices in this section were built and the microscope images taken by Dr Nathan Smith and Catherine Raptis of Sharp Laboratories of Europe.*

A natural extension of the splay-bend and twist structure, which are periodic pairs of adjacent stripes, is to vary the width of the stripes slowly along the surface as shown in figure 5.4. The director in the centre of the cell varies along the direction orthogonal to the length of the stripes. If such a cell is examined in transmission with a polarizing microscope with parallel polarizers, then when the polarization axis of the incident light is coplanar with the director interference fringes are observed due to the effective refractive

index contrast caused by the varying director field. These fringes are reminiscent of Newton's rings which may be observed with a plano-convex lens. If the cell is rotated between the polarizers, the fringes fade until, when the director is orthogonal to the polarizer, they disappear completely as in this orientation there is no dielectric contrast.

Cells of a design based on that depicted in figure 5.4—which are designed to act as a Graded Index Nematic (GRIN) lens[134, 135]—were constructed in both splay-bend and twist types, i.e. where the azimuthal easy axis on the planar stripes lay orthogonal to, or along the length of the stripes respectively. The overall pattern was periodic of wavelength  $200\mu\text{m}$  and the cell was  $25\mu\text{m}$  thick with identical patterns on either substrate and with the patterns were aligned so as to be in phase; the large planar region in the centre was  $60\mu\text{m}$  wide and the narrowest planar and homeotropic stripes were each  $2\mu\text{m}$  in a region of identically sized stripes  $40\mu\text{m}$  wide. The cells were filled with E7.

The twist cell appears as expected under the microscope: the director is everywhere orthogonal to the wavevector of the pattern and so the fringes are observed when the polarizer axes lie along the length of the stripes [fig. 5.5(a)]; no fringes are observed in the perpendicular orientation [fig. 5.5(b)]. The splay-bend cell is anomalous: In certain regions, where the stripe width is large ( $> 10\mu\text{m}$ ), the fringes are observed as expected when the polarizer axes are parallel to the wavevector of the stripes and hence the director lies in this direction [fig. 5.5(c)]; they disappear as anticipated in the orthogonal orientation [fig. 5.5(d)]. In other regions, where the width of each stripe is about  $2\mu\text{m}$ , the opposite behaviour is observed and there are no fringes when the polarizer axes are parallel to the wavevector of the pattern. Instead fringes *are* observed when the polarizer axes are parallel to the length of the stripes [fig. 5.5(d)]. The director in these regions has, therefore, apparently twisted round so as to lie along the length of the stripes: the director in the splay-bend structure has spontaneously adopted the twist configuration!

#### 5.4.2 Model

To understand the physical origin of this anomalous behaviour, it is suggestive to compare the free energy density of the splay-bend configuration

$$f_{SB} = \frac{K_1}{2} \left( \frac{\partial\theta}{\partial x} \sin\theta - \frac{\partial\theta}{\partial z} \cos\theta \right)^2 + \frac{K_3}{2} \left( \frac{\partial\theta}{\partial x} \cos\theta + \frac{\partial\theta}{\partial z} \sin\theta \right)^2 \quad (5.5)$$

to that of the twist configuration

$$f_{TW} = \frac{K_2}{2} \left( \frac{\partial\theta}{\partial x} \right)^2 + \frac{1}{4} (K_1 + K_3 + (K_1 - K_3) \cos 2\theta) \left( \frac{\partial\theta}{\partial z} \right)^2. \quad (5.6)$$

In the splay-bend case, derivatives of the director field with respect to both coordinates appear in both the splay and bend terms; the fact that no twist distortion is present in this configuration justifies the label "splay-bend". In the twist case, the derivative of  $\theta$  with respect to the  $x$  coordinate appears only in the

twist term and the derivative of  $\theta$  with respect to  $z$  appears only in the splay and bend terms. One might suppose that in the twist configuration, if  $K_2$  were different to  $K_1$  and  $K_3$ , the nematic ought to extend or reduce the penetration depth of elastic distortion accordingly so as to minimize the free energy. It appears from (5.5) and (5.6) that adjusting the relative strength of the splay and bend elastic constants should not produce a similar effect as derivatives of the director field are not decoupled in this way.

It is at least plausible then, that if  $K_2$  is different from  $K_1$  and  $K_3$ , then the splay-bend and twist configurations will no longer be energetically degenerate in the bulk; it remains to show this explicitly. The free energies (5.5) and (5.6) contain no transcendental functions of  $\theta$  if the simplifying assumption  $K_1 = K_3$  is made; for most nematic materials  $K_2 < K_1 \leq K_3$ . If the director is confined to a plane orthogonal to the plane of the substrate that makes an angle  $\phi$  with the wavevector of the pattern, the free energy density is

$$f/K_1 = \frac{1}{2} \left[ \kappa \left( \frac{\partial \theta}{\partial x} \right)^2 + \left( \frac{\partial \theta}{\partial z} \right)^2 \right] \quad (5.7)$$

where  $\kappa = [1 - (1 - \tau) \sin^2 \phi]$  and  $\tau = K_2/K_1$ . The Euler-Lagrange equation

$$\kappa \frac{\partial^2 \theta}{\partial x^2} + \frac{\partial^2 \theta}{\partial z^2} = 0 \quad (5.8)$$

is the Laplace equation following an anisotropic scale change. The Fourier series solution (5.4) gains a coefficient  $\sqrt{\kappa}$  in the exponent

$$\theta(x, z) = \theta_0 + 2 \sum_{n=1}^{\infty} \exp(-2n\pi\sqrt{\kappa}z) [p_n \sin(2n\pi x) + q_n \cos(2n\pi x)] \quad (5.9)$$

and so the characteristic penetration depth is modified to  $L = \lambda/(2\pi\sqrt{\kappa})$ . The coefficients  $\{p_n\}$  and  $\{q_n\}$  remain to be determined from the boundary conditions at the surface. Substituting (5.9) into (5.7) and integrating over  $x$  and  $z$  yields the bulk free energy per period

$$F_b/K_1 = 4\pi\sqrt{\kappa} \sum_{n=1}^{\infty} n(p_n^2 + q_n^2). \quad (5.10)$$

If the Fourier coefficients are nearly independent of  $\tau$ , as will be shown below, and  $K_2 < K_1$ , (5.10) has a minimum at  $\phi = \pi/2$ , which corresponds to the twist geometry, and a maximum at  $\phi = 0$  which corresponds to the splay-bend geometry; for  $K_2 > K_1$  the situation is reversed. The energy of a nematic in contact with each of the two configurations differs by a factor of  $1 - \sqrt{\tau}$ . It is possible then for a nematic with  $K_2 < K_1$  in contact with a splay-bend surface to spontaneously “twist out” to adopt the twist structure if the azimuthal anchoring is sufficiently weak. Conversely, a nematic with  $K_2 > K_1$  in contact with a twist surface may spontaneously adopt the splay-bend configuration. The energy cost at

the surface in both cases due to the azimuthal surface anchoring is

$$\begin{aligned} F_{s\phi} &= \frac{W_\phi \lambda}{2} \int_a^1 \sin^2(\phi - \phi_e) dx \\ &= \frac{W_\phi \lambda}{2} (1 - a) \end{aligned} \quad (5.11)$$

since  $\phi - \phi_e = \pi/2$ ; a criterion for the feasibility of the transition is in both cases that the energy difference between the two configurations in the bulk is greater than the energy cost at the surface

$$K_1 |F_{SB}(a, \lambda) - F_{TW}(a, \lambda, \tau)| > W_\phi \lambda (1 - a). \quad (5.12)$$

In the following sections, (5.12) shall be evaluated explicitly by solving for the Fourier coefficients from first a rigid polar anchoring boundary condition and second a weak polar anchoring boundary condition.

Neither the twist nor splay-bend configuration (depending on the ratio  $K_2/K_1$ ) necessarily represents the absolute energy minimum due to the assumption that the director is constrained to lie parallel to a single plane. It is conceivable that the energy may be reduced further by a periodic modulation of  $\phi$  that vanishes away from the surface. Spontaneous twist modulations that occur in other liquid crystal systems were listed in the previous chapter [87, 136] but they require very anisotropic elastic constants ( $K_2/K_1 < 0.3$ ) or submicron cell thickness. If only common nematic materials are considered, the amplitude of such a modulation in  $\phi$  will necessarily be very small and so (5.10) remains a good estimate of the free energy. If the elastic constants are very anisotropic, the possibility of a modulation in  $\phi$  might be explored by a variational method [136] or numerical solution of the Euler-Lagrange equations.

#### 5.4.2.1 Rigid Polar Anchoring

For most alignment techniques,  $W_\theta \gg W_\phi$  and as a first approximation, it may be assumed that  $\theta$  is fixed along the surface  $\theta(x, z) = \theta_e(x)$ . The constant  $\theta_0$  is simply the average value  $\langle \theta_e(x) \rangle = \pi a/2$  and the coefficients  $p_n$  and  $q_n$  are the coefficients in the Fourier expansion of  $\theta_e(x)$

$$p_n = \frac{\sin^2(na\pi)}{2n}, \quad q_n = \frac{\sin(2na\pi)}{4n}. \quad (5.13)$$

The associated bulk free energy

$$F_b/K_1 = \pi \sqrt{\kappa} \sum_{n=1}^{\infty} \frac{\sin(na\pi)^2}{n} \quad (5.14)$$

does not converge due to the poles in  $\nabla\theta$  at  $(x, z) = (0, 0)$  and  $(a, 0)$  which, in this rigid anchoring model, are disclination lines.

To deal with similar cases, others have postulated that above a certain magnitude of  $\nabla\theta$ , the nematic “melts” leaving a small isotropic region at the core of the disclination. Assuming that the core energy of the disclinations is independent of  $\tau$ , a cut-off radius  $r_c$  (a typical value is  $10^{-8}$  m [3]) may be defined

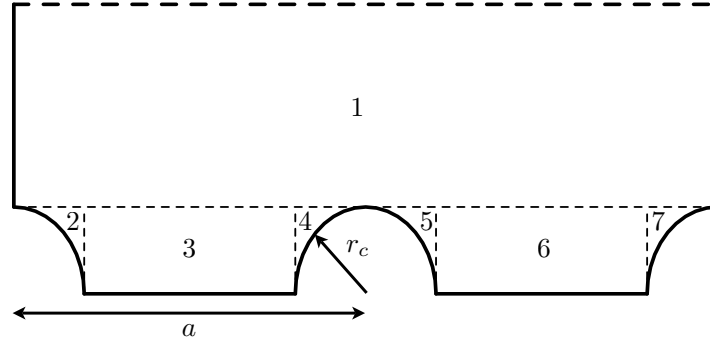


Figure 5.6: Numerical integration of the free energy density over the region excluding the two defects is achieved by dividing the domain into seven regions.

below which the elastic theory breaks down. The series solution for  $\theta(x, z)$  is everywhere convergent; substituting (5.13) into (5.9) and evaluating the sum gives

$$\theta(x, z) = \frac{a\pi}{2} + \frac{1}{4}i \ln \left[ \frac{(1 - R_-)(1 - AR_+^{-1})}{(1 - R_+^{-1})(1 - A^{-1}R_-)} \right] \quad (5.15)$$

where  $A = \exp(2i\pi a)$  and  $R_{\pm} = \exp[2i\pi(x \pm z\sqrt{\kappa})]$ . Substituting (5.15) into (5.7) yields an explicit expression for the free energy density

$$\frac{f}{K_1} = \frac{\pi^2}{4(XZ)^4} \left[ \frac{(XZ)^6(A-1)^2(A-X^2)^2(Z-1)^2}{(AX - A^2Z - X^2Z + AXZ^2)} - \left( \frac{1}{1-XZ} + \frac{A}{XZ-A} + \frac{X}{Z-X} + \frac{X}{X-AZ} \right)^2 \right] \quad (5.16)$$

where  $X = \exp(2i\pi x)$  and  $Z = \exp(2i\pi z\sqrt{\kappa})$ . This expression is locally convergent except at the poles and may therefore be integrated numerically over  $x$  and  $z$  excluding the two semicircles around the disclinations defined by  $x^2 + z^2 < r_c^2$  and  $(x-a)^2 + z^2 < r_c^2$ . The appropriate division of this domain into suitable regions of integration is illustrated in figure 5.6.

The azimuthal anchoring energy which just satisfies (5.12) for the splay-bend to twist transition is plotted in fig. 5.7 as a function of  $a$  for several values of  $\tau$ . An equivalent plot for the twist to splay-bend transition may be obtained by relabelling  $K_2/K_1 \rightarrow K_1/K_2$ . A second plot of  $W_{\phi_{critical}}$  with respect to  $\lambda$  shows that reducing the period also favours the transition (Fig. 5.8). If the period is short,  $a$  may be restricted in fabrication as the minimum width of a stripe developed with a mask is  $\approx 1\mu\text{m}$ . The calculated  $W_{\phi_{critical}}$  with is similar to that obtained experimentally for obliquely evaporated silicon oxide ( $W_{\phi} = 2.9 \times 10^{-6}\text{Jm}^{-2}$  [52]) and photoaligned polymer films ( $W_{\phi} < 1 \times 10^{-6}\text{Jm}^{-2}$  [137]) and so one might expect to observe the transition with these surface treatments; somewhat larger values of  $W_{\phi}$  ( $2.3 \times 10^{-5}\text{Jm}^{-2}$  [49]) are measured for rubbed polyimide films and so one would not expect to observed the transition on such a surface.

In a physical system, no fine boundary will exist between the stripes due, for example, to weak polar anchoring (which is considered below), misregistration in fabrication and order parameter reduction. The

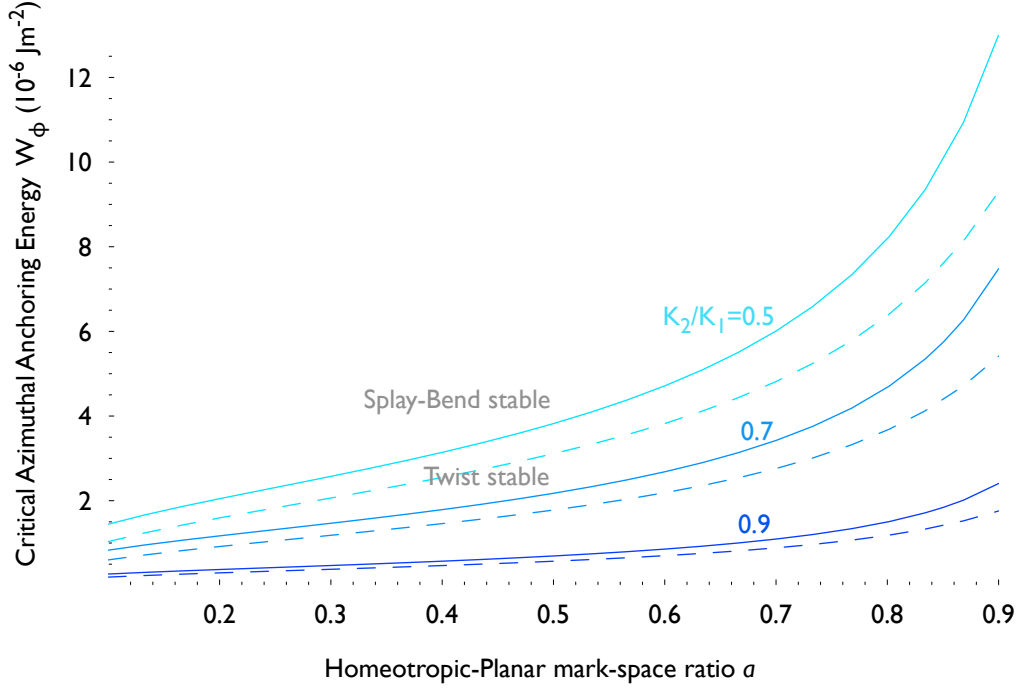


Figure 5.7: Critical azimuthal anchoring energy as a function of  $a$  for  $\lambda = 10\mu\text{m}$ ,  $K_1 = 1 \times 10^{-11}\text{N}$  and with rigid polar anchoring. Solid lines were computed with  $r_c = 10^{-8}\text{m}$  and dashed lines with  $r_c = 5 \times 10^{-8}\text{m}$ . Note that a transition from splay-bend to twist is feasible if  $W_\phi < W_{\phi\text{critical}}$ .

latter effects are tantamount to changing the defect radius  $r_c$  and in fig. 5.7 the results of the calculation with  $r_c = 5 \times 10^{-8}\text{m}$  are plotted; the effect on  $W_{\phi\text{critical}}$  is not sufficient to alter the conclusion that the transition is feasible with experimentally realistic values of  $W_\phi$ .

#### 5.4.2.2 Finite Anchoring

Next, consider the situation where  $\theta$  is allowed to vary at the surface with the simplifying approximation that the azimuthal part of the anchoring energy has no functional dependence on  $\theta$  other than that which removes the azimuthal contribution where the director is homeotropic. For the purposes of studying the possibility of a splay-bend structure spontaneously adopting the twist configuration, this approximation tends to an overestimate of the energy of the twist configuration: it ignores a slight reduction in the azimuthal anchoring energy as the director ‘peels away’ from the surface near the homeotropic-planar boundaries. Furthermore, attention is restricted to the situation where the polar anchoring energy is the same for both homeotropic and planar regions; it is likely that this is the case for patterns produced by some masking process where a single material is responsible for the anchoring.

The coefficients  $\{p_n\}$  and  $\{q_n\}$  are obtained by substituting (5.9) evaluated at  $z = 0$  into the weak anchoring boundary condition (1.22) with a suitable anchoring potential. An independent equation for each coefficient may be obtained by multiplying each side by  $\sin(2m\pi x)$  or  $\cos(2m\pi x)$  where  $m$  is an arbitrary positive nonzero integer and integrating, exploiting the orthogonality of the sine and cosine functions. This procedure is incompatible with the Rapini-Papoular potential:  $\theta - \theta_e$  appears in the argument of a

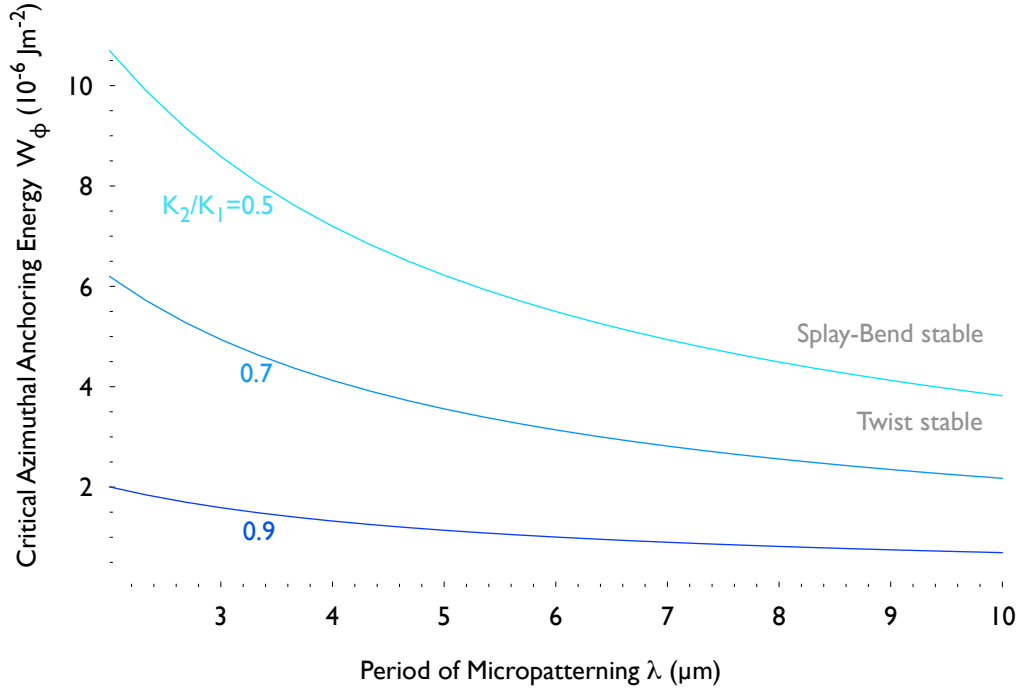


Figure 5.8: Critical azimuthal anchoring energy as a function of  $\lambda$  with rigid anchoring for  $a = 0.5$ ,  $r_c = 10^{-8}m$  and  $K_1 = 1 \times 10^{-11}N$ .

transcendental function and so it is not possible to evaluate the coefficients independently. Instead, the harmonic potential  $W_\theta(\theta - \theta_e)^2/2$ , which is of course equivalent to the Rapini-Papoular potential if  $\theta - \theta_e$  is small, may be used.

The boundary condition (1.22) for the harmonic potential is then explicitly

$$\left[ \frac{\partial \theta}{\partial z} - 2 \frac{1}{L_\theta} (\theta - \theta_e) \right]_{z=0} = 0, \quad (5.17)$$

where  $L_\theta = K_1/(W_\theta \lambda)$  is the penetration depth associated with polar anchoring due to the surface treatment (note that  $L_\theta \ll L$ ). Substituting (5.9) into (5.17) and following the procedure described in the previous paragraph, the Fourier coefficients are obtained

$$p_n = \frac{\sin^2(na\pi)}{2n(1 + 2nL_\theta\pi\sqrt{\kappa})}, \quad q_n = \frac{\sin(2na\pi)}{4n(1 + 2nL_\theta\pi\sqrt{\kappa})} \quad (5.18)$$

and the associated bulk free energy,

$$F_b = \pi\sqrt{\kappa} \sum_{n=1}^{\infty} \frac{\sin(na\pi)^2}{n^2(1 + 2L_\theta n\pi\sqrt{\kappa})}, \quad (5.19)$$

is convergent. It is also necessary to include in  $F_{SB}$  and  $F_{TW}$  the contribution to the free energy due to the polar surface anchoring term. Splitting the director field  $\theta(x, z)$  into the constant part  $\theta_0$  and the series



part  $\Theta$  so that  $\theta(x, 0) = \theta_0 + \Theta(x)$ , the surface energy may be expanded

$$\begin{aligned} F_{s\theta} &= \frac{W_\theta}{2} \int_0^1 [(\theta_0 - \theta_e(x)) + \Theta(x)]^2 dx \\ &= \frac{W_\theta}{2} \int_0^1 (\theta_0 - \theta_e(x))^2 + 2(\theta_0 - \theta_e)\Theta + \Theta^2 dx \end{aligned} \quad (5.20)$$

and integrated term by term

$$\begin{aligned} F_{s\theta} &= \frac{W_\theta}{2} \left[ \frac{\pi^2}{4} a(1-a) + 2 \sum_n (p_n^2 + q_n^2) + \right. \\ &\quad \left. + \sum_n \frac{1}{n} \{ p_n [a - 1 - a \cos(2n\pi) + \cos(2an\pi)] + q_n [a \sin(2n\pi) - \sin(2an\pi)] \} \right] \end{aligned} \quad (5.21)$$

Inserting the Fourier coefficients which were obtained from the boundary conditions yields

$$\begin{aligned} F_{s\theta} &= \frac{W_\theta}{2} \left[ \frac{\pi^2}{4} a(1-a) + \sum_n \frac{\sin(na\pi)}{2n^2(1+2nL_\theta\pi\sqrt{\kappa})^2} \left( \sin(na\pi) [a - 1 + (a-2)2L_\theta n\pi\sqrt{\kappa}] - \right. \right. \\ &\quad \left. \left. - a(1+2nL_\theta\pi\sqrt{\kappa}) \sin[(a-2)n\pi] \right) \right] \end{aligned} \quad (5.22)$$

and together with (5.19) may be used to evaluate the critical azimuthal anchoring energy directly.

Quantitatively identical results for  $W_{\phi_{critical}}$  as a function of  $a$  and  $\lambda$  to those calculated from the rigid anchoring model are obtained for  $W_\theta = 1 \times 10^{-4} \text{Jm}^{-2}$  [47] and  $W_{\phi_{critical}}$  grows logarithmically with  $W_\theta$  (Fig. 5.9). Increasing the polar anchoring strength in the weak polar anchoring model has an identical effect to reducing the defect core radius  $r_c$  in the strong anchoring model. This is physically compelling as the energy difference between the splay-bend and twist states must depend on how well the surface treatment is able to maintain the large distortion of the director field around the boundary between adjacent stripes.

## 5.5 Uniform–Distorted Transition due to Weak Polar Anchoring

As recognized by Kondrat *et al.* [118], the inclusion of weak polar anchoring into the model permits the possibility that the nematic may adopt a spatially uniform state if the polar anchoring energy of either the planar or homeotropic stripes is sufficiently lower than that of the other set. In fact it shall be shown in this section that this is also true if one of the stripes is much narrower than the other, i.e. as  $a \rightarrow 0$  or  $a \rightarrow 1$  even if the polar anchoring energies are the same.

The energy of the distorted state has already been calculated; it is the sum of the bulk energy (5.19), the surface energy due to polar anchoring (5.22) and a contribution from the azimuthal anchoring energy

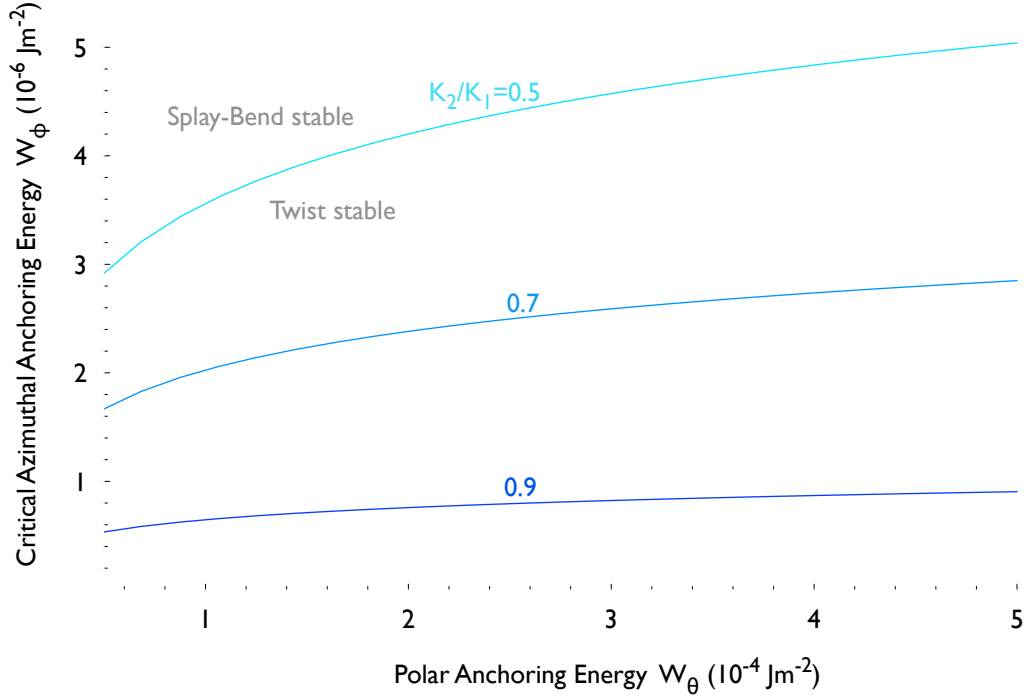


Figure 5.9: Critical azimuthal anchoring energy as a function of the polar anchoring energy  $W_\theta$  for  $a = 0.5$ ,  $\lambda = 10\mu\text{m}$  and  $K_1 = 1 \times 10^{-11}\text{N}$ .

(5.11) if the planar regions are nondegenerate. The energy of the uniform state is simply a contribution from the polar anchoring energy, which is for a uniform homeotropic state

$$\begin{aligned} F_{s\theta T} &= \frac{W_\theta \lambda}{2} \int_a^1 \sin^2(\pi/2) dx \\ &= \frac{W_\theta \lambda}{2} (1 - a) \end{aligned} \quad (5.23)$$

and analogously for a uniform planar state

$$F_{s\theta P} = \frac{W_\theta \lambda}{2} a. \quad (5.24)$$

In both cases, it is assumed that the Rapini-Papoular potential is valid for deviations of  $\pi/2$  from the easy axis; if this is not so then an alternative anchoring potential must be used (see section 1.3) and the  $W_\theta$  in (5.23) and (5.24) appropriately rescaled.

Phase diagrams in the  $\tau, a$  plane are plotted in figure 5.10 showing the regions of stability for the uniform planar, uniform homeotropic, twist and splay-bend configurations of a semi-infinite nematic in contact with a surface constructed with the azimuthal easy axis parallel to the wavevector of the pattern (which “naturally”, in the limit of rigid polar and azimuthal anchoring, would promote the splay-bend configuration). The critical lines are plotted for several values of the penetration depth associated with polar anchoring  $L_\theta$  [fig. 5.10(a)] and several values of the penetration depth associated with azimuthal anchoring  $L_\phi$  [fig. 5.10(b)]. To put the values into context, for a cell with period  $5\mu\text{m}$  and  $K_1 = 1 \times 10^{-11}\text{N}$ ,

a typical value of  $L_\theta$  is 0.02 which corresponds to  $W_\theta = 1 \times 10^{-4} \text{Jm}^{-2}$  and for azimuthal anchoring energies in the interval  $1 \times 10^{-6} < W_\phi < 1 \times 10^{-5} \text{Jm}^{-2}$ ,  $2 > L_\phi > 0.2$ .

For  $a$  sufficiently small or close to 1, a uniform configuration is favoured. The critical lines for the splay-bend—uniform transition are vertical as the energy of the splay-bend configuration is of course independent of  $\tau$ ; the width of the region of stability for the twist configuration increases as  $\tau$  decreases. There is at least one and potentially two tricritical points on the phase diagrams where the uniform planar, splay-bend and twist configurations and the uniform homeotropic, splay bend and twist configurations become degenerate. As  $L_\theta$  increases, i.e. if the period or the polar anchoring energy decrease or if the elastic constants increase, the region of stability of the uniform configuration widens. The principal effect of altering  $L_\phi$ , on the other hand, is to alter the position of the splay-bend—twist critical line.

An important consequence of the calculations presented is that while for  $\lambda = 10\mu\text{m}$  the critical  $a$  for the uniform region are very close to 0 or 1 (corresponding to a physical stripe width of about  $0.5\mu\text{m}$ ), for  $\lambda = 2\mu\text{m}$ , the critical  $a$  are much larger, nearly 0.3 and 0.7 (again about  $0.5\mu\text{m}$ ). If  $\lambda$  is reduced much further, or  $W_\theta$  were reduced (this might be done to preclude the splay-bend to twist transition), then the nematic will never adopt a distorted configuration and will always adopt the uniform state. The uniform texture was not observed in the structure described in section 5.4.1 as  $a = 0.5$  in that case.

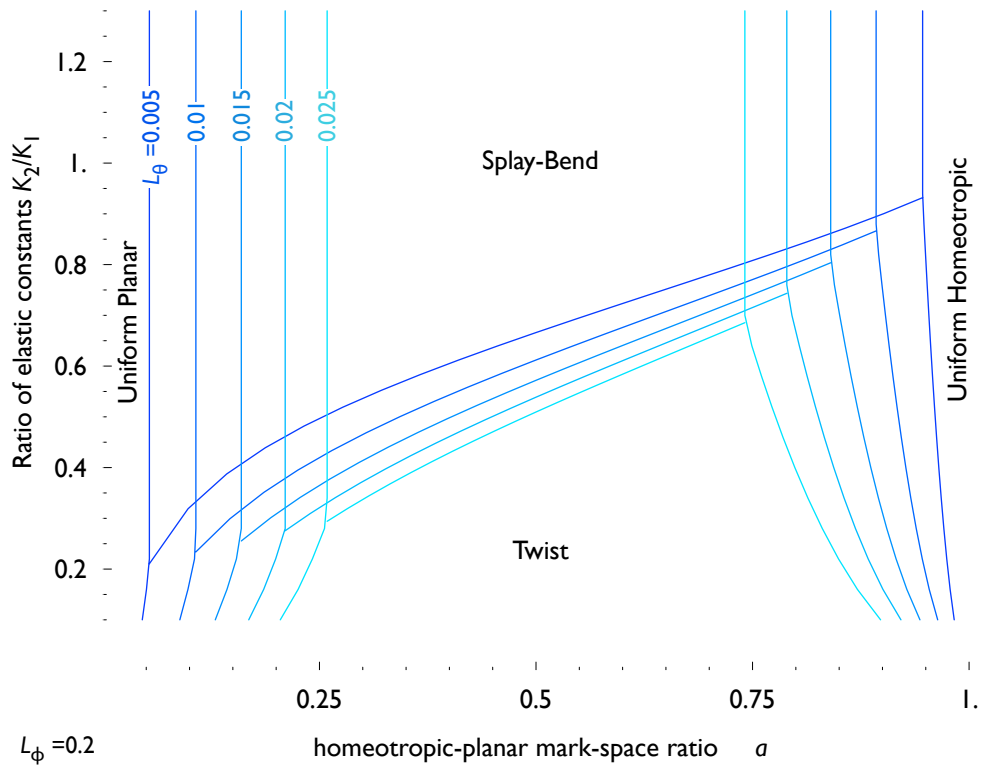
## 5.6 Switchable Diffraction Gratings

A recently demonstrated application of patterned surfaces is to create switchable diffraction gratings[132, 138, 139]; with the photoalignment technique a simple design is to pattern the substrate with stripes that promote planar alignment where the easy axis in one stripe lies parallel to the  $x$ -axis and in the adjacent stripe parallel to the  $y$ -axis. It has been proposed that a viable display might be built from a switchable diffraction grating that would not require two crossed polarizers and hence would benefit from reduced power consumption[139].

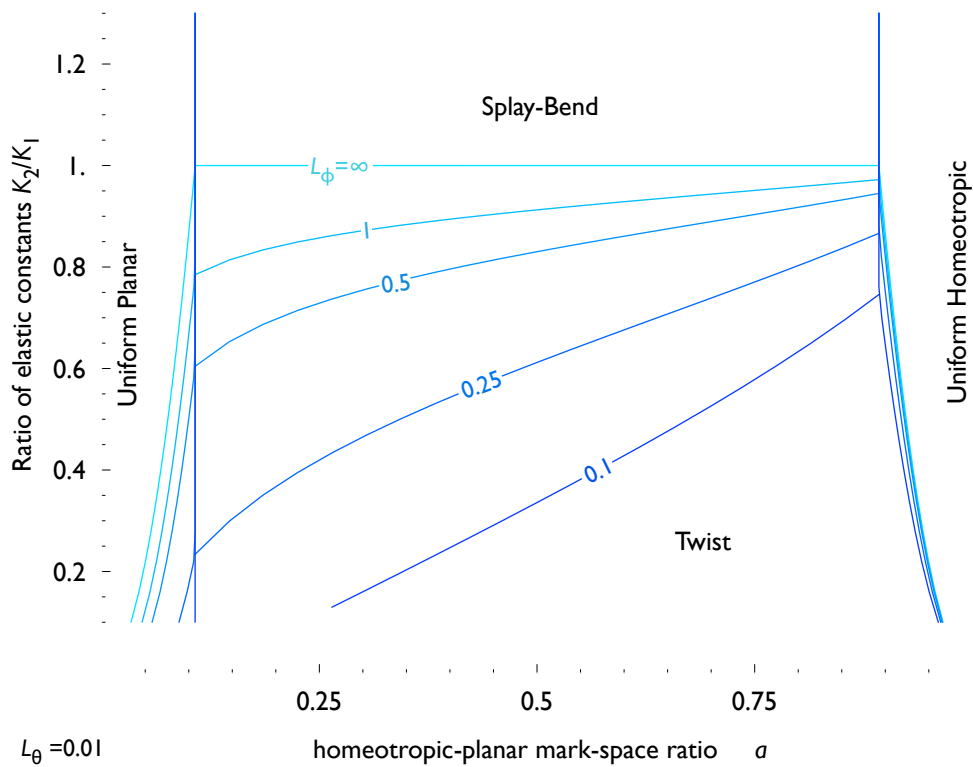
With no applied field, the director lies everywhere parallel to the  $x - y$  plane and follows the surface pattern. Incident light polarized along the wavevector of the pattern diffracts due to the refractive index contrast; the cell is constructed of thickness comparable to the wavelength of the pattern so that the director in the central region still varies appreciably and it is essential that patterns on either surface are exactly in phase. When an electric field is applied, the director becomes everywhere homeotropic except very near the surface and the cell no longer diffracts.

In such a cell when there is no applied field  $\theta = 0$  and it is the azimuthal director component  $\phi$  that varies spatially. The bulk free energy in the two constant approximation  $K_1 = K_3 \neq K_2$  adopted earlier is

$$f/K_1 = \frac{1}{2} \left[ \left( \frac{\partial \phi}{\partial x} \right)^2 + \tau \left( \frac{\partial \phi}{\partial z} \right)^2 \right] \quad (5.25)$$



(a)



(b)

Figure 5.10: Phase diagram showing the regions of stability of the uniform homeotropic (UT), uniform planar (UP), splay bend and twist configurations for a semi-infinite nematic in contact with a splay-bend type surface. Critical lines for several values of the penetration depths associated with (a) polar and (b) azimuthal anchoring are shown.

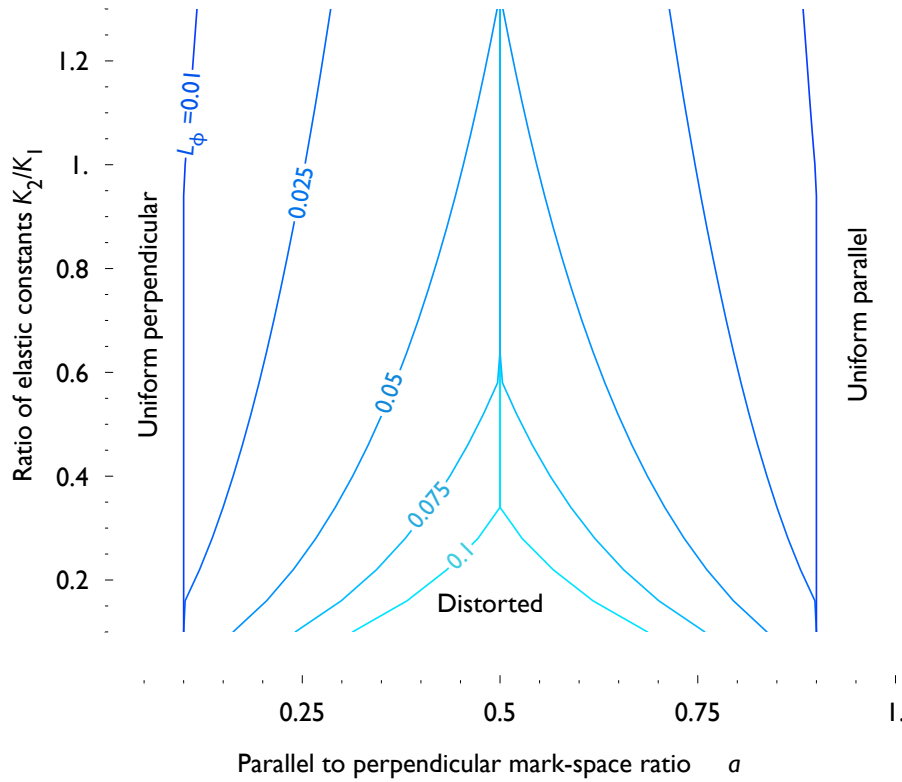


Figure 5.11: Phase diagram showing the regions of stability of uniform states parallel to ( $U_{\parallel}$ ) and perpendicular to ( $U_{\perp}$ ) the length of the stripes as well as the distorted configuration for a semi-infinite nematic in contact with a striped surface with planar stripes of antagonistic azimuthal easy axis. Critical lines for several values of the penetration depths associated with azimuthal anchoring are shown.

and notably differs from that of the twist structure as the ratio  $\tau$  of elastic constants is in front of the  $z$  term. The penetration length of the distorted surface region that follows the pattern therefore *increases* as  $\tau$  is lowered, implying that greater refractive index contrast may be achieved by using a material with low  $K_2$ .

Let  $a$  be the width of the stripe with azimuthal orientation parallel to the length of the stripes. Then, for  $a$  sufficiently small or close to 1 and if the azimuthal anchoring is weak, the diffraction grating cell should adopt a spatially uniform state where the director lies either parallel to or perpendicular to the length of the stripes. The model developed above is not strictly applicable as the cell thickness of the diffraction grating is typically comparable to the period of the stripes, some qualitative agreement may nonetheless be expected.

The energy of the uniform-parallel state is precisely that of (5.23) following the substitution  $W_{\theta} \rightarrow W_{\phi}$ ; the uniform-perpendicular state has energy (5.24) following a similar substitution. The energy of the diffracting state is that of the twist state (the sum of (5.19) and (5.22)) following  $W_{\theta} \rightarrow W_{\phi}$ ; there is no need to invert the ratio of the elastic constants  $\tau$ . A phase diagram showing the critical lines for typical values of the penetration length associated with azimuthal anchoring  $L_{\phi}$  is plotted in figure 5.11.

For some high values of  $L_{\phi}$ —low wavelength or very weak azimuthal anchoring—the model predicts that the distorted state is never stable and a uniform state always has lower energy. In such a case, is it true

then that when the mark-space ratio  $a$  is varied, only the uniform parallel and uniform perpendicular states represent energetic minima? It may be that for values  $a$  around 0.5, a configuration with  $0 < \phi_0 < \pi/2$  might become the ground state. This very much depends on the functional form of the anchoring potential. The energy of an intermediate state for some arbitrary anchoring potential  $g[\phi_0 - \phi_e(x)]$  is for the striped substrate

$$\begin{aligned} F_U/K_1 &= \int_0^a g(\phi_0 - \pi/2) dx + \int_a^1 g(\phi_0 - 0) dx \\ &= g(\phi_0 - \pi/2)a + g(\phi_0)(1 - a) \end{aligned}$$

which is minimized when

$$\frac{dg(\phi_0 - \pi/2)}{d\phi_0}a + \frac{dg(\phi_0)}{d\phi_0}(1 - a) = 0.$$

For the harmonic potential,  $g(\alpha) = \alpha^2/2$  the  $\phi_0$  varies continuously with  $a$ ,  $\phi_0 = a\pi/2$ . For the Rapini-Papoular potential  $g(\alpha) = \sin^2(\alpha)/2$  and only the uniform perpendicular  $\phi_0 = 0$  or uniform parallel  $\phi_0 = \pi/2$  states represent minima.

For the successful production of a device, the distorted state is necessary and, although the above calculation is at best an estimate of the minimum azimuthal anchoring energy needed to sustain the elastic deformation, the predicted minimum energy is similar to that of photoaligned polymers; it is conceivable that it might not be possible to manufacture the diffraction grating at all with some photopolymerizable materials. One solution is to eliminate the fine boundary between the two orientations and to have the easy axis rotate continuously; this might be manufactured for example by using a graduated mask with translucent regions or polarization holography [132, 111]. Suppose the easy axis varies sinusoidally,

$$\phi_e = \frac{\pi}{4} [1 + \sin(2\pi x)],$$

the director profile is

$$\phi(x, z) = \frac{\pi}{4} [1 + \sin(2\pi x) \exp(-2\pi z/\sqrt{\tau})]$$

and the associated energy is

$$F_b/K_1 = \frac{\pi^3}{32} \sqrt{\tau}.$$

The energy of a uniform state with constant  $\phi = \phi_0$  is simply the surface energy

$$F_s/K_1 = \frac{1}{2L_\phi} \int_0^1 \sin \left\{ \frac{\pi}{4} [1 + \sin(2\pi x)] - \phi_0 \right\}^2 dx$$

which is minimized when  $\phi_0 = \pi/4$  and  $F_s/K_1 \approx 1/(8L_\phi)$ . The critical  $L_\phi$  for the transition is then

$$L_{\phi c} = \frac{4}{\pi^3 \sqrt{\tau}}$$

which for common nematic materials where  $0.5 < \tau < 1$  lies in the interval  $0.1 < L_{\phi c} < 0.2$  and is much larger (requiring less azimuthal anchoring energy to maintain the distorted state) than that for the case of the stripes.

There is no transition analogous to the splay–bend to twist transition in the absence of an electric field; the uniform homeotropic state will always have higher energy than either uniform planar configuration since  $W_{\theta} \gg W_{\phi}$ . In the presence of an electric field with weak polar anchoring, the distorted surface region may spontaneously become uniform homeotropic for sufficiently high applied voltage.

## 5.7 Discussion

In this chapter, a Fourier series approach was used to compute the free energy of a nematic in contact with a striped surface within the approximations firstly that the director was confined to be parallel everywhere to a single plane and secondly that  $K_1 = K_3 \neq K_2$ ; this extended previous work in which the elastic constants were assumed to be isotropic. The resultant expressions for the free energy were used to determine regions of stability of different configurations of the director field with respect to the device parameters.

The bulk energy difference of a semi-infinite nematic region in contact with each of the splay–bend and twist patterned surfaces was computed for anisotropies in the elastic constants consistent with those measured in typical liquid crystal compounds (i.e.  $1/2 < K_2/K_1 < 2$ ). The energy difference was found to be sufficient to make a transition feasible between the two structures if the Rapini–Papoular azimuthal anchoring energy is less than  $10^{-5} \text{Nm}^{-2}$ : the transition was energetically favoured for surfaces designed to promote high pretilt angles where the planar stripe width was small compared to the homeotropic stripe widths (i.e. as  $a \rightarrow 1$ ); the transition was also found to be favoured if the stripe period  $\lambda$  is made smaller. The results of the model agree with experimental observation: the transition only occurs in the splay–bend cell as for the liquid crystal E7  $K_2 < K_1, K_3$  and furthermore, the transition only occurs when the stripe width is about  $2\mu\text{m}$ .

The transition is analogous to the situation where a nematic is confined to a cylinder [140]; in that case the director field may adopt a configuration where the director is everywhere parallel to the radial unit vector or it may “escape to the third dimension” where the director is along the axis in the centre of the cylinder and radial at the edges. In either case the system is frustrated by antagonistic boundary conditions and depending on the surface anchoring, may resolve that frustration by the director field rotating out of the plane which the anchoring conditions try to confine it to.

Whether or not the transition will actually occur in a cell depends on the validity of the phenomenological azimuthal anchoring potential for large displacements from the easy orientation and the Rapini–Papoular energy is very likely to be an underestimate. Grooved surfaces (where  $W_{\phi} \approx 10^{-5} \text{Jm}^{-2}$ ) are unlikely to allow the transition unless the polar anchoring energy is also much higher than  $10^{-4} \text{Jm}^{-2}$ ; the transition is likely to be possible on a photoaligned polymer surface  $W_{\phi} < 10^{-6} \text{Jm}^{-2}$ .

An interesting consequence is that a micropatterned surface with azimuthally degenerate planar stripes will nonetheless align a typical nematic with  $K_2 < K_1$  along the length of the stripes as the twist state has lower energy, as in fact has already been experimentally demonstrated [38]. The effective azimuthal anchoring energy of such a surface depends on the mark-space ratio as well as their overall width. Unlike the well-known mechanism described by Berreman[39] due to surface topography (see section 1.3.1 on page 30) this mechanism is purely due to elastic anisotropy.

Previous work predicted that for weak polar anchoring a spatially uniform configuration of the director field might be possible if either of the stripes were sufficiently narrow[118]. This work has been reexamined in light of the novel azimuthal transition and complete phase diagrams for the nematic in contact with the alternate homeotropic and planar stripes have been calculated for the first time. The same approach was also used to calculate the phase diagram of a nematic in contact with a striped planar surface where the stripes have alternate orthogonal azimuthal easy axis, a situation that is relevant to the construction of switchable diffraction gratings.



## Chapter 6

# Twisted Nematic Cells Constructed From Micropatterned Substrates

**M**ICROPATTERNING offers, as described in the previous chapter, the possibility of designing surfaces that promote any arbitrary bulk effective easy axis and, moreover, surfaces along which the bulk effective easy axis varies. This chapter shall consider the use of micropatterned surfaces to construct complete devices and in particular cells analogous to the very well studied Twisted Nematic cell[3]. Since even a single patterned surface can give rise to a rich phase diagram as shown in the previous chapter, it is to be expected that a number of possible configurations might be stable in a cell constructed with micropatterned surfaces. In particular, if the cell thickness is of the order of the penetration depth of elastic distortions in the liquid crystal caused by the micropatterning, then the director field will vary in all three dimensions. If, however, the cell thickness is much greater than the penetration depth, the director field is still dependent on two dimensions near the surfaces, but in the middle of the cell depends on one spatial coordinate only. In this case, which is the subject of this chapter, the cell should behave much more like a conventional device.

It is perhaps most attractive to use the stripe micropatterning to prepare surfaces that promote a bulk effective pretilt angle of around  $45^\circ$  which requires that the homeotropic and planar stripes are of the same width. Such an arrangement is optimal in that the period of the stripes can be reduced to the greatest extent possible within the constraint that only stripes above a certain width may be fabricated.

The directors near either surface of a the TN cell constructed from two such micropatterned substrates will lie, as in a conventional TN cell, parallel to two orthogonal planes that are mutually perpendicular to either substrate. The high surface tilt however means that some variation in the tilt angle as well as the azimuthal angle of the director may be favourable across the cell. It is straightforward to show that this is the case even in the absence of surface micropatterning: consider a cell with uniform surfaces where the surface tilt is constrained to be  $\theta = \pi/4$  and the azimuthal component is fixed at  $\phi = 0$  on one surface

and  $\phi = \pi/2$  on the other. Suppose the azimuthal component of the director  $\phi$  varies linearly over the cell thickness as in a conventional TN cell, but the polar component is perturbed in a manner consistent with the boundary conditions

$$\theta = \frac{\pi}{4} + c \sin(\pi z/d), \quad \phi = \frac{\pi z}{2d}, \quad (6.1)$$

where  $c$  is a free parameter that may be varied so as to minimize the total free energy. The free energy density for such a solution is, in the two-constant approximation adopted in the previous chapter (i.e.  $\tau = K_2/K_1$  and  $K_1 = K_3$ ),

$$f_{TNbulk}/K_1 = \frac{1}{2}\theta'^2 + \frac{1}{2}\cos^2\theta(\tau\cos^2\theta + \sin^2\theta)\phi'^2 \quad (6.2)$$

where the primes indicate derivatives taken with respect to the  $z$  coordinate. Integration over  $z$  yields an analytic expression for the total energy of the cell per unit area

$$G_{TNbulk}/K_1 = \frac{\pi^2}{64d} \left[ 1 + 16c^2 + 3\tau + (1 - \tau)J_0(4c) - \frac{c}{|c|}4\tau H_0(2|c|) \right] \quad (6.3)$$

where  $J_0$  is a Bessel function and  $H_0$  is a Struve function. This energy may be minimized numerically with respect to  $c$  (fig. 6.1). The amplitude  $c$  is always positive and so the director tilts toward homeotropic in the centre of the cell. This immediately presents a limitation for such cells as displays: the polarization conversion of the twisted state will be reduced and hence the display contrast ratio will be lower than that of a conventional TN display. Furthermore, using a material with exotic elastic constants cannot alleviate this problem as for no value of  $K_2/K_1$  is  $c$  negative and the director therefore never tilts towards planar orientation in the centre of the cell.

## 6.1 A Novel Uniform Configuration in a Micropatterned TN Cell

*The experimental work described in this section was performed by J. Bramble at the University of Leeds.*

It was shown explicitly in the previous chapter that a striped surface with alternate homeotropic and planar degenerate stripes would promote alignment of the director along the length of the stripes if the elastic constants of the nematic were anisotropic, even if the planar stripes had been prepared so as to be azimuthally degenerate. Twisted nematic cells prepared with two such surfaces have recently been demonstrated[141]: the cells were filled with 6CB and prepared with  $1\mu\text{m}$  stripes (i.e. the period of patterning  $\lambda = 2\mu\text{m}$ ) and were  $20\mu\text{m}$  thick, satisfying the earlier criterion  $d \gg \lambda$ .

When one of the cells was viewed between crossed polarizers under the microscope, a number of domains became apparent: the majority of the cell [fig. 6.2(a)] appeared bright and remained bright when the cell was rotated with the polarizers fixed; other regions [fig. 6.2(b)] behaved in a similar manner, but were separated from the first by dark lines; the final sort of observed region appeared dark when the striped

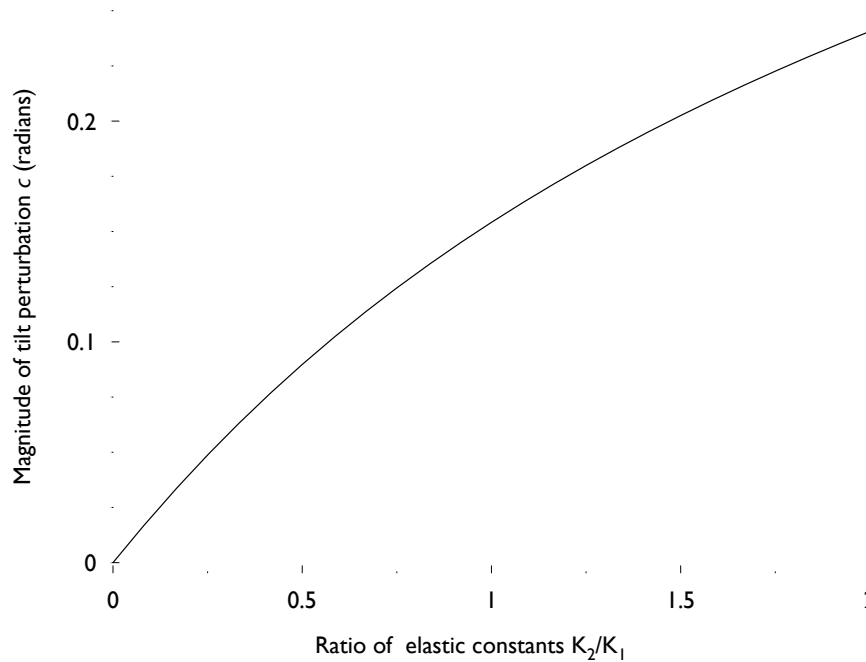


Figure 6.1: Variation of the amplitude of tilt perturbation in a twisted nematic cell as a function of the ratio of the twist and splay elastic constants.

surfaces were aligned with the polarizers, but became bright when the cell was rotated with the maximum intensity when the stripes were  $45^\circ$  to the polarizers. The latter regions were not separated from the former by a distinct line, rather they appeared to merge with a smooth intensity gradient between. No regions were observed that were dark irrespective of orientation with respect to the polarizers (the behaviour of a homeotropic cell).

The first and second regions are twist and reverse twist domains typical of a conventional Twisted Nematic cell where the director rotates azimuthally by  $\pi/2$  from the bottom substrate to the top substrate [fig. 6.3(a)]; these configurations convert the polarization of incident light and thus transmit polarized light independent of their azimuthal orientation. These sorts of domain shall be referred to henceforth in this chapter as the High Tilt Twisted Nematic (HTTN) state to distinguish it from the conventional Twisted Nematic (TN) state. The optical behaviour of the third region is identical to that of either a planar cell or a HAN cell and so the director in this region must be confined to a single plane. This latter sort of domain is not observed in a conventional TN cell.

Moving the focal plane of the microscope up and down through the cell, it was possible to focus on the surface micropatterning which was observed to be continuous and of a high quality. It is therefore improbable that the anomalous sort of domain corresponds to a HAN-like state since this would require the director to lift entirely away from the planar stripes; if, on the other hand, gaps had been observed in the micropatterning, a HAN-like state would very likely form in those regions. It is much more likely that the director in this state lies at some constant tilt angle throughout the bulk of the cell and makes some constant azimuthal angle  $\varphi$  with the wavevector of the stripes on the lower surface [fig. 6.3(b)]. In this Uniform Nematic (UN) state, the director near the micropatterned surfaces is highly distorted as

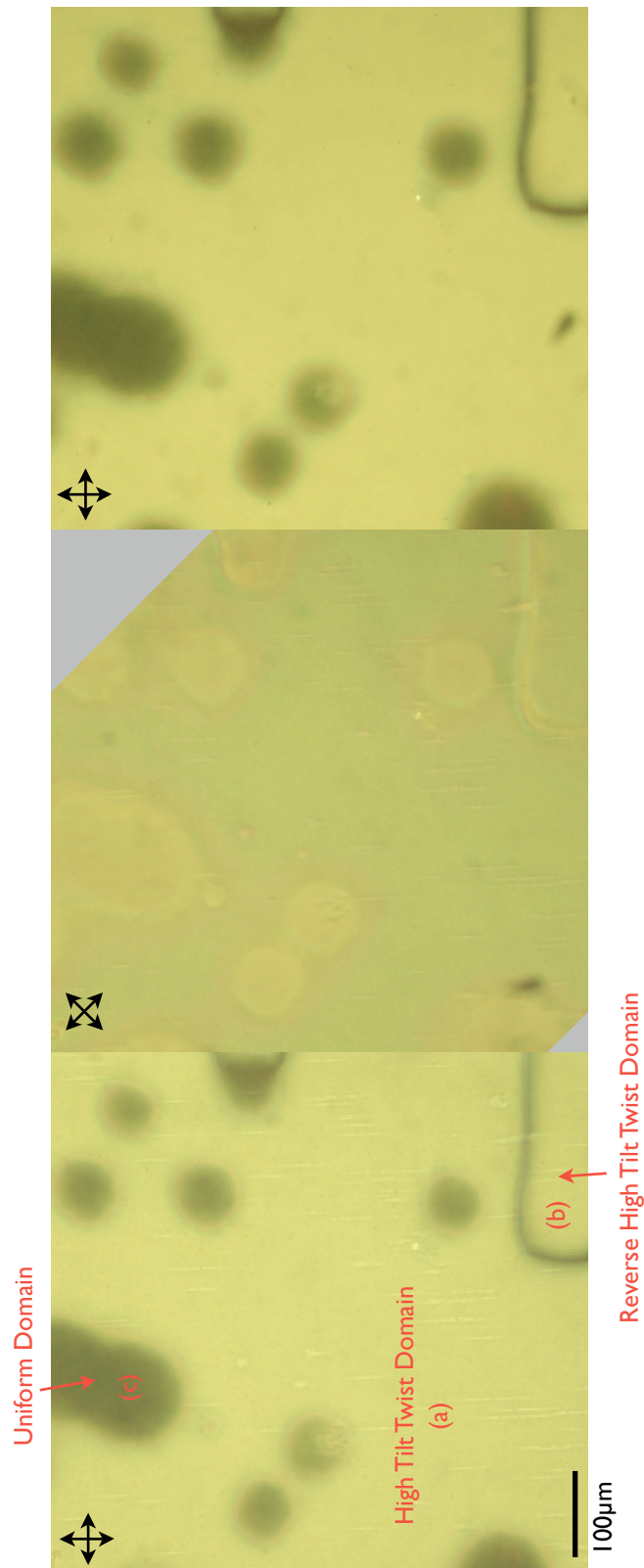


Figure 6.2: Polarizing microscope images of domains in a  $20\mu\text{m}$  twisted nematic cell constructed from two micropatterned surfaces with  $1\mu\text{m}$  wide alternate homeotropic and planar stripes. (Images reproduced with the kind permission of J. Bramble)

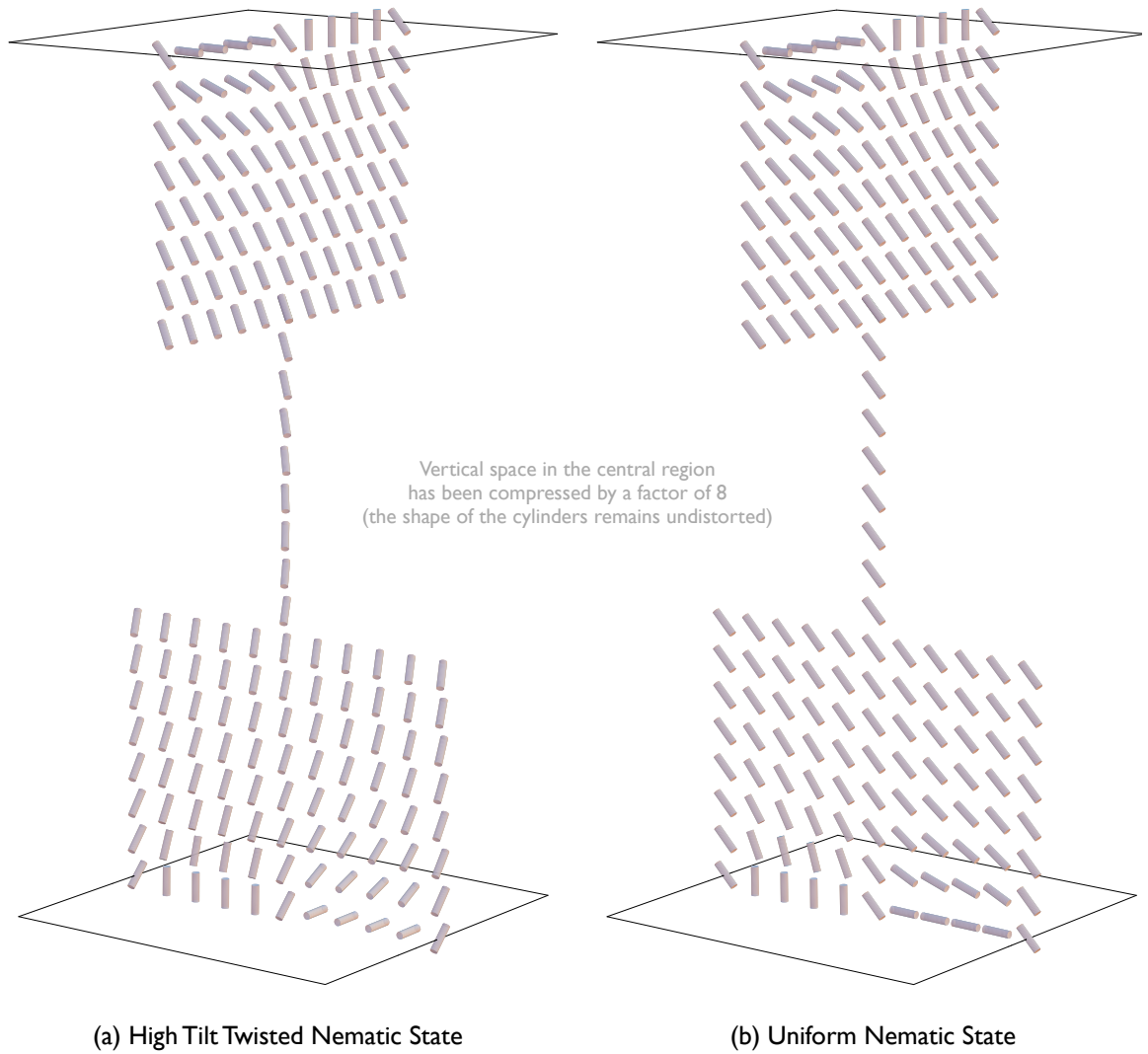


Figure 6.3: Schematic of (a) the High Tilt Twisted Nematic (HTTN) and (b) the Uniform Nematic (UN) states.

in the semi-infinite case, but is nonetheless consistent with both the planar degenerate and homeotropic boundary conditions. That both the HTTN and UN states are observed in equilibrium suggests that they are nearly degenerate. It is not possible to evaluate the exact free energy of both states analytically; it is, however, possible to use the results of the previous chapter to estimate their energies.

In the previous chapter (equation 5.10 on page 115) it was shown that the bulk energy per unit area of a nematic in contact with a striped surface is

$$F_b = \frac{4\pi}{\lambda} \sqrt{1 - (1 - \tau) \sin^2 \phi} \sum_{n=1}^{\infty} n(p_n^2 + q_n^2) \quad (6.4)$$

where the coefficients  $p_n$  and  $q_n$  were found from the boundary conditions at the surface; for the weak polar anchoring case (6.4) must be supplemented by a much smaller contribution (equation 5.22 on page 120) with a similar dependence on  $\phi$  that shall be ignored presently. The sum depends on  $\tau$ ,  $a$  and possibly  $L_\theta$

but is independent of  $\phi$  and it is therefore convenient to make this explicit by adopting the notation

$$\Xi(\tau, a, L_\theta, \lambda) = \sum_{n=1}^{\infty} n(p_n^2 + q_n^2). \quad (6.5)$$

The free energy for the HTTN state in the cell used in the experiment is therefore approximately the sum of a contribution (6.4) from each of the surfaces—where  $\phi = 0$  in each case—and also a contribution from the bulk (6.3). The Fourier series solution for  $\theta$  does not properly represent the spatial variation of the director in the surface region as it does not account for any variation in the azimuthal angle  $\phi$ ; (6.4) nonetheless remains a good estimate of the elastic energy in the surface regions since the scale of distortions in  $\theta$  is far shorter than that in  $\phi$ . The bulk contribution is changed very little when  $K_2/K_1 < 1$ , and immediately adopts a very simple form

$$F_{HTTN}/K_1 = \frac{1}{8d}(1 + \tau) \left(\frac{\pi}{2}\right)^2, \quad (6.6)$$

if the tilt angle is assumed to be constant  $\theta = \pi/4$  across the cell. The total energy of the liquid crystal in the HTTN configuration is therefore approximately

$$F_{HTTN}/K_1 \approx \frac{1}{8d}(1 + \tau) \left(\frac{\pi}{2}\right)^2 + \frac{8\pi}{\lambda} \sqrt{\tau} \Xi(\tau, L_\theta, \lambda). \quad (6.7)$$

The energy of the UN state, on the other hand, is simply the contribution of two surfaces since there is no elastic distortion in the bulk. If the director is everywhere confined to a plane orthogonal to the substrate that makes an angle  $\varphi$  with the wavevector of the pattern on the lower substrate, then the free energy is

$$F_{UN}/K_1 = \frac{4\pi}{\lambda} \left( \sqrt{1 - (1 - \tau) \sin^2 \varphi} + \sqrt{1 - (1 - \tau) \cos^2 \varphi} \right) \Xi(\tau, L_\theta, \lambda). \quad (6.8)$$

The minimum value of (6.8) is obtained when  $\varphi = 0$  or  $\varphi = \pi/2$ , i.e. when the director lies along either of the stripes; this was the situation observed earlier with polarizing microscopy and has energy

$$F_{UN}/K_1 = \frac{4\pi}{\lambda} (1 + \sqrt{\tau}) \Xi(\tau, L_\theta, \lambda). \quad (6.9)$$

The energy difference between the HTTN and UN domains is therefore approximately

$$\frac{F_P - F_{TN}}{K_1} = \frac{4\pi}{\lambda} (1 - \sqrt{\tau}) \Xi(\tau, L_\theta, \lambda) - \frac{1}{8d}(1 + \tau) \left(\frac{\pi}{2}\right)^2. \quad (6.10)$$

If the cell thickness is reduced, the UN solution is favoured (as the twist gradient and hence the second term in (6.10) is increased) and if the period of patterning is reduced, the HTTN domain is favoured. Using the weak polar anchoring solution for  $\Xi(\tau, L_\theta)$  from the previous chapter (eq. 5.19 on page 119)

$$\Xi(\tau, L_\theta, \lambda) = \sum_{n=1}^{\infty} \frac{\sin^2(n\pi/2)}{n^2 (1 + 2n\pi L_\theta \sqrt{\tau}/\lambda)^2} \quad (6.11)$$

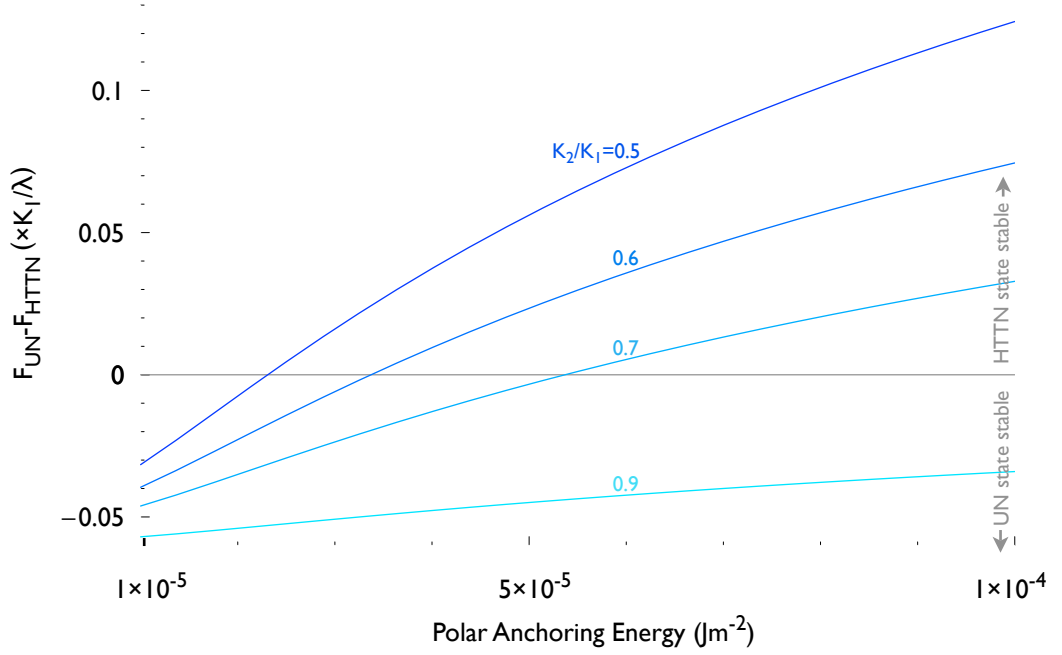


Figure 6.4: Energy difference between the Uniform Nematic and High Tilt Twisted Nematic states as a function of the polar anchoring energy of the micropatterned surfaces.

where  $L_\theta = W_\theta/K_1$  has units of length. For the experimental values of  $\lambda = 2\mu m$  and using typical values  $W_\theta = 1.4 \times 10^{-4} Jm^{-2}$ [47] and  $K_1 = 1.4 \times 10^{-11} N$ [3] (and so  $L = 0.07$ ), the sum  $\Xi(\tau, L_\theta, \lambda)$  has a value very nearly  $1/2$ .

The energy difference between the planar and twisted nematic domains is plotted with respect to  $W_\theta$  for several values of  $\tau$  in fig. 6.4. If  $\tau = 1$ , the distorted regions in the planar and TN domains become energetically degenerate and so the HTTN state will not occur since the additional bulk twist gives it higher energy. If HTTN and UN domains are to coexist then they must be very nearly degenerate and so the effective polar anchoring energy must be of the order of  $1 \times 10^{-5} < W_\theta < 1 \times 10^{-4} Jm^{-2}$ , in line with typical experimental values[3, 50, 47].

Contrast the situation with that of a conventional TN cell which has been prepared with uniform substrates: In such a cell the TN state has energy per unit area

$$F_{TN} = \frac{K_2}{2d} \left(\frac{\pi}{2}\right)^2 \quad (6.12)$$

while a hypothetical uniform state has energy per unit area

$$F_{HU} = \frac{W_\phi}{2} \quad (6.13)$$

assuming that the Rapini-Papoular anchoring energy is valid for large deviations from the azimuthal easy

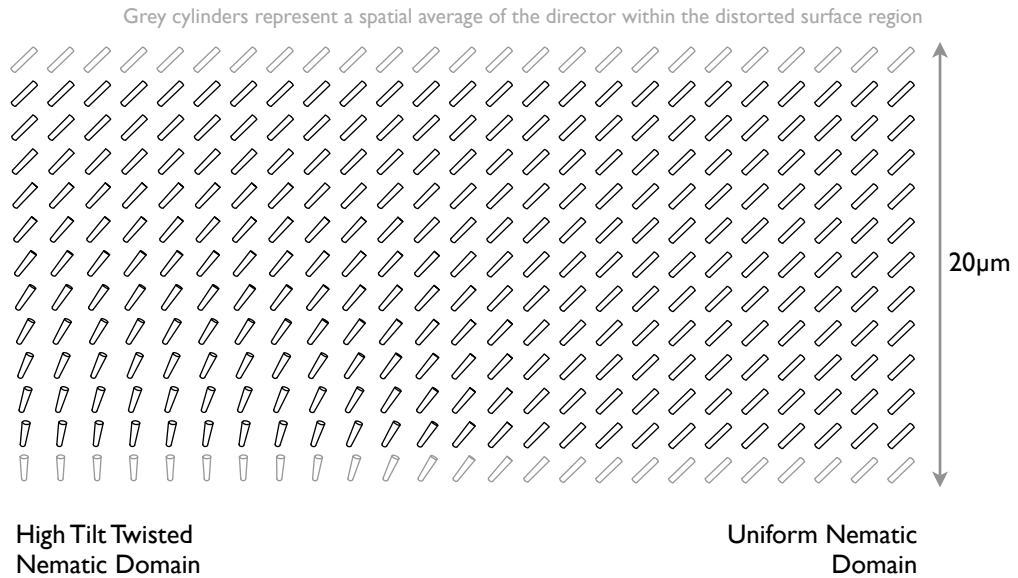


Figure 6.5: Schematic of the director field between the HTTN and UN domains.

axis. For the hypothetical uniform state to be stable

$$W_\phi < \frac{K_2}{d} \left(\frac{\pi}{2}\right)^2. \quad (6.14)$$

Inserting typical values  $K_2 \sim 1 \times 10^{-11}\text{N}$  and  $d \sim 5\mu\text{m}$ ,  $W_\phi$  must be less than—and probably much less than— $0.5 \times 10^{-6}\text{Jm}^{-2}$  which is very low; it is typical of photoaligned polymers[137] but not of rubbed polymers[49]. Uniform domains are therefore not observed in conventional TN cells.

A remaining question is the structure of the band that separates the HTTN and UN domains in which the intensity of transmitted light falls away. Such a region is often referred to as a domain wall as discussed in chapter 2. As distinct from reorientation of the director field around a disclination line, “wall” is used in this sense to mean a region between domains in which the director field must deform to match the appropriate configuration adopted by the liquid crystal adopted on either side. This reorientation may be envisaged as a progressive series of deformations to the director field in the domain on one side of the wall that gradually transform it to the director field of the other domain on the other side of the wall. The distorted region is of much higher elastic energy density than the surrounding regions (which may be reduced by widening the wall) but usually is energetically costly at the surface (which may be reduced by narrowing the wall): the ultimate width of the domain wall is determined by a balance of these factors. The observed appearance under the polarizing microscope depends on the detailed behaviour of the director field inside the domain wall.

One can readily envisage a continuous sequence of deformations to the director profile of the HTTN region that transform it into that of the UN region: simply rotate gradually the plane of the director azimuthally near one surface and as this side is rotated allow the bulk director to relax to follow this rotation. The director in the transition region follows such a continuous sequence (fig. 6.5): since each



intermediate step is consistent with the azimuthally degenerate boundary condition at the planar stripes, the domain “wall” is of width of the order of the cell thickness (this is analogous to the reorientation wall in a planar degenerate HAN cell observed in fig. 2.1 on page 40). Furthermore, as each intermediate state has a successively lower total change in  $\phi$  across the cell, that state has lower optical rotatory power; the domain wall ought to appear then as a progressive decrease in intensity from the bright HTTN domain to the dark UN domain when viewed between crossed polarizers. This behaviour is indeed what was observed under the polarizing microscope.

## 6.2 Numerical Simulation of TN Cells Constructed From Micropatterned Surfaces

Thus far, only approximate analytical methods have been used to simulate the configuration adopted by a nematic in contact with a micropatterned surface. These methods have the advantage that they provide useful estimates of the nematic energy but make assumptions about the nematic material that are quite restrictive; in particular they assume that  $K_1 = K_3$  and that the azimuthal component of the director changes over a much longer length scale than the polar component. In order to overcome these restrictions, it is necessary to resort to numerical solution of the Euler-Lagrange equations derived from the most general form of the free energy. In this section a suitable approach is described that is designed specifically to simulate complete cells with striped micropatterned surfaces, albeit within the limitation that  $\lambda \ll d$ . The resulting program is then used to elucidate the effect of elastic anisotropy on a splay-bend surface and to simulate the behaviour of the HTTN state with an applied electric field.

It is necessary first to select the appropriate representation of the director: near a micropatterned surface the director rapidly changes from homeotropic to planar and so the Cartesian representation is most appropriate. The polar representation is inconvenient since there is no unique solution for  $\phi$  whenever the director is homeotropic; this introduces sufficient instability into the numerical solution of the coupled Euler-Lagrange equations that they are in practice unsolvable for any problem where the director must be both homeotropic and planar at different points.

Initially, consider the director field in contact with one patterned surface only which was the situation in the previous chapter. Adopting the same coordinate system as before (fig. 5.3 on page 111), where the  $x$  axis lies orthogonal to the length of the stripes and the  $z$  axis is perpendicular to the surface, the director field  $\mathbf{n}$  must be a function of  $x$  and  $z$  alone. The director is represented by three components

$$\mathbf{n}(x, z) = [n_x(x, z), n_y(x, z), n_z(x, z)]; \quad (6.15)$$

subject to the constraint  $n_x^2 + n_y^2 + n_z^2 = 1$ . The actual director configuration is that which minimizes

the well-known free energy[3]

$$F = \frac{1}{2} \int [K_1(\nabla \cdot \mathbf{n})^2 + K_2(\mathbf{n} \cdot \nabla \times \mathbf{n})^2 + K_3|\mathbf{n} \times \nabla \times \mathbf{n}|^2 - \epsilon_0 \epsilon_{\perp} (\nabla U)^2 - \epsilon_0 \Delta \epsilon (\mathbf{n} \cdot \nabla U)^2] dV \quad (6.16)$$

where  $\epsilon_{\perp}$  is the dielectric permittivity of the liquid crystal associated with any direction orthogonal to the director,  $\Delta \epsilon$  is the dielectric anisotropy and  $U(x, z)$  is the electric potential field. If it is assumed that the director is fixed along the boundary, the surface terms including the saddle-splay term may be discarded. The director field that minimizes (6.16) is found by solving numerically the coupled Euler-Lagrange equations for each component

$$\mathcal{E}_{n_{\xi}} = \frac{\partial F}{\partial n_{\xi}} - \nabla \cdot \frac{\partial F}{\partial \nabla n_{\xi}} = 0, \quad \xi \in \{x, y, z\}. \quad (6.17)$$

and the Maxwell equation for the scalar potential

$$\mathcal{E}_U = \nabla \cdot (\epsilon \nabla U) = \nabla \cdot [\epsilon_{\perp} \nabla U + \Delta \epsilon (\mathbf{n} \cdot \nabla U) \mathbf{n}] = 0 \quad (6.18)$$

where  $\epsilon$  is the dielectric tensor<sup>1</sup>. Local normalization of the director may be achieved by introducing an auxiliary functional

$$F' = F + \int \lambda(x, z) (n_x^2 + n_y^2 + n_z^2 - 1) dV \quad (6.19)$$

with an associated Lagrange multiplier field (see section 1.2.2.2 on page 29). The auxiliary functional (6.19) contributes a new term to the Euler-Lagrange equations for the director components

$$\mathcal{E}'_{n_{\xi}} = \mathcal{E}_{n_{\xi}} + 2\lambda n_{\xi} = 0, \quad \xi \in \{x, y, z\}. \quad (6.20)$$

It shall be shown later that it is possible to solve for the Lagrange multiplier quite naturally within the numerical scheme chosen and so for the moment it is sufficient to only consider the solution of the unconstrained Euler-Lagrange equations (6.17) and the Maxwell equation (6.18). To do this, the computational domain is discretized onto a  $N_x \times N_z$  rectangular mesh with a unit cell of width  $\delta x = 1/(N_x - 1)$  and height  $\delta z = 1/(N_z - 1)$  and where the field variables  $n_x, n_y, n_z$  and  $U$  are stored at the corners of the rectangles. The Euler-Lagrange and Maxwell equations are then discretized to yield four nonlinear equations for each point in the mesh<sup>2</sup>: each field variable or functional  $q$  in the continuous form of the equations is replaced by their discrete counterpart  $q_{i,j}$  which represents its value at the mesh point corresponding to coordinates  $(x, z) = (i\delta x, j\delta z)$ . Derivatives of the field variables or functionals are then replaced by cell-centred finite differences

<sup>1</sup>The unconstrained Euler-Lagrange and Maxwell equations are displayed for one and two dimensional problems in Appendix D

<sup>2</sup>This approach is not the only numerical procedure that may be used; for another see Appendix E.

$$\nabla q \rightarrow \left( \frac{q_{i+1,j} - q_{i-1,j}}{2\delta x}, \frac{q_{i,j+1} - q_{i,j-1}}{2\delta z} \right)$$

$$\nabla^2 q \rightarrow \frac{q_{i+1,j} + q_{i-1,j} - 2q_{i,j}}{\delta x^2} + \frac{q_{i,j+1} + q_{i,j-1} - 2q_{i,j}}{\delta z^2}. \quad (6.21)$$

$$\frac{\partial q}{\partial x \partial z} \rightarrow \frac{(q_{i+1,j} - q_{i-1,j})(q_{i,j+1} - q_{i,j-1})}{4\delta x \delta z} \quad (6.22)$$

Different equations are needed for mesh points at the edges. At the bottom edge, each field quantity is fixed at some value representing the director profile at that surface: this yields four simple equations for each point of the form  $q_{1,j} = C_j$ . At the top surface, it is sufficient to impose the condition  $\nabla q = 0$  for the director components and  $U$  set to the value of an applied voltage. The director boundary condition may be most easily imposed by using at each mesh point in the top row equations of the form  $q_{i,N_z} - q_{i+1,N_z} = 0$  for each field variable.

At the left and right hand sides, periodic boundary conditions are imposed by substituting in the discretized equations used in the interior mesh points those quantities of the form  $q_{i-1,j}$  with  $q_{N_x,j}$  at the left boundary and at the right boundary replacing  $q_{i+1,j}$  with  $q_{1,j}$ .

Following the above procedure yields  $(N_x - 1) \times N_z \times 3$  equations for the director components and  $(N_x - 1) \times N_z$  equations for the scalar potential, all of which are of the form  $f_i = 0$  and the majority of which are nonlinear. There are an equal number of unknowns, namely the quantities of the field variables at each point.

Having reduced the problem to that of solving a large number of simultaneous nonlinear equations, it is possible to apply standard methods such as the Newton method[24]. Suppose the unknowns  $n_{x_i,j}$ ,  $n_{y_i,j}$ ,  $n_{z_i,j}$  and  $U_{i,j}$  are ordered into a single vector  $\{v\}$  and their associated equations  $\mathcal{E}_{n_{x_i,j}} = 0$ ,  $\mathcal{E}_{n_{y_i,j}} = 0$ ,  $\mathcal{E}_{n_{z_i,j}} = 0$  and  $\mathcal{E}_{U_{i,j}} = 0$  are correspondingly ordered and relabelled  $f_i = 0$ . Suppose  $\{v\}$  is initially assigned some trial solution  $\{v^0\}$  which may be substituting this into the  $f_i$  to give a vector of residuals  $F_i(\{v\})$  which, if the trial solution  $\{v\}$  were correct, would be zero. If the initial guess is “sufficiently close”<sup>3</sup> to the correct solution, an improved solution may be found by taking a single Newton step

$$v_i^1 = v_i^0 + J_{ij}^{-1} F_j(\{v^0\}) \quad (6.23)$$

where  $J_{ij}^{-1}$  is the inverse of the Jacobian matrix  $J_{ij} = \left. \frac{\partial f_i}{\partial q_j} \right|_{\mathbf{q}^0}$  and the Einstein summation convention is implied. The true solution is then found by repeating the process

$$v_i^{t+1} = v_i^t + J_{ij}^{-1} F_j(\{v^t\}) \quad (6.24)$$

<sup>3</sup>The meaning of “sufficiently close” is the set of inputs for which the Newton method converges. It is difficult to provide exhaustive criteria that define this set, but it is straightforward enough to verify if a particular solution is a member: some details are to be found in [24] and references therein. Virtually any trial solution of the correct order of magnitude is in practice suitable, in part because the equations to be solved arose from derivative operators whose eigenfunctions are naturally exclusively continuous functions.

iteratively, each time reevaluating the residual and Jacobian. The iteration is stopped after some convergence criterion is reached such as that the norm of the residual vector has dropped below some threshold value.

In order to maintain the local normalization constraint, it is helpful to stagger the solution of the potential and director component equations: firstly, updated scalar potential values  $U_{i,j}$  are computed via (6.24) using the Maxwell equations whilst holding the values of the director components constant and then the updated director components  $(n_x, n_y, n_z)_{i,j}$  are computed holding the scalar potential values constant, simultaneously solving for the local Lagrange multiplier as shall be discussed momentarily. The process is then repeated iteratively until all values of the field variables have converged according to some criterion.

The Newton step  $J_{ij}^{-1} F_j(\{v^t\})$  is the solution of the system of equations[24]

$$J_{ij} \Delta v_j^t = F_i(\{v^t\}), \quad (6.25)$$

i.e. each iteration represents a step that would solve the equations if they were linear. If the auxiliary functional is now incorporated into (6.25), the Jacobian of the constrained Euler-Lagrange equations (6.20) is  $J'_{ij} = J_{ij} + 2\lambda_{ij}$  where  $\lambda_{ij}$  is a diagonal matrix in which the Lagrange multiplier for each point appears exactly three times. There is no contribution to the residual from the auxiliary functional provided that the initial trial function is itself properly normalized. The modified Newton step is therefore found by solving

$$J_{ij} \Delta v_j^t = F_i(\{v^t\}) - 2\lambda_i \quad (6.26)$$

where the  $N_x \times N_z$  unique Lagrange multipliers  $\{\lambda\}$  are to be found by solving the  $N_x \times N_z$  equations

$$\begin{aligned} (n_x^{t+1})^2 + (n_y^{t+1})^2 + (n_z^{t+1})^2 - 1 &= (n_x^t + \Delta n_x^t)^2 + (n_y^t + \Delta n_y^t)^2 + (n_z^t + \Delta n_z^t)^2 - 1 \\ &= 0 \end{aligned} \quad (6.27)$$

where the  $\Delta n_\xi$  are the Newton steps for a single mesh point from (6.26). Any trial solution  $\{\tilde{\lambda}\}$  may be used to compute a proposed Newton step  $\tilde{\Delta v}^t$  which may then substituted into (6.27); the correct Lagrange multipliers  $\{\lambda\}$  may in this way be found using any nonlinear equation solver, including the Newton method. Evaluation of the Jacobian to solve the Lagrange multipliers is very expensive computationally and so there remains room for considerable optimization of this step. Once the Lagrange multipliers are found, the correct Newton step for the director components preserving their normalization may be taken; every few iterations the director is re-normalized locally at each point.

The program that was developed to implement the above has some useful features: it is possible to set any of the edges to any of the boundary conditions described, and in the case of a Dirichlet boundary to represent any arbitrary patterning and not just a pair of stripes. Two further features ensure the height and resolution of the computational mesh does not alter the solution: firstly, the program automatically

expands the height of the computational domain, adding rows of mesh points, until the norm of the difference between two successive steps (ignoring the extra row) is less than a second threshold value; secondly, the program after convergence then interpolates the solution onto a finer mesh and then iterates until convergence. The procedure of interpolation and solution is repeated until the norm of the difference between two successive solutions (ignoring the interpolated mesh points) is below a third tolerance value.

To simulate a complete cell, the Euler-Lagrange equations must in general be solved in all 3 spatial dimensions. If, however, the cell thickness is sufficiently large in the sense that  $d \gg \lambda$ , the director field in the centre of the cell depends on the  $z$  coordinate alone. The cell may therefore be divided into three regions: near the substrates the director is a function of the coordinate perpendicular to the length of the stripes and  $z$  and so the director field is solved in these two regions in 2 dimensions as described previously; in the centre of the cell a 1 dimensional solver is used. Boundary conditions at the connecting interfaces are imposed so that the field variables and their derivatives with respect to  $z$  are continuous; the three regions are combined into one Jacobian so that solution of the field variables throughout the whole cell can proceed simultaneously. The program is not restricted to a particular pattern: arbitrary (Dirichlet) boundary conditions may be imposed at either surface and there is no requirement that the cell be symmetric.

### 6.3 Simulation of a Twisted Nematic Cell with Micropatterned Surfaces

The two constant approach of the previous chapter had the restriction that it ignored splay/bend anisotropy. The program developed in the previous section does not suffer from this limitation and so was used to simulate a region of nematic in contact with a single patterned substrate (figure 6.6) to determine the effective pretilt—the orientation of the director far above the surface—as a function of the homeotropic-planar “mark-space ratio”  $a$ . The height  $h$  of the computational domain was successively extended automatically until the pretilt value obtained for each  $a$  was unchanged. The calculation was repeated for different  $K_3$ . In typical nematic compounds  $K_3$  is greater than  $K_1$ ; the calculation was performed using the ratio for E7  $K_3/K_1 = 1.6$ [50, 3] and again with the inverse. The effective pretilt tends towards homeotropic if  $K_3 > K_1$  and towards planar if  $K_3 < K_1$ . The twist elastic constant does not affect the effective pretilt when the director is perpendicular to the length of stripes as the twist term in the free energy (6.16) does not contribute to the free energy (discussed in the previous chapter).

A full twisted nematic cell constructed from two micropatterned substrates was then simulated where the alignment on the planar stripes was fixed to lie along the length of the stripes. The director profiles obtained (fig. 6.7) are plotted using the polar representation

$$\mathbf{n} = (\cos \theta \cos \phi, \cos \theta \sin \phi, \sin \theta) \quad (6.28)$$

computed from the Cartesian components. They differ significantly for those for a conventional Fredericks

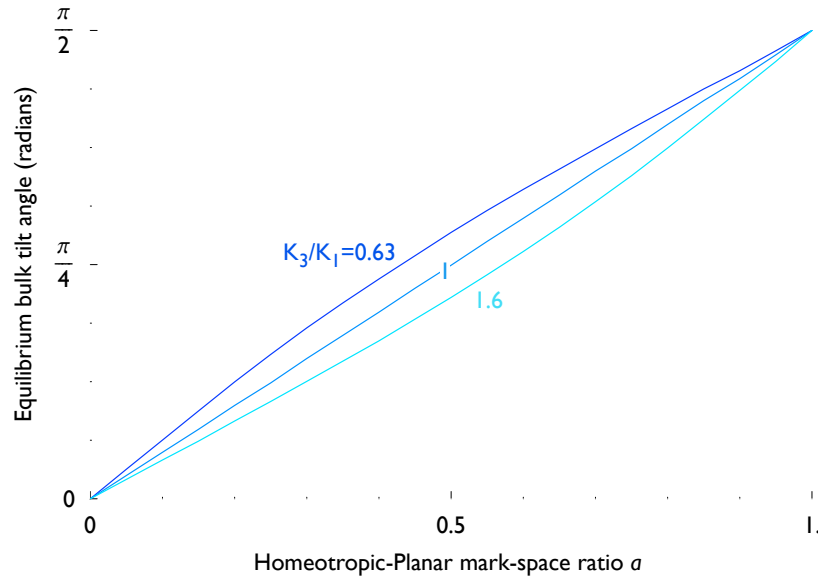


Figure 6.6: Equilibrium bulk tilt angle  $\bar{\theta}$  where  $n_z = \sin \theta$  as a function of relative homeotropic stripe width  $a$  with rigid anchoring.

twist cell[29] (where the surface pretilt is  $0^\circ$ ) in that the director tends toward homeotropic in the centre of the cell due to the large effective pretilt at the surfaces. The polar profile also varies considerably (fig. 6.8)—the central tilt changes by up to  $20^\circ$ —with what amounts to natural differences in elastic constants between physical liquid crystal materials. As in the semi-infinite case,  $K_3 > K_1$  favours homeotropic alignment and  $K_3 < K_1$  favours planar alignment; the situation is reversed for  $K_2$ :  $K_2 > K_1$  favours planar alignment and  $K_2 < K_1$  favours homeotropic alignment.

Finally, the response of the director field to an applied voltage (fig. 6.9) was simulated with  $\epsilon_\perp = 1$ ,  $\Delta\epsilon = 1$  and  $K_1 = K_2 = K_3 = 1 \times 10^{-11} \text{Jm}^{-2}$ . A conventional TN cell with  $\theta = 0$  at each surface only switches above a threshold voltage which is, in the 1-constant approximation[29],

$$V_C = \sqrt{\frac{K}{\epsilon_0 \Delta\epsilon}}. \quad (6.29)$$

For the values used here  $V_C \approx 3.3V$ . The micropatterned TN cell simulated has, in contrast to the conventional TN cell, virtually switched at  $V = V_C$ .

## 6.4 Smectic Liquid Crystals in Contact with Micropatterned Surfaces

*The cell studied in this section was constructed by Jonathan Bramble of the University of Leeds; the microscope images were taken by the author using the Leica SP5 confocal microscope at Exeter.*

The orientational order of a nematic in contact with micropatterned surfaces is, as has been shown, greatly distorted in the region immediately adjacent to a striped micropatterned surface but the distortion relaxes away from the surface to a spatially constant orientation in the bulk; the elastic distortion to do this nec-

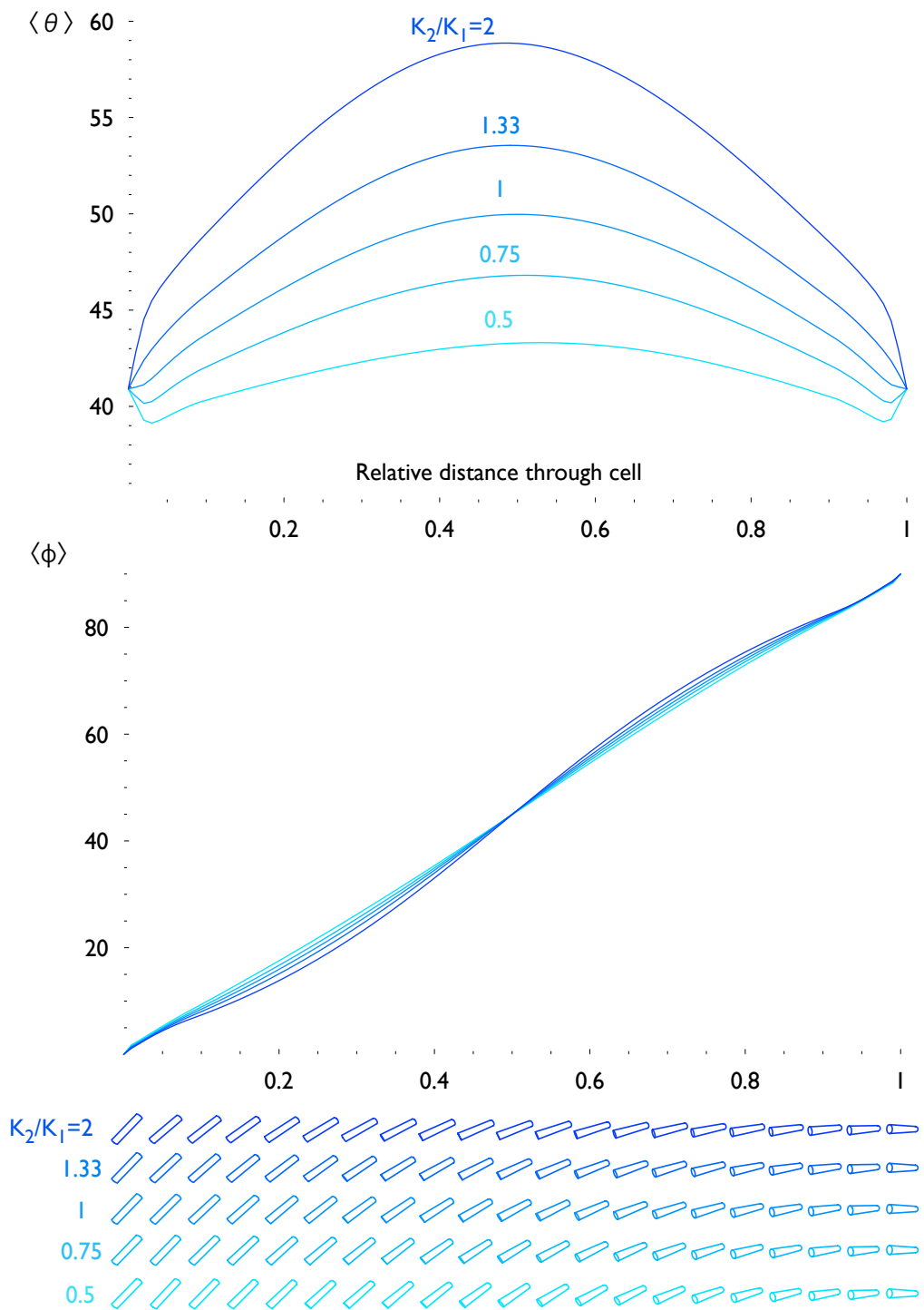


Figure 6.7: Director profiles for a simulated cell of  $20\mu\text{m}$  thickness with identically patterned substrates of  $2\mu\text{m}$  period for different values of  $K_2/K_1$ . Director values are shown averaged over the  $x$  coordinate.

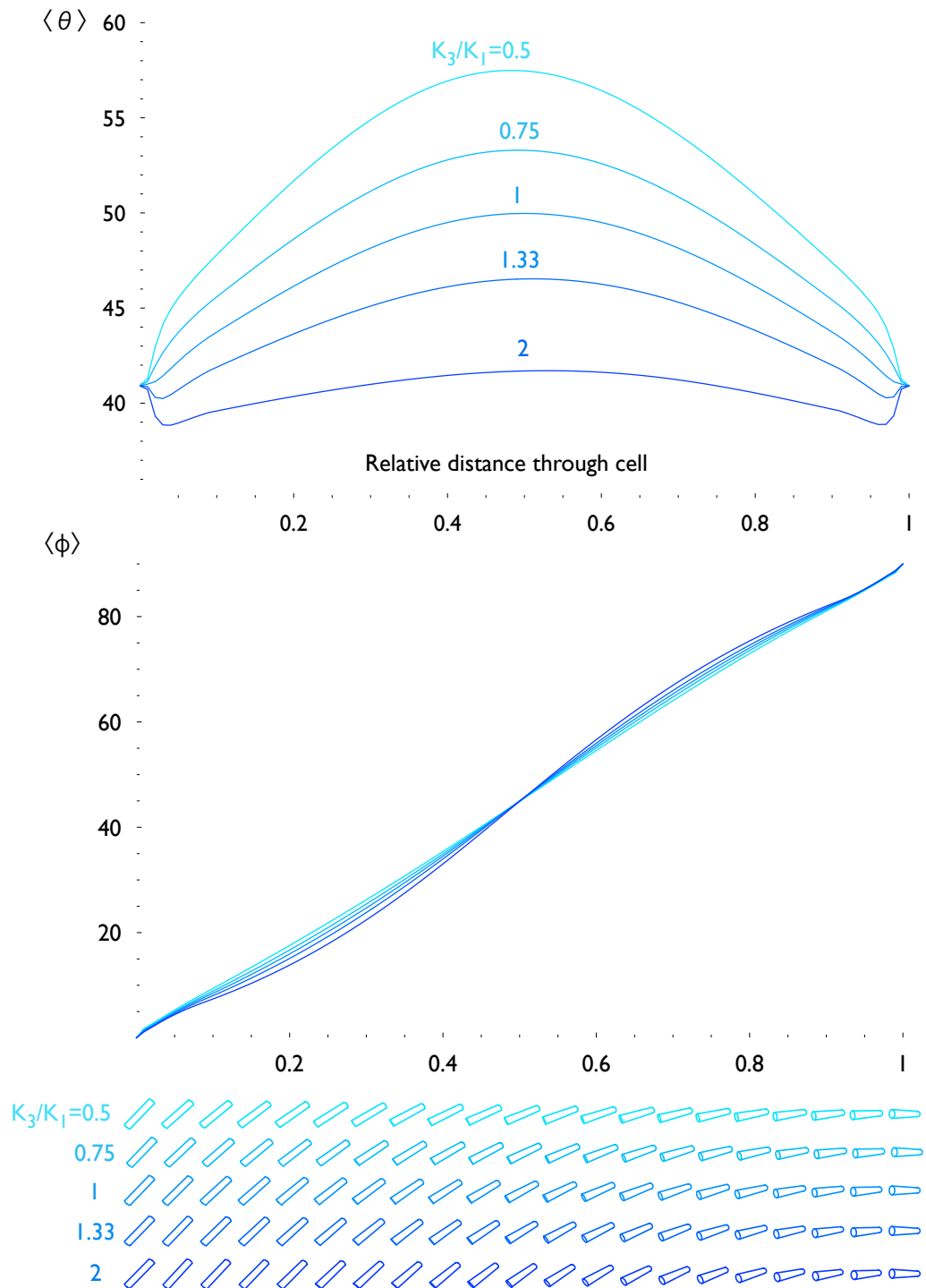


Figure 6.8: Director profiles for a simulated cell of  $20\mu\text{m}$  thickness with identically patterned substrates of  $2\mu\text{m}$  period for different values of  $K_3/K_1$ . Director values are shown averaged over the  $x$  coordinate.



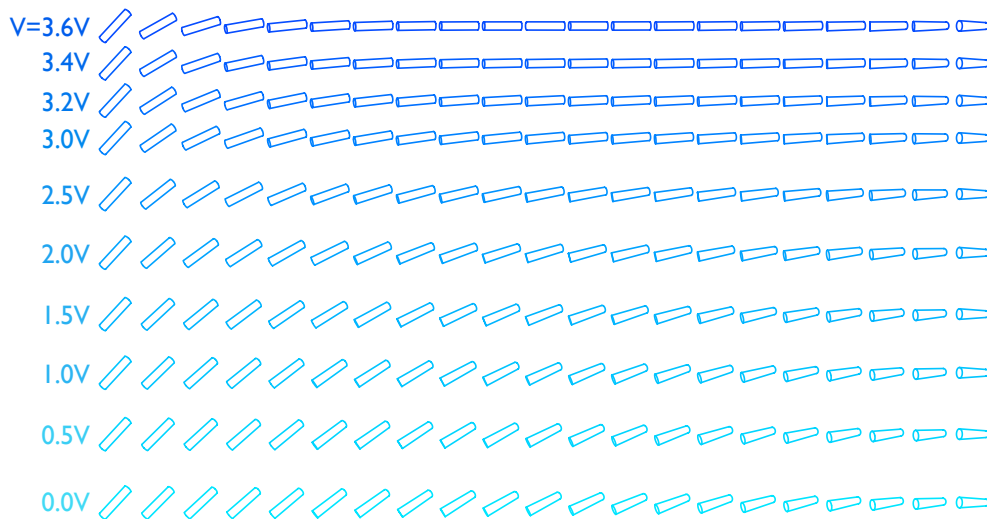
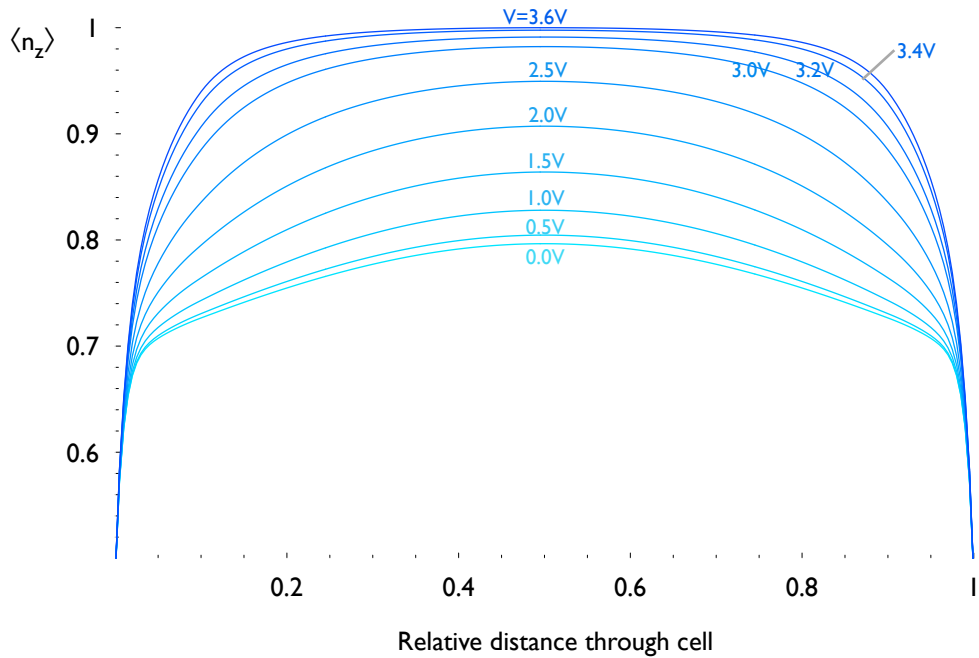


Figure 6.9: Director profile, averaged over the  $x$  coordinate, for a simulated cell of  $20\mu\text{m}$  thickness with identically patterned substrates of  $2\mu\text{m}$  period at several values of applied voltage; the elastic constants used are typical of common nematic materials i.e.  $K_3/K_1 = 1.6$ ,  $K_2/K_1 = 0.6$ .

essary includes some bend and possibly twist distortion. In a smectic, however, bend and twist distortions are forbidden and so the liquid crystal is forced to break up into domains. It has recently been shown[142] that a smectic in contact with a striped homeotropic/planar surface adopts a homeotropic configuration above the homeotropic stripes and splits into a linear array of circular domains whose appearance under the polarizing microscope is consistent with that of focal conic domains.

FCM images were taken of 8CB in a cell with one surface prepared with microcontact printed SAMS (see section 5.2 on page 107) with planar degenerate stripes that were  $\sim 10\mu\text{m}$  wide and the other surface a coverslip treated with a homeotropic polyimide; the surfaces were held apart by  $12\mu\text{m}$  beads dispersed throughout the cell. An axial section from just above the micropatterned surface (fig. 6.10) shows the line of focal conic domains which appear as bright circles surrounded by regions of homeotropic smectic which appear dark: In cross section however (fig. 6.10 below) the hyperbolic defect cores appear very clearly to be *asymmetric* despite the fact that the planar stripes was prepared so as to be azimuthally degenerate.

It is clear from the earlier discussion of Dupin cyclides in chapter 4 (in particular fig. 4.8 on page 101) that for small eccentricities the shape of the ellipse changes rather imperceptibly but for the hyperbola the same change is quite manifest. It is possible to visually fit hyperbolae to the cross section image (shown as red lines in fig. 6.10) provided that the cross section is properly scaled so that the bright band corresponds to the known cell thickness. A value of 0.3 for the eccentricity of the hyperbolae was obtained. This value is entirely consistent with the shape of the ellipses from the axial section.

## 6.5 Discussion

Micropatterned surfaces offer the possibility of constructing TN cells with arbitrary preferred surface alignment orientations, in particular polar angles around  $45^\circ$  which are very difficult to achieve with conventional uniform substrates. The tendency of a striped surface to align the director along the length of the stripes was shown in this chapter by the work of others to be sufficient to stabilize an analogue of the Twisted Nematic cell. This chapter has explored such a cell and described some important differences between the micropatterned TN cell and the conventional TN cell. Foremost, an experimentally observed anomalous tendency for the micropatterned TN cell to develop spatially uniform regions not present in a conventional TN cell was explained by extending the description of the previous chapter to estimate the energy of that state.

A second effect due to the high surface tilt (a corollary of the micropatterning) was shown at the start analytically to favour variation of the polar component of the director throughout the cell. This effect was visible, as was an azimuthal perturbation of somewhat smaller amplitude, in the physically realistic simulations conducted in the second part of the chapter. The simulation split the cell into two 2-dimensional regions adjacent to either substrate and a 1-dimensional region in the cell centre—an approach significantly more efficient than solving the full 3-dimensional Euler-Lagrange equations as would be necessary

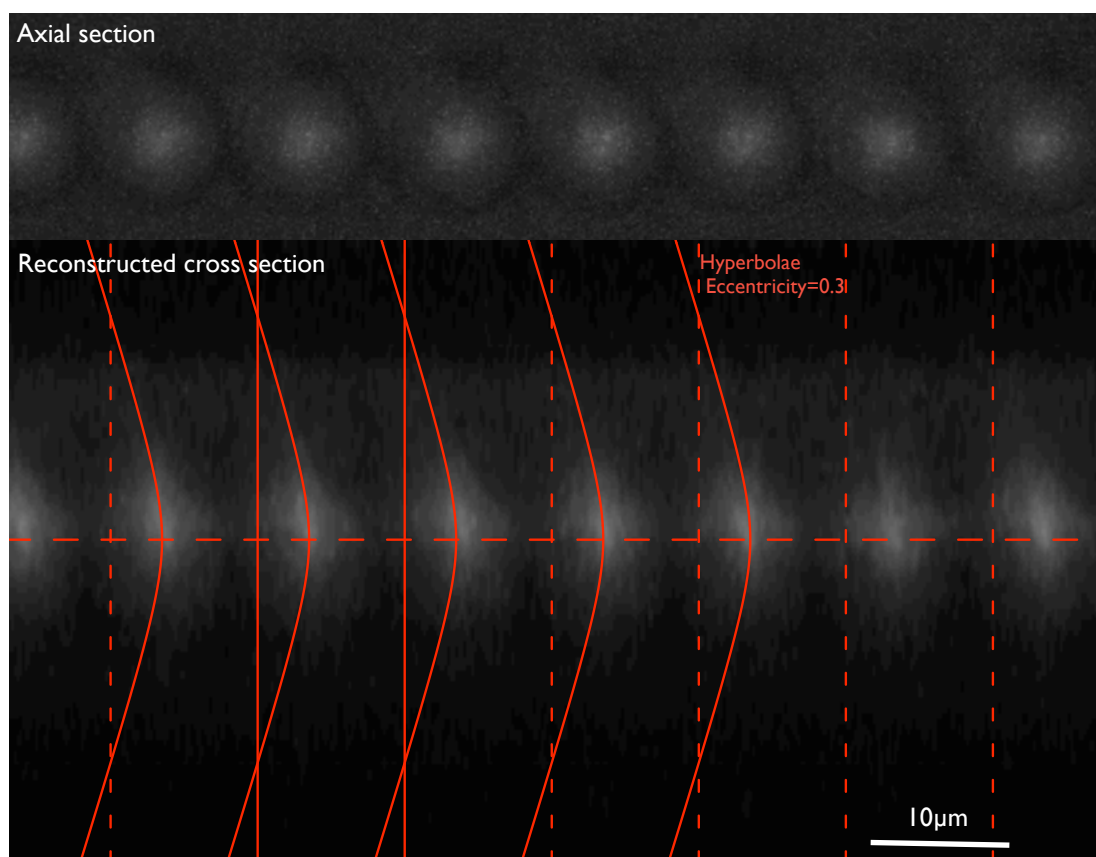


Figure 6.10: FCM images of Dupin cyclide focal conic domains (above) an axial section near the micropatterned surface (below) reconstructed cross section with fitted hyperbolae.

if the cell thickness were close to the period of the patterning.

It was shown in this chapter that the resulting cells offer essentially threshold-less switching and require much lower voltages than conventional TN cells to completely switch the cell. Furthermore, the director profile in the cell depends very strongly on the elastic constants; such cells may potentially be used experimentally to measure ratios of elastic constants although there remains the problem of covariance between the two ratios  $K_2/K_1$  and  $K_3/K_1$ .

Finally, the focal conic domains formed by a smectic liquid crystal were shown to be asymmetric by confocal microscopy and, for the first time, the eccentricity was measured directly from an axial cross section. The physical origin of the asymmetry remains an open problem. In the nematic phase the stripes align the liquid crystal along their length (as shown in the previous chapter) and the cell adopts one of the two possible HAN-like configurations (see section 3.2 on page 58), breaking the mirror symmetry perpendicular to the length of the stripes. It is possible that this is the origin of the asymmetry; it is also possible that the eccentricity may further be controlled by adjusting the ratio of the cell thickness to the stripe width.

## Part III

# Conclusions

## Chapter 7

# Conclusion

### 7.1 Summary of Results

CHAPTERS 3 and 4 considered the configuration adopted by a smectic liquid crystal in a hybrid-aligned cell. The structure discovered by Ruan *et al*[2] was shown, on cooling from the nematic phase through the nematic–smectic transition, to self-organize through a complicated sequence of intermediate phases: the well-known HAN configuration in the nematic phase; a “stripe” configuration stable over a very narrow temperature range  $\sim 0.1\text{K}$ ; upon further cooling, a stripe configuration modulated along the length of the stripes and, into the smectic phase, the known structure of fan-shaped domains arranged on a hexagonal lattice.

The intermediate “stripe” structure was shown to be exactly that discovered long ago by Cladis and Torza[1], but was studied *in situ* for the first time by confocal microscopy: the stripe structure was shown to be a sequence of smectic wedges at the planar surface, with the region immediately above possibly nematic. These results partly support the model of Cladis and Torza except that the corresponding wedges on the homeotropic surface were not observed in the cross-sections from confocal microscopy. It is clear that the dominant physical effect that causes the transition to the periodic striped state is the expulsion of the bend deformation present in the conventional HAN state by the fluctuating presmectic order.

There are, however, two possible mechanisms by which the wedges might form: the explanation suggested by Cladis and Torza is that the surface-enhanced smectic order grows into the cell just above the transition, compressing the central nematic region that undergoes some sort of buckling instability. This central nematic region remains stable over a short temperature range even below the normal critical temperature due to a renormalization of the transition temperature by the presence of director deformations with nonzero curl. The alternative explanation for the stripes is a spontaneous periodic curvature analogous to other examples of pattern formation in nematics, e.g. the situation where a liquid crystal with very anisotropic elastic constants is deformed with a magnetic field.

The linear relationship between cell thickness and the period of the structure was shown to hold over a much wider range of thicknesses than measured by Ruan *et al.* There nonetheless remains some suggestion in fig. 3.14 ( on page 70) that for thin cells, the period might be rather smaller than the cell thickness. Additionally, the period of the stripes in the very thick cells studied originally by Cladis and Torza is only about two-thirds of the cell thickness. It might be interesting, therefore, to see if the linear dependence falls off at either thinner or much thicker cells with 8CB. For the case of thin cells, there will undoubtedly be a transition to an undistorted state below some critical thickness [95].

The shape of the domains that form the unit cells of Ruan *et al.*'s structure are rather different to the corresponding domains in the structure of Cladis and Torza: while the latter are cylindrically symmetric Toroidal Focal Conic Domains (TFCDs), those of Ruan *et al.* have only mirror symmetry about the rubbing direction at the planar substrate. The evidence of confocal microscopy from Pishnyak *et al.*[72], and the present study in chapter 3, suggest that their structure is nonetheless focal conic (of either tilted Toroidal or Dupin cyclide of nonzero eccentricity) in contrast to the spherocylindrical model presented in [2].

Confocal microscopy in the nematic phase of the region between HAN domains of opposing orientation shows very clearly that the orientation of the nematic at the planar substrate is not parallel to the surface, but inclined at some angle. The surface pretilt breaks the mirror symmetry of the two possible opposing HAN configurations, and so the emission intensity profile for each state appears quite different: cross-sections were obtained of a disclination line between two such domain lines, and the intensity difference at the planar substrates suggests a surface tilt angle of around  $15^\circ$ .

It was shown that if the surface pretilt was also effective in the smectic phase, then the polar anchoring energy per unit area for a TFCD could be minimized by tilting the domain with respect to the surface normal and removing regions with high anchoring energy density; this mechanism is quite consistent with the confocal microscopy and probably acts in conjunction with the azimuthal anchoring mechanism suggested by Pisknyak *et al.*[72]; it is readily extended to tilted Dupin cyclide domains with suitable combinations of eccentricity and inclination of the line disclination with respect to the surface normal.

In the smectic phase of 8CB in cells prepared with evaporated silicon oxide to promote planar alignment, the domains were hexagonal in shape and were shown by confocal microscopy to be TFCDs without the interdomain homeotropic regions of the Cladis and Torza structure, instead separated from one another by curvature walls. A complete phenomenological theory was constructed for the circular-hexagonal transition: this showed that the close-packed hexagonal structure reduced the splay energy by excluding the highly distorted regions near the defect ellipse as well as minimizing the polar anchoring energy by eliminating the need for interdomain homeotropic regions; both at the expense of introducing curvature walls. It was furthermore shown that the circular state was favourable for large cell thicknesses, regardless of the value of the anchoring energy.

Both Ruan *et al.*'s structure, and that of the silicon oxide cells are interesting because curvature walls are normally too energetically expensive to be observed in smectics. In most situations, the size of the do-

mains reflects a compromise between the surface and bulk energies. The smectic in the hybrid-aligned cell, however, represents a system frustrated not just between the constraint of constant layer spacing and the boundary conditions, but also by a periodic boundary condition imposed by the intermediate stripe structure. The technique of surface micropatterning offers the possibility of imposing similar periodic boundary conditions and hence suggests the new possibility of designing surfaces that cause a smectic to self-assemble into some useful structure.

Chapter 5 looked at a liquid crystal system frustrated by a micropatterned surface: that of a nematic in contact with a series of alternate homeotropic and planar stripes, where the planar stripes were prepared so as to have some preferred azimuthal orientation. Recent results from Sharp Laboratories of Europe showed that, if the period of the stripes was sufficiently small, then the liquid crystal might violate the azimuthal anchoring condition at the planar stripes. A model proposed in this thesis, of a semi-infinite nematic in contact with such a surface, shows that this is possible only if the twist elastic constant is different to the bend and splay elastic constants and also if the azimuthal anchoring energy is rather weak  $\lesssim 5 \times 10^{-6} \text{Jm}^{-2}$ . In particular, it was shown that if  $K_2 < K_1$  and  $K_3$  then the elastic energy would favour alignment of the nematic director along the length of the stripes and if  $K_2 > K_1$  and  $K_3$ , the elastic energy would favour alignment orthogonal to the length of the stripes.

A new phase diagram for the semi-infinite nematic liquid crystal in contact with the striped substrate was also presented, extending previous work that predicted the nematic might adopt a uniform state if either set of stripes were sufficiently narrow[118]. A similar model was constructed for a nematic in contact with a striped surface where the stripes alternately promoted planar alignment of orthogonal azimuthal easy axis; it was shown that a distorted–uniform transition might take place if one set of stripes were sufficiently narrow, but that a planar–homeotropic transition could not take place.

The tendency of a micropatterned surface to align a nematic due to elastic anisotropy has recently been shown by the Leeds group to be sufficient to permit the construction of a Twisted Nematic Cell[142]. The behaviour of the nematic in such a cell is rather different from that in a conventional TN cell and was explored in chapter 6. The high effective surface tilt was shown to cause the director to rotate towards homeotropic in the centre of the cell; the same effect was shown to occur in TN cells prepared with uniform high-tilt substrates.

It was also shown that if the polar anchoring energy was reasonably weak ( $\sim 5 \times 10^{-5} \text{Jm}^{-2}$ ), that a state spatially uniform in the bulk was nearly degenerate with the twisted state, explaining some of the results of the Leeds group. This new uniform configuration has too much azimuthal anchoring energy to be observed in conventional TN cells. A complete simulation of a cell with surface micropatterning was presented for the first time within the limit that the cell thickness was much greater than the length scale of the patterning. These simulations show that the director profile in such a cell is very sensitive to the ratio of the elastic constants, and that the voltage by which such a cell has fully switched—the switching itself is threshold-less—is much lower than for a conventional TN cell. The chapter concluded with a brief

look at a smectic structure self-assembled by means of a micropatterned surface with confocal microscopy, measuring the eccentricity of the Dupin cyclide Focal Conic Domains formed for the first time from the reconstructed cross-section.

## 7.2 Open Problems and Future Work

Although the reason for the highly regular structure of Ruan *et al* has now been explained as being due to nucleation of the focal conic domains along the smectic wedges of the intermediate “stripe” phase, the mechanism by which the stripes form remains unclear. Cross-sections of the stripes from confocal microscopy suggest that as the wedges form, the smectic order parameter has not reached its equilibrium value. It seems very likely that the model of Cladis and Torza is incomplete since it is unable to explain the observed period of the stripes in 8CB; however, a more complete model would be very complicated, requiring spatially varying magnitude and phase of the smectic order parameter, nematic–smectic coupling, and inevitably requiring numerical simulation. In contrast to the situation with nematics, there has been very little work on the numerical simulation of smectics. Some preparatory work exists, including a complete elastic theory for smectic-A with a tensor representation of the smectic order parameter[14]; it would be helpful to develop from this a numerical simulation comparable to the Q-tensor methods[33, 101].

The structure found by Ruan *et al* and the work of chapter 4 suggests that surface pretilt may persist into the smectic phase. Unlike the elastic energy, the surface energy and curvature wall energies of the various admissible smectic configurations have not been studied extensively; with the new possibility of controlling the structure adopted by smectics as shown briefly in chapter 6, it might be useful to establish the relative surface energies of each sort of smectic configuration for arbitrary position and orientation of the surfaces. A significant obstacle to such a programme is that the functional form and strength of the smectic–surface anchoring potential are not well known. It remains a significant open problem to develop a microscopic model for the smectic–surface anchoring; there is very likely some insight to be gained from realistic Monte-Carlo simulations of the smectic–surface molecular interaction.

The technique of Confocal Microscopy has been shown in the literature and in this thesis to be tremendously powerful in that it permits non-destructive *in-situ* images of a structure of interest. What has not so far been attempted is the quantitative reconstruction of the director field (the analogous procedure for confocal microscopy does not appear to have been attempted either; a suitable procedure is described and applied to an example image in appendix B) or underlying parameters directly from the intensity measurements. The attraction of such an approach is that it is compatible with *high-throughput* machine vision techniques that permit rapid optimization of the design of a device by allowing the parameter space to be explored.

There are two obstacles to the quantitative analysis: The forward problem of computing an intensity distribution from a known director configuration is complicated and a complete model incorporating the



many physical effects has not yet been formulated. It was, however, identified in passing in chapter 2 that there is quite a unique prior that may be used to regularize the inverse problem: the boundary between a region of zero intensity (i.e. the substrate) and the dye-doped region (the liquid crystal) ought to be fine and the side of the deconvolved intensity function ought to be a step function. Intuitively then, it might be expected that a good deal of information on the axial dependence of the point spread function might be obtained with little ambiguity. Fluorescent microspheres have been commonly used in Biology[55] and their known shape used as a prior in the deconvolution problem; this might well be of use in the liquid crystal problem. Furthermore, there has been to date no analysis of whether the detailed emission spectrum (rather than its integral as heretofore used) contains additional information on the ordering.

It is anticipated that the recent development of cells with two- or three-dimensional liquid crystal structure—the ZBD, PABN and micropatterned TN geometries—will provoke a demand for some technique capable of resolving the dynamic behaviour of a liquid crystal as it is switched. Fast-scanning confocal microscopy[46, 55] may well be capable of resolving behaviour on timescales of a few microseconds or greater, but an alternative approach (analogous to that used in the Dynamic Fully Leaky Guided Mode technique[143]) is to gather data continuously, switching the cell periodically many times, and then recover the dynamic response by averaging over many periods.

The situation of the Twisted Nematic cell constructed from micropatterned surfaces was, in chapter 6, considered in the simplifying assumption that the length scale of the pattern was much smaller than the cell thickness. It was therefore possible to analyse the regions adjacent to each surface in two dimensions only rather than three. For cells of conventional display thickness, however, the director should depend on all three spatial coordinates and it is very likely that some interesting stability phenomena are to be found therein. In order to study this situation, it is necessary to extend the simulation presented in chapter 6 to three dimensions.

It remains finally to remark that the most interesting possibility suggested by this thesis: that of using surface micropatterning to produce highly ordered smectic structures, is an area virtually unexplored.

### 7.3 Publications

- T. J. Atherton and J. R. Sambles, “*Orientalional transition in a nematic liquid crystal at a patterned surface*”, Phys. Rev. E 74 022701 (2006)
- T. J. Atherton and J. R. Sambles, “*Numerical simulation of a twisted nematic cell constructed from micropatterned substrates*”, Mol. Cryst. Liq. Cryst., *submitted*

## 7.4 Conference Presentations

### Oral

- BLCS (British Liquid Crystal Society Annual Meeting) at York, UK 2006: “*Oriental transition in a nematic liquid crystal at a patterned surface*”
- BLCS at Exeter, UK 2005: “*How the tiger got his stripes: Periodic structure in hybrid-aligned 8CB above the nematic-smectic-A phase transition*”
- Rank Prize Conference Talk (Invited Speaker) at Grasmere, UK 2004: “*Periodic Frustration Structures in Liquid Crystal Films*”

### Poster

- ILCC at Keystone, CO 2006: “*Anomalous structures in cells constructed from micropatterned substrates*”
- SET for Britain at UK Parliament, London 2005: “*Imaging 3D Liquid Crystal Structures by Fluorescence Confocal Microscopy*”
- Institute of Physics Einstein Conference at Warwick, UK 2005: “*Novel Periodic Structures in Hybrid-Aligned Liquid Crystal Films*”
- ECLC (European Liquid Crystal Conference) at Sexten, Italy 2005: “*Periodic structure in hybrid-aligned 8CB in the vicinity of the nematic-smectic-A transition*”
- BLCS Poster at Manchester, UK 2004: “*Frustration Structures in Hybrid Aligned Smectic Cells*”

# Appendices

## Appendix A

# Derivation of the Natural Boundary Conditions for the Neumann-Dirichlet (Mixed) Problem

A liquid crystal free energy typically has the form

$$F = \int f(q_i, q_{i,j}) dV + \int g(q_i, \bar{q}_i) dS \quad (\text{A.1})$$

where the  $q_i(x_j)$  are a set of field quantities that together represent the liquid crystal order parameter and  $q_{i,j}$  are their derivatives  $\frac{\partial q_i}{\partial x_j}$  with respect to the components  $x_j$  of an orthogonal system of spatial coordinates. The bulk free energy  $f(q_i, q_{i,j})$  is to be integrated over the volume of the liquid crystal (or a unit volume if appropriate) and the surface free energy  $g(q_i, \bar{q}_i)$  is to be integrated over the surfaces. Extrema of A.1 may be found using variational calculus however the surface term, which quantifies the energy cost of changing the components of the order parameter from some preferred value  $\bar{q}_i$ , is not generally present in the sort of problems solved in textbooks on variational calculus which are normally from classical mechanics; nor is it to be found in liquid crystal textbooks. This appendix shall elucidate the necessary extension to the derivation of the Euler-Lagrange equations in the hope it may be of assistance to future readers.

Extrema of  $F$  may be found by variations of the free energy

$$\begin{aligned} \delta F &= \delta \int f(q_i, q_{i,j}) dV + \delta \int g(q_i, \bar{q}_i) dS \\ &= \int \delta f(q_i, q_{i,j}) dV + \int \delta g(q_i, \bar{q}_i) dS \\ &= \int \sum_{i,j} \left[ \frac{\partial f(q_i, q_{i,j})}{\partial q_i} \delta q_i + \frac{\partial f(q_i, q_{i,j})}{\partial q_{i,j}} \delta q_{i,j} \right] dV + \int \sum_i \frac{\partial g(q_i, \bar{q}_i)}{\partial q_i} \delta q_i dS. \quad (\text{A.2}) \end{aligned}$$

The second term in the volume integral may be integrated by parts

$$\delta F = \int \sum_{ij} \delta q_i \left[ \frac{\partial f(q_i, q_{i,j})}{\partial q_i} - \frac{\partial}{\partial x_j} \frac{\partial f(q_i, q_{i,j})}{\partial q_{i,j}} \right] dV + \int \sum_i \delta q_i \left[ s_j \frac{\partial f(q, q_{i,j})}{\partial q_{i,j}} + \frac{\partial g(q_i, \bar{q}_i)}{\partial q_i} \right] dS \quad (\text{A.3})$$

where  $s_j$  are components of the surface normal in the orthogonal coordinate system.

At extremal  $F$  with respect to arbitrary infinitesimal variations  $\delta q_i$  of the components of the order parameter field, each term of each sum in both integrands must equate to zero. The terms of the sum in the bulk integral give the well-known Euler-Lagrange equations

$$\frac{\partial f(q_i, q_{i,j})}{\partial q_i} - \frac{\partial}{\partial x_j} \frac{\partial f(q_i, q_{i,j})}{\partial q_{i,j}} = 0 \quad (\text{A.4})$$

where  $i$  and  $j$  are free indices. The surface integrand gives the natural boundary conditions

$$s_j \frac{\partial f(q, q_{i,j})}{\partial q_{i,j}} + \frac{\partial g(q_i, \bar{q}_i)}{\partial q_i} = 0 \quad (\text{A.5})$$

as required.

## Appendix B

# On the Automated Reconstruction of Director Profiles from Polarizing Microscope Images

Chapter 2 introduced the use of polarizing microscopy to analyse liquid crystal structures, a technique which was of use because the quantity of interest—the director field as a function of position—caused some variation or contrast in an observable quantity—the intensity of light—that also happened to be a function of position (albeit two-dimensional). It is natural to ask then, given such an image, to what extent it is possible to reconstruct a *quantitative* director field *automatically* from a polarizing microscope image.

It is clear that only the in-plane (azimuthal) component of the director can be reconstructed in this way and it is therefore necessary to restrict attention to such systems where, firstly, the azimuthal component of the director field does not vary significantly through the distance of the cell and secondly, the polar variation of the director field in the vertical direction does not significantly alter the intensity distribution observed. The HAN cell is such a system and it is therefore appropriate to attempt such an analysis on fig. 2.3.

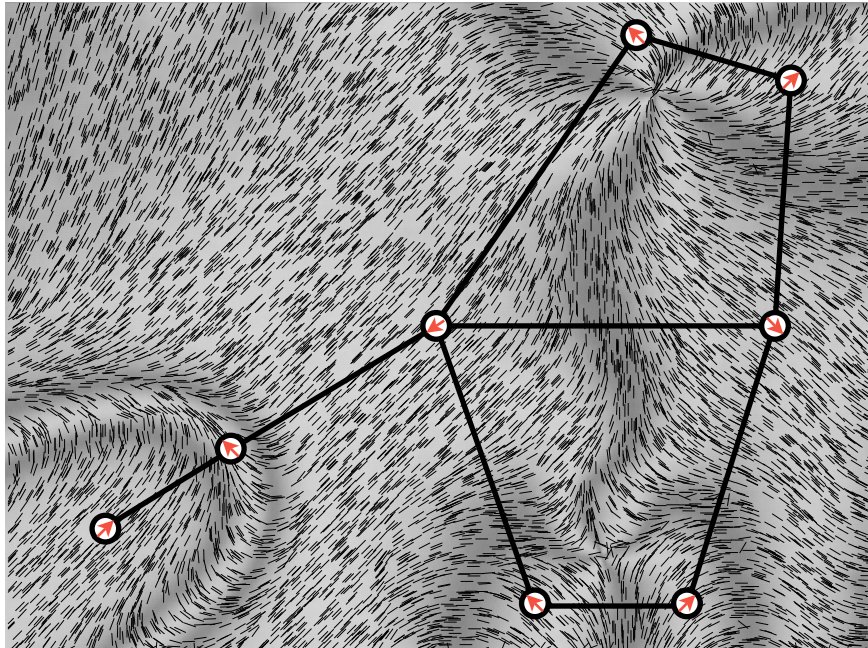
The mapping of the director field to the intensity field (fig. B.1) is problematic in that it is such that many possible director angles are mapped to a single intensity value. It is straightforward to obtain some angle from the intensity by applying an inverse function if the intensity is appropriately scaled so as to lie in the interval  $0 \leq I \leq 1$ ,

$$\psi = \frac{1}{2} \arcsin \sqrt{I}; \quad (\text{B.1})$$

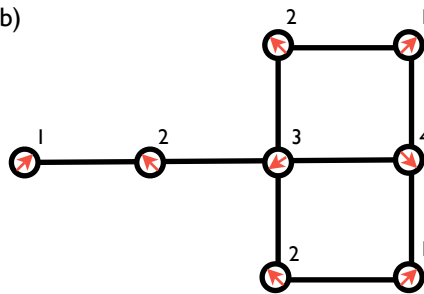
the angle obtained then lies in the interval  $0 < \phi < \pi/4$ . Having scaled intensity values in the entire image appropriately, this inverse function can be applied to the image  $I_{ij}$  to yield a corresponding matrix



(a)



(b)



(c)

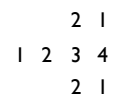


Figure B.2: (a) Deconstruction of a polarizing microscope image of a HAN cell with defects and domain wall into a graph representation of its distinct areas showing one possible quadrant labelling for each node (b) redrawn version of the graph with quadrants labelled by number and (c) a simplified notation for the same graph.



		4	3			4	3
3	2	1	2		3	4	1
		4	3			4	3
		2	3			2	3
3	2	1	4		3	4	1
		2	3			2	3

Table B.1: Four possible labellings of quadrants from the graph depicted in fig. B.2; three further distinct configurations may be obtained from each of these by making cyclic permutations of the sequence 1, 2, 3, 4

case of the image from the HAN cell (fig. B.2), there is two further restrictions: firstly, since the band to the bottom left represents a reorientation wall, the two regions outside cannot be assigned the same quadrant (the director must differ by  $\pi$ ); secondly, the nodes on opposite sides of the disclination must also be different. With this restriction, the 16 possible assignments for the quadrants may be enumerated (table B.1). A program, written to perform the whole process automatically, was used to produce the reconstructed director profile in fig. 2.3.

This appendix has outlined a general procedure for the reconstruction of the director field from a polarizing microscope image, and for determining all possible physical director fields that may have produced a particular image. It is envisioned that a similar procedure may be utilized in the reconstruction of director profiles from FCM/FCPM image stacks.

## Appendix C

# Critical Exponents for the Twist and Bend Elastic Constants at the Nematic–Smectic–A Transition in 8CB

In chapter 4, it was mentioned that although a number of studies that measured the behaviour with temperature of the elastic constants, very few studies attempted to extract values for the critical exponents. In this appendix, a probabilistic approach is used to extract the critical exponents from these published studies.

It is expected that the twist and bend elastic constants follow some power law as discussed in section 4.1

$$K_i' = K_i^N + \delta K_i (T - T_c)^{-\nu_i}. \quad i \in \{2, 3\} \quad (\text{C.1})$$

The fitting procedure used in the CBOOA papers[78, 79, 80, 81] is to take the logarithm of equation C.1,

$$\log(K_i - K_i^N) = \log(\delta K_i) - \nu_i \log(T - T_c), \quad (\text{C.2})$$

which implies that for known  $K_i^N$  and  $T_c$ , a plot of  $\log(K_i - K_i^N)$  against  $\log(T - T_c)$  will yield a straight line of negative gradient  $\nu_i$ , a parameter that may be extracted by the least squares procedure. In practice,  $K_i^N$  and  $T_c$  are not known precisely—the presence of deformations with  $|\nabla \times \mathbf{n}| = 0$  in fact makes the transition temperature rather ill-defined for measurements involving a Fredericks transition (see section 4.2)—and so must be used as fitting parameters. Some reason for the experimental difficulty in determining the critical exponents is suggested immediately by the form of (C.2): the errors associated with each of the measured values  $\{K_i\}$  are typically of similar size but when scaled logarithmically, errors far away from the transition become proportionately larger. It is therefore necessary to measure the elastic constants very

close to the transit on temperature (with the consequent problem of maintaining temperature stability) in order to determine the critical exponents with any precision. Certain studies—those of Hakemi *et al*[85] and Coles *et al*[144]—do not measure the elastic constants sufficiently close to the transition to give useful information about the critical exponents but do confirm the inequality  $K_2 < K_1 < K_3$  away from the transition.

A significant problem with the least squares procedure is that it is only justified if the errors are constant and of known magnitude, and gives no indication of the error associated with the fitted parameters. An approach that does is to compute the probabilistic likelihood function for the model parameters given the data<sup>1</sup>

$$P(\nu, K^N, T_c, \delta K | \{K, T, \sigma\}) = \exp\left(-\sum_{j=1}^N \frac{[\ln(K_j - K^N) - \ln(\delta K) + \nu \log(T_j - T_c)]}{\sigma_j^2}\right) \quad (\text{C.3})$$

where the errors  $\{\sigma\}$  have been scaled logarithmically. The expression C.3 is not rigorously justified as it assumes that the errors associated with each measurement are distributed according to a Gaussian, which is evidently not the case. It has been shown that the Gaussian distribution is the least informative distribution for the noise (see [74] for a detailed review) and so it is to be anticipated that the error estimates of this section are perhaps a little larger than justified by the data. A second assumption implicit in C.3 is that no information at all was known about  $\nu, K^N, T_c$  and  $\delta K$ . In fact there are some natural constraints on the value of the parameters, e.g.  $K^N < \min\{K\}$  and  $T_c < \min\{T\}$  and moreover, it is natural to reject fitted values of  $T_c$  that imply unfeasibly large values of  $|\nabla \times \mathbf{n}|$ . These constraints, properly formulated as *prior distribution functions* for the parameters are naturally incorporated within the probabilistic scheme by use of Bayes' theorem [74].

A significant advantage of the probabilistic approach is that, since the only parameter of interest is the value of  $\nu$ , and the values of  $K_i^N, T_c$  and  $\delta K_i$  are superfluous, it is possible to integrate (C.3) over all possible values of these “nuisance parameters” to yield a probability distribution function for  $\nu$

$$P(\nu | \{K, T, \sigma\}) = \frac{\int \int \int P(\nu, K^N, T_c, \delta K | \{K, T, \sigma\}) dK^N dT_c d\delta K}{\int \int \int \int P(\nu, K^N, T_c, \delta K | \{K, T, \sigma\}) dK^N dT_c d\delta K d\nu}$$

where the denominator ensures that the probability distribution is properly normalized. The probability distributions for  $\nu_2$  and  $\nu_3$  are plotted in fig. C.1 from the studies of Malraison *et al* [84], Karat *et al* [82] and DasGupta *et al* [86]. They suggest that  $\nu_3 > \nu_2$ , although the measurements are not particularly consistent and the distributions are very wide. The conclusions of this thesis rely merely on  $K_3 > K_2$  which appears to be the case experimentally.

---

<sup>1</sup>to be read “The probability density that the model parameters have values  $\nu, K^N, T_c, \delta K$  given the set of measured elastic constants and temperatures and their associated errors  $\{K, T, \sigma\}$ ”

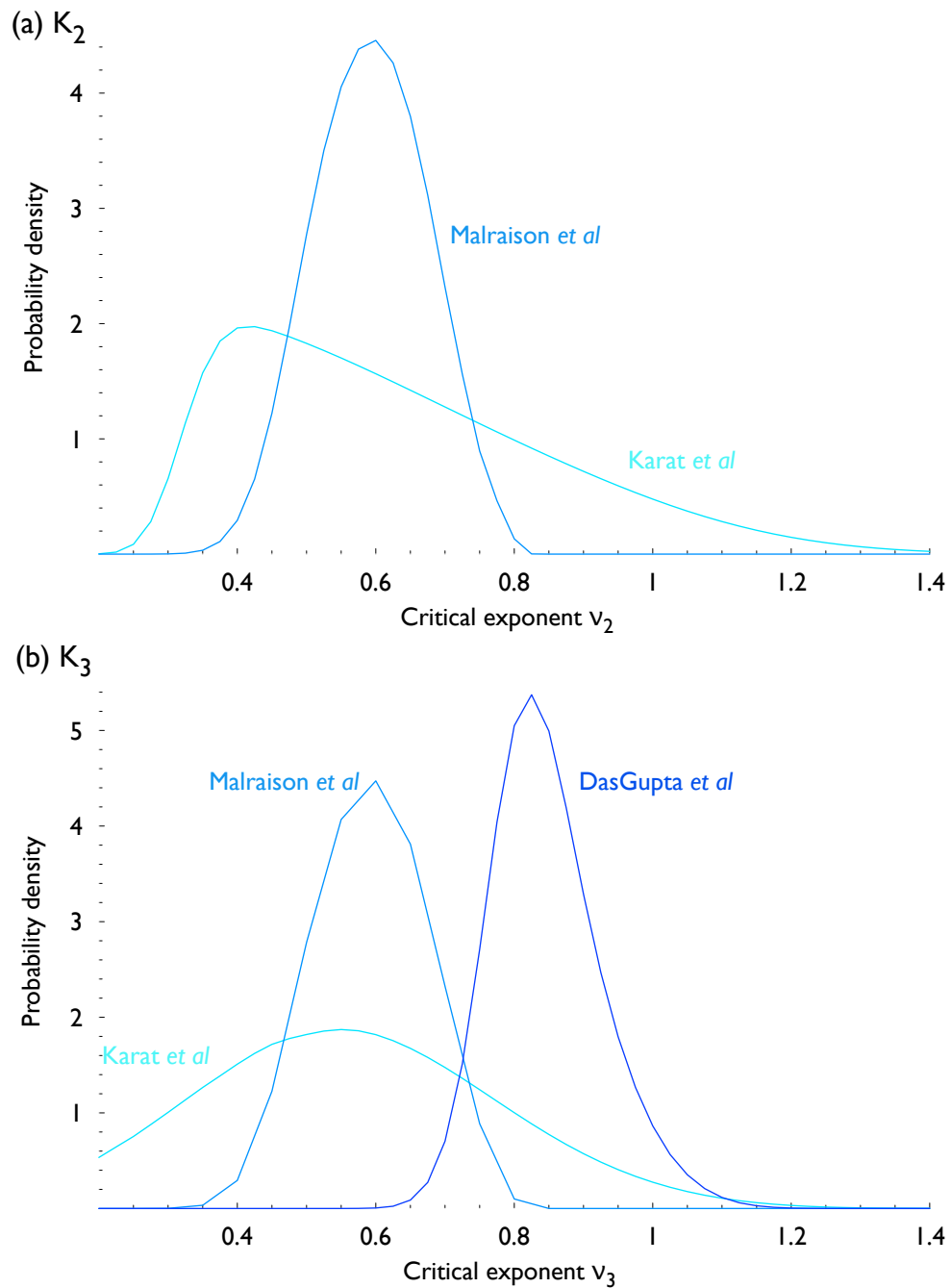


Figure C.1: Normalized probability distribution functions for the critical exponents associated with the elastic constants in 8CB (a) the twist exponent  $\nu_2$ , (b) the bend exponent  $\nu_3$ .

## Appendix D

# The Free Energy and Unconstrained Euler-Lagrange Equations for the Cartesian Representation of the Director

### One-Dimensional Problem

Adopting the representation of the director

$$\mathbf{n} = \{n_x(z), n_y(z), n_z(z)\}, \quad (\text{D.1})$$

the free energy density is, in units of  $K_1$ ,

$$f = [(k_2 - k_3)n_y^2 + k_3] n_x'^2 + 2(k_3 - k_2)n_x n_y n_y' n_x' + K [(k_3 - k_2)n_y^2 + (k_3 - k_2)n_z^2 + k_2] n_y'^2 + n_z'^2 - \epsilon_\perp \epsilon_0 V'(z)^2 - \Delta \epsilon \epsilon_0 n_z^2 V'(z)^2 \quad (\text{D.2})$$

where  $k_2 = K_2/K_1$ . The left hand sides of the unconstrained Euler-Lagrange equations are then

$$\begin{aligned} \mathcal{E}_{n_x} &= (k_3 - k_2) n_x'' n_y^2 - (k_2 - k_3) (2n_x' n_y' - n_x n_y'') n_y + (k_2 - k_3) n_x n_y'^2 - k_3 n_x'' \\ \mathcal{E}_{n_y} &= (k_2 - k_3) n_y'' n_y^2 + (k_2 - k_3) (2n_x'^2 + n_y'^2 + n_x n_x'') n_y + \\ &\quad + 2(k_2 - k_3) n_z n_y' n_z' + (k_2 - k_3) n_z^2 n_y'' - k_2 n_y'' \\ \mathcal{E}_{n_z} &= -n_z'' - n_z (k_2 - k_3) n_y'^2 + \Delta \epsilon \epsilon_0 V'(z)^2 \\ \mathcal{E}_V &= \frac{\epsilon_0}{K_1} \frac{d}{dz} [V'(z) (\epsilon_\perp + \Delta \epsilon n_z^2)] \end{aligned} \quad (\text{D.3})$$

## Two-Dimensional Problem

Adopting the notation

$$\begin{aligned} n_{\xi,x} &= \frac{\partial n_{\xi}}{\partial x}, & n_{\xi,z} &= \frac{\partial n_{\xi}}{\partial z} \\ n_{\xi,x,x} &= \frac{\partial^2 n_{\xi}}{\partial x^2}, & n_{\xi,x,z} &= \frac{\partial^2 n_{\xi}}{\partial x \partial z}, & n_{\xi,z,z} &= \frac{\partial^2 n_{\xi}}{\partial z^2} \end{aligned} \quad (\text{D.4})$$

the free energy density is

$$\begin{aligned} 2f &= n_{x,x}^2 + [(k_2 - k_3) n_y^2 + k_3] n_{x,z}^2 + k_2 n_z^2 n_{y,x}^2 - k_3 n_z^2 n_{y,x}^2 + k_3 n_{y,x}^2 + k_2 n_y^2 n_{z,x}^2 - k_3 n_y^2 n_{z,x}^2 + \\ &+ k_3 n_{z,x}^2 + n_{z,z}^2 + [(k_3 - k_2) n_y^2 + (k_3 - k_2) n_z^2 + k_2] n_{y,z}^2 + 2(k_3 - k_2) n_y n_z n_{y,x} n_{z,x} - \\ &- 2(k_2 - k_3) n_x n_{y,z} (n_z n_{y,x} - n_y n_{z,x}) + 2n_{x,x} n_{z,z} - \\ &- 2n_{x,z} [(k_2 - k_3) n_{z,x} n_y^2 + (k_3 - k_2) n_z n_{y,x} n_y + (k_2 - k_3) n_x n_{y,z} n_y + k_3 n_{z,x}] - \\ &- \frac{\epsilon_0}{K_1} [\epsilon_{\perp} (V_x^2 + V_z^2) + \Delta \epsilon (n_z^2 V_z^2 - n_y^2 V_x^2 - n_z^2 V_x^2 + V_x^2 + 2n_x n_z V_z V_x)] \end{aligned} \quad (\text{D.5})$$

and the left hand sides of the Euler-Lagrange equations are

$$\begin{aligned} \mathcal{E}_{n_x} &= (k_2 - k_3) (2n_{x,z} n_{y,z} - 3n_{z,x} n_{y,z} + n_{y,x} n_{z,z} + n_z n_{y,x,z} - n_x n_{y,z,z}) n_y + \\ &+ (k_2 - k_3) (n_{x,z,z} - n_{z,x,z}) n_y^2 + 2k_2 n_z n_{y,x} n_{y,z} - 2k_3 n_z n_{y,x} n_{y,z} + n_{x,x,x} + \\ &+ k_3 n_{x,z,z} + n_{z,x,z} - k_3 n_{z,x,z} + (k_3 - k_2) n_x n_{y,z}^2 - \frac{\epsilon_0}{K_1} \Delta \epsilon n_z V_x V_z \\ \mathcal{E}_{n_y} &= (k_2 - k_3) n_{y,z,z} n_y^2 + 2(k_2 - k_3) n_y (n_{x,z}^2 + n_{y,z}^2 + 2n_{x,z} n_{z,x}) + \\ &+ k_2 n_y (2n_{z,x}^2 - n_z n_{x,x,z} + n_x n_{x,z,z} + n_z n_{z,x,x} - n_x n_{z,x,z}) + \\ &+ k_3 n_y (n_z n_{x,x,z} - n_x n_{x,z,z} - n_z n_{z,x,x} + n_x n_{z,x,z} - 2n_{z,x}^2) + \\ &+ (k_2 - k_3) n_z [n_{x,z} n_{y,x} - 2n_{z,x} n_{y,x} + n_{y,z} (n_{x,x} + 2n_{z,z}) + 2n_x n_{y,x,z}] + \\ &+ k_2 (n_x n_{y,z} n_{z,x} + n_x n_{y,x} n_{z,z} - n_{y,z,z}) - k_3 (n_x n_{y,z} n_{z,x} + n_x n_{y,x} n_{z,z} + n_{y,x,x}) \\ &+ (k_2 - k_3) (n_{y,z,z} - n_{y,x,x}) n_z^2 + \frac{\epsilon_0}{K_1} \Delta \epsilon n_y V_x^2 \\ \mathcal{E}_{n_z} &= k_2 (n_{x,x,z} n_y^2 - n_{z,x,x} n_y^2 + 3n_{x,z} n_{y,x} n_y - n_{x,x} n_{y,z} n_y - 2n_{y,x} n_{z,x} n_y - n_x n_{y,x,z} n_y) + \\ &+ k_3 (n_{z,x,x} n_y^2 - n_{x,x,z} n_y^2 - 3n_{x,z} n_{y,x} n_y + n_{x,x} n_{y,z} n_y + 2n_{y,x} n_{z,x} n_y + n_x n_{y,x,z} n_y) - \\ &- n_{x,x,z} - n_{z,z,z} - 2k_2 n_x n_{y,x} n_{y,z} + n_z (k_2 - k_3) (2n_{y,x}^2 - n_{y,z}^2 - n_y n_{y,x,x}) + \\ &+ k_3 (n_{z,x,x} - 2n_x n_{y,x} n_{y,z} - n_{x,x,z}) - \frac{\epsilon_0}{K_1} \Delta \epsilon [n_z (V_z^2 - V_x^2) + n_x V_x V_z] \\ \mathcal{E}_V &= -\frac{\epsilon_0}{K_1} \nabla \cdot \begin{pmatrix} \epsilon_{\perp} + \Delta \epsilon n_x^2 & \Delta \epsilon n_x n_z \\ \Delta \epsilon n_x n_z & \epsilon_{\perp} + \Delta \epsilon n_z^2 \end{pmatrix} \begin{pmatrix} V_x \\ V_z \end{pmatrix}. \end{aligned} \quad (\text{D.6})$$

## Appendix E

# Explicit Solvers for the Cartesian Component Representation of the Director are Numerically Stable

In chapter 6, the Euler-Lagrange equations for a nematic liquid crystal were solved numerically. The method adopted was to simultaneously solve the coupled Euler-Lagrange equations for all mesh points simultaneously by iteratively taking Newton steps from an initial trial solution; this scheme is referred to as *fully implicit* as the updated values of the field variables at each point depend implicitly on their values at all other points.

Another scheme is to recast the Euler-Lagrange equations as a source term in a diffusion equation

$$\frac{\partial n_\xi}{\partial t} = \mathcal{E}_{n_\xi} \quad (\text{E.1})$$

which may be discretized in time to give an iteration formula

$$n_\xi^{t+1} = n_\xi^t + \gamma \mathcal{E}_{n_\xi} \quad (\text{E.2})$$

where the notional discrete time interval  $\gamma$  must be small enough to ensure numerical stability. Such a scheme is referred to as *explicit*—the updated director components depend explicitly on their previous values—and are very easy to program but are very rarely numerically stable.

Explicit schemes are, however, attractive in that it is very easy to impose the normalization constraint. Replacing the left hand side of the unconstrained Euler-Lagrange equations with that of the constrained Euler-Lagrange equations contributes a term  $+2\gamma\lambda n_\xi^t$  to the right hand side of (E.2). Squaring each side

and summing over each director component yields a quadratic equation for  $\lambda$

$$\sum_{\xi} \left( n_{\xi}^{t+1} \right)^2 = (1 + 2\gamma\lambda)^2 \sum_{\xi} \left( n_{\xi}^t \right)^2 + \gamma^2 \sum_{\xi} \mathcal{E}_{n_{\xi}}^2 + 2\gamma(1 + 2\gamma\lambda) \sum_{\xi} n_{\xi}^t \mathcal{E}_{n_{\xi}} = 1 \quad (\text{E.3})$$

which may be solved and substituted into the constrained form of (E.2). This scheme just described was in fact numerically stable and converges if  $\gamma \lesssim 1/8$ . It is however, not possible to incorporate the potential field into such a scheme as the stability is then lost.



# Bibliography

- [1] P. E. Cladis and S. Torza. Growth of a smectic A from a bent nematic phase and the smectic light valve. *J. Appl. Phys.*, 46:584–599, 1975.
- [2] L. Z. Ruan, J. R. Sambles, and I. W. Stewart. Self-organized periodic photonic structure in a nonchiral liquid crystal. *Phys. Rev. Lett.*, 91(3):033901, July 2003.
- [3] S. Chandrasekhar. *Liquid Crystals*. Cambridge University Press, 2nd edition, 1992.
- [4] P. G. de Gennes and J. Prost. *The Physics of Liquid Crystals*. Clarendon Press, 1995.
- [5] E. B. Priestley, P. J. Wojtowicz, and P. Sheng. *Introduction to Liquid Crystals*. Plenum Press, 1974.
- [6] S. J. Elston and J. R. Sambles, editors. *The Optics of Liquid Crystals*. Taylor & Francis, 1998.
- [7] R. N. McRuer, L. R. McAdams, and J. W. Goodman. Ferroelectric liquid-crystal digital scanner. *Opt. Lett.*, 15:1415–7, 1990.
- [8] M. Stalder and M. Schadt. Beam steering devices based on switchable liquid crystal phase gratings. In *16th Int. Disp. Res. Conf.*, pages 434–437. Society for Information Display, 1996.
- [9] D. Duca, A. V. Sukhov, and C. Umeton. Detailed experimental investigation on recording of switchable diffraction gratings in polymer dispersed liquid crystal films by UV laser curing. *Liq. Cryst.*, 26:931–937, 1999.
- [10] K. Rai, A. E. Fox, and A. K. Fontecchio. Holographically formed polymer dispersed liquid crystal films for compact transmission spectrometer applications. In *Poster Presentation, ILCC 2006 Conference, Denver*, 2006.
- [11] T. Larsen, A. Bjarklev, A. Hermann, and J. Broeng. Optical devices based on liquid crystal photonic bandgap fibres. *Optics Express*, 11:2589–2596, 2003.
- [12] P. E. Cladis. New liquid crystal phase diagram. *Phys. Rev. Lett.*, 35:48–51, 1975.
- [13] D. Guillon, P. E. Cladis, and J. Stamatoff. X-ray study and microscopic study of the reentrant nematic phase. *Phys. Rev. Lett.*, 41:1598–1601, 1978.
- [14] M. Linehan. *Towards Rigorous Theories of Liquid Crystals*. PhD thesis, University of Exeter, 1999.

- [15] J. Als-Nielsen and J. D. Lister. Observation of algebraic decay of positional order in a smectic liquid crystal. *Phys. Rev. B*, 22(1):312–320, July 1980.
- [16] M. Kleman. Energetics of the focal conics of smectic phases. *J. Phys. France*, 38:1511–1518, 1977.
- [17] M. Nakagawa. A theoretical study of smectic focal domains. *J. Phys. Soc. Jap.*, 59(1):81–89, January 1990.
- [18] I. W. Stewart. On the parabolic cyclide focal-conic defect in smectic liquid crystals. *Liq. Cryst.*, 15(6):859–869, December 1993.
- [19] C. S. Rosenblatt, R. Pindak, N. A. Clark, and R. B. Meyer. The parabolic focal conic: A new smectic-A defect. *J. Phys. France*, 38:1105–1115, 1977.
- [20] Ingo Dierking. *Textures of Liquid Crystals*. Wiley-VCH, 2003.
- [21] Ph. Boltenhagen, O. D. Lavrentovich, and M. Kleman. Focal conic domains with positive gaussian curvature and saddle-splay rigidity of smectic  $l_\alpha$  phases. *Phys. Rev. A*, 46:R1743–6, 1992.
- [22] P. G. de Gennes. An analogy between superconductors and smectics A. *Solid State Comm.*, 10(9):753–756, 1972 1972.
- [23] W. L. McMillan. Simple molecular model for the smectic A phase of liquid crystals. *Phys. Rev. A*, 4(3):1238–1246, September 1971.
- [24] W. H. Press, S. A. Teukolsky, W. T. Vetterling, and B. P. Flannery. *Numerical Recipes in C: The Art of Scientific Computing*. Cambridge University Press, 1988.
- [25] D. C. Rapaport. *The art of molecular dynamics simulations*. Cambridge University Press, 1995.
- [26] Z. E. Hughes, M. R. Wilson, and L. M. Stimson. Coarse-grained simulation studies of a liquid crystal dendrimer: towards computational predictions of nanoscale structure through microphase separation. *Soft Matter*, 1:436–443, 2005.
- [27] M. P. Allen and D. Frenkel. Calculation of liquid-crystal Frank constants by computer simulation. *Phys. Rev. A*, 37:1813–16, 1988.
- [28] M. Rotunno, M. Buscaglia, C. Chiccoli, F. Mantegazza, P. Pasini, T. Bellini, and C. Zannoni. Nematics with quenched disorder: pinning out the origin of memory. *Phys. Rev. Lett.*, 94:097802, 2005.
- [29] I. W. Stewart. *The static and dynamic continuum theory of liquid crystals*. Taylor & Francis, 2004.
- [30] R. B. Meyer. Piezoelectric effects in liquid crystals. *Phys. Rev. Lett.*, 22:918–921, 1969.
- [31] P. Rudquist and S. T. Lagerwall. On the flexoelectric effect in nematics. *Liq. Cryst.*, 23:503–510, 1997.

- [32] M. G. Calkin. *Lagrangian and Hamiltonian Mechanics*. World Scientific, 1996.
- [33] N. Mottram and C. Newton. Introduction to q-tensor theory. 2004. URL <http://www.maths.strath.ac.uk/research/reports/2004/10.pdf>.
- [34] A. A. Sonin. *The Surface Physics of Liquid Crystals*. Gordon and Breach, 1995.
- [35] M. C. Petty. *Langmuir-Blodgett Films: An Introduction*. Cambridge University Press, 1996.
- [36] V. K. Gupta and N. L. Abbott. Azimuthal anchoring transition of nematic liquid crystals on self-assembled monolayers formed from odd and even alkenethiols. *Phys. Rev. E*, 54:R4540–R4543, 1996.
- [37] V. K. Gupta and N. L. Abbott. Design of surfaces for patterned alignment of liquid crystals on planar and curved substrates. *Science*, 276:1533–1536, 1997.
- [38] B. W. Lee and N. Clark. Alignment of liquid crystals with patterned isotropic surfaces. *Science*, 291:2576–2579, 2001.
- [39] D. W. Berreman. Solid surface shape and the alignment of an adjacent nematic liquid crystal. *Phys. Rev. Lett.*, 28:1683, 1972.
- [40] G. Barbero and G. Durand. Order parameter spatial variation and anchoring energy for nematic liquid crystals. *J. Appl. Phys.*, 69:6968–6973, 1991.
- [41] J. Kerslake. *Fully guided mode studies of hybrid-aligned nematics*. PhD thesis, University of Exeter, 2005.
- [42] G. P. Sinha, C. Rosenblatt, and L. V. Mirantsev. Disruption of surface-induced smectic order by periodic surface corrugations. *Phys. Rev. E*, 65:041718, 2002.
- [43] A. Rapini and M. Papoular. Distortion d’une lamelle nématique sous champ magnétique conditions d’ancrage aux parois. *J. Phys. Colloq. France*, 30:C4–54, 1969.
- [44] S. V. Shiyankovskii, A. Glushchenko, Y. Reznikov, O. D. Lavrentovich, and J. L. West. Tensor and complex anchoring in liquid crystals. *Phys. Rev. E*, 62:R1477–R1480, 2000.
- [45] Z. Li and O. D. Lavrentovich. Surface anchoring and growth pattern of the field-driven first-order transition in a smectic-A liquid crystal. *Phys. Rev. Lett.*, 73:280–283, 1994.
- [46] C. J. R. Sheppard and D. M. Shotton. *Confocal Laser Scanning Microscopy*. Bios Scientific Publishers Ltd, 1997.
- [47] F. Yang, J. R. Sambles, Y. Dong, and H. Gao. Fully leaky guided wave determination of the polar anchoring energy of a homogeneously aligned nematic liquid crystal. *J. Appl. Phys.*, 87:2726–2735, 2000.

- [48] F. Yang and J. R. Sambles. Optical characterization of liquid crystals by means of half-leaky guided modes. *J. Opt. Soc. Am. B*, 10:858–866, 1993.
- [49] F. Yang, J. R. Sambles, and G. W. Bradberry. Half-leaky guided wave determination of azimuthal anchoring energy and twist elastic constant of a homogeneously aligned nematic liquid crystal. *J. Appl. Phys.*, 85:728–733, 1999.
- [50] S. A. Jewell and J. R. Sambles. Fully leaky guided mode study of the flexoelectric effect and surface polarization in hybrid aligned nematic cells. *J. Appl. Phys.*, 92:19–24, 2002.
- [51] K. R. Welford, J. R. Sambles, and M. G. Clark. Guided modes and surface plasmon-polaritons observed with a nematic liquid crystal using attenuated total reflection. *Liquid Crystals*, 2(91):91–105, January–February 1987.
- [52] B. T. Hallam, F. Yang, and J. R. Sambles. Quantification of the azimuthal anchoring of a homogeneously aligned nematic liquid crystal using fully-leaky guided modes. *Liq. Cryst.*, 26:657–662, 1999.
- [53] L. Taylor, R. Richardson, and J. Ebbutt. X-ray diffraction studies of surface stabilised ferroelectric liquid crystals in both low and high pre-tilt devices. *Ferroelectrics*, 180:71–82, 1996.
- [54] C. W. Garland and G. Nounesis. Critical behavior at nematic–smectic-A phase transitions. *Phys. Rev. E*, 49(4):2964–2971, April 1994.
- [55] S. Inoue. *Handbook of Biological Confocal Microscopy*, chapter 1, pages 1–17. Plenum Press (New York), 1995.
- [56] G. A. Held, L. L. Kosbar, I. Dierking, A. C. Lowe, G. Grinstein, V. Lee, and R. D. Miller. Confocal microscopy study of texture transitions in a polymer stabilized cholesteric liquid crystal. *Physical Review Letters*, 79:3443–3446, 1997.
- [57] R. Petkovsek, J. Pirs, S. Kralj, M. Copic, and D. Suput. Influence of polymer network in polymer-stabilized ferroelectric liquid crystals and its direct observation using a confocal microscope. *J. Appl. Phys.*, 99:014102, 2006.
- [58] O. D. Lavrentovich. Fluorescence confocal polarizing microscopy: Three-dimensional imaging of the director. *Pramana*, 61:373–384, 2003.
- [59] I. I. Smalyukh, S. V. Shiyonovskii, and O. D. Lavrentovich. Three-dimensional imaging of orientational order by fluorescence confocal polarizing microscopy. *Chem. Phys. Lett.*, 336:88–96, 2001.
- [60] D. Yelin, Y. Silberberg, Y. Barad, and J. S. Patel. Depth-resolved imaging of nematic liquid crystals by third-harmonic microscopy. *App. Phys. Lett.*, 74(21):3107–3109, 1999.

- [61] I. I. Smalyukh and O. D. Lavrentovich. Three-dimensional director structures of defects in grandjean-cano wedges of cholesteric liquid crystals studied by fluorescence confocal polarizing microscopy. *Phys. Rev. E*, 66(5):051703, 2002.
- [62] H. Matthias, T. Roder, R. B. Wehrspohn, H. S. Kitzerow, S. Matthias, and S. J. Picken. Spatially periodic liquid crystal director field appearing in a photonic crystal template. *Appl. Phys. Lett.*, 87:241105, 2005.
- [63] I. I. Smalyukh, R. Pratibha, N. V. Madhusudana, and O. D. Lavrentovich. Selective imaging of 3d director fields and study of defects in biaxial smectic-A liquid crystals. *Eur. Phys. J. E*, 16:179–191, 2005.
- [64] G. Liao, I. I. Smalyukh, J. R. Kelly, O. D. Lavrentovich, and A. Jakli. Electro-rotation and electro-translation of colloidal particles in liquid crystals. *IElec. Liq. Cryst. Comms.*, 2005.
- [65] I. I. Smalyukh, O. D. Lavrentovich, A. N. Kuzmin, A. V. Kachynski, and P. N. Prasad. Elasticity-mediated self-organization and colloidal interactions of solid spheres with tangential anchoring in a nematic liquid crystal. *Phys. Rev. Lett.*, 95:157801, 2005.
- [66] I. C. Khoo. Optically induced molecular reorientation and third-order nonlinear optical processes in nematic liquid crystals. *Phys. Rev. A*, 23(4):2077–2081, 1981.
- [67] F. Simoni and O. Francescangeli. Effects of light on the molecular orientation of liquid crystals. *J. Phys.: Cond. Matt.*, 11:R439–R487, 1999.
- [68] S. F. Gibson and F. Lanni. Diffraction by a circular aperture as a model for three-dimensional optical microscopy. *J. Opt. Soc. Am. A*, 6:1357–1367, 1989.
- [69] S. F. Gibson and F. Lanni. Experimental test of an analytical model of aberration in an oil-immersion objective lens used in three dimensional light microscopy. *J. Opt. Soc. Am. A*, 8:1601–1613, 1991.
- [70] D. Kundur and D. Hatzinakos. Blind image deconvolution. *Signal Processing Magazine, IEEE*, 13:43–64, 1996.
- [71] A. Cichocki and S. Amari. *Adaptive Blind Signal and Image Processing: Learning Algorithms and Applications*. Wiley, 2002.
- [72] O. P. Pishnyak, Y. A. Nastishin, and O. D. Lavrentovich. Comment on “self-organized periodic photonic structure in a nonchiral liquid crystal”. *Physical Review Letters*, 93:109401, 2004.
- [73] Data sheet, Octocyanobiphenyl (8CB). Technical report, Merck.
- [74] G. L. Bretthorst. *Bayesian Spectrum Analysis and Parameter Estimation*. Number 48 in Lecture Notes in Statistics. Springer-Verlag, 1988.

- [75] H. Nyquist. Regeneration theory. *Bell Sys. Tech. J.*, 11:126–147, 1932.
- [76] F. Kahn. Ir-laser-addressed thermo-optic smectic liquid-crystal storage displays. *Appl. Phys. Lett.*, 22:111–3, 1972.
- [77] J. B. Fournier, I. Dozov, and G. Durand. Surface frustration and texture instability in smectic-A liquid crystals. *Phys. Rev. A*, 41:2252–2255, 1990.
- [78] L. Cheung, R. B. Meyer, and H. Gruler. Measurements of nematic elastic constants near a second order nematic-smectic-A phase change. *Phys. Rev. Lett.*, 31:349–352, 1973.
- [79] M. Delaye, R. Ribotta, and G. Durand. Rayleigh scattering at a second-order nematic to smectic-A phase transition. *Phys. Rev. Lett.*, 31:443–445, 1973.
- [80] P. E. Cladis. Study of the bend elastic constant near a smectic-A-nematic phase transition. *Phys. Rev. Lett.*, 31:1200–1203, 1973.
- [81] K. C. Chu and W. L. McMillan. Static and dynamic behavior near a second-order smectic A nematic phase transition by light scattering. *Phys. Rev. A*, 11:1059–1067, 1975.
- [82] P. P. Karat and N. V. Madhusudhana. Elasticity and orientational order in some 4'-n-alkyl-4-cyanobiphenyls: part ii. *Mol. Cryst. Liq. Cryst.*, 40:239–245, 1977.
- [83] D. Davidov, C. R. Safinya, M. Kaplan, S. S. Dana, R. Schaezting, R. J. Birgeneau, and J. D. Litster. High-resolution x-ray and light scattering study of critical behaviour associated with the nematic-smectic-A transition in 4-cyano-4'-octylbiphenyl. *Phys. Rev. B*, 19:1657–63, 1979.
- [84] B. Malraison, Y. Poggi, and E. Guyon. Nematic liquid crystals in high magnetic field: quenching of the transverse fluctuations. *Phys. Rev. A*, 21:1012–1024, 1980.
- [85] H. Hakemi, E. F. Jagodzinski, and D. B. DuPre. The determination of the elastic constants of a series of n-alkylcyanobiphenyls by anisotropy of turbidity. *J. Chem. Phys.*, 78:1513–8, 1983.
- [86] S. DasGupta, P. Chattopadhyay, and S. K. Roy. Effect of a rigid nonpolar solute on the splay, bend elastic constants and on rotational viscosity coefficients of 4,4'-n-octyl cyanobiphenyl. *Phys. Rev. E*, 63:041703, 2001.
- [87] F. Lonberg and R. B. Meyer. New ground state for the splay-fréedericksz transition in a polymer nematic liquid crystal. *Phys. Rev. Lett.*, 55:718–721, 1985.
- [88] A. Kilian. New Freedericks thresholds in three dimensions. *Phys. Rev. E*, 50:3774–83, 1994.
- [89] D. Krzyzanski and G. Derfel. Magnetic-field-induced periodic deformations in planar nematic layers. *Phys. Rev. E*, 61:6663–8, 2000.

- [90] D. W. Allender, R. M. Hornreich, and D. L. Johnson. Theory of the stripe phase in bend-Freedericksz-geometry nematic films. *Phys. Rev. Lett.*, 59:2654–7, 1987.
- [91] D. Golovaty, L. K. Gross, S. I. Hariharan, and E. C. Gartland. On instability of a bend Freedericks configuration in nematic liquid crystals. *J. Math. Ana. App.*, 255:391–403, 2001.
- [92] G. Barbero and V. M. Pergamenschchik. Intermediate periodic “saddle-splay” nematic phase in the vicinity of a nematic–smectic-A transition. *Phys. Rev. E*, 66:051706, 2002.
- [93] V. M. Pergamenschchik. Spontaneous deformations of the uniform director ground state induced by the surfacelike elastic terms in a thin planar nematic layer. *Phys. Rev. E*, 61:3936–41, 2000.
- [94] O. D. Lavrentovich and V. M. Pergamenschchik. Patterns in thin liquid crystal films and the divergence (“surfacelike”) elasticity. *Int. J. Mod. Phys. B*, 9:2389–2437, 1995.
- [95] G. Barbero and R. Barberi. Critical thickness of a hybrid aligned nematic liquid crystal cell. *J. Phys. France*, 44:609–16, 1983.
- [96] A. Sparavigna, O. D. Lavrentovich, and A. Strigazzi. Periodic stripe domains and hybrid-alignment regime in nematic liquid crystals: Threshold analysis. *Phys. Rev. E*, 49:1344–52, 1994.
- [97] V. M. Pergamenschchik. Surfacelike-elasticity-induced spontaneous twist deformations and long-wavelength stripe domains in a hybrid nematic layer. *Phys. Rev. E*, 47:1881–92, 1993.
- [98] O. D. Lavrentovich and V. M. Pergamenschchik. Stripe domain phase of a thin nematic film and the  $k_{13}$  divergence term. *Phys. Rev. Lett.*, 73:979–82, 1994.
- [99] W. L. McMillan. Measurement of smectic-A-phase order-parameter fluctuations near a second order nematic–smectic-A phase transition. *Phys. Rev. A*, 7:1419–22, 1973.
- [100] L. A. Parry-Jones and S. J. Elston. Flexoelectric switching in a zenithally bistable nematic device. *J. Appl. Phys.*, 97(9):093515, 2005.
- [101] T. J. Spencer and C. M. Care. Modelling of nematic liquid crystal display devices. 2006. URL [arXiv:cond-mat/0602421](https://arxiv.org/abs/cond-mat/0602421).
- [102] C. S. Santangelo and R. D. Kamien. Bogomol’nyi , prasad, and sommerfield configurations in smectics. *Phys. Rev. Lett.*, 91:045506, 2003.
- [103] C. D. Santangelo and R. D. Kamien. Curvature and topology in smectic-A liquid crystals. *Proc. Roy. Soc. A*, 461:2911 – 2921, 2005.
- [104] O. D. Lavrentovich, M. Kleman, and V. M. Pergamenschchik. Nucleation of focal conic domains in smectic A liquid crystals. *J. Phys. II France*, 4:377–404, 1994.

- [105] C. Blanc and M. Kleman. Curvature walls and focal conic domains in a lyotropic lamellar phase. *Eur. Phys. J. B*, 10:53–60, 1999.
- [106] O. D. Lavrentovich and M. Kleman. Field-driven first-order structural transition in the restricted geometry of a smectic-A cell. *Phys. Rev. E*, 48:R39–42, 1993.
- [107] H. Naito, M. Okuda, and O. Zhong-can. Preferred equilibrium structures of a smectic-A phase grown from an isotropic phase: Origin of focal conic domains. *Phys. Rev. E*, 52:2095–2098, 1995.
- [108] S. Faetti and M. Riccardi. The phenomenological functions that characterize the surface free energy density of nematic liquid crystals: a microscopic analysis. *J. Phys. II France*, 5:1165–91, 1995.
- [109] J. H. Kim, J. Yoneya, J. Yamamoto, and H. Yokoyama. Surface alignment bistability of nematic liquid crystals by orientationally frustrated surface patterns. *Appl. Phys. Lett.*, 78:3055, 2001.
- [110] J. H. Kim, Makoto Yoneya, and H. Yokoyama. Tristable nematic liquid-crystal device using micropatterned surface alignment. *Nature*, 420:159–162, 2002.
- [111] J. Eakin, Y. Xie, R. A. Pelcovits, M. D. Radcliffe, and G. P. Crawford. Zero voltage Fredericksz transition in periodically aligned liquid crystals. *Appl. Phys. Lett.*, 85:1671, 2004.
- [112] J. T. Wan, O. K. C. Tsui, H. S. Kwok, and P. Sheng. Liquid crystal pretilt control by inhomogeneous surfaces. *Phys. Rev. E*, 72:021711, 2005.
- [113] M. Behdani, S. H. Keshmiri, S. Soria, M. A. Bader, J. Ihlemann, G. Marowsky, and Th. Rasing. Alignment of liquid crystals with periodic submicron structures ablated in polymeric and indium tin oxide surfaces. *Appl. Phys. Lett.*, 82:2553–2555, 2003.
- [114] P. Patricio, M. M. Telo da Gama, and S. Dietrich. Geometrically-controlled twist transitions in nematic cells. *Phys. Rev. Lett.*, 88:245502, 2002.
- [115] B. Wen, R. G. Petschek, and C. Rosenblatt. Nematic liquid crystal polarization gratings by modification of surface alignment. *Appl. Opt.*, 41:1246–1250, 2002.
- [116] M. Yoneya, J. H. Kim, and H. Yokoyama. Simple model for patterned bidirectional anchoring of nematic liquid crystal and its bistability. *Appl. Phys. Lett.*, 80:374–376, 2002.
- [117] L. Harnau, S. Kondrat, and A. Poniewierski. Phase behaviour of a nematic liquid crystal in contact with a chemically and geometrically structured substrate. *Phys. Rev. E*, 72:011701, 2005.
- [118] S. Kondrat, A. Poniewierski, and L. Harnau. Orientational phase transition and the solvation force in a nematic liquid crystal confined between inhomogeneous substrates. *Eur. Phys. J. E*, 10:163–170, 2003.
- [119] K. Okano, K. Kitahara, and E. Ushizawa. Surface disclinations on modified substrate. *Japanese Journal of Applied Physics*, 33(11):6262–6267, November 1994.



- [120] L. R. Evangelista and G. Barbero. Theoretical analysis of actual surfaces: The effect on the nematic orientation. *Phys. Rev. E*, 48(2):1163–1171, August 1993.
- [121] L. R. Evangelista and G. Barbero. Walls of orientation induced in nematic-liquid-crystal samples by inhomogeneous surfaces. *Physical Review E*, 50:2120–2133, 1994.
- [122] C. A. R. Yednak, F. C. M. Freire, E. K. Lenzi, and L. R. Evangelista. Exact tilt profiles for splay-bend deformations in nematic liquid crystals. *Liq. Cryst.*, 33:409–415, 2006.
- [123] G. Barbero, T. Beica, A. L. Alexe-Ionescu, and R. Moldovan. Anchoring energy and easy direction of non uniform surfaces. *J. Phys. II France*, 2:2011–2024, 1992.
- [124] B. Wen, J. H. Kim, H. Yokoyama, and C. Rosenblatt. Depression of the nematic-isotropic phase transition temperature at nanopatterned surfaces. *Phys. Rev. E*, 66:041502, 2002.
- [125] M. Monkade, Ph. Martinot-Lagarde, G. Durand, and C. Granjean. Sio evaporated films topography and nematic liquid crystal orientation. *J. Phys. II France*, 7:1577–1596, 1997.
- [126] P. M. Alt and P. Pleshko. Scanning limitations of liquid-crystal displays. *IEEE Trans. El. Dev.*, 21(2):146–155, 1974.
- [127] S. Kitson and A. Geisow. Controllable alignment of nematic liquid crystals around microscopic posts: Stabilization of multiple states. *Appl. Phys. Lett.*, 80(19):3635–3637, 2002.
- [128] M. Stalder and M. Schadt. Photoaligned bistable twisted nematic liquid crystal displays. *Liq. Cryst.*, 30(3):285–296, 2003.
- [129] G. P. Bryan-Brown, C. V. Brown, J. C. Jones, E. L. Wood, I. C. Sage, P. Brett, and J. Rudin. *SID DIGEST XXVIII*, 5.3:37, 1997.
- [130] A. J. Davidson and N. J. Mottram. Flexoelectric switching in a bistable nematic device. *Phys. Rev. E*, (65):051710, 2002.
- [131] M. Schadt, K. Schmitt, and V. Kozinkov. Surface-induced parallel alignment of liquid crystals by linearly polymerized photopolymers. *Jpn. J. Appl. Phys.*, 31:2155–2164, 1992.
- [132] G. P. Crawford, J. Eakin, M. D. Radcliffe, A. Callan-Jones, and R. A. Pelcovits. Liquid crystal diffraction gratings using polarization holography alignment techniques. *J. Appl. Phys.*, 98:123102, 2005.
- [133] B. Zhang, F. K. Lee, O. K. C. Tsui, and P. Sheng. *Phys. Rev. Lett.*, 91:215501, 2003.
- [134] N. Smith, P. Gass, M. Tillin, C. Raptis, and D. Burbridge. Micropatterned alignment of liquid crystals. *Sharp Technical Journal*, 92:5–10, 2006.

- [135] N. J. Smith, P. A. Gass, J. P. Bramble, M. D. Tillin, and B. M. Musgrave. Control of liquid crystal alignment in an optical device. US Patent 2005/0248705A1, November 2005.
- [136] O. D. Lavrentovich and V. M. Pergamenschik. Periodic domain-structures in thin hybrid nematic layers. *Mol. Cryst. Liq. Cryst.*, 179:125–132, 1990.
- [137] X.T. Li, D. H. Pei, S. Kobayashi, and Y. Iimura. Measurement of azimuthal anchoring energy at liquid crystal/photopolymer interface. *Jpn. J. Appl. Phys.*, 36:L432–L434, 1997.
- [138] M. Zhu, G. Carbone, and C. Rosenblatt. Electrically switchable, polarization-independent diffraction grating based on negative dielectric anisotropy liquid crystal. *Appl. Phys. Lett.*, 88:253502, 2006.
- [139] M. J. Escuti, W. J. Jones, C. Oh, R. K. Komanduri, C. Sanchez, C. W. M. Bastiaansen, and Broer D. J. Polarization-independent modulation and simplified spectropolarimetry using LC polarization gratings. In *Oral Presentation, ILCC 2006 Conference, Denver, 2006*.
- [140] I. Vilfan, M. Vilfan, and S. Zumer. Defect structures of nematic liquid crystals in cylindrical cavities. *Phys. Rev. A*, 43:6875–6880, 1991.
- [141] J. Bramble. Private communication. April 2006.
- [142] J. Bramble. Private communication. June 2006.
- [143] T. S. Taphouse. PhD thesis, University of Exeter, 2006.
- [144] H. J. Coles and M. S. Sefton. Pretransitional behaviour of the splay and twist elastic and viscosity constants for the nematic to smectic A phase transition in octocyanobiphenyl (8CB). *Mol. Cryst. Liq. Cryst. Lett.*, 4:123–33, 1987.

# Index

- 5CB, 84
- 6CB, 129
- 8CB, 39, 82, 85, 87, 145
  - Phase sequence, 57
- Air-nematic interface, 31
- Alkanethiol, 108
- Anchoring energy, 33, 54
  - Azimuthal, 33, 117, 120, 134
  - Effective due to pattern, 106
  - for Smectics, 98
  - Polar, 33, 112, 120, 134
- Anchoring potential, 33, 119
  - Harmonic, 125
  - Rapini-Papoular, 125
- Annihilation of defects, 59
- Atomic force microscope (AFM), 108
- Biaxiality, 20
- Birefringence, 19, 20
  - Effect on confocal microscopy, 50
  - Importance to Microscopy, 38
  - Temperature dependence, 26
- Bistable display, 106
  - PABN, 107
  - via AFM nanopatterning, 108
  - ZBD, 107
- Boundary conditions
  - for Numerical methods, 138
  - from Variational Calculus, 155
  - Harmonic Potential, 119
  - Surface anchoring, 35
- Brushes, *see* Schlieren textures
- BTBP, 48
- Burger's number, 89
- Calamitics, 19
- CBOOA, 79, 82, 85
- Cell construction, 56
- Chirality, 20
- Cholesteric, 20, 27, 52
  - Bistable displays, 107
  - Confocal microscopy, 46
  - Grandjean-Cano wedge, 47
- Cleaning of substrates, 56
- Coarse graining, 26
- Computer simulation, 26
- Confocal Laser Scanning Microscopy, 43
- Confocal microscopy, 42
  - Contrast ratio, 48
  - Deconvolution, 50
  - Limitations, 48
  - Point spread function, 50
- Conformal mapping, 109, 112
- Contrast ratio
  - Confocal microscopy, 48
  - Micropatterned TN cell, 129
- Curvature walls, *see* Domain walls
- Cybotactic clusters, 81
- Cylindrical cavities, 47, 126
- Defects, 27
  - in "Stripe" structure, 59, 88
- Depth of field, 43

- Dielectric permittivity, 28, 137
- Differential scanning calorimetry, 38
- Diffraction grating, 122
- Director, 27
  - Cartesian representation, 29, 136
  - Polar representation, 29, 109
  - Reconstruction from microscope images, 39, 42, 157
- Disclinations, 30, 116
  - Appearance under microscope, 38
  - Core radius, 92
- Discotics, 19
- Distribution function
  - Mass, 22
  - of guest fluorescent dye, 45
  - Orientational, 20, 22, 24
  - relationship to Contrast ratio, 50
- Divergence theorem, 27
- Domain walls, 20, 39
  - Energy, 97
  - HAN cell, 63
  - Micropatterned TN cell, 130, 135
- Dupin cyclides, 22, 54
  - Anchoring energy, 100
- E7, 20, 48, 114
- Easy axis, 33, 128
  - Effective due to pattern, 106
  - Effective for a striped surface, 110
- Eccentricity (of Ellipse), 101
- Einstein summation convention, 138
- Elastic constants
  - Bend, 27, 54, 115, 140
  - Critical exponents, 82
  - Critical phenomena, 81, 85
  - One constant approximation, 109
  - Saddle-splay, 27, 80
  - Splay, 27, 80, 115
  - Temperature dependence, 26
  - Twist, 27, 115, 122
- Elastic theory, 27
- Electric field, 28
- Electrodes, 56
- Electron microscope, 43
- Electrophoresis, 47
- Elliptic function, 34
- Elliptic integral, 36, 86
- Ericksen-Leslie theory, 27
- Euler-Lagrange equations, 29, 30, 166
  - HAN cell, 35
  - in One dimension, 164
  - in Two dimensions, 165
  - Numerical solution, 136
  - Single stripes surface, 115
  - Striped surfaces, 109
- Eulerian description of smectics, 80, 89
- Explicit solvers, 166
- Extrapolation length, 33
- Fan-shaped structure, *see* Ruan's structure
- Ferroelectric
  - Bistable displays, 107
  - Confocal microscopy, 46
- Finite anchoring, 118
- Finite differences, 137
- First order transitions, 24
- Flexoelectricity, 28, 107
- Fluctuations, 26
- Fluorescence Confocal Microscopy, 45, 69, 80, 145
  - Signal-to-noise ratio, 48
- Fluorescence Confocal Polarizing Microscopy, 46, 47, 73
- Fluorescent dye
  - BTBP, 48

- Ordering and contrast ratio, 50, 72
- Phase separation, 51
- Quenching, 51
- Stokes shift, 50
- Focal conics, 22
  - Domains, 47, 145
- Fourier series, 34, 109, 110, 115, 117, 119, 126, 133
- Fourier transform, 66
- Frank free energy, 27, 137
  - Diffraction grating cell, 122
  - HAN cell, 35
  - HTTN state, 133
  - in One dimension, 164
  - in Two dimensions, 165
  - Periodic perturbation in a HAN cell, 85
  - Striped surfaces, 109, 132
  - TN cell, 129
  - UN state, 133
- Freedericks transition
  - FCM study, 47
  - FCPM study, 47
  - Magnetic, 83
  - Threshold voltage, 141
- Frustration, 15, 33, 54, 112, 126
- Galvanic mirror, 43
- Glass
  - Homeotropic alignment, 31
- Grandjean-Cano wedge, 47
- Green's functions, 109, 112
- Guest-host effect, 45
- Guided Mode techniques, 43
- HAN cell, 35, 54, 107
  - around Nematic-Smectic transition, 58
  - Image analysis, 157
  - Microscope image, 39, 58
  - Opposing domains, 63
  - Periodic instabilities, 83
  - Reorientation wall, 39, 135
- HAN state
  - in Micropatterned TN cell, 130
- High Tilt Twisted Nematic state (HTTN), 130
- Homeotropic alignment, 30, 35, 107, 108, 128
  - Appearance under microscope, 39
  - Materials, 56
  - Patterning, 106
  - Surfactants, 30
- Homogeneous, *see* Planar
- Implicit solvers, 166
- Indium Tin Oxide, 56
- Intensity
  - FCPM, 46
  - Inverse problem, 157
  - Polarizing microscopy, 39
- Lagrange multiplier, 30, 137
- Lagrangian description of smectics, 80
- Landau coefficients, 26, 30
- Landau-de Gennes theory, 25
- Landau-Peierls Instability, 20
- Langmuir-Blodgett, 31
  - Periodic instability, 84
- Laplace equation, 109, 115
- Laplace's equation, 110
- Laser
  - Heating, 48
  - Molecular reorientation, 48
  - Tweezers, 47
- Lecithin, 56
- Legendre polynomials, 24, 33
- Leica (Confocal microscopes), 48, 69, 141
- Likelihood function, 67
- Liquid Crystal Display, 19, 128
- Lyotropic, 19

- Machine Vision, 157
- Maier-Saupe theory, 25
- Mass density, 22
- Maxwell equations, 137
- Mesophases, 19
  - Characteristic textures, 38
- Metropolis algorithm, 26
- Mettler heat stage, 58, 63
- Microcontact printing, 108
- Micropatterning, 107, 128
- Microscope
  - Confocal, 42
  - Depth of field, 38
  - Polarizing, 20, 38
  - Third-harmonic, 46
- Molecular Dynamics, 26
- Molecular-statistical theories, 25
- n-methylpyrrolidone, 56
- Nematic
  - phase, 15, 20
  - Reentrant, 20
- Nematic-Smectic transition, 58
- Newton method, 138
- Newton's rings, 114
- Nonlinear optics, 46
- Numerical integration, 117
- Numerical stability
  - of Solvers for the Euler-Lagrange equations, 166
- Nyquist theorem, 66
- One constant approximation, 109
- Onsager theory, 25
- Order parameter, 22
- Oseen-Zocher-Frank theory, 27
- Parabolic cyclides, 22
- Patterned surfaces, 106
- Penetration depth, 110, 115, 128, 134
- Phase diagram
  - Single striped surface, 121
- Photoalignment, 107, 122, 125
- Photomultiplier tube, 43
- Pinhole (confocal microscopy), 43
- Planar alignment, 30, 35, 107
  - Degenerate, 30, 39, 108
  - Materials, 56
  - Patterning, 106, 128
  - Photopolymer, 107
- Polar anchoring energy, *see* Anchoring energy
- Polarization conversion, 38
- Polarization holography, 108, 125
- Polarizing microscope, 38, 58, 113, 129
  - Image analysis, 157
- Polyimides, 56
- Polymer-stabilized liquid crystals, 45, 46
- Polymorphism, 19
- Post-aligned bistable display, 107
- Pretilt angle, 30, 128
- Q-Tensor, 24, 30
- Raman scattering, 24
- Rapini-Papoular potential, 112, 118, 134
- Rigid anchoring, 31, 36, 116
- Ruan's structure, 54, 59, 79, 100
  - Tilted TFCD model, 103
- Scalar order parameter, 24
- Schlieren texture, 39, 47
- Schuster periodogram, 66
- Second order transition, 24
- Self-assembled monolayers (SAMS), 108
- Self-assembly, 31
- Self-organization, 54, 82
- Silicon oxide, 31, 56, 63, 80, 89, 106

- Smectic, 15, 20, *see* Focal conics
  - A, 20, 22
  - B, 22
  - C, 20
  - Correlation length, 81
  - Elastic energy, 80
  - Fluctuations, 81
  - in HAN cell, 54
  - in Micropatterned TN cell, 141
  - Order parameter, 22
- Spherocylinder model, 54
- Splay-Bend configuration, 110, 116, 118, 122
  - Anomalous, 114
  - Euler-Lagrange equation, 115
  - Free energy density, 114
- Splay-Bend to Twist transition, 114
- Stability, *see* Numerical stability
- Stability criterion
  - HTTN to UN transition, 133
  - Splay-Bend to Twist transition, 116
  - UN state in conventional TN cell, 135
- Stokes shift, 50
- Stokes' theorem, 81
- Storage display, 79
- Stripe structure, 39, 59, 79
  - Confocal microscopy, 69
  - Linearized perturbation model, 84
  - Model, 84
  - Model of Cladis and Torza, 85
  - Polarizing microscopy, 58
- Stripe structure
  - Analogous phenomena in other geometries, 82
- Striped patterned surface, 110
- Surface energy, 155, *see* Anchoring energy
  - Striped surface, 120
- Surface melting, 31
  - due to nanopatterning, 106
- Symmetry, 15, 19
  - Relationship with order parameter, 22
- Tag (Fluorescent), 43, 47
- Temperature stage, 38
- Thermotropic, 19
- Toroidal coordinates, 91
- Toroidal Focal Conic Domain, 80
- Toroidal Focal Conic Domain (TFCD), 54, 77, 101
  - Anchoring energy, 95
  - Confocal microscopy, 73
  - Elastic energy, 92
  - in HAN cells prepared with silicon oxide, 91
- Tricritical point, 122
- Tristable device, 109
- Twist configuration, 110, 114, 116, 122
  - Free energy density, 114
- Twist modulation, 116
- Twisted Nematic cell
  - Appearance under microscope, 39
  - HTTN state, 130
  - Micropatterned surface, 128
  - Simulation, 140
  - UN state, 130
- Two constant approximation, 129
- Uniaxiality, 20
- Uniform configuration, 122, 124
- Uniform Nematic (UN) state, 130
- Uniform to distorted transition, 120
- V-shaped defects, *see* Defects
- Viscosity, 20
- Voxel, 43, 46
- Walls, *see* Domain walls
- X-Ray diffraction, 20, 43
- Zenithal bistable display (ZBD), 107

ZLI2293, 20